EFFICIENT MACHINE TOOL THERMAL ERROR MODELLING STRATEGY FOR ACCURATE OFFLINE ASSESSMENT

Thesis Submitted to

The School of Computing and Engineering

of

The University of Huddersfield

By

Naeem Shaukat Mian

In Partial Fulfilment of the Requirements for the Degree of

Doctor of Philosophy

December 2010

ABSTRACT

The requirement for improved dimensional accuracy to achieve ever tightening tolerances in manufactured parts increases the need for high precision machine tools. Machine tool accuracy is affected by various errors from which thermal errors have been identified as one of the largest contributors. These are primarily caused by heat generated by the machine as it operates and exogenous influences, mainly in the form of varying environmental temperature, that result in deformation of the machine structure.

There is a complex interaction between the structural components having different heat sources, thermal time constants and thermal expansions and therefore the combined effect on tool position accuracy is often non-linear and difficult to correct easily. There has been considerable research effort to model this behaviour, usually based on temperature information, to compensate the induced errors. The methods and techniques have proved their capabilities with excellent thermal prediction and compensation results but they often require significant effort for effective implementation constraints for complexity, robustness, cost and time consumption.

One of the most significant resources required is thermal testing on the machine and can be the main obstacle for the implementation of many of such methods for industries where production machine availability cannot be compromised.

This research provides a method where the machine downtime can be reduced significantly using offline simulation techniques for extended and complex real world machine operations. In this research FEA is used to simulate the thermal behaviour of the entire structure of a small milling machine using Abaqus/CAE Standard FEA software.

In order to ensure accurate simulations, heat source parameters need to be obtained for which an efficient methodology was created to calculate body heat flux values from a short test. Additionally, a study was conducted to understand the heat flow mechanism across structural joints requiring Thermal Contact Conductance (TCC) values. This research contributes experimentally obtained, and therefore accurate, TCC values for structural interface conditions compatible with CNC machine tool joints not previously

available. This was followed by the investigation of the thermal behaviour of the machine due to both internal heat and external environmental fluctuations

A broad range of operating and static stability tests were conducted to validate the FEA modelling strategy for simulating the thermal behaviour of the machine for internal heating and environmental temperature fluctuations. The simulated and experimental movement of the tool matched by more than 60% in all cases; and by more than 70% in most cases. The most significant cost benefits from this project may result from understanding behaviour during the long and very long term simulations that are impractical or unfeasible to complete experimentally. This information facilitates capability assessment and model development.

Within this research, simple linear models compatible with existing compensation capabilities in modern NC systems was targeted. Extracted FEA data is used to identify temperature-displacement sensitive areas within the full machine structure. The identification method locates structural nodes whose temperature change correlates with error at the tool to effectively install temperature sensors permanently at those positions for simple linearly correlated thermal error compensation.

ACKNOWLEDGEMENT

First and foremost I offer my sincerest gratitude to my supervisors, Dr. Simon Fletcher, Dr. Andrew Longstaff and Professor Alan Myers for supervising the project and providing support and guidance throughout the duration of the work. I owe my deepest gratitude to Dr. Simon Fletcher's encouragement and effort and without him this thesis would not have been completed or written. One simply could not wish for a better or friendlier supervisor.

Sincere thanks to Mr. Anthony Poxton for his invaluable technical support and for his generous contribution of time and advice.

I am indebted to my parents Dr. Shaukat Mahmood and Mrs. Talat Naheed Shaukat, brother Mian Adnan Shaukat, sister Fareena Faisal and other family members for their encouragement and moral support from the beginning of the project.

Sincere thanks to the laboratory staff who provided technical assistance and made available the facilities for the project.

Last, but not least, I would like to thank all my friends and colleagues who have helped in many ways, both professionally and personally.

TABLE OF CONTENTS

ABSTRACT ..... **I**

ACKNOWLEDGEMENT ..... **III**

TABLE OF CONTENTS ..... **IV**

LIST OF FIGURES ..... **X**

LIST OF TABLES ..... **XVIII**

LIST OF NOTATIONS ..... **XIX**

1 INTRODUCTION **1**

1.1 Machine tool errors **2**

1.2 Volumetric error **2**

1.3 Geometric errors **3**

1.4 Non-Rigid Errors **5**

1.5 Thermal errors **7**

1.5.1 Internal heat sources 7

1.5.2 External heat sources 8

1.5.3 Radiation sources 9

1.6 Categorizing thermal errors **11**

1.6.1 Position dependant thermal errors (PDTE) 11

1.6.2 Position independent thermal errors (PITE) 11

1.7 Thermal error effects on the machine (internal and environmental) **12**

1.8 Thermal error significance and its control **14**

1.8.1 Internal temperature control 14

1.8.2 External temperature control 15

1.9 Cost: A major issue **15**
1.9.1 Intervention costs 16
1.9.2 Machine downtime 16

1.10 Global challenges and requirements **16**

1.11 Thermal error reduction: Priorities **17**

1.12 Summary of the chapter **18**

2 LITERATURE REVIEW **20**

2.1 Machine tool calibration **20**

2.2 Thermal error consideration and avoidance **21**

2.3 Reducing structural temperature change **21**
2.3.1 Control by the machine manufacturer during design stages 22
2.3.1.1 Controlling temperature from primary heat sources 22
2.3.1.2 Controlling temperature from secondary heat sources 23
2.3.1.3 Controlling the rate of heat flow from heat sources to the structure 23
2.3.1.4 Controlling the heat magnitude by applying cooling medium 24
2.3.2 Control by the machine User 24
2.3.2.1 Warm-up cycles to reduce gradients 24
2.3.2.2 Controlling external temperature changes 25
2.3.2.3 Controlling swarf temperature 25
2.3.2.4 Controlling workpiece temperature through flood cooling 26
2.3.2.4.1 During cutting 26
2.3.2.4.2 Before machining 26

2.4 Reducing the effect of structural temperature change **27**
2.4.1 Thermal error Compensation 28
2.4.1.1 Direct measurement techniques for thermal error compensation 28
2.4.1.2 Indirect modelling techniques for thermal error compensation 30
2.4.1.2.1 Neural Networks 31
2.4.1.2.2 Regression analysis methods 34
2.4.1.2.3 Other methods 36

2.5 Finite element Analysis (FEA) **40**

2.6 Concluding past research 43

2.7 Research Aims 45

3 THERMAL STUDY OF THE MACHINE TOOL 47

3.1 Conduction 47

3.1.1 Heat flow mechanism within the machine structure through conduction 48

3.2 Convection 49

3.3 Radiation 51

3.3.1 Emissivity 52

3.4 The effect of temperature gradients 54

3.4.1 Linear thermal expansion 54

3.4.2 Non-linear thermal distortions 54

3.5 THERMAL CONTACT RESISTANCE (TCR): 55

3.5.1 TCC testing 58

3.5.1.1 Testing procedure and calculations for the convection 62

3.5.1.2 Data used for calculating the clamping force 66

3.6 Determination of convective heat transfer coefficients during tool rotation (h) 68

3.6.1 Testing procedure 68

3.6.1.1 Calculations for convective heat transfer coefficient 70

3.6.2 Summarizing convective coefficient *'h'* tests 71

3.7 Implementation of the research 72

3.8 Summary of the chapter 74

4 MACHINE TOOL INTERNAL THERMAL TESTING AND OFFLINE MODELLING 75

4.1 Benchmarks 75

4.1.1 Abaqus heat transfer benchmarks 75

4.1.1.1 Benchmark (Single Block) 75

4.1.1.2 Software modelling and FEA 76

4.1.1.2.1 Body Heat Flux (BHF) calculations (Single Block) 77

4.1.1.2.1 FEA benchmark simulation (Single block) 78
4.1.1.3 Benchmark (Assembly) 80
4.1.1.3.1 Body Heat Flux (BHF) calculations (Assembly) 81
4.1.1.3.2 Effect of thermal contact conductance 83
4.1.2 Abaqus mesh benchmark testing 85
4.1.2.1 Hexahedron meshing 85
4.1.2.2 Tetrahedron meshing 86

4.2 Machine CAD modelling 87
4.2.1 Symmetry 88
4.2.2 Machine FEA modelling setup 89
4.2.2.1 Meshing and applied constraints 89
4.2.2.2 Location of modelled heat sources in the FE model 92
4.2.2.3 Computer specifications 93

4.3 Thermal study of the machine 93
4.3.1 Machine testing 94
4.3.2 Basic machine operation at 8000rpm 95
4.3.2.1 Displacement monitoring 96
4.3.3 FEA modelling and transient simulations 100
4.3.3.1 Volume selections to obtain BHF values 100
4.3.3.1.1 Spindle (bearings and spindle belt drive heat sources) 102
4.3.3.1.2 Carrier head (belt drive and spindle motor mount plate heat sources) 103
4.3.3.1.3 Z axis motor bracket 104
4.3.3.2 BHF results 107
4.3.3.2.1 BHF calculations for the lower bearing 107
4.3.3.2.2 Abaqus Keywords Editor programming 114
4.3.3.3 Application of TCC values to the structural joints 115
4.3.3.4 Application of ambient temperatures to the FEA model 115
4.3.4 Correlations (Stabilization period) 117
4.3.5 Correlations (Machine thermal behaviour) 119
4.3.5.1.1 Calculating correlations 120
4.3.6 Re-testing the machine 121
4.3.7 Basic machine operation at 4000rpm 126

4.4 Summary of the chapter 131

5 VALIDATION OF THE APPROACH WITH LONG TERM TESTING.....133

5.1 Long term operation 133
5.1.1 Complex duty cycle operation 137

5.2 Assumptions made for calculations and internal heating simulations 140

5.3 Summary of the chapter 141

6 MACHINE TOOL ENVIRONMENTAL TEMPERATURE TESTING AND OFFLINE MODELING.....142

6.1 Long term environmental testing (summer) 142

6.2 FEA simulations (summer test) 144
6.2.1 Setup of FEA initial conditions 145
6.2.2 Determination of the settling zone 145
6.2.2.1 Application of the technique 146
6.2.3 Use of real sink temperatures for the first step 146
6.2.4 Summer test correlations 147

6.3 Long term environmental testing (winter) 148

6.4 FEA simulations (winter test) 150
6.4.1 Setup of initial conditions and time span selection 150
6.4.2 Winter test correlations 151

6.5 Summary of the chapter 152

7 FEA NODAL MANIPULATIONS.....154

7.1 Nodal data extraction 154

7.2 Internal heating test - Carrier sensitivity against the Y axis displacement 155
7.2.1 Matlab program routines 155

7.3 Internal heating test- Carrier sensitivity against the Z axis displacement 159

7.4 Environmental test –Sensitivity against the Y axis displacement 161
7.4.1 Carrier head 161

7.4.2 Column 162
7.4.3 Base 163
7.4.4 Table 165

7.5 Environmental test –Sensitivity against the Z axis displacement 166
7.5.1 Carrier head 166
7.5.2 Column 167
7.5.3 Base 168
7.5.4 Table 169

7.6 Summary of the chapter 170

8 CONCLUSIONS AND SUGGESTIONS FOR FUTURE WORK 172

8.1 Suggestions for future work 176
8.1.1 Contour plotting 176
8.1.2 Y axis tilt 177

8.2 Workpiece modelling 178

LIST OF REFERENCES 179

APPENDIX A - MATERIAL PROPERTIES AND BENCHMARK CALCULATIONS 186

APPENDIX B - CAD MODELLING OF MACHINE STRUCTURAL PARTS 187

APPENDIX C - BHF CALCULATIONS FOR HEAT SOURCES 198

APPENDIX D – MATLAB FUNCTIONS 215

LIST OF FIGURES

Figure 1-1: Possible 6 degrees of freedom for translation along an axis 3
Figure 1-2: Effect of angular rotation of a machine tool table 6
Figure 1-3: A NAS-979 component 10
Figure 1-4: Levels of remaining error after applying geometric and thermal compensation 10
Figure 1-5: Expansion and contraction of the structural elements 12
Figure 1-6: Bending of the structural elements 13
Figure 1-7: Thermal error in a machine axis due to internal heating 13
Figure 1-8: Typical thermal error in a machine due to environmental fluctuations 14
Figure 1-9: Cost vs. Tolerance 17
Figure 2-1: Modelling methods categorized according to their use 30
Figure 3-1: Heat transfer in a medium by conduction 48
Figure 3-2: A sectioned view of a typical machine tool column showing design features . 49
Figure 3-3: Convection: The heat transfer between the fluid passing over and the surface 50
Figure 3-4: A hot object radiating to cold surroundings [106] 52
Figure 3-5: An illustration of temperature gradients distorting a machine component 55
Figure 3-6: General overview of a thermal resistance across joints 55
Figure 3-7: Effects of contact pressure, contact temperature and surface roughness on interface conductance n in stainless steel 57
Figure 3-8: Test setup 59
Figure 3-9: Surface flatness (Top plate) 60
Figure 3-10: Surface flatness (Bottom plate) 60
Figure 3-11: Testing procedure to obtain TCC 61
Figure 3-12: Test conducted for 55Nm torque 61
Figure 3-13: Testing procedure for the convection (h) 62
Figure 3-14: TCC graph obtained for the test conducted with 55Nm torque 65
Figure 3-15: Clamping force and conductance values in cleaned dry and oiled conditions 66
Figure 3-16: Clamping force and thermal conductance values with curve fits (dry) 67
Figure 3-17: Clamping force and thermal conductance values with curve fits (oiled) 68
Figure 3-18: Thermal imaging of spindle and carrier 69
Figure 3-19: Thermal imaging of rotating spindle 69

Figure 3-20: Temperature measured at the test mandrel upper surface 69
Figure 3-21: Test mandrel selected area for convection calculations 70
Figure 3-22: Position of the surface and ambient sensors around the machine 71
Figure 3-23: Cincinnati Arrow 500 Vertical Milling Machine 73
Figure 4-1: Simulated temperature for the first single block benchmark..... 79
Figure 4-2: Nodal temperature showing temperature increase from 20°C to 25°C 79
Figure 4-3: Simulated temperature for the second single block benchmark 80
Figure 4-4: Nodal temperature showing temperature increase from 20°C to 24.84°C with an exponential decay trend..... 80
Figure 4-5: Created assembly in Abaqus..... 81
Figure 4-6: Simulated temperatures in assembly with very large TCC (1.e^8 W/m^2/°C) 82
Figure 4-7: Simulated temperatures in assembly with lowest contact conductance (1300W/m^2/°C)..... 83
Figure 4-8: Simulated temperatures in assembly with an assumed higher contact conductance (10000W/m^2/°C)..... 84
Figure 4-9: Temperature trend comparison between the middle and side nodes at different TCC values..... 84
Figure 4-10: Thermal deformation of the block (Hex meshing) 86
Figure 4-11: Thermal deformation of the block (Tetrahedral meshing) 87
Figure 4-12: Assembly of the machine (view 1) 88
Figure 4-13: Assembly of the machine (view 2) 89
Figure 4-14: Meshed model of the machine..... 90
Figure 4-15: Location of the applied symmetry constraint 91
Figure 4-16: Location of the applied displacement constraint 92
Figure 4-17: location of modelled heat sources in the FE model..... 92
Figure 4-18: Temperature sensors with flexible circuit board 93
Figure 4-19: ThermaCAM S65 thermal imaging camera..... 94
Figure 4-20: Thermal sensors location on the machine..... 95
Figure 4-21: Thermal image of machine head after one hour heating (8000rpm) 96
Figure 4-22: Top view thermal image of the machine (8000rpm) 96
Figure 4-23: NCDTs located around the test mandrel..... 97
Figure 4-24: Position of the NCDT nest located on the table 97

Figure 4-25: Movement of the machine in Y direction during one hour stabilisation period 98
Figure 4-26: Movement of the machine in Z direction during one hour stabilisation period 98
Figure 4-27: Machine behaviour during one hour stabilisation test 98
Figure 4-28: Measured temperature at Spindle Boss (Basic machine operation) 99
Figure 4-29: Y axis error (approx. 70µm) 99
Figure 4-30: Z axis error (approx. 23µm) 99
Figure 4-31: Measured Z displacements at the Spindle boss and the test mandrel 100
Figure 4-32: Carrier head model surface sensor strips 101
Figure 4-33: Carrier head model showing location of possible heat sources 101
Figure 4-34: Overview of structure volume selection procedure for calculating BHFs ... 101
Figure 4-35: Volume selection (Spindle) 102
Figure 4-36: Selected volume for the upper bearing 103
Figure 4-37: Selected volume for lower bearings set 103
Figure 4-38: Selected volume for the spindle belt drive heat source 103
Figure 4-39: Volume selection (Carrier) 103
Figure 4-40: Temperature sensor strip location 103
Figure 4-41: Selected volume for the belt drive heat source 104
Figure 4-42: Selected volume for the spindle motor mount plate heat source 104
Figure 4-43: The temperature data was selected from this set for BHF calculations 104
Figure 4-44: Machine column (back side) 105
Figure 4-45: Thermal image of machine column (back side) 105
Figure 4-46: Temperature data obtained from inserted points 105
Figure 4-47: Volume selection (Column) 106
Figure 4-48: Selected volume for the Z axis motor heat source 106
Figure 4-49: Trend line plotted on the spindle boss sensor data 107
Figure 4-50: Exposed area of the lower spindle housing 109
Figure 4-51: Test mandrel selected areas 109
Figure 4-52: Measured spindle boss temperature at 8000rpm 111
Figure 4-53: Initial test at 4000rpm to validate the use of a single BHF value 112
Figure 4-54: Initial stage temperature profiles correlation (8000rpm) 113

Figure 4-55: Heat flux obtained for the lower bearing at 8000rpm 113
Figure 4-56: Cp based on the temperatures at 8000rpm..... 114
Figure 4-57: Correlations for temperature profiles (8000rpm/programmed)..... 115
Figure 4-58: Convection applied to the base and table 116
Figure 4-59: Convection applied to the spindle and carrier 116
Figure 4-60: Convection applied to the column 116
Figure 4-61: Convection applied to the test mandrel 116
Figure 4-62: Ambient temperature measured inside the machine (8000rpm)..... 117
Figure 4-63: Ambient temperature measured at machine column (8000rpm) 117
Figure 4-64: Ambient temperature measured at table and base structures (8000rpm)..... 117
Figure 4-65: Nodes used to extract displacement data for both axes 118
Figure 4-66: Z-axis movement during the stabilization period 118
Figure 4-67: Y-axis movement during the stabilization period..... 118
Figure 4-68: Column bending resulted in machine deformations in Y and Z axes..... 119
Figure 4-69: Thermal image showing temperature gradients across the carrier head..... 119
Figure 4-70: Simulated temperature gradients across the carrier head 119
Figure 4-71: Position of the ambient sensors around the machine..... 121
Figure 4-72: Measured ambient temperature between column and carrier (8000rpm)..... 122
Figure 4-73: Measured ambient inside the column (8000rpm) 122
Figure 4-74: Measured ambient temperature between column and electrical cabinet (8000rpm)..... 122
Figure 4-75: Column sink temperature (1)..... 123
Figure 4-76: Column sink temperature (2)..... 123
Figure 4-77: Column sink temperature (3)..... 123
Figure 4-78: Column sink temperature (4)..... 123
Figure 4-79: Y-Displacement profiles correlation (8000rpm) 124
Figure 4-80: Z-Displacement profiles correlation (8000rpm)..... 124
Figure 4-81: Spindle boss Z-Displacement profiles correlation (8000rpm) 125
Figure 4-82: Simulated visual representation of deformation of the machine due to internal heating 126
Figure 4-83: Comparison of the spindle temperature at 4000rpm and 8000rpm speeds... 127
Figure 4-84: Ambient temperature measured inside the machine..... 127

Figure 4-85: Ambient temperature measured at the column 127
Figure 4-86: Ambient temperature measured at table and base structures 128
Figure 4-87: Measured ambient temperature between column and carrier (4000rpm) 129
Figure 4-88: Measured ambient inside the column (4000rpm) 129
Figure 4-89: Measured ambient temperature between column and electrical cabinet (4000rpm) 129
Figure 4-90: Temperature profiles correlation (4000rpm) 130
Figure 4-91: Y-Displacement profiles correlation (4000rpm) 130
Figure 4-92: Z-Displacement profiles correlation (4000rpm) 131
Figure 5-1: Measured ambient temperature inside the machine (long-term 4000rpm) 134
Figure 5-2: Measured ambient temperature at the column (long-term 4000rpm) 134
Figure 5-3: Measured ambient temperature between column and carrier (4000rpm) 135
Figure 5-4: Measured ambient inside the column (4000rpm) 135
Figure 5-5: Measured ambient temperature between column and electrical cabinet (4000rpm) 135
Figure 5-6: Temperature profiles correlation (4000rpm) 136
Figure 5-7: Y-Displacement profiles correlation (4000rpm) 136
Figure 5-8: Z-Displacement profiles correlation (4000rpm) 137
Figure 5-9: Correlations for temperature profiles (complex duty cycle) 138
Figure 5-10: Correlations for Y axis displacement profiles (complex duty cycle) 138
Figure 5-11: Correlations for Z axis displacement profiles (complex duty cycle) 139
Figure 6-1: Model of the machine with carrier head moved upward 143
Figure 6-2: Temperature profiles obtained over 3 days period 144
Figure 6-3: Measured movement in Y 144
Figure 6-4: Measured movement in Z 144
Figure 6-5: Axis offset is caused by the use of constant temperature values 145
Figure 6-6: Thermal state of the machine after first step (summer test) 147
Figure 6-7: Correlation between the measured and simulated Y axis movement with settling zone removed 148
Figure 6-8: Correlation between the measured and simulated Z axis movement with settling zone removed 148
Figure 6-9: Temperature data obtained over 3 days period 149

Figure 6-10: Measured movement in Y 149
Figure 6-11: Measured movement in Z 149
Figure 6-12: Thermal state of the machine after first step (winter test) 150
Figure 6-13: Correlation between the measured and simulated Y axis movement with settling zone removed 151
Figure 6-14: Correlation between the measured and simulated Z axis movement with settling zone removed 151
Figure 7-1: Temperature data extraction for spindle carrier 155
Figure 7-2: Slope and hysteresis plot for two random nodes 156
Figure 7-3: Node locations on the carrier 156
Figure 7-4: Part of Matlab program code for assigning range (8000rpm-Y axis) 157
Figure 7-5: Filtered nodes (8000rpm-Y axis) 158
Figure 7-6: Slope and hysteresis plot (8000rpm-Y axis) 158
Figure 7-7: Y axis carrier node location - 8000rpm 159
Figure 7-8: Part of Matlab program code for assigning range (8000rpm-Z axis) 159
Figure 7-9: Filtered nodes (8000rpm-Z axis) 160
Figure 7-10: Slope and hysteresis plot (8000rpm-Z axis) 160
Figure 7-11: Z axis carrier node location - 8000rpm 160
Figure 7-12: Matlab function calls for assigning filter range (Env-Y axis carrier head) 161
Figure 7-13: Filtered nodes (Env-Y axis carrier head) 161
Figure 7-14: Slope and hysteresis plot (Env-Y axis carrier head) 161
Figure 7-15: Y axis carrier node location - Environment 162
Figure 7-16: Matlab function calls for assigning filter range (Env-Y axis column) 162
Figure 7-17: Filtered nodes (Env-Y axis column) 163
Figure 7-18: Slope and hysteresis plot (Env-Y axis column) 163
Figure 7-19: Y axis column node location - Environment 163
Figure 7-20: Matlab function calls for assigning filter range (Env-Y axis base) 164
Figure 7-21: Filtered nodes (Env-Y axis base) 164
Figure 7-22: Slope and hysteresis plot (Env-Y axis base) 164
Figure 7-23: Y axis base node location - Environment 164
Figure 7-7-24: Matlab function calls for assigning filter range (Env-Y axis table) 165
Figure 7-25: Filtered nodes (Env-Y axis table) 165

Figure 7-26: Slope and hysteresis plot (Env-Y axis table) 165
Figure 7-27: Y axis table node location - Environment 165
Figure 7-28: Part of Matlab program code for assigning range (Env-Z axis carrier head) 166
Figure 7-29: Filtered nodes (Env-Z axis carrier head) 166
Figure 7-30: Slope and hysteresis plot (Env-Z axis carrier head) 166
Figure 7-31: Z axis carrier head node location - Environment 167
Figure 7-32: Part of Matlab program code for assigning range (Env-Z axis column) 167
Figure 7-33: Filtered nodes (Env-Z axis column) 168
Figure 7-34: Slope and hysteresis plot (Env-Z axis column) 168
Figure 7-35: Z axis column node location - Environment 168
Figure 7-7-36: Part of Matlab program code for assigning range (Env-Z axis base) 169
Figure 7-37: Filtered nodes (Env-Z axis base) 169
Figure 7-38: Slope and hysteresis plot (Env-Z axis base) 169
Figure 7-39: Z axis base node location - Environment 169
Figure 7-40: Part of Matlab program code for assigning range (Env-Z axis table 169
Figure 7-41: Filtered nodes (Env-Z axis table) 170
Figure 7-42: Slope and hysteresis plot (Env-Z axis table) 170
Figure 7-43: Z axis table node location - Environment 170
Figure 8-1: Thermal image 177
Figure 8-2: Contours plotted 177
Figure 8-3: Cutting tool tilt 178
Figure B-1: Machine Carrier head (view1) 188
Figure B-2: Machine Carrier head (view 2) 188
Figure B-3: Machine Column (view1) 189
Figure B-4: Machine Column (view2) 189
Figure B-5: Machine Table (view1) 189
Figure B-6: Machine Table (view2) 190
Figure B-7: Machine Base (view1) 190
Figure B-8: Machine Base (view2) 191
Figure B-9: Machine Saddle (view1) 191
Figure B-10: Machine Saddle (view2) 191
Figure B-11: Machine Spindle belt drive section (Top part) 192

Figure B-12: Machine Spindle (Bottom part) 193
Figure B-13: Upper and lower Bearings 193
Figure B-14: Test mandrel..... 194
Figure B-15: Guide ways for Column 194
Figure B-16: Carriage..... 195
Figure B-17: Motor support structure..... 195
Figure B-18: Structure representing spindle motor housing mount plate 196
Figure B-19: Structure representing the belt drive heat source at Spindle..... 196
Figure B-20: Structure representing the belt drive heat source inside Carrier head 197
Figure B-21: Structure representing Z axis drive motor support bracket..... 197
Figure C-1: Trend line plotted on the upper bearing sensor data 198
Figure C-2: Trend line plotted on the Line 1 sensor 3sensor data..... 200
Figure C-3: Trend line plotted on the temperature data from thermal imaging 203
Figure C-4: Trend line plotted on the temperature data from lower bearing 206
Figure C-5: Trend line plotted on the temperature data from upper bearing 207
Figure C-6: The temperature data was selected from this set for BHF calculations (4000rpm)..... 208
Figure C-7: Trend line plotted on the temperature data from carrier belt drive..... 208
Figure C-8: Trend line plotted on the temperature data from thermal imaging 209
Figure C-9: Calculated Cp values applied within ‘Artificial’ material 214
Figure C-10: Method of defining material within Abaqus Keywords editor 214
Figure C-11: Defining material for the heating cycle 214
Figure C-12: Defining material for the cooling cycle 214

LIST OF TABLES

Table 3-1: Convection values commonly used 51
Table 3-2: Emissivities of various materials found in machine tools 53
Table 3-3: Experimental values for clamping forces and conductance values at different torque ranges 67
Table 4-1: Temperature at selected nodes of the model simulated with different values of thermal contact conductance 84
Table 4-2: Machine FE model meshing information 91
Table 4-3: Lower bearing data used for BHF calculations..... 108
Table 4-4: Test mandrel data used for BHF calculations 110
Table 4-5: Calculated body heat flux values at 8000rpm spindle speed 112
Table 4-6: Calculated body heat flux values for 4000rpm spindle speed 126
Table 6-1: Comparison of measured and simulated surface temperatures after twelve hours (summer test)..... 147
Table 6-2: Comparison of measured and simulated initial surface temperatures (winter test) 151
Table A-1: Thermal conductivity values for common machine tool associated materials 186
Table A-2: List of thermal expansion coefficients for common metals 186
Table A-3: Properties of steel, cast iron and invar used in Abaqus 186
Table C-1: Upper bearing data used for BHF calculations 198
Table C-2: Carrier belt drive data used for BHF calculations..... 200
Table C-3: Spindle motor mount plate data used for BHF calculations..... 201
Table C-4: Spindle belt data used for BHF calculations 203
Table C-5: Z-axis motor mount plate data used for BHF calculations..... 205
Table C-6: Obtained Cp values with spindle boss temperature 213
Table C-7: Cp values and the corresponding temperature values (averaged to 90 points) 213

LIST OF NOTATIONS

Heat transfer

BHF	=	Body Heat Flux (W/m^3)
h	=	Convective heat transfer coefficient ($W/m^2/°C$)
h_c	=	Thermal contact conductance ($W/m^2/°C$)
Q'	=	Energy (W)
q_{conv}	=	Energy transfer through convection (W)
q_{cond}	=	Energy transfer through conduction (W)
ΔT	=	Temperature difference (°C)
k	=	Conductivity (W/m/°C)
A	=	Area (m^2)
ΔL	=	Change in Length (m)
m	=	Mass (Kg) = density (Kg/m^3) x Volume (m^3)
Cp	=	Specific heat capacity (J/Kg/°C)
t	=	Time (s)
T_{surf}	=	Surface temperature (°C)
T_{amb}	=	Ambient air temperature (°C)
dT/dx	=	temperature gradient in the x direction (°C/m)
q_{rad}	=	Energy transfer through radiation (W)
T_s	=	Temperature of the surrounding (°C)
σ	=	Stefan-Boltzmann constant (5.676x10-8 $W/m^2/°C^4$).
ε	=	Emissivity (dimensionless)
E_λ	=	Emissivity of a real body at a given wavelength
$E_{\lambda b}$	=	Emissivity of a black body at a given wavelength
$\propto$	=	Absorptivity
ρ	=	Reflectivity
τ	=	Transmissivity
α	=	Coefficient of thermal expansion
Δx_1	=	Length of wall 1
Δx_2	=	Length of wall 2

Clamping force

Pi	=	Clamping force
T	=	Applied torque
K	=	Torque coefficient
D	=	Bolt nominal shank diameter
p	=	thread pitch (bolt longitudinal distance per thread).
α	=	thread profile angle
μ_t	=	thread coefficient of friction.
μ_c	=	collar coefficient of friction.

CHAPTER - 1

1 INTRODUCTION

CNC machine tools have been used for many years due to the continuing high demand for high volume automated production with reduced time scales and cost from the precision engineering industry. The requirement for improved dimensional accuracy to achieve ever tightening tolerances in manufactured parts increases the need for high precision machine tools. This has driven machine tool manufacturers to characterize production machine tools with their ability to deliver high accuracy, long term stability and repeatability. These characteristics deliver the following advantages;

- Greater interchangeability with the reduction of hand fitting of mating parts.
- Long term machine operations which allow components to be rough machined and finish machined in one production cycle.
- Increased precision and accuracy resulting in reduced component tolerances.
- Cost reduction due to reduction of scrap and rework of out of tolerance components

Over the years, CNC machine tools have proved their significance in terms of reduced manufacturing timescales, scrap and cost causing and upsurge in CNC machine tool production. Jablonowski [1] conducted a survey of 28 countries indicated production of CNC machine tools rose to an estimated $81.5 billion in 2008, rising by 15% despite a widespread recession in the latter part of the year. The top five countries include Japan, Germany, China, Italy and Taiwan. The survey elaborates the importance of CNC machine tools which are used widely in the automotive and aerospace industries. Due to the increasing trend for manufacturing enhancements and efficiently designed products into the international markets, machine tools are expected to have an efficient, accurate and reliable behavior. Large scale production, with reduced manufacturing timescales, requires machine tools to be stable, repeatable and less susceptible to the volumetric errors which build-up during the machining operations. Machine accuracy is affected by structural geometry, thermal instability, non-rigid and dynamic effects.

1.1 Machine tool errors

Machine tool accuracy is affected by errors which lead to dimensional errors in the manufactured components. During the machining process, the dimensional accuracy of the component is dependent upon the accuracy of the relative position between the cutting tool and the work piece. The error in the relative positional accuracy is produced by the volumetric error.

1.2 Volumetric error

Volumetric error is termed as a combination of errors affecting relative positional accuracy of the tool and the work piece. This overall variability in positioning capability is caused by a number of errors, including:

- Geometric errors
- Non-rigid or loading errors
- Thermal errors
- Cutting forces induced errors
- Tool wear
- Fixturing errors
- Servo errors

Geometric, thermal and non-rigid errors fall into the category of significant contributors in machine tool deformation. The remaining errors strongly depend upon the setup procedures, work load and life of the equipment used in the manufacturing process. Several systems have been developed in light of resolving these errors. Tool wear is generated by erosion during the cutting process and its effect can be avoided or controlled by periodic inspection and replacement. Fixturing errors can have many causes including variable setting-up procedures, errors in probing, inaccuracies in the geometric tolerances and misalignments of the fixture and can often be avoided or controlled by careful fixture design and careful setup procedures. Servo errors are caused by the mismatch between the applied controller feed rates and the limited servo response or holding capacity which

can be manually controlled by the careful selection of feed rates and synchronizing the controller and servos.

1.3 Geometric errors

Geometric errors assume the structural elements to be rigid bodies. Fundamental, built-in errors are caused by dimensionless inaccuracies in the structural geometry of the machine tool. Mechanical imperfections such as misalignments of the structural members result in non-linear movements of the axes. These imperfections change over time by continuous usage, for example moving an axis towards a point and back over the lifetime of the machine will exhibit mechanical settling and wear which create changes in surface properties and shape. Imperfect axis movement results in six unwanted degrees of freedom associated to that axis which remains throughout the machine volume distorting the tool position relative to the work piece. Possible 6 degrees of freedom associated to an axis is shown in Figure 1-1.

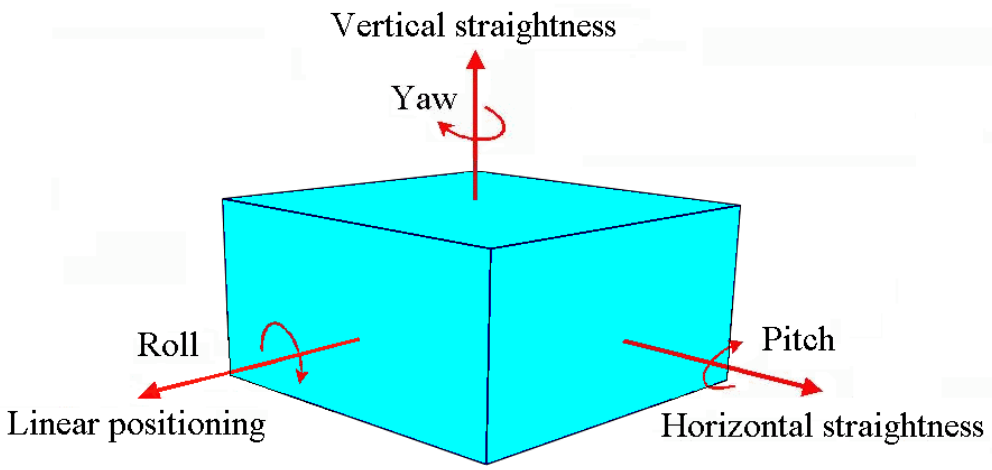

Figure 1-1: Possible 6 degrees of freedom for translation along an axis

The degrees of freedom are categorized as three translational i.e. linear positioning, horizontal and vertical straightness and three rotational i.e. roll, pitch and yaw associated to an axis. Normally for a 3 axis machine, these degrees of freedom add up to 18. Erroneous orthogonal movement of the axes or squareness also exist. Three squareness errors make the total of 21 possible geometrical error components associated with a 3 axis machine tool.

Postlethwaite [2] shows that geometrical error components have two main constituents; these are systematic or repeatable and random or non-repeatable errors. Systematic errors are dominant in machine tools and may be measured to quantify the accuracy of a machine tool. Due to its repeatable nature, these errors can be eliminated using compensation techniques such as, changing the part program or in-built NC functions. The systematic errors can be broken down further into 1) Non-cyclic or progressive error, 2) Cyclic error, and 3) Backlash error.

Random or non repeatable constituent cannot be measured directly however can be analyzed and expressed statistically. The non-repeatable nature of these errors restrict elimination using compensation techniques, however the information obtained from these errors can be utilized as a guide to improve the degree of accuracy used in compensation systems.

White [3] has summarized various methods that can be used to reduce geometric errors such as

- Mechanically resetting/correcting the machine.
- Modifying the part program.
- Positioning the workpiece in a part of the machine volume that exhibits less error.
- Orientating the workpiece such that critical dimensions are affected by an axis or axes that exhibits less error.
- Correcting the effects of the geometric error during machining by forcing the machine's axes to re-position.
- On and off line probing or measurement and correction.
- Geometric error compensation systems

A geometric compensation system was created by Postlethwaite [2] and proved this method's success in reducing geometric errors exhibited on a wide variety of machines, in some cases the achieved accuracy was observed to be 20:1 on a larger axis travel machines. Research by Longstaff et al [4] revealed even greater success achieving up to

97% reduction of the measured geometric errors. The results have shown that an excellent understanding among engineers has been gained towards reduction of geometrical effects through the implementation of the compensation systems.

1.4 Non-Rigid Errors

Geometric errors are also known as rigid body errors as they are assumed to be applied without any specified loading conditions. Lack of rigidity in the machine tool structure can lead to non rigid effects or load induced errors. These result from factors such as inertia, own and workpiece mass or cutting forces. These errors vary with different speed, cutting and loading conditions. [3, 5-8]. The overall effect of these errors is generally small compared to geometric errors but can become significant if those have been compensated or due to:

- Machine axis movement

  Movement of the machine axis causes a new mass distribution on the machine structure, resulting in deformation and an effective change in the geometric error components.

- Mass of the work piece

  Adding a component to the machine table produces a change of loading of the machine structure, movement of the axis during machining will cause a change in deformation.

- Cutting loads

  Forces present during the cutting process introduce loading into the machine structure. Taking deep cuts into the workpiece can produce large errors, however high accuracy is not normally required during heavy cuts.

- Cutting tool mass

  Single tool mass should not provide excessive loading of the structure, however, multiple tool turrets introduce concentrated loading onto the headstock, causing extra loading close to the point of machining.

- Fixture stiffness

The stiffness of fixtures is usually relatively high compared to the more complex machine tool structure. However, this may not true, as work holding and fixture design becomes increasingly complex and less material is used for clamping.

There are a number of methods which can be used to eliminate these errors, better selection of the cutting speeds, feed rate and depth of cut can reduce cutting load errors. Mechanical adjustments and pre-loading of the structural elements could reduce excessive and uneven loading problems by even distribution of the mass. Fixture stiffness relies on good design as well as cutting parameters. The other three are fundamental to the operation of the machine tool and cannot be greatly influenced by the user. Some prevention can be achieved by controlling mass distribution such as keeping workpiece and fixture mass in the middle of the table to minimise cantilever effects.

Non-rigid errors manifest themselves as small angular errors that change as a result of one or more axes moving. These angular changes might be small in comparison with some of the other errors experienced on a machine but they can become more significant on larger machines. How angular errors affect volumetric accuracy is sometimes misunderstood. Figure 1-2 shows that as the headslide of a machine moves away from the table, the resultant error '$\in$' increases. The distance from the centre of rotation to the tool/workpiece interface is called the 'Abbe' offset.

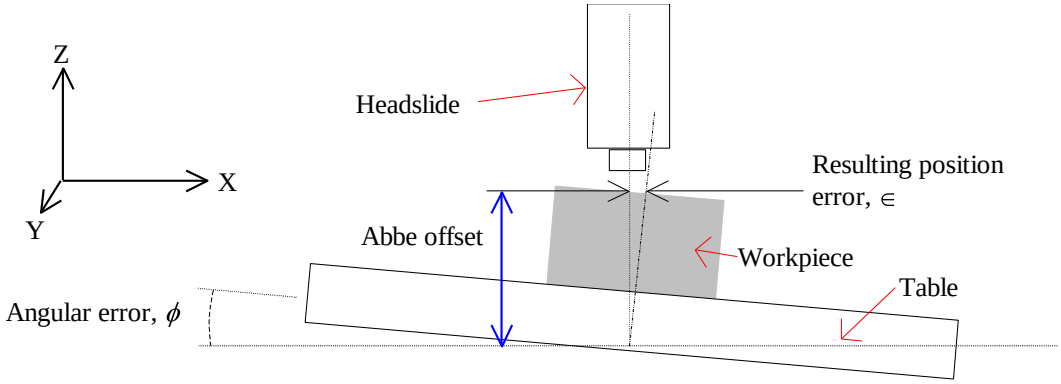

Figure 1-2: Effect of angular rotation of a machine tool table

The effect described can be represented by the simple equation 1.1

$$\in_x = \phi_{X(Y)} \cdot Z \quad \text{..... (1.1)}$$

Using this equation, a 5 arc-second pitch error (rotation of the X axis about the Y axis) will result in 24μm of error over 1m. On large machines, the angular effects can be magnified considerably.

Comparatively, non-rigid errors are considered as one of the smallest contributor towards inaccuracy of the machine tool, consequently there has been limited research in reducing or compensating non rigid.

1.5 Thermal errors

Thermal errors in machine tools are produced due to temperature changes in the structure. Variations in the temperature arise from heat sources which can be categorized into internal heating, external environmental variations and radiation. Temperature gradients lead to non-linear thermal expansion of structural elements and ultimately a complex interaction between the tool and workpiece.

Each thermal source can be further categorized:

1.5.1 Internal heat sources

Internal heat sources are produced by machine structural elements that self generate temperature gradients across the machine tool structure. They are the most influential source of temperature excitation as they due to the movement of machine axes, spindle bearings etc. Typical internal heat sources are motors, spindle bearings and belt drives where friction is a significant cause of temperature rise. Other contributors to internal heat include transmission systems such as gear boxes; friction from axes drive systems and seals; and viscous hydraulic systems. The generated heat flows through the machine structure in the form of temperature gradients and disseminates throughout structure volume resulting in thermal expansions of structural components. The heat flow also depends on the machine operating conditions such as hard machining process where spindle operates at high speeds, can produce severe distortions if temperature variations are significant.

1.5.2 External heat sources

External heat sources, in general, are creators of the change in temperature around the machine vicinity. There are various sources which cause environmental temperature to vary in a typical workshop environment for example, a natural temperature fluctuation that arise from the day and night transitions. Fletcher [9] has discussed other sources as

- Opening and closing of workshop doors

  In workshops, doors are used for people access, deliveries of the goods etc. which creates draughts and variations in ambient temperature.

- Heat generated by the machining process

  During machine cutting operations heat generates due to localised friction between the tool edges and the work piece. This heat then flows through the tool to into the machine structure.

- Heat gain from the machine control system

  This heat comes from the electrical compartments and the associated cabling passing through the structure inducing localised variation in environmental temperature conditions.

- Heat generated by other machines in the vicinity

  Other machines operating in parallel within a shop floor cause an environmental temperature rise. The fluctuations in the environmental temperature affect machine tool structural behaviour.

- Workshop heating

  There are several factors which are responsible for workshop temperature rise. For example, outside temperature, long term openings of the doors for deliveries, heating and cooling systems within building etc. can result in producing vertical thermal gradients in workshop.

- Direct sunlight

  Positioning the machine under direct sunlight coming through windows change the temperature of the directly exposed structure.

1.5.3 Radiation sources

Radiation originates from special heat sources. In a typical workshop it may come from the warmth of the sun and other hot surfaces to which the machine tool surfaces are exposed. Radiative sources other than the sun are generally much lower in energy transfer due to the low temperature ranges experienced in machines.

Each error discussed contributes within the machine tool working volume resulting in the distortion of positional accuracy between the cutting tool and the work piece. The compound effect of the errors is termed as the machine tool volumetric error. Bryan discussed that thermal error can represent 70% of the total volumetric error [10] which is a significant proportion. Research undertaken at the University of Huddersfield (GR/R13401/01) used a NAS-979 (circle-diamond-square) component to validate geometric and thermal. Three test pieces were produced from aluminium under similar test conditions: with an uncompensated machine; with geometric compensation only; with both geometric and thermal compensation. Figure 1-3 shows one such component. Some representative dimensions, which were measured on a CMM, are:

- Size of square (D1, D2)
- Size of diamond (D3, D4)
- Diameter of circle

Figure 1-4 shows the errors for the three samples and highlights the significant contribution from thermal errors. . For example feature D1 (square) shows the machine error of approximately 38µm. The geometric compensation was first applied which achieved approximately 40% reduction of the error to 23µm. With thermal compensation also applied the error was further reduced to approximately 3µm. This shows that thermal error alone represented more than 50% of the error. Similarly with the feature D3 (diamond), geometric compensation reduced the total error of approximately 37µm to approximately 31µm (15%). The remaining error was then further reduced to

approximately 3µm by the application of thermal compensation, representing 75% of the total error.

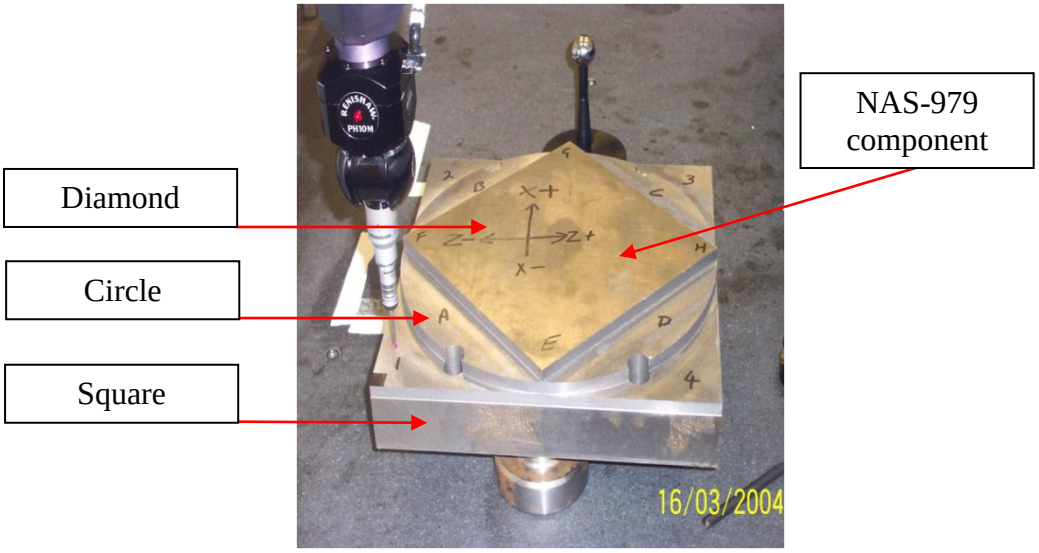

Figure 1-3: A NAS-979 component

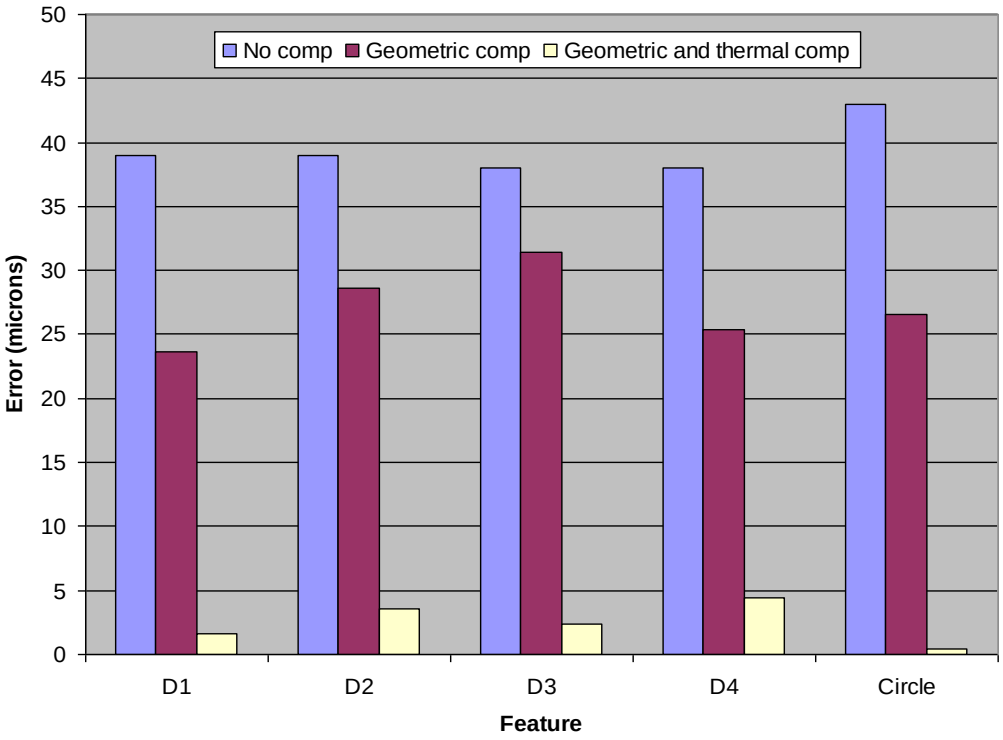

Figure 1-4: Levels of remaining error after applying geometric and thermal compensation

High importance was therefore given to evaluate and quantify the significance of thermal errors in order to reduce their effect within machine tools by development of efficient thermal compensation techniques.

1.6 Categorizing thermal errors

Thermal error sources fall into two categories. Allen [11] has discussed these categories to be

- Position dependant thermal errors (PDTE)
- Position independent thermal errors (PITE)

1.6.1 Position dependant thermal errors (PDTE)

PDTE produce changes in the linear positioning of the machine which occur due to thermal expansions of machine structure and position feedback systems. PDTE change with temperature and with position of the axes. For example PDTE will occur if the coefficient of thermal expansion of the machine does not match that of component.

1.6.2 Position independent thermal errors (PITE)

PITE produce drift in the offsets of the machine which occurs due to changes in temperature and are which are independent of the position of the machine axes. The effect of PITE on component accuracy is strongly dependent on the rate of change of PITE relative to the time taken to produce the component. Even large changes in PITE may result in little error if there is no significant time taken to machine a component.

Slowly changing PITE can, however, be particularly significant if the component is rotated as part of the manufacturing process and the distance between cuts made before and after rotation is critical. Any offset that exists between the tool and workpiece will be reproduced on the component and if the component is reversed then the total error will be double the offset. If the component is not moved then, although the offset will appear on all the machined surfaces, the distances between surfaces should be accurate.

1.7 Thermal error effects on the machine (internal and environmental)

Machine tools behave differently when subjected to internally generated heat or external temperature variations. Internal heat distribution involves heat flow within the main structural elements and associated complex discrete structures often producing significant temperature gradients. Combined with different thermal time constants of the materials and elements, this complex interaction produces non linear thermal deformation of the machine. The total deformations or the error produced is the compound effect of the linear and non linear behaviour of the structural elements due to uneven heat distribution mainly across the joints.

Unlike machine internal heat distribution and the deformations where structural elements respond to minor temperature changes, external temperature variations affect larger areas of machine structure where a group of structural elements expands and contracts according to the fluctuating environment. The deformations produced in this case again can be linear or non linear due to the uneven temperature gradient distribution within the structure mainly produced by fluctuating temperature magnitudes.

Temperature gradients produced by the internal and external heat sources cause expansions, contractions and bending of the structure. Figure 1-5 and Figure 1-6 show the typical behaviour of a machine tool.

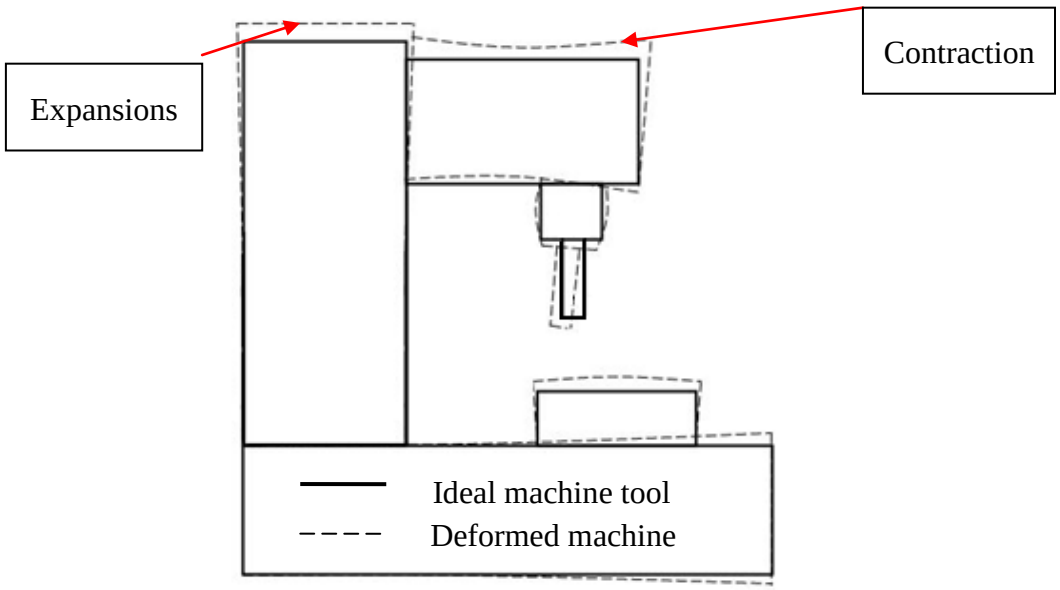

Figure 1-5: Expansion and contraction of the structural elements

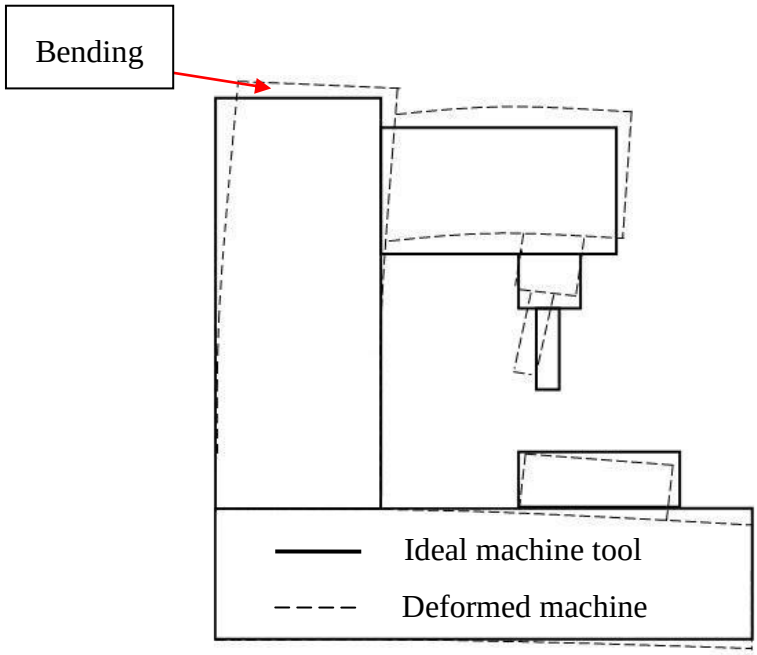

Figure 1-6: Bending of the structural elements

Figure 1-7 shows measured thermal error magnitude of approximately 20µm exhibited by the machine under research in the Y axis direction during one hour spindle heating followed by the cooling period; and Figure 1-8 (cited from Longstaff et al [12]) shows typical thermal error magnitudes exhibited by a machine due to environmental fluctuations over 50 hours period exhibiting approximately 40µm error at the spindle boss.

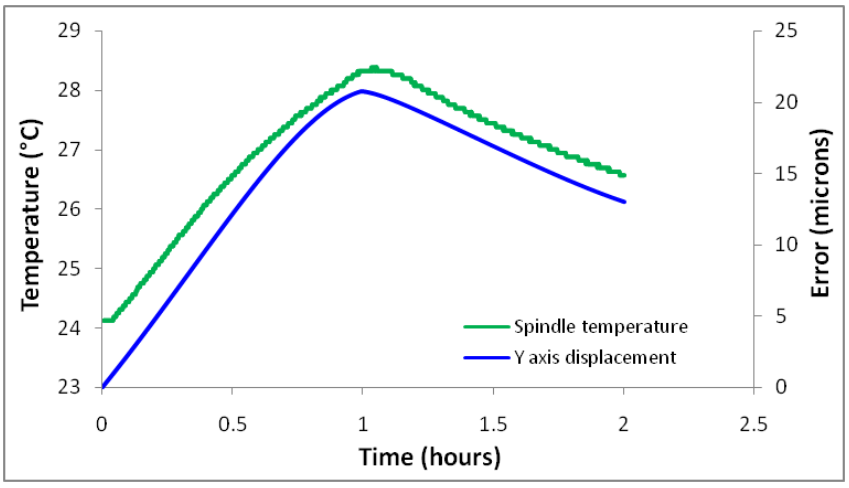

Figure 1-7: Thermal error in a machine axis due to internal heating

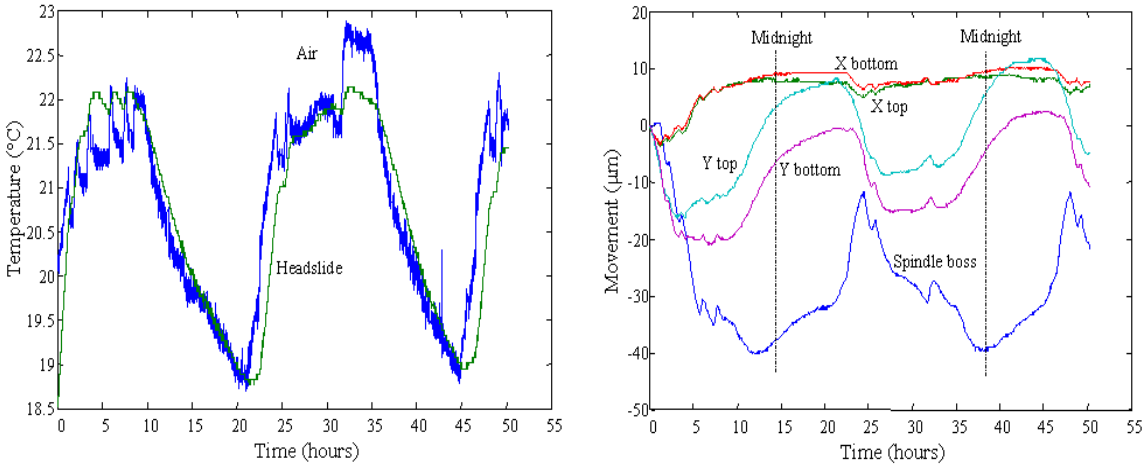

Figure 1-8: Typical thermal error in a machine due to environmental fluctuations

1.8 Thermal error significance and its control

Thermal errors have been a major issue for achieving tighter tolerances in manufactured parts. A machine tool has to be reliable and stable in order to drive through the demands of accomplishing higher accuracy goals, to achieve this a machine tool has to acquire thermal stability i.e. be less susceptible to internal and external temperature effects.

Control of temperature and its effects in machine tools has been an important research area that has been conducted for a number of decades. Postlethwaite and Ramesh [13, 14] has carried out thermal error reviews and appraisals in which significance of thermal problems were highlighted which followed by another state of the art review by Li et al [15]. From the reviews it can be elaborated that thermal error is considered a significantly important factor where internal heat and external temperature variations act as major threats to machine tool accuracy.

Several methods have been discussed in the reviews [13-15] in view for controlling internal and external temperature as follows:

1.8.1 Internal temperature control

Friction is widely recognized as a major source of elevating temperature in spindle bearings and contacting seals. Temperature rise can be reduced by using proper lubrication and by replacing the bearing type for example heat generated by the plain bearings could be reduced by replacing them with angular contact ball bearings. Spindle

cooling systems can significantly reduce the excess heat produced by the bearing friction. Heat produced by friction in contacting seals could be reduced by using less number of seals with minimum oil lubrication. Coolant systems are very effective when it comes to reduce the heat generation in the tool due to friction produced during the cutting process. Kaminski [16] has discussed a possible way to reduce tool tip temperatures by spraying the coolant straight onto the tool tip which sees highest temperatures during cutting.

1.8.2 External temperature control

External temperature variation in a typical workshop can be controlled by the installation of a temperature control system. This will reduce the uncertainty of thermal error contribution from the natural day and night temperature fluctuations. Temperature rise due to other machining operations around the machine's vicinity also contributes in the total thermal error and a crucial element. Locating machine tools at a suitable distance will reduce the possibility of the temperature rise that varies the machine structural temperature. Temperature variations incurred by opening and closing the doors can be controlled by placing the machine tools away from doors. Radiation effects can be controlled by locating the machine tool in areas where direct sunlight can be avoided.

1.9 Cost: A major issue

'It is very common for manufacturers to unknowingly expend significant resources and costs' (quoted from [17]). Cost is a significant factor and a major concern among industry when controlling the sources of errors to reduce their effects. Costs related to rescheduling, reworking and reproducing the out of tolerance parts are sometimes beyond the scope for such industries where production timescales are critical and cannot be compromised over remanufacture. Furthermore it is often the case that an industrial problem will be neglected because the relative cost of assigning time and resources to analysis and rectification will exceed the perceived benefits of reduced reworking and scrap etc. Pascual et al [18] has discussed a general approach in effectiveness with respect to expected life cycle cost rate. The paper classifies the cost in two categories, intervention costs and machine downtime costs.

1.9.1 Intervention costs

Intervention costs relate to a system where a problem such as equipment failures can be rectified by involving labour and material. Intervention costs can be easily quantified as standard accounting procedures.

1.9.2 Machine downtime

Pascual [18] highlighted the complexities involved with overcoming downtime issues for companies as it depends on several external factors such as production rates, stock prices and system design parameters. Both categories discussed can be translated to a machine tool manufacturer.

A machine tool could be out of production due to a number of reasons such as maintenance, testing, calibration, analysis of the error sources and procedures for compensating errors. If a machine tool fails to achieve its required accuracy during production, the costs associated with the labour and material required for machine check-up and rectification respectively falls into the category of intervention costs; and the time taken by the machine to resume with its normal schedule falls into the category of machine downtime costs. Both intervention and downtime adds to define the global cost.

1.10 Global challenges and requirements

The goal for any manufacturing industry is to produce parts within the required accuracy. The increasing trends for higher accuracy among industries such as Aerospace have ramped up extreme quality controls for the manufactured parts. In order to meet industrial quality control requirements, machine tool manufacturers aim to deliver competitively functional, robust, reliable and efficient machine tools. ‘The ideal case for a machine tool would be for every axis to be perfectly straight and square’ [17]. However, continuous usage of the machine increases its sensitivity to errors and decreases its reliability. This in turn increase the risks involved in achieving required tolerances on finished parts resulting in scrap and waste.

As a challenge, machine tool builders aim to continually improve machine tool accuracy which in most cases, is not practical or cost effective to further improve machine accuracy through machine design modifications. Figure 1-9 shows a cost vs.

tolerance (precision) chart representing that the cost rises sharply with small tolerances i.e. increased precision.

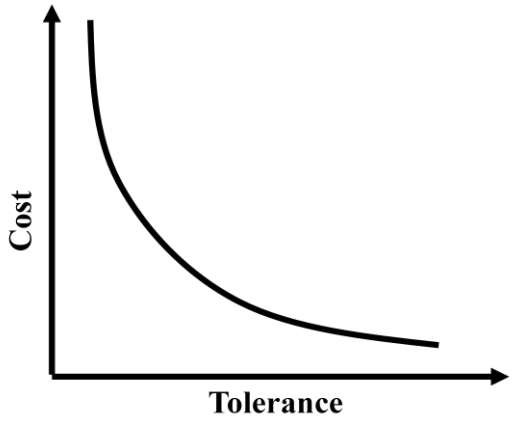

Figure 1-9: Cost vs. Tolerance

However, for machine tool consumers, machine downtime is one of the challenges besides achieving the required accuracy in produced parts and greater customer satisfaction. As discussed by Dorf et al [19], industries are always on the risk of encountering machine downtime when a machine tool malfunctions, which primarily comes from the error sources described previously. The following discussion highlights the challenges associated with thermal errors.

Thermal errors are critical because of their non-repeatable nature especially those caused by the varying environment. Thermal error control is a major challenge for both the manufacturer and the consumer of machine tools. The importance of thermal errors led research to be carried out into controlling thermal errors. Several techniques and methods were developed for thermal error reductions such as temperature control from heat sources, structural design changes, structural material selection and thermal compensation. Research into reduction techniques and methods with their applications will be covered in detail in chapter 2.

1.11 Thermal error reduction: Priorities

Issues related to costs, machine downtime, labour, maintenance and material etc. led industry to set priorities for selection of thermal error reduction strategy, focusing on utilizing a technique which is efficient, quick, robust and also a low cost solution. For

example, if thermal error affected a machine tool, the procedure of investigation can follow:

- Experimental testing, possibly in accordance with ISO standards
- Data manipulation
- Thermal error estimation
- Corrective procedures or software based compensation

As mentioned earlier that achieving accuracy through machine structural design modifications is not practical or cost effective consequently software based thermal compensation methods have gained popularity within industries. However compensation methods are mostly based on the above specified online investigation procedures which impose significant machine downtime before a machine is fully functional and back to its normal production cycle. A number of thermal compensation methods are reviewed in chapter 2.

Offline thermal assessments and reduction techniques are ones to which industry and research seek due the advantage of reduced downtime i.e. releasing the machine to work as normal after acquiring enough suitable data for offline assessments. This research focuses on dramatically reducing the costs associated with the current methods and procedures for thermal error reduction by creating a method for offline thermal assessment to predict thermal behaviour of a machine tool. Details of using this method and associated research will be covered in later chapters.

1.12 Summary of the chapter

Demands for automated productions with higher accuracy and tight tolerances have led CNC machine tools to be used extensively. Automated production increases productivity and flexibility while reducing manufacturing time and labour costs.

Volumetric error is a combination of errors affecting machine tool accuracy; it constitutes errors such as geometric, thermal, non-rigid, wear, servo, cutting forces, fixturing etc. Thermal errors can be the most significant contributor to the overall capability.

Geometric errors can be controlled or corrected through various methods but primarily, and most cost effectively, through the use of software error compensation systems. Non-rigid errors are often the smallest contributor in overall volumetric error and consequently there has been limited research into non-rigid error reduction and compensation. Thermal errors are complex and can have the greatest influence on the accuracy of the part but be the most difficult to solve due to the complex non-linear and non repeatable affect on the tool workpiece interface. They become more vital when higher accuracies with tight tolerances are required.

Thermal errors are produced by heat generated internally and environmental temperature fluctuations within the machine vicinity. Dominant internal heat sources are bearings, motors and belt drives. Transmission systems such as gear boxes, hydraulics systems etc. also cause structural temperature rise. Dominant sources that contribute towards environmental changes i.e. the shop floor temperature fluctuations are opening and closing of the doors, machining processes around the machine vicinity, workshop heating, direct sunlight etc. and radiation. Both internal and external sources cause temperature gradients in machine structural elements resulting in structural expansion and bending. Thermal errors fall into two categories which are

- Position dependant thermal errors (PDTE)

  Change in linear positioning error of the machine due to position and temperature

- Position independent thermal errors (PITE).

  Change in machine offsets due to changes in temperature

Thermal error reduction and control is a major challenge accepted worldwide. There have been requirements and priorities set by industry over control and reduction of thermal errors. One of the highlighted priorities is reducing machine downtime associated with machine testing and corrective procedures. Cost is a significant factor associated with machine downtime resulting in loss of production. Cost and machine downtime issues have led industries to seek reliable and efficient offline methods for thermal assessments and reduction.

CHAPTER - 2

2 LITERATURE REVIEW

The previous chapter discussed the significance of machine tool thermal errors. It has been identified that thermal effect can often represent the largest proportion of errors within the machine tool. Thermal errors are complex, non-repeatable and in most cases produce non- linear deformations due to uneven temperature gradients through machine structural elements. Each constituent element of the assembly is likely to behaviour possess differing characteristics such as thermal expansion coefficient, thermal time constant and heat distribution leading to complex non-linear deformations.

Identifying error components through appropriate measurement in a machine tool helps provide a platform where the machine can be checked against acceptable tolerance and specification bands.

2.1 Machine tool calibration

Wang [9, 20] highlighted that regular calibration can provide an early warning for detection and prediction when a machine tool is likely to need attention. Calibration provides a means of characterising machine performance, diagnosing specific accuracy problems and providing raw data for error compensations.

Calibration requires robust testing regimes which can deliver useful data required for a specific error measurement. ISO 230 Part 3 [21] provides a test code for machine tool thermal error measurements and standardizes testing regimes applicable to most of the machine tool types, however to make it universally applicable, compromises may be required. Longstaff et al [12] discussed the practical experience of testing with reference to ISO 230 Part 3. Different machines were tested in differing environments while working to the basic principles of this standard. It was suggested that the reason for testing should be determined first as it may modify or deviate from the standard applicable to the machine requirement and environment.

Standardizing testing methods have simplified calibrations of machine tools for identifying errors. Measurement standards help selection of suitable error identification

techniques whilst ensuring which, where and how to use the technique is essential, especially when it comes to extensive industrial applications. Knowledge and expertise in understanding the machine behaviour and requirements is critical before a technique is selected and as previously mentioned, the procedure may require to be modified specific to the machine application for calibrating and retrieving error data.

Suitable calibration technique will identify one or more thermal errors. Once identified, error reduction strategies can be deployed to ovoid, reduce or compensate using various commercially available techniques. This will be discussed in later sections, to review the work carried out to date in reduction of thermal errors.

2.2 Thermal error consideration and avoidance

Industries have concerns over the reduction of thermal errors; however careful selection of reduction strategy is critical considering the cost associated with factors such as the efficiency and machine downtime required for successful application.

In order to reduce thermal errors it is necessary to determine possible sources which contribute to generation of the thermal errors. Error avoidance is a technique which is effectively used to reduce or eliminate the sources of errors or their effects. Avoiding common sources such as unnecessary use of workshop lighting, varying workshop temperature, excess frictions etc may decrease the uncertainty of their contribution in the total magnitude of thermal error, consequently leading to better control on thermal error reduction.

Thermal error reductions are possible by

- Reducing structural temperature change
- Reducing the effect of structural temperature change

2.3 Reducing structural temperature change

Reducing structural temperature change can be achieved in a number of ways. Heat from the sources internal to the machine and external temperature variations must be controlled to reduce inevitable structural distortion. There are many possible methods that could be applied that aid structural temperature control and reduction. These methods

may be categorized by their application during and after machine design stages which follows:-

a) Control by the machine manufacturer during design stages

- Controlling temperature from primary heat sources
- Controlling temperature from secondary heat sources
- Controlling the rate of heat flow from heat sources to the structure
- Controlling the heat magnitude by applying cooling medium

b) Control by the machine User

- Warm-up cycles to reduce gradients
- Controlling environment and external temperature
- Controlling workpiece temperature through flood cooling

2.3.1 Control by the machine manufacturer during design stages

2.3.1.1 Controlling temperature from primary heat sources

Primary heat sources can significantly affect machine structure due to the higher magnitude of the resulting temperatures. Suitable measures must be applied during the machine design stages in order to control the energy transfer.

- Efficient motors and converters can significantly reduce the risk of excess temperature generation by having better control on energy losses [22].
- Temperature rise in bearings can be controlled by replacing traditional constant pressure preload with variable preload technology. Jiang et al [23] investigated and showed that varying preload at high spindle speeds produces less temperature rise compared with traditional constant pressure preloads.
- Corning [24] highlighted that proper bearing lubrication provides a means to restrict excess heating problems. Loss of lubricant, grease incompatibility, incorrect grease,

grease degradation and excess lubrication are some typical causes of bearing temperature rise and bearing failure.

- Electrical servo drives can significantly produce less heat compared to hydraulic servo drives.

- Motors on vertical axes are constantly energised to hold against gravity. Mechanical counterweight or over specifying the motor power can reduce the heat generated.

2.3.1.2 **Controlling temperature from secondary heat sources**

Secondary heat sources produce lower temperature magnitudes and have a less significant affect on the machine structure as heat disseminates gradually causing structural temperature rise to occur more uniformly which in turn produce more linear deformations. Methods can be used to avoid the effect of these heat sources such as:-

- Electrical cabinets can be located at a suitable distance from the structure so that the heat generated from the electrical power systems is not transmitted to the structure.

- Movements between mechanical components such as axes over guide ways, ball screws and support bearings etc generate heat due to friction. This heat can be controlled by reducing friction between the surfaces using manufacturer recommended lubrication methods or by applying cooling systems.

- Careful selection of feed rates and coolant to reduce the heat generated during the cutting process itself.

- Heat generated by coolant pumps and other external systems can be controlled by isolating the equipment away from the machine structure so that the heat convected does not cause a temperature rise in to the structure.

2.3.1.3 **Controlling the rate of heat flow from heat sources to the structure**

- Postlethwaite [13] discussed that the easiest way for the manufacturer is to place the motors outside of the machine structure so that the heat drawn from the motors can be directly convected away without passing through the structure which would otherwise cause an increase in the structure temperature.

- Thermal insulations can be applied to prevent conductive heat flow from the heat sources mounted on the structure.

- Kushnir [25] discussed a way to control the heat flow by the use of low conductivity materials such as polymer composites for manufacturing machine tool structural components.

- Swarf left over from the cutting operation contains high temperature and its contact with the machine structure should be avoided. Swarf removal systems and coolant reduce this problem.

2.3.1.4 **Controlling the heat magnitude by applying cooling medium**

Abele et al [26] has discussed methods such as channelling coolant flow through the structural loop local to heat sources and spraying mechanisms are considered at design stages of a machine tool. The main heat sources such as spindles are often equipped with internal cooling systems by spindle manufacturers.

Machine tool ballscrews are sometimes cooled in a similar way by applying coolant mechanisms within their structure such as hollow shaft ballscrews. Chang et al [27] discussed a cooling system for ballscrews equipped with an external chiller unit which circulates chilled oil or water through the screw to maintain a constant temperature.

Cooling mechanisms described above can provide significant control of the heat dissipation and are well considered at design stages, however such systems are often expensive due to their design requirements and hardware/maintenance costs [27].

2.3.2 Control by the machine User

2.3.2.1 **Warm-up cycles to reduce gradients**

Warm-up cycle is a time period during which a machine tool retains its thermal stability when it is used after periods of standing idle for hours. A common way to achieve is by de-activating the E-Stop which activates axis drives and motors which are used to hold structural parts in position. The activation causes them to warm up due to which heat disseminates into associated structures and continues until a state of thermal equilibrium is achieved.

2.3.2.2 **Controlling external temperature changes**

Previous sections detailed how machine tools are affected by external heat sources followed by the discussion on controlling techniques. As a machine tool user, control should be considered for the environment where the machine will be used. Sagar [28] has discussed and highlighted the importance of controlling long term temperature variations in order to achieve required accuracy and true process capability. Seasonal changes, day and night transitions, machine location, workshop location, thermal characteristics of the machine shop, sunlight exposures, opening and closing the doors for material delivery are few of the contributing sources of external temperature change, often producing very large temperature variations of more than ±5°C experimentally shown by Longstaff et al [12] Sagar et al [28] and Weck et al [29].

Shop floor temperature control can assure temperature stability for such industries where long term production cycles take place. The machines structure and the components waiting to be machined will be safe from temperature variations. Although temperature control is effective, it is often a very expensive solution and few industries can justify implementation, however few practical alternatives exist to avoid environmental temperature variations such as those caused by the natural day and night or seasonal transitions.

Previously discussed external sources such as opening and closing of the doors and workshop lighting are areas where a machine tool user is responsible. Even a temperature controlled environment does not work if there are significant interruptions due to unnecessary or frequent localised disturbances.

2.3.2.3 **Controlling swarf temperature**

The swarf from the cutting process contains heat generated by friction between the cutting tool and the work piece surface. If not managed this can raise the temperature of the machine structure and/or the workpiece leading to distortion. Swarf temperature may be reduced through the use of coolant which can also aid swarf removal from the cutting zone.

2.3.2.4 **Controlling workpiece temperature through flood cooling**

2.3.2.4.1 During cutting

Continuous coolant spray may prevent temperature increase due to the fluids high heat capacity. There have been many aspects and issues related to the use of the flood cooling mechanisms. Hoff [30] highlighted issues regarding coolant mechanisms such as chip build-up blocking free flow of coolant, time consuming and laborious removal of sump cleaning, contamination with lubricants, chemical reactions issues with hydraulic hoses and electrical cables and environmental health and safety hazards. Fluid disposal, toxicity, filterability, misting, staining and surface cleanliness are areas where coolants acts as environmental hazards.

Compared to flood cooling Boelkins [31] discussed that Minimum Quantity Lubrication (MQL) or near dry machining is one of the methods which have gained popularity in an effort to minimize environmental effects. In this method, minute amount of high efficiency lubricant is applied precisely to the cutting tool and workpiece interface. The most common lubricants used in MQL are biodegradable vegetable oils due to their polarity, exhibiting extensive friction reducing properties.

Sreejith [32] considered environmentally safe cutting or green cutting and dry machining as valuable solutions towards environmental hazards. Sharma [33] suggested air, water vapours and environment-friendly gases as better solutions for green cutting. Donmez et al [34] avoided liquid cooling and showed a novel technique using Coanda-Effect tubing, achieved 30% reductions in spindle thermal drift using compressed air. However it was not stated how to implement such method for reducing temperatures from major heat sources such as belt drives i.e. complexities involved in wrapping up tubing around those sources and further discussions would have benefitted the approach. Similarly the heat dissipated by the compressors may eventually cause the overall temperature rise around vicinity of the machine which will affect the structure thermally.

2.3.2.4.2 Before machining

Workpieces ready or waiting to be machined are susceptible to the varying environmental temperature which adversely changes their thermal state. To prevent this, parts should be placed in temperature controlled environments. Workpiece temperature

control can also be achieved by soaking workpieces for hours up to a known thermal state such as, at or near, the coolant temperature before machining which may differ from the ambient temperature.

As mentioned, there have been several suggested workpiece cooling methods using cooling mediums. Coolant issues are also resolved by MQL utilizing biodegradable lubricants. This research deals with the analysis of the machine structure affected by the internal heating and varying environmental effects. Research and methods have been applied to the cooling of spindles and ball screws which are expensive methods to employ. Application of the cooling techniques to the machine structures such as channelling, hollowing the structures for the cooling medium to flow is often a compromise with arising structure stiffness problems and these can also be expensive and therefore rarely implemented.

2.4 Reducing the effect of structural temperature change

Controlling or reducing structural temperature change has been discussed in the previous section. The practical limitations of this design effort result in inevitable adverse temperature profiles requiring effort to be made also in reducing the effect of structure temperature change to minimize thermal error.

- **Design changes**

    - **Machine tool spindles**: Utilizing one moving bearing support ensure constant axial load in a spindle bearing set despite machine tool heating. This prevents bearing overloading and problems due to thermal expansions of the spindle [35, 36]). Elastic preloading mechanism keep the bearing preload constant even when thermally induced relative movements between the spindle and the housing takes place [26].

    - **Low coefficient of thermal expansion**: Using low thermal expansion materials such as Zerodur, Invar and Carbon Fiber help reduce thermal expansions in machine tool. Suh et al [37] investigated the thermal characteristics of reinforced composite sandwich structure consisting of compounding layers of steel and carbon epoxy composites with fibre honey comb cores in between. The sandwich composite structure was used in the

manufacturing of X axis slide for a machine tool. It was found that the material exhibited less thermal deformations than expected due to the heat input by the linear motor. The fiber honey comb acted as insulation decreasing the heat magnitude from 50°C to approximately 30°C.

- **Ball screws**: To minimize the effect of ball screw thermal expansion, linear scales are fitted to remove the ball screw from the positioning loop [9, 35, 38].

Design changes applied to reduce structural temperature rise (section 2.3.1.3) and its effect particularly in the areas explained above can be successful in minimizing thermal errors however they can be costly methods with regard to the efforts required for the significant redesigning of major structural elements and their implementation time scales. It is also the fact that despite all design efforts such as applying cooling jackets to the spindles, most machines still exhibit errors from main heat sources such as spindles [39]). These issues have drawn research attentions towards utilizing alternative methods i.e. compensation.

2.4.1 Thermal error Compensation

Compensation is a method of correction of thermal errors present at a particular time by adjusting the position of the tool and workpiece. The advantage of this method is that significant design changes are not required and the existing axes can be adjusted for compensating thermal error [35].

Several techniques have been created to compensate the effect of thermal errors. Potential solutions investigated can be divided into two categories:

- Direct measurement techniques for thermal error compensation
- Indirect modelling techniques for thermal error compensation

2.4.1.1 Direct measurement techniques for thermal error compensation

Direct measurement of the thermal error on the machine tool for compensation may be achieved using special purpose equipment such as probes and artefacts. The use of on-machine can enable measurement of the thermal error on specific machine components or

specifically designed artefacts. Deviations can be corrected by the controller as standard offset adjustments.

A probing method has been used for calibrating and compensating thermally induced error both in real time and under static conditions by Chen [40]. This was achieved in real time using on- machine probes and an artefact and found that thermal errors in real cutting were distinct from those in air cutting. Yang et al [41] proposed a method of measuring both geometric and thermal errors by means of on-machine measurement using two spherical balls and a touch trigger probe. The data was used to train a proposed neural network method to predict the errors. Kim et al [42] developed an on-machine inspection system that uses a 3D artefact for the modelling of geometric and transient thermal errors. Geometric errors are determined periodically by the offline calibration procedure and thermal errors were estimated by measuring the artefact twice when the on-machine measurement of a machined part is required. The total time for measuring the artefact was quoted to be less than 5 minutes. Allen et al [43] developed a direct method to measure and correct for thermal expansion of the linear scale using a thermally stable invar bar equipped with a non-contact displacement transducer. The technique was successfully applied to a CNC lathe to measure and correct for spindle growth. After correction, the residual error remained within 10% of the original value. The method was proved to be fast; however the equipment often requires difficult physical modifications in order to fit onto the machine.

The methods explained above have significantly improved the accuracy of the machine; however there can be complications associated with their implementation. Probing methods require interruptions during machining cycles for thermal checks. Ambiguity of temperature instability may arise if the thermal state of the machine has changed gradually due to the environmental changes while probing cycles are performed. Interruptions may also introduce issues such as machine downtime, uncertainty of the obtained compensation data due to the amount of cool down during the probing cycle. An artefact may have to loaded and unloaded adding downtime. It may be necessary for the artefact to be stored in a temperature controlled environment to prevent thermal expansion of the material. Material selection and design intent to create an artefact is expensive and require extra technical skills for its quick sequential implementation i.e.

mounting on the machine, calibration and measurement regimes and dismounting from the machine for accurate measurements and compensation data acquisition.

2.4.1.2 **Indirect modelling techniques for thermal error compensation**

Indirect modelling and compensation methods can avoid process intermitting however can be complicated to implement. The methodology employed deals with temperature data measurements from specific spots or thermally sensitive points on the machine that contribute towards thermal growth of the structure and resulting in thermal error. A model is required to convert the temperature information into machine error. The calculated error is then compensated by such methods as part program modification, offsets and adjustment of the machine axes. Several modelling methods for indirect measurement have been developed to calculate the thermal errors. These methods have been used as a single and in combination of more than one method. Figure 2-1shows a chart which gives an overview of the published research where modelling methods have been categorised according to their use. This has been compiled by a joint review within the Engineering Control and Machine Performance Group (ECMPG) of University of Huddersfield (UoH) to show the distribution of efforts towards compensating thermal errors.

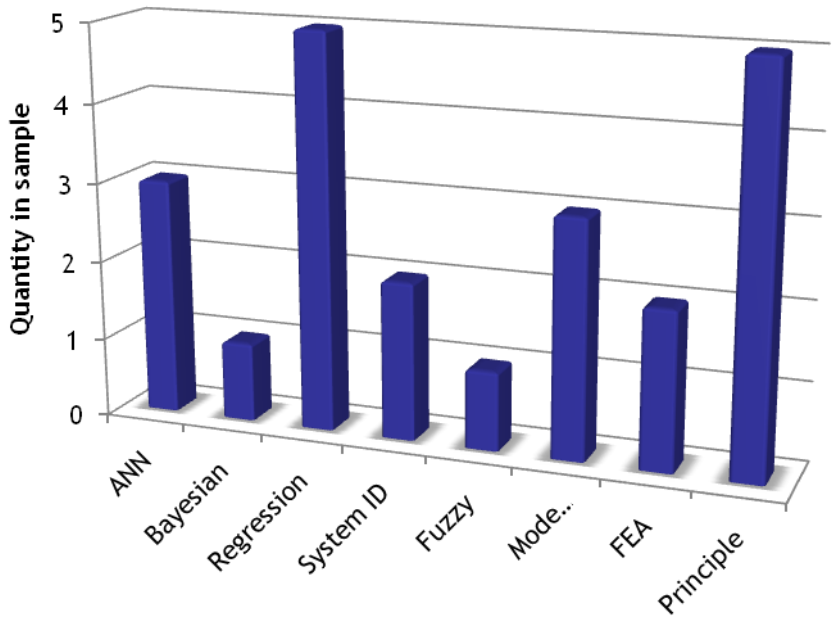

Figure 2-1: Modelling methods categorized according to their use

Therefore main methods can be categorised according to their use.

2.4.1.2.1 Neural Networks

Neural Networks or Artificial Neural Networks (ANN) are an empirical method of chain element architectures interconnected in layers with collective computational abilities. A typical neural network is composed of three layers, an input layer, a number of hidden layers and an output layer that provides correlative relationship between thermal error and temperatures. The input layer receives temperature measurements and the output layer stores the thermal errors. The hidden layers are used for data handling, computations and noise suppression between the temperature inputs and thermal errors [15]. A number of methods have been derived from the working principals of ANNs and used in research to overcome thermal error issues. Feed forward Neural networks (FNN), Integrated Recurrent Neural Networks (IRNN), hybrid networks, Back Propagation Neural Network (BPN) and Cerebellar Model Articulation Controller networks (CMAC) and are few of the most widely used techniques. Chen [44] implemented a three layer FNN modelled with 15 input nodes, 15 hidden nodes, and six output nodes. 540 training pairs made a training set that were used to train the model. Since the model produced valuable results with selected cutting conditions, a new cutting condition which was not within the collected training pairs was used to test the prediction accuracy of the ANNs model. Thermally induced errors of the spindle and leadscrew were measured and compensated. The experimental results showed that more than 85% thermal error can be reduced after compensation. Other research conducted by Chen [45] used a hybrid model composed of an FNN and Multiple Regression Analysis (MRA) to study the characteristics of thermal error in both air and real cutting conditions. A performance comparison of the hybrid model (FNN and MRA) was made with the FNN method which showed that FNN is more suitable for predicting thermal errors in air cutting but unacceptable for real machining conditions. The hybrid model was sufficiently accurate for predicting thermal error induced from both air and real cutting sources with reasonable accuracy. Ahn et al [46] developed a compact measurement technique capable of measuring time variant machine tool errors. A FNN model with a new concept of input values was developed to estimate the thermally induced errors during cutting. The developed FNN model consisted of 8 input nodes, 15 hidden nodes and 5 output nodes. The author suggested replacing the method of inputs to the NN. The input, temperature distributions of the entire machine structure was suggested, replacing with the new inputs

i.e. the environmental temperature and the cutting conditions can significantly simplify the training methods and increase the estimation accuracy reasonably. Kang et al [47] modified FNN by utilizing the hybrid filters to increase the accuracy and reduce computation times. The hybrid filter was consisted of linear regression, moving average, and auto regression methods. Finite element model was introduced for the determination of error margins used for the comparison of the modified model with the traditional models ARMA, FNN and LR/NN. The results showed better accuracy of the modified model in comparison with the traditional models. The errors were reduced by a maximum of 48% for the Y axis and 70% for the Z axis for various experimental testing conducted on a grinding machine. The training time for the modified model was reduced to 8 hours compared with the conventional FNNs which took more than 48 hours. Other research conducted by Kang et al [48] proposed a hybrid model composed of auto-regressive moving average (ARMA) filter and a FNN to increase the prediction accuracy and to reduce the learning time for the estimation of thermal deformation. The ARMA model outputs were defined as the state variables and treated as inputs to the FNN. The FNN model consisted of 2 inputs nodes, 10 hidden nodes and 1 output node, 28 thermal sensors were used with 18 sensors placed on the machine and 10 sensors measuring ambient temperature. Three experiments were conducted, the first experiment was used to train the prediction model and the other experiments were used to evaluate the prediction accuracy. The comparison revealed that the hybrid model exhibited good accuracy compared with the ARMA and conventional FNN methods and the training time can be reduced to 3 hours. The comparison would have been easier if the technique was applied to other machines for its robustness, learning times and accuracy .Yang et al [49] developed a modelling methodology to track non-linear time varying machine tool errors under various thermal conditions; and the dynamics i.e. non stationary nature of the thermo-elastic system has been modelled using a new technique, Integrated Recurrent Neural Network (IRNN). Compared with FNN's unidirectional data information flow (forward direction), the IRNN method allows bidirectional flow, in forward and backward directions. Experiments were conducted for the measurement of spindle thermal expansions; the results were used to train the IRNN. The model performance comparison of IRNN with Recurrent NN, Multi-layer FNN, and the MRA in terms of model accuracy and robustness yielded that IRNN is more robust in terms of relative

error and standard deviation testing and that the IRNN model can predict 80% of the maximum thermal error with the maximum residual error of less than 15μm due to spindle rotation.

The research methods elaborated important aspects that need to be considered while modelling a NN model such as consideration of the operating conditions of the machine tool and carefully extracting the information to train and further develop a neural network model. The issue is well addressed by Ramesh et al [50] who developed a hybrid Bayesian Network (BN) combined with Support Vector Machines (SVM) model to measure thermal behaviour of the machine tool under specific operating conditions. The SVM model was used to predict the error after the experimental data classification using BN. The SVM proved to be powerful regression tool that carries out efficient mapping of the temperature data with error. A BN is a probabilistic representation for uncertain relationships such as those on a machine control; a SVM is a learning system that uses a hypothesis space of linear functions in a high dimensional feature space trained with a learning algorithm from the optimization theory. CMAC method has been used by researchers due to its robustness and fast learning capabilities [51]. Yang et al [52] proposed a CMAC neural network for modelling spindle drift errors and found that the model exhibited fast learning, good modelling capability, insensitivity to sensor placements and robustness to sensor failure compared with MRA and MFN. Fast learning capability was illustrated as per observation criteria; it would have been beneficial if the comparison was made with respect to the learning times.

Neural networks with back propagation (BPNN) capability have been used extensively in various research activities [53, 54]. Modifications have been applied to the BPNN to improve accuracy. Guo et al [55] introduced Ant Colony Algorithm to the BPN (ACO-BPN) which was applied to the NC machine tool to predict thermal errors. It was found that the method has reduced the input temperature variables from 12 to 4. The workpiece diametrical error was reduced from 33μm to 8 μm after compensation. Machine downtime and training time required for the model is not mentioned. Hao et al [56] proposed a Genetic Algorithm based BPN model for thermal error prediction of a turning center. The GA-BPN thermal model was based on five key temperature points. Real-time compensation for thermal errors was implemented and the diameter error of the

workpiece was reduced from 27μm to 10μm. It was stated that GA-BPN can reduce computational costs and increase accuracy however the training time for the NN model was not stated. The GA-BPN technique was further implemented by Wang et al [57] on a vertical machining center. The author used four key temperature points and achieved 60% increase in the machine tool precision. The model training time was not mentioned.

The research based on neural networks has revealed good prediction accuracy and creation of robust models for the validation exercises reported. It can also be determined that NN models can be created by finding temperature key points without the knowledge of the actual structure. The computation time and hardware cost required for building a faster and reliable NN model has been a major constraint. Model training normally requires hours of learning due to the number of variable manipulations such as temperature and displacement data variables. Sensor locations must be well understood and sensors must be robust for a reliable prediction model; however that may require hours of machine testing under a variety of conditions and the information going through a large number of iterations and computations. Methods for overcoming sensor failures are based on value estimations which may not be accurate and it may not be straight forward to replace the sensor and train it again.

2.4.1.2.2 Regression analysis methods

Regression analysis, another empirical method, is a technique that finds relationships between a single variable and a dependant variable. Multi Regression Analysis (MRA) is one of the widely used regression methods in this field where relationships are found between the groups of temperature variables and a single dependant variable i.e. thermal error of the machine tool to predict the accuracy of the machine. Yang et al [58] tested a NC twin-spindle for both geometric and thermal errors. He used MRA to form an error synthesis model which combines both the geometric and thermal error. Estimation of the slope variations enabled the separation of both errors and the experimental results indicated that the size variations of the workpiece could be reduced from 60 to 14 μm and the taper could be reduced from 50 to 15 μm/cm. In another research, Yang et al [59] tested an INDEX-G200 turning center and used MRA technique to predict its thermal accuracy. The analysis result showed that the thermal error range for radius direction on that machine was approximately 18 μm, higher than expected. 14 thermal sensors were

installed in groups and only one ambient sensor was used. While modelling, six temperature groups with variables were constructed and the model was assumed to be a linear function for the environmental temperature rise. The predicted thermal error between the spindle and the cutter revealed a residual error of 5μm from a maximum error of approximately 18μm for a test length of 4 hours. Modelling time was not mentioned. Tseng [60] used MRA to apply thermal error compensation to a vertical machining centre. Only one sensor was used to measure ambient temperature along with sensors placed at key locations and compensation revealed the displacement error reduced to within 4 μm. The compensation control suffered over-reaction and to minimize this effect, a maximum of 3°C temperature deviation within the machine tool structure was suggested. In other research, Tseng et al [61] proposed two regression models; a linear MRA model and a non-linear exponential regression model for predicting thermal errors of a high precision CNC lathe. Apparently, eight temperature sensors were placed at key locations on the structure with only one sensor for ambient temperature measurement. The experimental results showed that 40% of thermal errors can be reduced by their linear MRA and 60% of thermal errors can be reduced by their non-linear model.

Chen et al [62] employed and compared two different models (MRA and ANN) to predict the time variant thermal error components under different spindle speeds and temperature on a horizontal machining centre. Both models exhibited similar performance. Only one ambient temperature sensor was used for modelling the prediction models and the compensation showed workpiece thermal distortion reducing from 92.4μm to 7.2μm with the spindle thermal growth reduced from 196μm to 8μm. The time spent on developing the models was not mentioned. Pahk et al [63, 64] modelled the spindle thermal error based on three different modelling techniques, MRA, NNs and System Identification. It was found that the system identification method exhibited higher accuracy than the other two. Feed axis thermal errors were also modelled and a Homogeneous Transformation Matrix (HTM) method was used to combine both spindle and feed axis thermal error models. Real time compensation was implemented by interfacing with the machine tool controller resulting in an accuracy improvement of 4-5 times. One of the regression techniques known as orthogonal regression technique was employed by Du et al [65]. This technique was applied to more than 100 turning centers

of the same type and specifications. It was found that the technique was able to reduce the cutting diameter thermal error from 35μm to 12μm. The technique was stated as robust due to its year round repeatable improvement in accuracy. The accuracy is expected to increase if long term shop floor environmental temperatures fluctuations were considered. This work is also stated by Liu et al [66]. Lin et al [67] analyzed the issues related to the spindle thermal displacement on acceleration using MRA method. However it states that, since spindle thermal behaviour of every machine tool is not exactly the same; the developed model may not be applicable directly to other machine tools. Modifications and adjustments may be required according to the machine behaviour before implementation. Tachiya et al [68] utilized MRA technique to develop approximation equations for their use in the thermal compensation system. He developed a stochastic method that finds relationships between the thermal deformations and the temperature changes of plural positions of the machine tool and determines the appropriate temperature measuring points.

Although regression techniques may work well for modelling , this technique requires various complex parameters and relationships as pre-requisites i.e. prior assumptions regarding functional relationships such as linear, quadratic, higher-order-polynomial and exponential between outputs and input decision variables [69]. Similar to NNs, sensor placements and sensor robustness are critical in regression techniques, incorrect sensor placements may result in incorrect or unreliable relationships between temperature and the thermal error. Sensor failure is critical which may lead to machine downtime required for the sensor replacement followed by repetitive iterations and computations to regain relationships and accuracy. Expertise is required for optimizing and adjusting a regression model to make it suitable to different machines tool configurations and for a variety of usage conditions. Re-testing for finding key sensor locations and their placement on new machines is time consuming therefore the technique cannot be applied immediately.

2.4.1.2.3 Other methods

A Variety of research has been undertaken using other indirect temperature based modelling methods to compensate thermal errors. Yang et al [70] employed a recursive model adaptation strategy based on the Kalman filter parameter estimation technique.

The model coefficients are modified recursively in real time by the thermal error parameters monitored and predicted by the process-intermittent probing and system identification techniques respectively. 11 thermal sensors were mounted on the machine tool; however no sensor was placed to measure the ambient temperature. The model performance was validated by testing the Z axis of the machine. Three tests were conducted with a variety of spindle speeds and feedrate and each test had a length of 7.5 hours. The validation revealed averaged residual errors of approximately 12μm from a maximum of approximately 50μm error. Lee et al [71] developed a thermal distortion compensation method based on Independent Component Analysis (ICA) method. This method extracts thermal sources from the temperature variables for thermal model construction and eliminates insignificant temperature variables. The thermal sources were assumed to be mutually statistically independent. The thermal error in the Z axis was reduced dramatically from 155 μm to 3.5μm after compensation but the reported time for the implementation of this method along with training and computation was approximately 28 hours (more than a day) and this method may suffer even larger implementation and computation time on machines with complex structures. Ambient conditions were neglected

Zhu et al [72] proposed a new technique of modelling thermal error through a thermal mode concept. FEA was first utilized to find dominant thermal modes on the spindle unit and the Z axis (column). Temperature sensors were placed at the dominant thermal mode locations. Regression models were utilized to find the position dependant and independent thermal errors. For FEA, assumed heat flux input was used to generate heat and an assumed convection coefficient was applied to all parts. Environmental temperature was kept constant at 20°C. Delbressine et al [73] modelled the thermo-mechanical behaviour of multi axis machine tools. An Extended Lumped Capacitance Method (eLCM) was used to model the temperature distribution in the machine structural elements and the accompanying deformation was then calculated based on the temperature models. The structural elements of the machine tool were modelled as flat plate structures. Validations were carried out using new measuring equipment (Telescopic Double Ball Bar – TDBB) and a strategy that measures the positional accuracy of the machine at multiple locations within the machine working volume. The research revealed 60% accuracy improvements. However, the research was based on

several assumptions such as modelling the machine parts as a flat plate structures and linear temperature gradients. Yun et al [74] used Modified Lumped Capacitance Method (MLCM) and Genius Education Algorithm (GEA) to model the thermal behaviour of the ball screw, and FEA technique to model the thermal behaviour of the guide way. After modelling, the total thermal error was obtained by adding both. The experimental validation was performed by measuring the linear positioning error of the Z axis feed drive system using a laser interferometer, achieving approximately 90% improvement in accuracy when compared with the model estimations. The modelling technique should be useful if applied on the full machine structure. Attia et al [75, 76] and Fraser et al [77] developed a generalized modelling methodology to compensate thermal errors of the machine tools in real time. This model, which is empirical based, used the inverse heat conduction problem (IHCP) in which temperature measurements are carried out at only two points near the heat source to estimate the time variation of the heat input in real time. Computations involved in obtaining the IHCP [78] include transfer functions which are sensitive particularly in the case of temperature sensor failure in real time. A thin flat plate was used as a reference for the development of generalized model. Similarly a simple structure was used to represent a vertical milling machine. Two types of heat inputs i.e. ramped and sinusoidal were used to compare the performance of both generalized model and FEA. The results were compared by using only two 30 minutes tests. Although the generalized model exhibited good accuracy and is quoted to be two orders of magnitude faster in comparison with FEA however validation on a real machine i.e. on a complex geometry would be of great interest with respect to the modelling time this empirical model may take. Tseng et al [79] proposed a thermal error prediction model derived from the neural-fuzzy theory. IC-type temperature sensors and a Renishaw MP4 probe system were used to measure the temperature changes and thermal deformations respectively. Sensors were attached to the spindle motor, spindle sleeve side with one sensor measuring environmental variations. The prediction model improved the machining accuracy from 80 μm to 3 μm. The prediction model was further compared with MRA revealing accuracy improvements of ±10 μm to ±3 μm. However, the model training times and machine downtime are accountable issues with this research. Zhou et al [80] used a fuzzy-neural based hybrid approach for error compensation in machine tools. The fuzzy neural network error compensation model was

based on two variables as its input variables and its output variable for offsetting the relevant coordinates of the CNC machine part program. The two variables were obtained using a touch-trigger In-Cycle Measuring (ICM) system. Lee et al [81] presented a thermal error model using a fuzzy logic strategy. 14 temperature sensors were placed on the machine tool structure, environmental temperature was not measured. In comparison with the other techniques such as linear regression and engineering judgment models, it exhibited good accuracy whilst utilizing less number of variables. White et al [82] identified and studied the mechanisms of thermal errors in CNC machine tools for which 10 different machines were tested. Testing concluded that even different machines of the same make and configuration exhibit different thermal behaviour. Using thermal imaging equipment during testing is very useful to locate even smaller temperature magnitudes and gradients. White also developed a thermal bending model based on breaking the machine into its constituent parts for measuring the thermal behaviour in a vertical machining centre [83, 84]. The bending model revealed the importance of the knowledge and magnitude of temperature gradients on machine bending for over a wide variety of machine usage conditions. White then developed a cost effective and easily applicable sensor system which required only a single heat and cooling test for calibration. 58 sensors were placed on the machine head in two strips of 29 sensors for thermal error compensation. The compensation resulted in reduction by 6 times (from a maximum of 54µm to approximately 9µm) of the Y axis thermal error and the technique is quoted to be applicable to a variety of machine tools due to its flexibility. More accuracy is anticipated if variations due to the environmental drifts were also included in the compensation model.

Allen et al [85, 86] extensively used thermal imaging techniques for acquiring temperature data and understanding the behaviour of temperature gradients for machine tool thermal error compensation. He developed distortion models based on relating surface temperatures to the structural distortion; one was the machine head slide distortion model. A short term heating and cooling test revealed compensation holding the error within 10µm for the head slide. A long term test may have revealed a better evaluation of the technique where ambient conditions begin to contribute.

2.5 Finite element Analysis (FEA)

Finite Element Analysis (FEA) is a computational mechanics technique to develop and simulate a spatially discretised mathematical model of a continuum system using a numerical method [87]. It is a technique where the machine structure is split into a number of smaller elements subjected to the heat flow. Each element, with its estimated thermal characteristics, exhibits effects on the neighbouring elements, leading to an overall estimate of the total thermal behaviour of the machine structure. The FEA utilizes standard heat flow equations i.e. conduction, convection and radiation to estimate the thermal behaviour.

Min et al [88] used FEA for the modelling of machine tool bearings. Thermal contact resistance (TCR) controls the thermal conductance between joints, has been thoroughly considered, along with the heat generation of the bearings during the development of the model. It has been concluded that simulated FEA model accuracy was significantly increased by considering TCR. Haitao et al [89] showed the simulation of thermal behaviour of a machine tool spindle. The spindle was modelled without simplifications, other than assumed symmetry, in order to maximise the accuracy of the simulation. Thermal key points were obtained by undertaking a sensitivity analysis, rather than the empirical use of a thermal imaging camera. Simulation of a four hour test was run and compared to validation data from the modelled machine. It has been reported that the finite element method used in this research gave promising simulated results of the spindle and suggestions were made for replacement of experiments with simulations. The time spent on the modelling and testing phase is not mentioned. Jedrzejewski et al [90] tested a 3 axis machine and presented a method of combining FEA and the Finite Difference Method (FDM) into one hybrid model to simplify geometry by avoiding excessive meshing techniques. Three types of different headstocks were analysed; an electrospindle on rolling bearings, a conventional spindle and an electrospindle on aerostatic bearings. Promising results were presented, such as an improvement from 100μm to 20μm for a 50,000rpm machining centre headstock. No figure is given for the time required for the simulation time. Creighton et al [91] tested a high speed micro-milling spindle for analysis of the thermal errors at a variety of operating speeds (10,000 rpm to 50,000 rpm). A simplified CAD model of the spindle, motor and housing structure

was created using ANSYS FEA software. Thermal errors were well predicted using FEA and led to compensation accuracy of 80% under a random stepped speed test. Wu et al [92] showed a systematic method to investigate the thermal characteristics of a feed drive system. A ballscrew was analysed at different preloads using nine thermal sensors. The ballscrew was operated at a selected feedrate but due to the complexity involved in attaching sensors, temperatures were noted after stopping the ball screw rather than during rotation. Displacements were monitored using capacitance probes and laser interferometer. A simplified FEA model of the ball screw was developed and the heat fluxes were adjusted until a proper thermal distribution was achieved. The paper shows a simple approach of using FEA to predict thermal behaviour of a ball screw and achieved a good agreement between measured (269µm) and predicted (240µm) results revealing 10.8% deviation at 20m/min feedrate. The results were better at lower feedrates of 10m/min and 15m/min revealed deviations of -2% and 9.5% respectively. The modelling time was not mentioned as it is suspected that the numerical approach may have taken excessive time. The FEA results obtained were based on several assumptions. The results may improve if the actual environmental boundary conditions and flux inputs were selected. Kim et al [93] analysed a ball screw system for two dimensional temperature distributions both in real time and steady state using FEA. The proposed FEM model was based on the assumption that the screw shaft and the nut are solid and hollow cylinders respectively. The convective coefficient was also assumed to be constant. Temperature distribution at the tool tip and within the workpiece resulting from cutting, milling and hard turning operations; and thermo-mechanical behaviour of the structural parts during machining has been successfully investigated and predicted using FEA in various research activities [37, 94-97].

In an attempt to analyze temperature distribution across the full machine structure, Kim et al [98] investigated a machine tool equipped with high speed linear motors. A full machine CAD model was created using SolidWork2001/CosmosWorks and investigated for thermal deformations particularly due to the internal temperature distribution due to axes movements. For FEA, assumed parameters such as boundary conditions were applied. Heat flux was only calculated using the measured temperature for the primary part of the linear motor however assumed for the roller bearings of all three axes that generate heat into the linear motion guide ways during axis travel. Experiments were

conducted by operating machine axes at various feedrates. The Z axis exhibited 17μm of thermal error which was predicted as 15.48μm revealing an 8.9% prediction error. . Denkena et al [99] presented a finite element method to compensate thermal errors in a machine tool. Internal and environmental effects were considered along with position dependent and independent errors. The results were presented only for the Z-axis direction. The carriage was moved back and forth for approximately 4 hours between Z positions 10mm and 700mm which showed an error of approximately 15μm and 55μm respectively. Three sensors were used to measure temperature drifts and the results showed a good correlation between the measured and simulated results, the remaining error reduced to below ±5μm for both positions. Jedrzejewski et al [100] discusses the complexities involved with improving the design of a machine tool when considerations of reducing thermal error are in focus. A highly accurate thermal model of the machine is presented and consideration of various parameters contributing to the thermal behaviour. For example, the design criteria considered the effects of environmental variations for 2.5 days, thermal effects arose due to the presence of guarding and bearing sets of high speed spindles. Quartz straight edges were modelled for environmental effect after mounting on the machine centre support beam. It was found that the straight edge fixed on the left side produced the lowest error of the other three locations tested. It would be of great interest if simulation time was mentioned. Huo et al [101] carried out an FE analysis on a grinding machine aimed to integrate the effects of thermal deformation of the machine structure and the heat produced by the machining process. At first, FEA was conducted to simulate the temperature distribution following validations by the on-machine measurements. The temperature information was then used to estimate the thermal deformation. The machining process was also simulated to obtain the temperature distribution within the cutting zone and its effect on the machine. This temperature information was used as an input heat source to the FEA model. The preliminary results for simulated temperature distribution and displacements, only in Z axis direction, are shown for 3.6 minutes, quoted as promising. Environmental effects were not considered. Mayr et al [102] used an integrated FDM-FEA method to compare the thermo-mechanical behaviour of two (old and new) frame designs of a machine tool. The FDM was used to calculate the temperature distribution at discrete time points and used as the input temperature field for the FEA. It is quoted that, with a standard PC, it takes less

than 5 minutes to carry out full simulation over 24 hour simulation time. This approach suits the application well in terms of quick application towards the prediction of thermo-mechanical behaviour at the machine design stage. Mayr et al [103] conducted another research exercise using the FDM in which a high speed precision machining centre headstock was investigated to determine its optimal operating characteristics in detail. The FDM was used to calculate the temperature distribution at discrete time points and used as input to the FEA. The TCP (Tool Centre Point) displacements were calculated using a 3D space lattice technique and tested on a three axis milling machine. During testing, the procedure considered measurements of the TCP displacements and boundary conditions in the operating time for a 6 hour machining trial. The comparison between the calculated values and the values measured at 5 different locations in the work space shown a good correlation that resulted in 50% reduction in the maximum TCP displacements after compensation. However, it is reported that the method requires improvements in terms of detailed modelling and further considerations for the introduction of internal heat sources, boundary conditions, temperature dependent component properties and the influence of cooling lubricant. The nodal compatibility between the FDM and the FEM may be an issue particularly if the FEA is modelled from a complex geometry. It was not mentioned if the model can robustly handle the nodal mismatch.

FEA techniques have proved promising in predicting temperature distributions and thermal deformations and are used widely in a variety of research activities for predicting thermal deformations in machine tools. There have been significant reductions in the time required to model thermal deformations compared with the empirical methods, however most FEA models lacked detailed analysis of the long term environmental effects over the full machine tool. Also, most FEA models were based on assumed heat flux values as inputs to simulate temperature distribution in the structure.

2.6 Concluding past research

It has been observed that significant research has been conducted and various strategies and methods developed and implemented with regard to the control, modelling and compensation of thermal errors in machine tools. Several methodologies for structural temperature control are discussed which can be applied at the design stage of

the machine such as primary and secondary heat sources, selection of low thermal expansion materials, application of cooling mediums by channelling through the structure where heat is dominant. These techniques if implemented will have significant control on the structural temperature rise of the machine however they are generally expensive and difficult to implement, particularly as a retrofit solution. Machine tool performance depends heavily on the operating environment where there are issues such as temperature control of the workpiece, swarf and external temperature control that are critical and need to be addressed when precision machining takes place. Environmental friendly coolants such as bio-degradable coolants are an efficient solution to control the localized temperature rise during cutting. Temperature controlled factory floors eliminate uncertainties involved with varying environment conditions that inevitably changes the thermal state of the machine structure and workpieces. Environmental temperature control can be very effective but expensive to implement and maintain particularly where large machines or a large number of small machines require control.

Methods used to compensate the effect of temperature change i.e. the thermal error, are categorized as direct and indirect. Direct methods provide means of accurate detection of the thermal error in machine tools using special, purpose made, equipment such as artefacts and probes. The material used to develop them may benefit from being thermal stable in order to cope with the environmental changes, particularly if fitted permanently. For instance, Zerodur is one of the materials with negligible thermal expansion coefficient but it can be prohibitively expensive. Direct measurement techniques are difficult to implement due to the required modifications to the machine structure to fit the equipment permanently. Mechanical and space constraints sometimes restricts the capability for the probe to reach a certain target. This could result in inaccurate measurements or a proportional measurement of the total thermal error that is not sufficient for the compensation. Physical constraints may cause restricted mechanical movements which can increase the risk of impacts. Damage or contamination of sensors in the hostile machining environment is another prime issue which can seriously deteriorate the performance of a direct measurement system.

Indirect thermal error measurement and compensation methodologies are the most widely researched using a variety of advanced modelling techniques to predict thermal

errors in a machine tool. ANNs revealed good prediction accuracy however a reliable NN can require from several hours to days of machine downtime to train the model under various working conditions which is not practical. The temperature sensor locations are of prime importance and the reliability of a NN is always questionable if sensor failure occurs and replacing a temperature sensor or refurbishment of parts of the machine may result in re-training of the model. Regression techniques provide good prediction accuracy but require several hours of training and computations resulting in longer machine downtimes. Prior to the creation of a regression model the relationship between the input and output variables needs to be defined. The relationship may be, for example, linear, quadratic or exponential. Skills are required for efficient implementation of the technique on different machine tools with different working conditions. Sensor placements are again very crucial in order to efficiently train the regression model. FEA technique have proven promising and shown good prediction accuracy. The development of an FEA model can be quicker in comparison with the empirical approaches. Most FEA research reviewed has involved assumed thermal parameters such as heat fluxes, boundary conditions and varying environment which have restricted confidence in FEA for thermal error predictions under varying operating conditions. A variety of other efficient thermal error prediction methods have also been addressed but they lack consideration of the main issues such as machine downtime, considerations of varying environmental conditions and their modelling times which restrict them to be successful candidates for practical and broadly applicable machine tool thermal compensation.

2.7 Research Aims

The review of past research has revealed a variety of highly capable modelling methodologies. Despite the potential accuracy improvements, certain issues remain that preclude industrial implementation. It is thought that the most dominant of these is the required downtime for testing and implementation, secondly the complexity of the methodologies and thirdly the lack of consideration of effect of environmental temperature change which may be perceived as the most difficult to solve by other error reduction strategies. There is a requirement for an efficient thermal modelling technique that is offline, simple to implement, applicable to other machine tools, robust and accurate. It must be an efficient and intelligent system addressing and considering the

main issues that are currently lacking. This research will deal with all those issues in detail. The project aims are,

- To create an efficient technique to measure the temperature flow and spatial thermal gradients in a machine tool during short term internal heating trials and to optimize the modelling technique that is fully applicable to the long term extended machining operations based on short term testing therefore dramatically reducing machine downtime

- To provide an understanding of local ambient temperature conditions specifically termed as ‘air pockets’ and their effect on the machine during machining operations.

- To provide a method for effectively determining the heat inputs for the heat sources based on the measurements to simulate internal heat flow replicating real world machine operations.

- To measure the influences of the long term environmental variations in a machine tool such as shop floor temperatures.

- To develop an offline and quick modelling technique that is able to predict the thermal behaviour of the machine tool with good accuracy.

- To locate thermal sensitive points within the machine tool structure that will allow permanent temperature sensor installation for simplified compensation ideally utilising where possible existing facilities within modern NC systems.

CHAPTER - 3

3 THERMAL STUDY OF THE MACHINE TOOL

There are three basic mechanisms of heat transfer within the machine structure, conduction, convection and radiation. This chapter details the study of the thermal processes that occur in a machine tool subjected to internal and external heat sources. As explained in earlier chapters, internal heat is mainly generated by the excitation of various machine elements such as spindle bearings, motors, hydraulics and belt drives etc. External heat sources refer to the change in environment effects around the vicinity of the machine and the workshop, which generate temperature variations and gradients within the structure. Both sources result in the inevitable non-linear deformations and affect the machine accuracy.

3.1 Conduction

Conduction takes place in the machine structure where the heat generated flows through a series of interconnected surfaces via interfacial gaps. Conduction varies from one metal to another due to the differences in their thermal characteristics such as thermal conductivity and specific heat capacity. It is well known that Fourier's first law of heat conduction explains the heat transfer mechanism; the expression formulated by Fourier explains the relationships between the temperature gradient, rate of heat flow and the medium through which the heat flow occurs. The expression is shown in equation 3.1

$$q_{cond} = -kA\frac{dT}{dx} \quad \text{..... (3.1)}$$

where q_{cond} is the heat transfer rate in the x direction (Watts), k is the thermal conductivity of the medium (W/m/°C), A is the area over which conduction is taking place (m^2), and dT/dx is the temperature gradient in the x direction (°C /m). Figure 3-1 illustrates heat transfer through a block due to conduction, the negative sign shows that the heat is transferred in the direction of decreasing temperature.

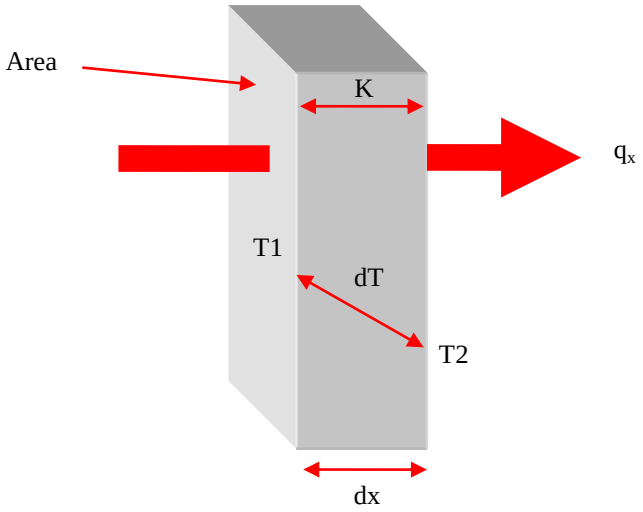

Figure 3-1: Heat transfer in a medium by conduction

Thermal conductivity of a material is a temperature dependent property for example carbon steel experiences a decrease in the thermal conductivity at the temperature range of 400°C to 1000°C. However for a standard machine tool application, the temperature magnitudes are less significant and this variability can be neglected.

3.1.1 Heat flow mechanism within the machine structure through conduction

A machine tool assembly comprises of a series of interconnected metallic components. The majority of the machine structural components are manufactured from steel or cast iron; the geometries are often very complex due to the addition of cast or machined features to comply with the design requirements. The addition of features such as apertures, voids, protrusions, holes, ribs, chamfers and fillets result in complex geometric assemblies through which the heat experiences a non-uniform flow with each interconnected component offering inconsistent thermal properties. Figure 3-2 shows an example of features incorporated in the design of a typical machine column. The non-uniformity refers to, for example, (Attia [104] cited in White[4]) the heat flow mechanism that will be completely different through a steel component (k=52W/m/°C) and the adjoining aluminium part (k = 237 W/m/°C). Typical materials associated with machine tools are listed in Appendix A along with their range of conductivity values. These values however can have a high level of uncertainty due to small variations in the material actual properties and non-homogeneity in the material which may affect the heat conduction through the full machine structural loop. Conduction is also affected by the

local configurations of the structural joint interfaces that alter the heat flow characteristics. This will be covered in more detail in section 3.5.

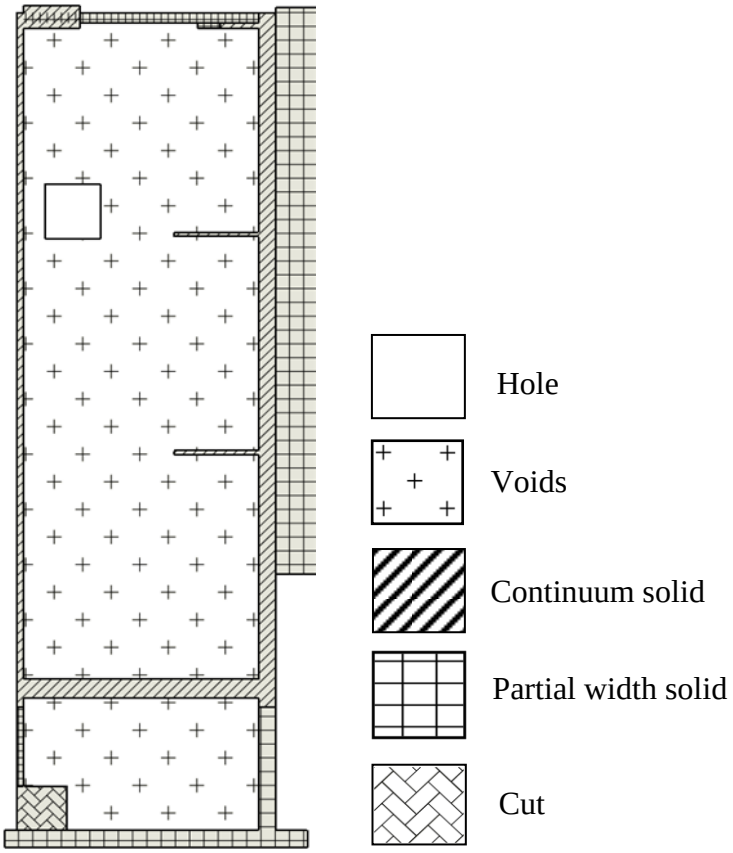

Figure 3-2: A sectioned view of a typical machine tool column showing design features

3.2 Convection

Convection is a mode of heat transfer which occurs when the heat energy is transferred between solids and fluid layer (oil, coolant, air) due to temperature gradients. Figure 3-3 shows the generic illustration of the convection process. Once the heat is transferred, the remaining process of heat transfer within the solid and fluids is through conduction. It is well known that Newton's law of cooling defines the heat transfer through convection and states that the rate of change of the temperature of an object is proportional to the difference between its own temperature and the relative fluid temperature. Newton formulated the basic rate equation as (equation 3.2)

$$q_{conv} = hA(T_{surf} - T_{fluid}) \quad \ldots\ldots\ldots\ldots\ldots\ldots\ldots\ldots \quad (3.2)$$

where q_{conv} is the rate of convective heat transfer (Watts), h is the coefficient of convective heat transfer (W/m^2/°C), A is the surface area over which the convection is

taking place (m^2), T_{surf} is the temperature of the surface (°C), T_{fluid} is the temperature of the fluid (oil, coolant, surrounding air or ambient) (°C).

Note: T_{fluid} is *denoted* as T_{air} to represent ambient air temperature.

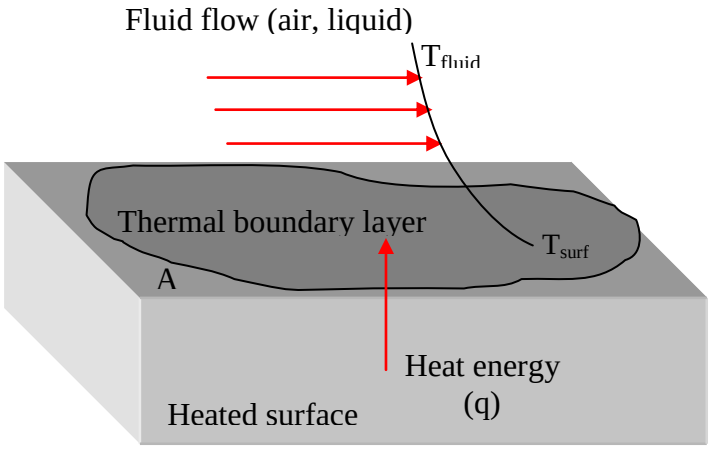

Figure 3-3: Convection: The heat transfer between the fluid passing over and the surface

In a machine tool application, convection occurs in various modes for example the heat transfer between the cutting tool/workpiece and the coolant where the heat drawn from the motors/belt emanates into the surrounding environment by natural (free) convection and forced convection phenomena. Natural (free) convection is a process where a heat source releases its energy to the surrounding without any externally applied force. Forced convection is a process where the heated surface releases its energy proportional to the pressure applied by the moving fluid over the surface. The value of convection *'h'* is higher in forced convection due to the fact that the energy release is higher in proportion with the fluid flow rate. Finding *'h'* is critical as it strictly depends on various parameters such as fluid velocity, type of fluid, laminar or turbulent flow, and surface geometry and roughness. Common values of the convection heat transfer coefficient have been given by Incropera [105] and are shown in Table 3-1.

Mechanism	Coefficient of convective heat transfer h (W/m^2/°C)
Natural (Free) convection	
Gases	2 – 25
Liquids	50-1000
Forced convection	
Gases	25-250
Liquids	100-20,000

Table 3-1: Convection values commonly used

Since the values of the convection coefficient (h) vary significantly for gases and liquids in both mechanisms (Table 3-1) it is therefore necessary to obtain the convection coefficient experimentally in accordance with the parameters described above, even from a machine tool point of view where forced convection takes place in the form of coolant spray over the cutting tool/workpiece area and in the form of air circulating across rotating parts such as cutting tool.

3.3 Radiation

Thermal radiation is a process where a body at a finite temperature emits thermal energy. Unlike conduction and convection, radiation requires no medium to transmit thermal energy as the energy travels through electromagnetic waves which can travel even through a vacuum. All objects with a temperature above absolute zero radiate thermal energy. Figure 3-4 shows an illustrative view of a radiation process.

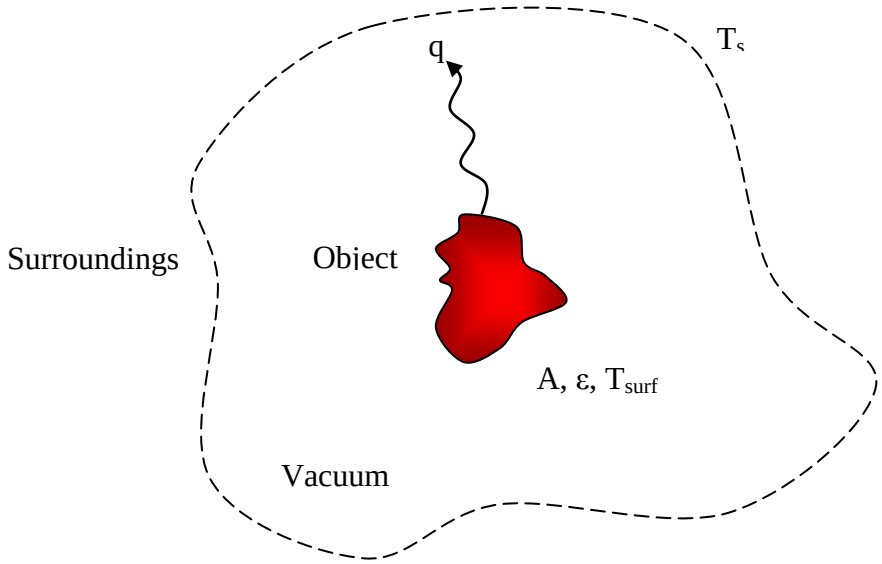

Figure 3-4: A hot object radiating to cold surroundings [106]

An ideal radiator and absorber of thermal energy is termed as a black body, the name refers to the characteristic of non-reflecting light as being a perfect absorber. The thermal energy released through radiation emission or gained due to radiation absorption is given by:

$$q_{rad} = \varepsilon\sigma A(T_s^4 - T_{surf}^4) \quad \ldots\ldots\ldots\ldots\ldots\ldots\ldots\ldots \quad (3.3)$$

where

- q_{rad} is the radiant emission (W),
- A is the area of the emission (m^2),
- T_s is the temperature of the surrounding (°C),
- σ is the Stefan-Boltzmann constant (5.676×10^{-8} $W/m^2/°C^4$).
- ε is the emissivity (dimensionless)

3.3.1 Emissivity

Emissivity is a radiation property that allows comparison of a real surface with reference to a black body and therefore it is a ratio of the radiation emitted by a real surface to that of a black body. Emissivity depends of various factors such as surface

temperature, surface finish, the type of surface and the wavelength and direction of the emitted radiation.

The emissivity varies from material to material and surface to surface. In case of machine tools, structural elements will have a range of emissivities values that are dependent on their material and surface finish. Table 3-2 gives a list of emissivities for common materials [106].

Material	Emissivity
Aluminium (heavily polished)	0.038 – 0.06
Aluminium (heavily oxidised)	0.28 - 0.31
Cast Iron (oxidised at 1100°C)	0.64-0.78
Cast Iron (rough, strongly oxidised)	0.95
Steel (roughly oxidised)	0.81
Oil Based Paint – all colours	0.92 – 0.96
Water	0.96
Masking tape	0.96

Table 3-2: Emissivities of various materials found in machine tools

For example an oil based painted large cubic machine tool structure with surface area of $0.054m^2$ (L=0.3m, B=0.15m, H=0.2) and high emissivity of 0.96 heats up to 50°C with surrounding temperatures of 25°C during a machining operation. Using equation 3.3, the radiation energy generated by that surface can be calculated as 0.017W (17mW) which is a negligible parameter to have any significant effect on the thermal behaviour of the machine as the working temperature ranges are not very high in machine tools.

The discussion has looked into various modes through which heat transfer occurs within a machine tool i.e. through conduction, convection and radiation in response to various internal and external heat sources. In reality, the amount of radiated heat is negligible unless from direct sunlight striking the surface of the machine. However, it plays a very important part for thermography and the parameters must be understood for accurate measurement of temperature using this method. This research uses thermography to measure temperature flow in the machine structure using a thermal

imaging camera; and uses high tack masking tape on reflective surface for measurement accuracy. The remaining heat transfer modes result in the development of thermal gradients across the machine structure resulting in structural deformations. It may be difficult to obtain the accurate heat transfer measurements due to the complexity of machine tool structure since a smaller region may exhibit complex thermal characteristics depending on the part geometry and its surface finish and nature of temperature gradients around it.

3.4 The effect of temperature gradients

3.4.1 Linear thermal expansion

The change in linear dimension of a material can be obtained by using equation 3.4.

$$\Delta L = \alpha(T_2 - T_1)L. \quad \text{..... (3.4)}$$

where ΔL is the change in length due to temperature change ΔT. The coefficient of thermal expansion (α) does not vary significantly with temperature unless a material is subjected to higher temperatures (for materials relevant to this research). For instance, a commonly found material in machine tools is cast iron, this has a stable thermal expansion coefficient of 9µm/m.°C over temperature range of 21°C to 100°C, however the coefficient value increases to 11µm/m.°C for higher temperature ranges. Since limited differential temperature changes are encountered in machine tool applications, the coefficient of thermal expansions for materials are assumed to be constant in this research. Appendix A gives the list of the coefficient of thermal expansion of various metals found in machine tools. An Invar test mandrel and test stand was used in this research, this material may not be common in conventional machine tools due to its cost.

3.4.2 Non-linear thermal distortions

Complex material geometry such as fillets and protrusions behave differently to the heat flow which leads to the formation of local temperature gradients resulting in local distortion. This may also result in an angular error which may be amplified by large Abbe offsets. Figure 3-5 shows an illustration of an ideal machine tool component distortion when subjected to a heat input. This caused temperature gradients in the structure that led it to distort (bend and expand) while supported from the top surface.

Ideal machine component

Distorted (bent) machine component due to temperature gradients

Figure 3-5: An illustration of temperature gradients distorting a machine component

Machine tools are constructed from a variety of materials and in response to temperature gradients (local or global), thermal characteristics of materials and interfacial thermal characteristics at structural joints may exhibit non-linear thermal behaviour.

3.5 Thermal Contact Resistance (TCR):

TCR is the phenomenon of resistance to conductive heat transfer through the interface of two solid surfaces in contact that results in a sudden temperature drop across the interface. Figure 3-6 illustrates a microscopic view of two surfaces in contact shows areas of intimate contact and voids [106]. The interfacial resistance is a function of interfacial parameters that can alter the heat flow through the interface.

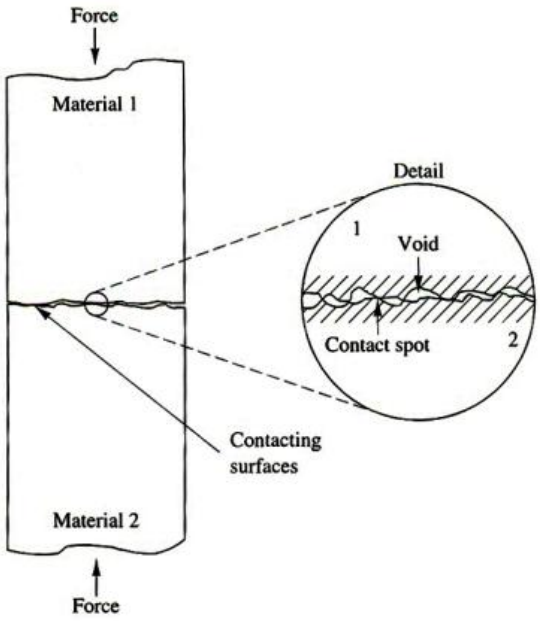

Figure 3-6: General overview of a thermal resistance across joints

These main parameters include contact pressure, number of contact points, size and shape of contact points, size of voids, type of interfacial fluid in voids, pressure of

interfacial fluids, hardness, flatness, modulus of elasticity, average surface finish and surface cleanliness of contacting surfaces. Similar case is of machine tools where the heat generated in the machine flows through mechanical joints and structural linkages which involve contacting surfaces. The combination of the parameters described above causes variation in the interfacial surface film characteristics which in turn produces resistance to the heat flowing across mechanical joints. [14, 104]. So far the TCR has been the term most appropriate to describe the phenomenon of how machine tool joints reduce heat flow, however the formulae for calculating heat flow use conductive heat transfer or Thermal Contact Conductance (TCC) which is the inverse of TCR.

TCC is a complex phenomenon due to its dependence on various parameters therefore it is necessary to develop an understanding of the thermal behaviour across structural joints of the machine to improve modelling accuracy. Considerable amount of experimental and theoretical work has been reported in the literature for obtaining thermal contact conductance, however it is also reported that experimentally obtained results have been the most reliable [107]). Heat conduction across joints has been identified by Attia et al ([104] cited in white [3]) as being important in the role of heat flow from one machine tool structural element to another. Attia showed that the 1.5 metre long arm of a horizontal milling machine exhibited significantly different temperature gradients, and hence thermal deflection, according to the contact pressure distribution of the joint which is dependent on the parameters such as material properties, surface finish of the joint interface, machining type of the joint interface, flatness deviations at the joint interface, initial loading type (tightness of fixing bolts, and force applied to the joint), type of relative movement between the contacting components.

This range in contact pressure was entered into a model calculating temperature differences using a finite difference method. The thermal deformation of the arm was then calculated using the finite element method. The range of thermal deformations resulting from varying distributions of the contact pressure was found to be at least 50μm for extension of the arm along its length, and approximately 60μm for vertical deformation due to bending.

This result showed that the heat transfer across a machine tool joint cannot easily be predicted by viewing or testing the external attributes of the joint. Indeed, Attia ([104]

cited in white [3]) states that the range of heat flow across a joint in a machine tool can vary between 3.5 and 9.5 kW/m^2/°C.

Özişik [107] showed graphically the relationship between contact pressure, contact temperature, and surface roughness on the interface conductance of two stainless steel plates in contact from many empirical tests on heat exchangers. The graph in Figure 3.2 has been reproduced and represents the contact conductance when two stainless steel plates are in contact ([Ozisik [107] cited in White [3]).

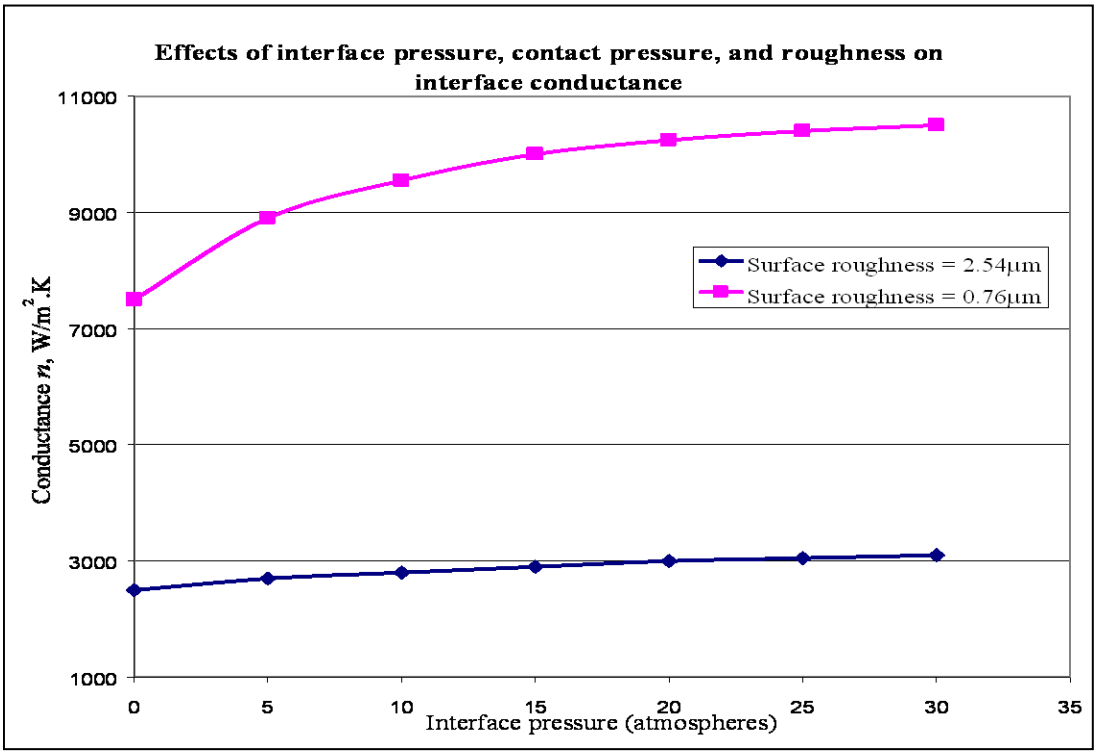

Figure 3-7: Effects of contact pressure, contact temperature and surface roughness on interface conductance n in stainless steel

Figure 3-7 shows that surface roughness of the joint interface significantly affects heat conduction across a stainless steel joint.

Thermal conductance across a joint can also vary significantly depending on the interface pressure. Tirovic et al [108] conducted a study of interface pressure distributions and thermal contact resistance of a large automotive bolted joint to determine the conductive heat dissipation accurately from a commercial vehicle disc brake. Tirovic tested the effect of the interface pressure at two positions, in the bolt proximity and between the bolts using same interface pressure and surface parameters.

The tests were conducted on the interface of a disc made of gray cast iron and the wheel carrier made of spheroidal graphite iron with surface roughness of Ra ranging from 1µm - 3.3µm. The testing revealed that for an averaged interface pressure from 10MPa to 55MPa, the thermal contact conductance varied from 3700W/m^2/°C to 10200W/m^2/°C respectively in the bolt proximity and from 2900W/m^2/°C to 6350W/m^2/°C respectively between the bolts. The result confirmed that the thermal conductance is much higher in the proximity of the bolt than between the bolts despite of same interface pressure and surface characteristics.

This result confirmed that bolt pressure distribution along with surface parameters can cause a variable thermal conductance across the joint and that experiments should be conducted in order to have confidence in obtaining values for specific task. Since the studies that were conducted to obtain thermal conductance values are limited to the selected material and specific type of interface characteristics, the values are not readily transferable. Therefore experiments were conducted to obtain the thermal conductance values for the structural joints of the machine.

The conductance values for the joints were obtained from materials that are commonly used in machine tools. Steel plates were used so that the values can be used for cast iron joints or steel-cast iron joints since the conductivity values for both steel and cast iron are very close (steel- 51.9 W/m/°C and cast iron – 52.329 W/m/°C). The clamping force data range used for the assembly joints was obtained from the machine drawings provided by the manufacturer. The TCC range obtained can be varied using curve fitting and extrapolation techniques for suiting them to most machine joints.

3.5.1 TCC testing

Experiments were carried out using two rectangular steel plates. Both plates had the same dimensions of

Length = 0.0235m , Width = 0.145m , Height = 0.092m

The surface finish and flatness of the plate's interfacing surfaces were given prime importance to ensure the reliability of the contact. This in essence can replicate machine tool joints where surface finish is given importance to increase precise assembly. The interface of the steel plates has an average surface finish value Ra of 2µm. Due to the

unavailability of the surface finish values from the engineering drawings of the machine under research, this value was selected from the machine engineering drawings from an Italian machine manufacturer. They use a surface finish of 3.2µm to assemble large structure such as column to the base. Ra of 0.8µm is used for the sliding joints and Ra of 2µm is used for smaller high presicion joints. Therefore the selected value (Ra of 2µm) represents more appropriate for the joints of machine under research.

Surface flatness was measured at 14µm which is eliminated with standard clamping force and therefore has negligible effect on the heat flow. Four digital temperature sensors were embedded into the plates to ensure high accuracy measurement of the core temperatures. Figure 3-8 shows the test setup with two horizontally placed steel plates. Details of the temperature sensors will be addressed in Chapter 4.

Figure 3-9 and Figure 3-10 show the surface flatness of both plates measured by a Ziess Coordinate Measuring Machine (CMM).

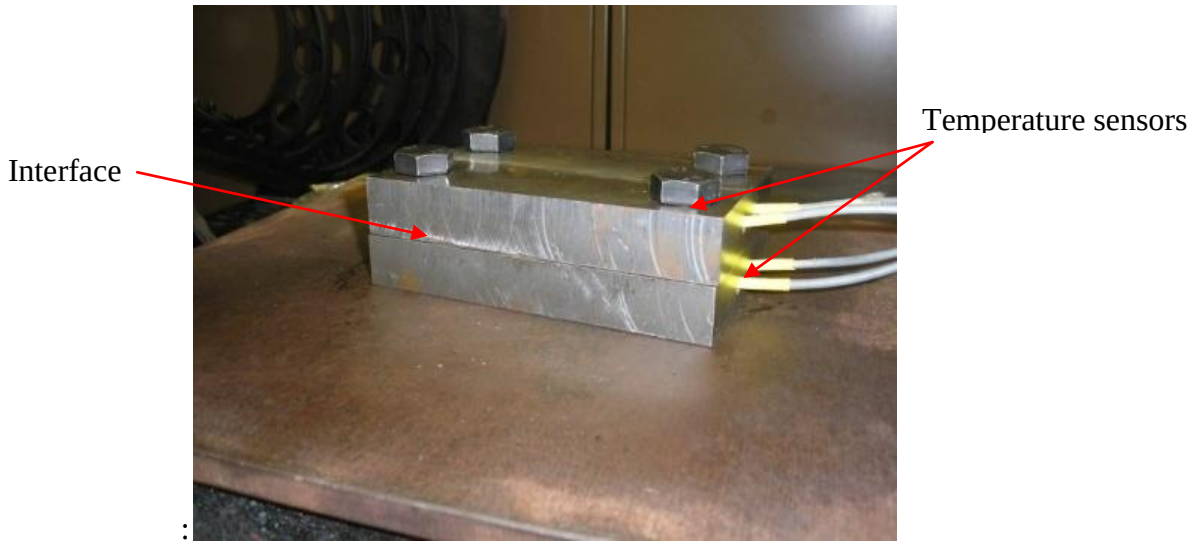

:

Figure 3-8: Test setup

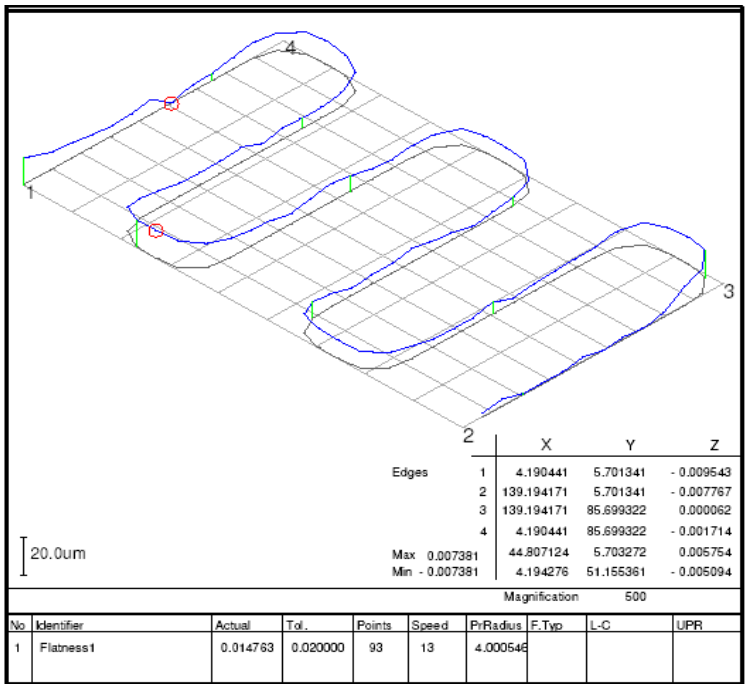

	X	Y	Z
Edges 1	4.190441	5.701341	- 0.009543
2	139.194171	5.701341	- 0.007767
3	139.194171	85.699322	0.000062
4	4.190441	85.699322	- 0.001714
Max 0.007381	44.807124	5.703272	0.005754
Min - 0.007381	4.194276	51.155361	- 0.005094
Magnification		500	

No	Identifier	Actual	Tol.	Points	Speed	PrRadius	F.Typ	L-C	UPR
1	Flatness1	0.014763	0.020000	93	13	4.000548			

Figure 3-9: Surface flatness (Top plate)

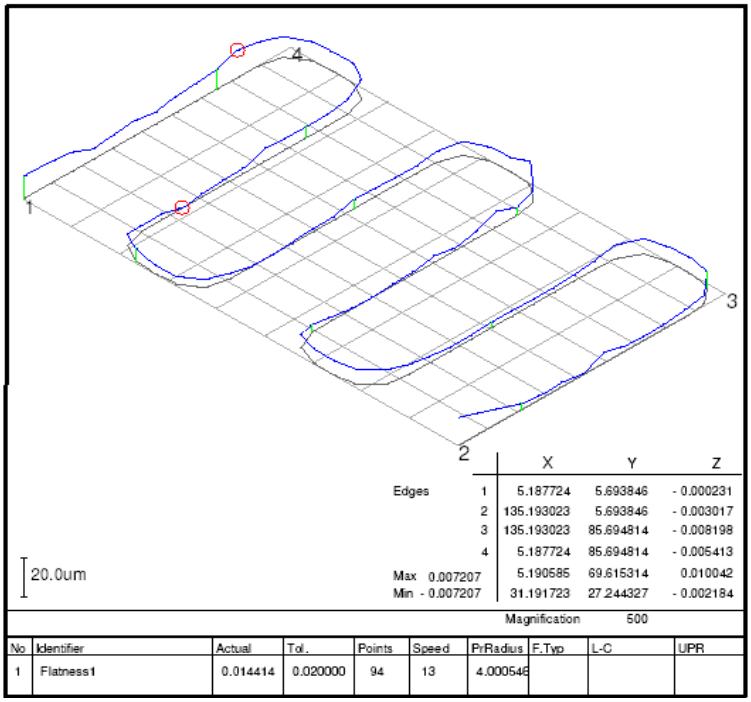

	X	Y	Z
Edges 1	5.187724	5.693846	- 0.000231
2	135.193023	5.693846	- 0.003017
3	135.193023	85.694814	- 0.008198
4	5.187724	85.694814	- 0.005413
Max 0.007207	5.190585	69.615314	0.010042
Min - 0.007207	31.191723	27.244327	- 0.002184
Magnification		500	

No	Identifier	Actual	Tol.	Points	Speed	PrRadius	F.Typ	L-C	UPR
1	Flatness1	0.014414	0.020000	94	13	4.000548			

Figure 3-10: Surface flatness (Bottom plate)

The experiments were carried out in two phases, firstly with cleaned dry plates and then with oiled plates. In the first phase, plate-1 was heated to approximately 52˚C and plate-2 clamped immediately onto the heated plate-1 using four M14 bolts. The heater was turned off immediately after clamping plate-2. Contact pressure at the joint was

varied by using torque values ranging from 35Nm to 85Nm, which was considered typical for machine tool joints, applied to the fastening bolts to evaluate the effect of increasing contact pressure or clamping force on the thermal conductance value across the joint.

The aim is to measure temperature during the very initial phase when the heat energy from the bottom plate starts to propagate into the top plate through the interface to cause an increase in the temperature of the top plate. Figure 3-11 is the illustration of sensor positions within the plates and shows the pictorial view of the testing procedure. Figure 3-12 shows the temperature profiles measured at both plates when the torque of 55Nm was applied.

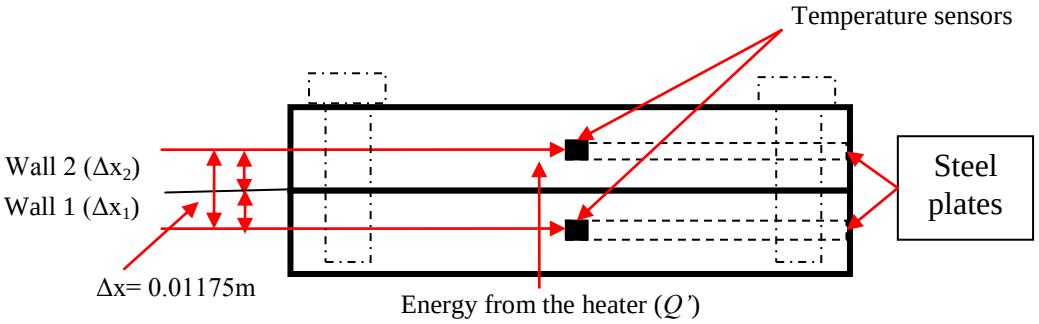

Figure 3-11: Testing procedure to obtain TCC

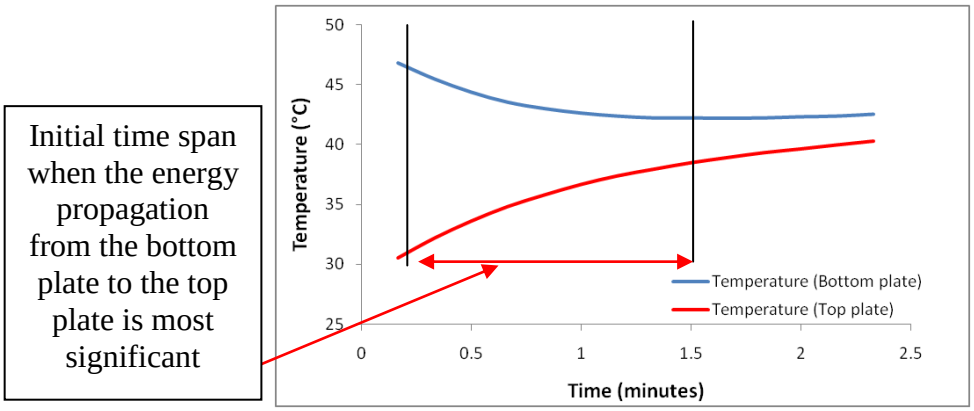

Figure 3-12: Test conducted for 55Nm torque

The heat energy flowing from the lower plate to the top plate was calculated transiently using the heat transfer equation (3.5). This can be explained as the heat energy required by a body of a given mass and specific heat capacity to a temperature rise in a given time period.

$$Q = mCp(T_2 - T_1)/t \ldots\ldots\ldots \quad (3.5)$$

Where Q is the heat energy input in Watts, m is the mass, Cp is the specific heat capacity of the steel, $(T_2 - T_1)$ is the change in temperature of the top plate and t is the time for the testing period.

Prior to the experiments, it was important to obtain the convective heat transfer coefficient or heat loss to the air during heating and cooling phases of the body. This has influence on the surface of the body and results in decreasing the surface temperature.

3.5.1.1 Testing procedure and calculations for the convection

In order to obtain the convection coefficient value, one plate was heated up to 50˚C and suspended horizontally and allowed to cool to room temperature of 20˚C in a free convection mode. Figure 3-13 illustrates the testing procedure for the convection where the heated plate was allowed to cool down in a natural convection mode. Three temperature sensors were used. The sensor inside the plate and on the surface were used to obtain an average temperature of the body. The ambient sensor was placed adjacent to the plate to monitor ambient temperatures.

Equation 3.5 was used to calculate the transient energy release Q (W) from the plate to the ambient. After obtaining the energy release, equation 3.2 was solved and used to calculate the convection coefficient h (equation 3.11). The calculations were performed transiently. The final convection coefficient value of 6W/m^2/°C was obtained after averaging. This value was assumed to be constant through all transient TCC calculations.

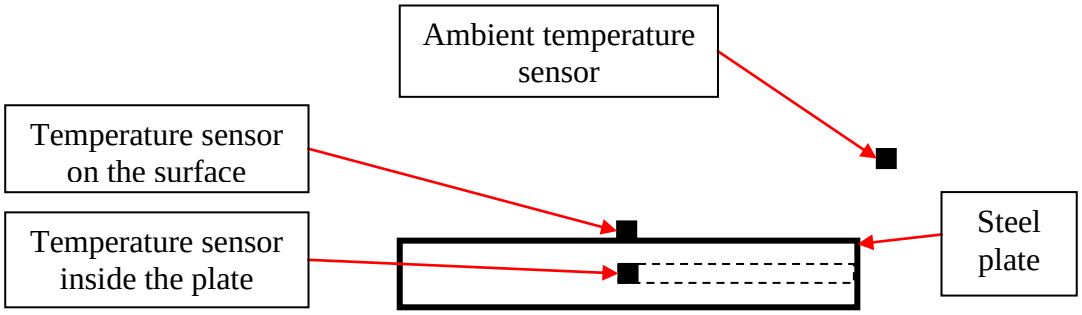

Figure 3-13: Testing procedure for the convection (h)

As convection is always taking place, the total heat energy Q' (equation 3.6) was obtained by adding equations 3.5 and 3.2.

$$Q' = mCp(T_2 - T_1)/t + hA(T_{surf} - T_{air}) \text{ ..... } (3.6)$$

Equation 3.6 is then used to calculate the energy transfer rate from the bottom plate to the top plate. T_{surf} in this case is the temperature from the top plate. The heat transfer through conduction does not affect the energy balance for the calculation of the heat flux and is therefore not required. The approach of temperature change that is dependent on the specific heat capacity of the material along with the energy released through convection was considered in equation 3.6. It should be noted that the equation 3.6 is used throughout the thesis with the similar approach as explained above. More details on the use of this equation can be found in chapter 4.

After determining the heat energy transfer through the plates, the conductance through the joint was calculated using the approach of one dimensional steady conduction in a composite wall with contact resistance at the interface [106]

$$Q' = \frac{(T_{bp} - T_{tp})}{\frac{\Delta x_1}{k_1 A} + \frac{1}{h_c A} + \frac{\Delta x_2}{k_2 A}} \text{ ..... } (3.7)$$

Where Q' is the energy in Watts, Δx_1 and Δx_2 are the length of wall 1 and wall 2 respectively. k_1 and k_2 are the conductivities of bottom and top plate respectively and h_c is the thermal conductance through the joint. T_{bp} is the temperatures obtained from the sensor placed in the bottom plate and T_{tp} is the temperature obtained from the sensor placed in the top plate. All calculations were performed transiently (10s) for the time span shown in Figure 3-12 to account for the non-linear propagation of the energy from the bottom plate to the top plate.

Both plates (Figure 3-8) have the same dimensions and are made of same material, therefore the value of conductivity and the length were considered to be the same.

Δx_1 *and* $\Delta x_2 = \Delta x$

k_1 *and* $k_2 = k$

Solving for the thermal conductance across the joint (h_c), the equation can be represented as equation 3.8.

$$h_c = \frac{Q'k}{\left(Ak(T_{bp} - T_{tp}) - 2Q'\Delta x\right)} \quad \ldots\ldots\ldots \quad (3.8)$$

Calculations for the first two out of 12 iterations are presented. Ambient temperature during the test was 24°C. Calculations were performed using SI (m) units system. When considering convection during each iteration, an average of the start and end temperatures are used.

1) *Q' = (2.45*473*(34.22-32.91))/10 + 6*0.01334*(33.57-24)*

   Q' = 153 W

   This *(Q')* value is then used to obtain the thermal conductance value using equation 3.8.

$$h_c = \frac{153 * 52}{\left(0.01334 * 52 * (44.92 - 32.91) - 2 * 153 * 0.01175\right)}$$

This gives $\boldsymbol{h_c = 1674\ W/m^2°C}$

2) *Q' = (2.45*473*(35.32-34.22))/10 + 6*0.01334*(34.77-24)*

   Q' = 127 W

   This *(Q')* value is then used to obtain the thermal conductance value using equation 3.8.

$$h_c = \frac{127 * 52}{\left(0.01334 * 52 * (43.95 - 34.22) - 2 * 127 * 0.01175\right)}$$

This gives $\boldsymbol{h_c = 1765\ W/m^2°C}$

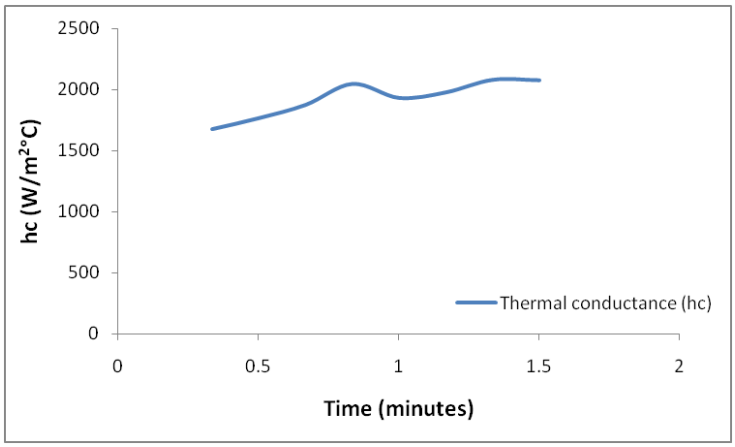

Figure 3-14: TCC graph obtained for the test conducted with 55Nm torque

Figure 3-14 shows the graph of the obtained values of the TCC for the test conducted for 55Nm torque. The plot shows a fluctuating trend of TCC values, the variation of which is suspected to be due to small local thermal stresses such as bending of plates resulting in variation in pressure and therefore the conductance. These transiently obtained TCC values were averaged to obtain a single value of 1956W/m^2 °C (for 55Nm clamping force) for use during modelling the machine (Chapter 4)

Clamping forces were calculated using equation 3.9 (Euler [109]).

$$Pi = T / KD \quad \ldots\ldots\ldots\ldots\ldots\ldots \quad (3.9)$$

Where *Pi* is the clamping force, *T* is the torque applied, *K* is the torque coefficient and *D* is the bolt nominal diameter. The range of torque values were obtained from machine assembly drawings. *K* can be calculated using equation 3.10, [109]

$$K = \{[0.5p/\pi] + [0.5\mu t(D - 0.75p\sin\alpha)/\sin\alpha] + [0.625\mu cD]\}/D \quad \ldots\ldots\ldots (3.10)$$

Where

- D Bolt nominal shank diameter
- p Thread pitch (bolt longitudinal distance per thread)
- α Thread profile angle = 60°/2
- µt Thread coefficient of friction
- µc Collar coefficient of friction

3.5.1.2 **Data used for calculating the clamping force**

The data used to obtain the torque coefficient (K) is shown below. (Euler [110]). The value of K was calculated as 0.24 using equation 3.10.

D = 13.026 mm
P = 1.5mm (fine thread)
α = 30° = 0.52 rad
π = 3.142
The thread coefficient of friction was assumed to be [111]
μt = 0.14 for dry conditions (averaged)
0.12 for oiled conditions (averaged)
The collar coefficient of friction was assumed to be
μc = 0.20 for dry conditions (averaged)
0.14 for oiled conditions (averaged)

In phase 2, the test was repeated with oil applied to the plate's contacting surfaces and bolt threads to modify the condition from dry to wet or from clean to contaminated. As expected, an increased trend of conductance was observed with increasing torque and from dry to oiled conditions. After calculating the torque coefficient for both dry and oiled conditions, the clamping force (P_i) was calculated using the equation 3.9. Figure 3-15 shows the clamping force and thermal conductance profiles in dry cleaned and oiled conditions.

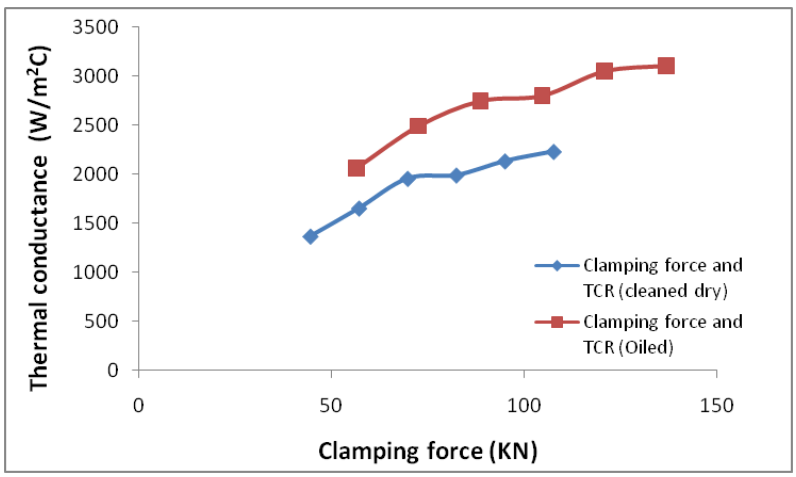

Figure 3-15: Clamping force and conductance values in cleaned dry and oiled conditions

Table 3-3 show the values obtained in dry conditions and oiled conditions for thermal conductance values and the clamping forces across the joint.

Torque	Clamping forces Pi (KN) for four M14 bolts		Thermal conductance ($W/m^2/°C$)	
T	cleaned dry	Oiled	cleaned dry	Oiled
35Nm	44	56	1367	2061
45Nm	57	73	1653	2490
55Nm	70	89	1956	2746
65Nm	82	105	1990	2800
75Nm	95	121	2134	3049
85Nm	107	137	2231	3106

Table 3-3: Experimental values for clamping forces and conductance values at different torque ranges

The increasing trend of the thermal conductance values sees a sudden drop at the torque of 65Nm and since this behaviour is repeated in both conditions (dry and oiled) it is considered to be the slip of the bolt threads. The approximated value at 65Nm can however be obtained using curve fitting and extrapolation techniques. Figure 3-16 and Figure 3-17 shows two curve fits techniques (pure and double exponential) to predict values beyond the tested range due to exponential nature of the curves. A value can be selected as an average of both. The decrease in the thermal conductance values with the increasing torque was expected as the state of the heat flow stabilization was achieved.

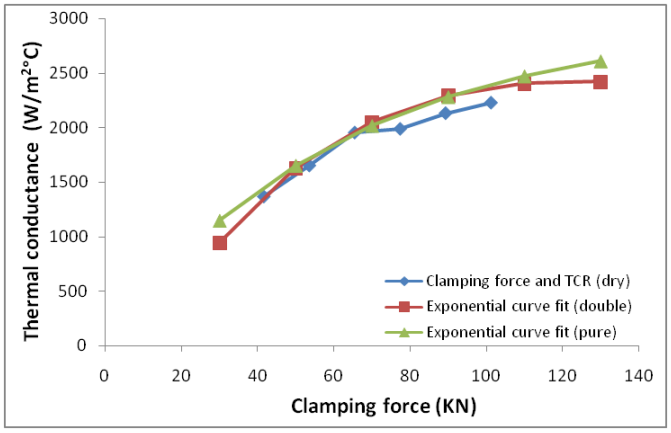

Figure 3-16: Clamping force and thermal conductance values with curve fits (dry)

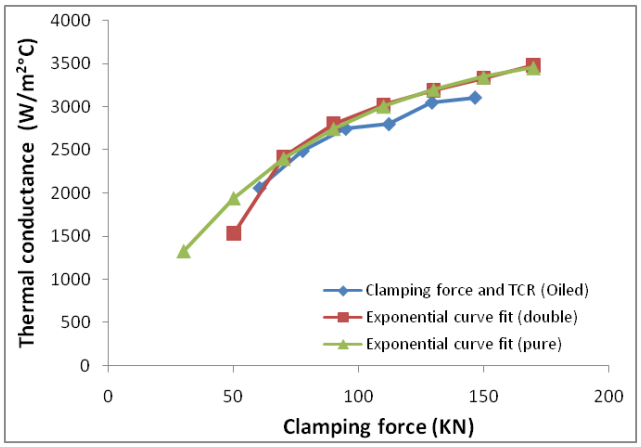

Figure 3-17: Clamping force and thermal conductance values with curve fits (oiled)

This discussion has given an understanding of the structural joints characteristics on which the heat transfer depends. In this research, the obtained thermal conductance values will be applied at the joining surfaces of the machine CAD model assembly for FEA. The application will be detailed in chapter 5.

3.6 Determination of convective heat transfer coefficients during tool rotation (h)

To ensure the accuracy of the FEA simulation results it was necessary to devise an effective strategy to calculate the convective heat transfer coefficient (h) due to airflow across test mandrels or generic tooling during spindle rotation. This convection coefficient was used during heating cycle simulations to represent the temperature loss at the rate expressed by the coefficient value. A thermal imaging camera was used to view the surface temperature variation around the spindle housing and test mandrel.

3.6.1 Testing procedure

The thermal imaging camera was placed at a position where the test mandrel and other machine structure were visible (see Figure 3-18). Masking tape was applied to the mandrel to increase the emissivity to a known value of 0.96. A temperature sensor was positioned adjacent to the test mandrel to measure the ambient temperature change during heating and cooling phases. The spindle was rotated at 8000 rpm for one hour and stopped for a cool down period. The heating and cooling cycle data was recorded with a thermal imaging camera (1Hz);

Figure 3-19 shows a thermal image of the temperature distribution during spindle rotation.

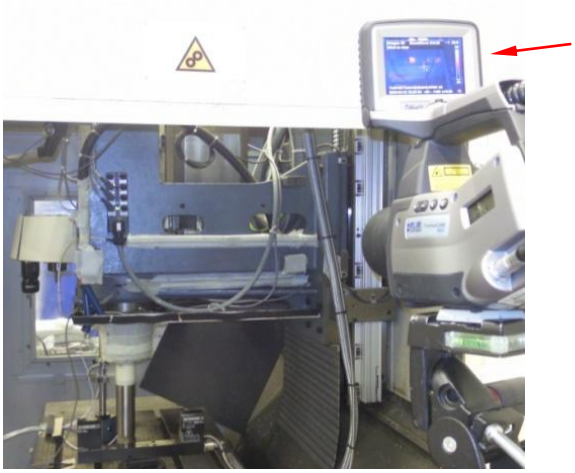

Figure 3-18: Thermal imaging of spindle and carrier

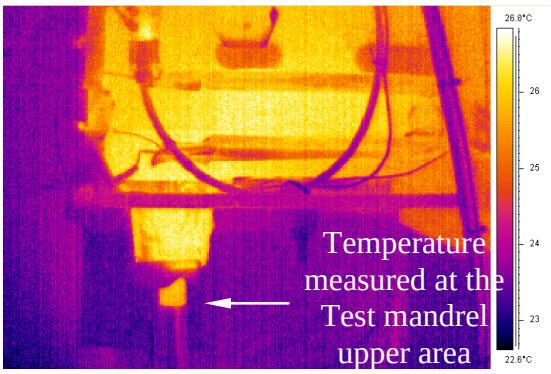

Figure 3-19: Thermal imaging of rotating spindle

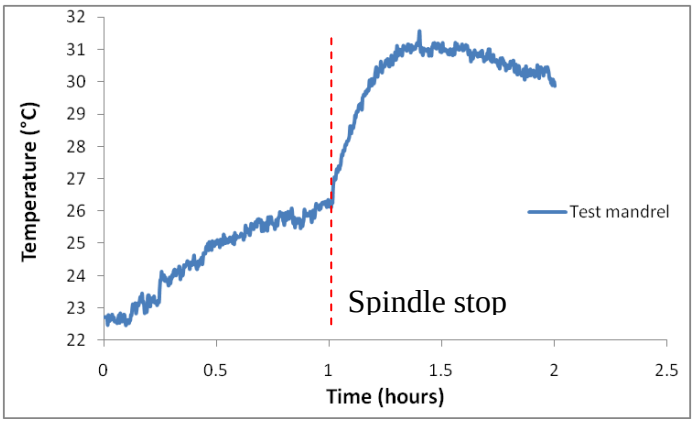

Figure 3-20: Temperature measured at the test mandrel upper surface

Figure 3-20 shows the temperature from the surface of the test mandrel against time. The plot shows two perspectives; the first is targeted towards the cause of the temperature rise at the test mandrel's upper area as explained in section 4.3.3.2.1. The other perspective is to specifically target the convection procedure. The heat convects at a high rate during the tool rotation which limits the increase in test mandrel temperature. It can be seen that the temperature starts to increase after the spindle is stopped due to the reduced convective heat loss. It is assumed that the actual heat flow into the mandrel is the same for a short duration after stopping the spindle to enable a calculation of the change in convection coefficient.

3.6.1.1 **Calculations for convective heat transfer coefficient**

Figure 3-21 shows the selected section of the test mandrel model. The energy entering the test mandrel from the spindle was calculated using equation 3.5 transiently using the surface temperatures from the test mandrel rotating at 8000rpm.

$$Q = mCp(T_2 - T_1)/t \quad \text{..... (3.5)}$$

The test mandrel was made of the material Invar The selected section had the volume of 162573 mm^3 that revealed the mass of 0.0013tonnes. After obtaining the energy (Q) in Watts, this energy can be related to the energy (q_{conv}) in equation 3.2 therefore equation 3.2 can be transformed for calculating convection h as shown in equation 3.11

$$h = \frac{q_{conv}}{A(T_{surf} - T_{air})} \quad \text{.....(3.11)}$$

Where A is the exposed area of the test mandrel (13987mm^2). T_{fluid} in this case is the temperature of the air circulating across the test mandrel (T_{air}). Again the values of h were averaged from which a value of 92W/m^2/°C was obtained for the spindle running at 8000rpm which was applied to the test mandrel during the heating cycle simulations conducted for the 8000rpm.

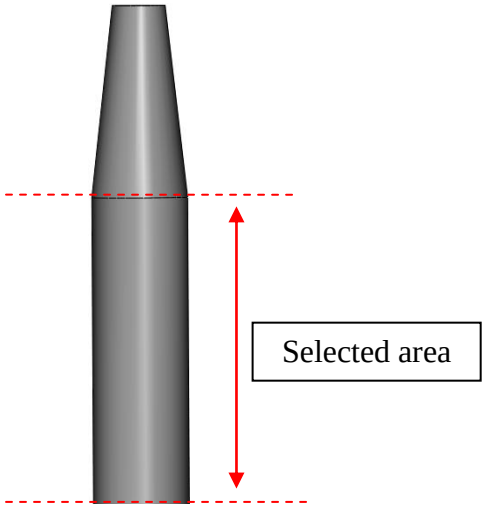

Figure 3-21: Test mandrel selected area for convection calculations

Although the convective heat transfer coefficient of 6W/m^2/°C was obtained using steel plates, a separate test was conducted as a secondary validation for calculating h on a complicated geometry i.e. the machine structure in static conditions (i.e. during the

cooling cycle) for which an additional ambient sensor was placed adjacent to the column. The spindle and carrier structures used the same ambient sensor discussed in the previous section. The machine was run for a heating cycle and then stopped for a cool down and *'h'* values were calculated for the cooling cycle. The convection values of approximately 9W/m^2/°C and 2W/m^2/°C were obtained for the spindle and carrier respectively, averaged to 6W/m^2/°C. This value was also considered for the test mandrel for the cooling phase simulations. The lower value obtained for the carrier corresponds to the slower cooling process which is suspected to be due to the presence of air pockets within the complex geometry where heat confinement causes lower cooling rate of the structure. Separate calculations were performed to obtain the *'h'* value for the column using the column ambient sensor. The average of two surface sensors on the column revealed a value of 5.7W/m^2/°C which was rounded up to 6W/m^2/°C and applied to the column. Since the secondary validation confirmed the value of *'h'* therefore the base and table structures were also applied the similar *'h'* value. Figure 3-22 shows the positions of the surface and ambient sensors used to calculate the *'h'* values for the spindle, carrier and column structures. The base sensor shown is used

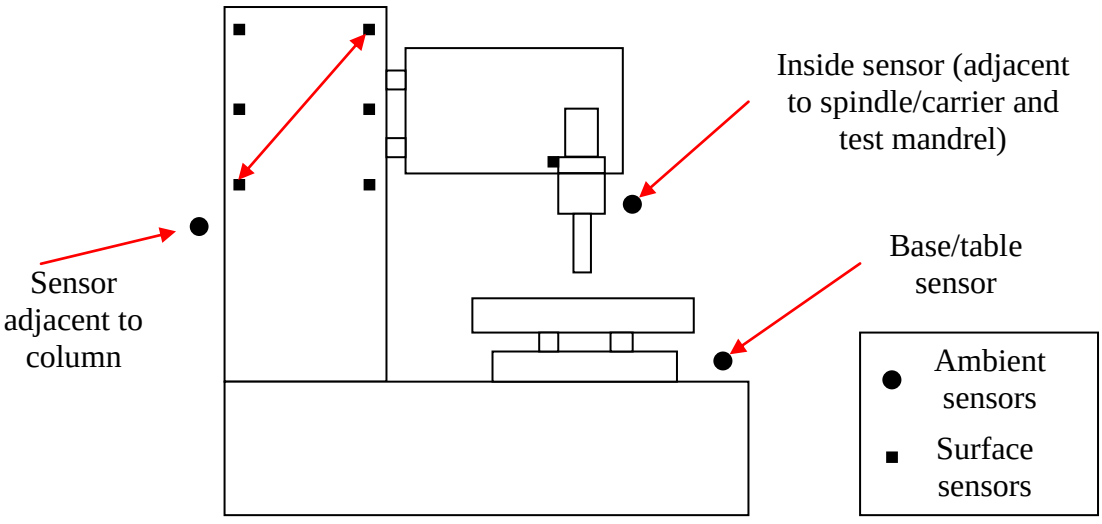

Figure 3-22: Position of the surface and ambient sensors around the machine

3.6.2 Summarizing convective coefficient *'h'* tests

Various tests for the convective heat transfer coefficient *'h'* were conducted. Firstly *'h'* was calculated for the rotating spindle. The testing at 8000rpm revealed convection

value of 92W/m^2/°C. A separate test was also conducted to determine the convection value for the rotating test mandrel at 4000rpm using the same procedure which revealed the convection value of 58W/m^2/°C (chapter 4). These values are only used at the test mandrel selected area shown earlier and during the heating cycle simulations only (chapter 4).

Convection values were also calculated for the machine in a static mode. Various tests revealed an overall value of 6W/m^2/°C. This value is applied to the full FEA model during both heating and cooling cycles apart from the test mandrel where two different *'h'* values were applied only during the heating cycle.

It should be noted that these convection values were applied to the FEA model as a uniform parameter i.e. the convection was assumed to be constant throughout the simulation time.

3.7 Implementation of the research

This research aims to study the thermal behaviour of the machine tool followed by the software based FEA, an offline method to predict the thermal deformations in the machine tool structure. The Computer Aided Drawing (CAD) models of the machine tool structural components were created from manufacturer's 2D engineering drawings using the FEA software to avoid importing models from other CAD packages due to problems such as geometrical incompatibility issues. The research was carried out on a three axis Cincinnati Arrow 500 Vertical Machining Centre (VMC) located at the University of Huddersfield shown in Figure 3-23.

Figure 3-23: Cincinnati Arrow 500 Vertical Milling Machine

The machine CAD assembly was generated and used as a virtual machine and simulated using FEA software subject to internal and external temperature sources to increase modelling accuracy. The obtained TCC values were applied at the model joint surfaces. The machine dynamics is not considered in this research therefore the sliding surfaces of the machine were applied an averaged TCC value of approximately 2000 ($W/m^2/°C$) and is an assumption based on the contacting surface area of the bearings with pre-load and small amount of lubrication. The magnitude of the heat flowing across these joints is small and therefore inaccuracy in the assumed value can be tolerated for this first phase of the work. The affect of varying TCC across a joint is shown in assembly benchmark conducted in chapter 4. However in future experimental work may be needed to obtain accurate TCC values for sliding joints. Chapter 4 details the modelling approach used during the development of the individual CAD models and the final assembly of the machine. The following chapters detail the practical study conducted on the machine when subject to internal and external environmental temperature fluctuations. The online test results were then used to obtain the required parameters for the offline simulation.

Internal heating tests were carried out at different spindle speeds during which the machine thermal behaviour was investigated. The spindle, associate bearings, spindle and axis hold motors; and belt drive are the primary internal heat sources on this machine. Dynamic movement of machine axes is not considered in this research activity primarily because most precision machine tools employ linear scales for position feedback,

eliminating the mechanical drive elements from the feedback loop dramatically reducing associated thermal errors. The rolling element guide ways were modelled to complete the main machine structure but similarly, negligible heat is generated by them.. The heat dissemination through the structure due to spindle heating is of prime importance; however an additional issue is the structural temperature increase due to the increase in local ambient temperature caused by the machine operation.

3.8 Summary of the chapter

This chapter looked at the various modes of heat transfer mechanisms that occur in a machine tool structure i.e. conduction, convection and radiation. The major heat transfer mode is through conduction where the heat flow occurs internally. Convection is associated with the bi-directional heat flow between the machine structure and external fluid, in this case the surrounding air. Convection is a complex process and is dependent on various factors. Radiation can be considered to be negligible in the context of energy flow but the associated parameters are important for thermography.

Temperature gradients in machine tool structures depend on various factors that include properties of the material, modes of heat transfer and thermal characteristics of structure joints. Temperature gradients result in thermal distortions of the structure which may be linear or non-linear depending on various parameters. Non-linear distortions occur when uneven local temperature gradient occur due to a variety of structural and joint thermal characteristics such as TCR that is responsible for controlling the heat flow across joints. Thermal contact conductance values, convective heat transfer value for the rotating tool and for static machine were experimentally obtained.

The scope of the research has been presented along with the procedure that will be followed to carry out tasks. Typical internal heat flow through a 3 axis VMC has been illustrated and the importance of ambient temperature rise has been discussed. Similarly the existence and importance of external environmental fluctuations are given and the illustration of the environmental heat flow directions is shown. The creation of the machine structural components CAD models for FEA and the experimental thermal error testing and offline error predictions using FEA are detailed in chapter 4.

CHAPTER - 4

4 MACHINE TOOL INTERNAL THERMAL TESTING AND OFFLINE MODELLING

The previous chapter discussed the various modes of heat transfer mechanisms used in this research which are present in a machine tool. This chapter will discuss the CAD modelling of the VMC to perform a FEA. This is followed by the experiments conducted to obtain the thermal behaviour of the machine due to the excitation of internal heat sources. The behaviour of the machine was monitored using standard precision metrology equipment and methods described in the ISO 230 part 3 standard for thermal testing. The experimental data was then used to obtain the required parameters to conduct FEA simulations and analyze the thermal behaviour.

Dassault Systemmes Simulia Abaqus/CAE 6.7-1 FEA [112] simulation software was selected due to its ability to handle large geometrically complex problems. It allows development of user programmable subroutines for carrying out analyses with complex boundary conditions such as programming temperature dependent heat fluxes and spatial boundary conditions that includes varying environmental temperatures [113]

4.1 Benchmarks

Benchmark simulations were completed to validate the correct application of the thermal parameters and determine the accuracy of the thermal simulations compared to hand calculations for different mesh types and densities.

4.1.1 Abaqus heat transfer benchmarks

4.1.1.1 Benchmark (Single Block)

Part of this research deals with the prediction of thermal behaviour in a 3 axis VMC using FEA software. It is necessary to qualify the best parameters settings and simulation methodology using the proposed FEA software to get an optimised prediction capability and accuracy of the analysis therefore benchmark tests and trials are undertaken to use as points of reference. A model of a steel block with dimensions of 100mm x 40mm x

40mm was created to compare the behaviour of a block in the FEA software when subjected to a calculated heat flux input.

The heat transfer was simulated to confirm the mathematical relationship explained in chapter 3, equation 3.6.

$$Q' = mCp(T_2 - T_1)/t + hA(T_{surf} - T_{air}) \ldots\ldots\ (3.6)$$

The software provides the heat transfer feature where an object is simulated for its thermal behaviour. Abaqus provides three types of heat loads to an object. 1) Surface heat flux is the input applied to a surface of a given area. 2) Body heat flux is the input flux applied to a body disseminating heat within itself or to the other material attached to it. For example bearings can be considered as a body of a given volume that disseminates heat into the spindle. 3) Concentrated heat flux is the input flux targeted to specific points. Body heat flux (BHF) was used throughout this research as a convenient way to represent the machine tool heat sources based on the measured surface temperatures.

Two benchmarks were conducted using a single block. In the first benchmark, transient analysis was performed using a constant BHF value to predict the required temperature increase for the steel block that is expected to rise its surface temperature by at least 5°C (from 20°C to 25°C) over a one hour period. The first benchmark assumes that no convection is taking place. In the second benchmark, transient analysis is performed with a constant BHF value and with natural convection and ambient conditions considered. The first benchmark will confirm the capability of the mathematical relationship shown in equation 3.6. The second benchmark will represent the real testing condition where boundary conditions such as surface convection and ambient temperatures vary surface temperatures.

4.1.1.2 **Software modelling and FEA**

This section will detail the FEA heat transfer benchmark methods used. The material properties of the steel block are listed in Appendix A.

A transient heat transfer FEA simulation was setup with the total simulation time set to 1 hour (3600s) with one second increments. Boundary conditions were not considered.

Equation 3.6 is the main equation used to obtain BHF values. The total heat energy *Q'* is first calculated in Joules which is then converted into Watts by dividing with the analysis time. After obtaining the value of *Q'* in Watts, the value is divided by the volume of heat source to obtain BHF (W/m^3) for a particular heat source which in this case is the block itself. The calculations performed were based on the SI (mm) units system of Abaqus.

4.1.1.2.1 Body Heat Flux (BHF) calculations (Single Block)

Equation 3.6 is the main equation used to obtain BHF values.

$$Q' = mCp(T_2 - T_1)/t + hA(T_{surf} - T_{air}) \ldots\ldots\ (3.6)$$

For the first benchmark the calculations data used is shown below.

Mass of block = 0.001249 tonnes

Temperature difference (T_2-T_1) = 5°C

Total time = 3600s

Exposed area of the block = 19200 mm^2

By applying these values in equation 3.6, the value for the *Q'* can be calculated. Calculations for the first two out of 3600 iterations are presented.

*1) Q' = (0.001249*473000000*(20.00139-20))/3600 + 0.006*19200*(20-20)*

Q' = 820.39 mW

To obtain the BHF value that could raise the body temperature to 5°C, the value of *Q'* is required to be divided by the volume of the heat source which in this case is the volume of the block itself. Therefore using *Q'* from the first iteration the value of BHF can be obtained as

q' = 820.48 mW / 160000 mm^3 which gives the BHF value as

***Q'* = 0.005127 mW/mm^3**

The second benchmark calculation was performed using the similar method however this time the boundary conditions in terms of surface convection and ambient conditions were considered. Ambient temperature around the block was assumed to be constant at 20°C over the period of 1 hour simulation. The convection from the surface of the block was considered 6W/m^2/°C as previously calculated (Chapter 3). Calculation for the first out of 3600 iterations is shown below.

1) *Q'= (0.0012*473000000*(20.00278-20.00139))/1 + 0.006*19200*(20.00139-20)*

   Q' = 820.6 mW

Following the similar approach as used in the previous benchmark, the value of *Q'* was divided by the volume of the heat source i.e. the block itself.

$\dot{q}$ = 820.48 mW / 160000 mm^3 which gives the BHF value as

Q' = 0.00513 mW/mm^3

Since the BHF values were expected to vary, an averaged value of the BHF was obtained.

Q' = 0.0069 mW/mm^3

4.1.1.2.1 FEA benchmark simulation (Single block)

For first benchmark simulation, the BHF value was applied to the FEA model for transient analysis. An initial temperature of 20°C was applied to the block, boundary conditions were not considered. Figure 4-1 shows the temperature through the block. The graph in Figure 4-2 shows temperature from the selected node which confirms the temperature increase from 20°C to 25°C and therefore validates the mathematical approach. NT11 refers to the nodal temperatures and indicates the temperature increase of the block from 20°C to 25°C over a one hour period.

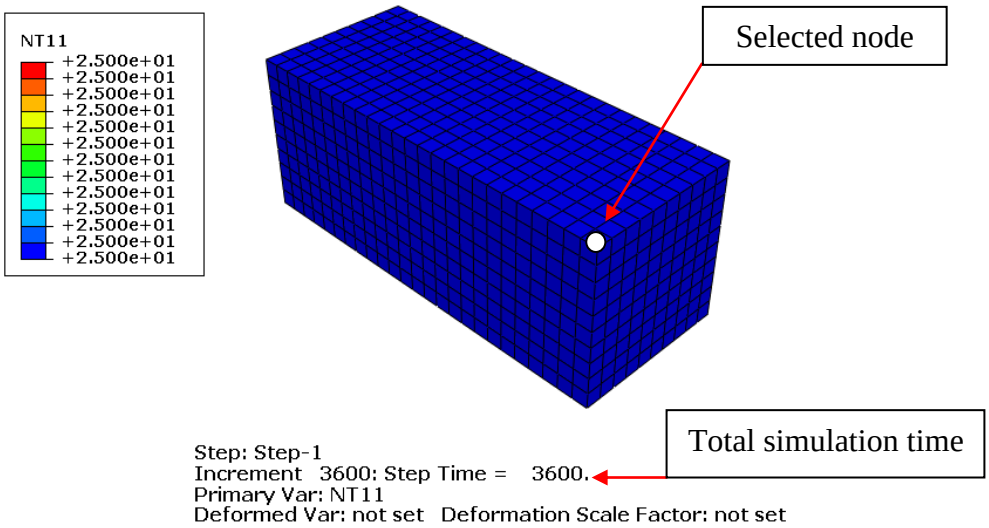

Figure 4-1: Simulated temperature for the first single block benchmark

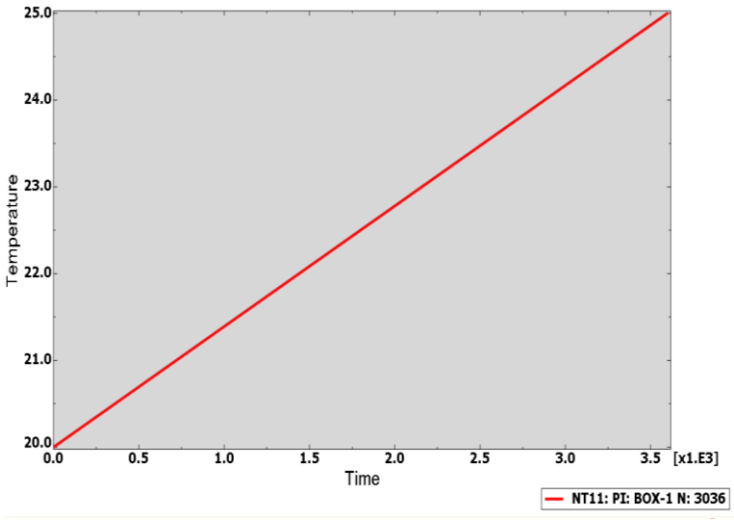

Figure 4-2: Nodal temperature showing temperature increase from 20°C to 25°C

For the second benchmark simulation, the BHF value was applied in to the FEA model for transient analysis. Boundary conditions were applied to the model in the software. An initial temperature of 20°C was applied to the block and after defining the parameters the FEA simulation was carried out. Figure 4-3 shows the temperature through the block with gradients. These gradients are present due to convection from the surface of the block. Figure 4-4 shows the temperature profile with an exponential decay trend. The temperature increased from 20°C to 24.84°C. This benchmark confirms that the expected final temperature is predicted with over 99% accuracy and therefore validates the use of equation 3.6 for obtaining required BHF values for simulations.

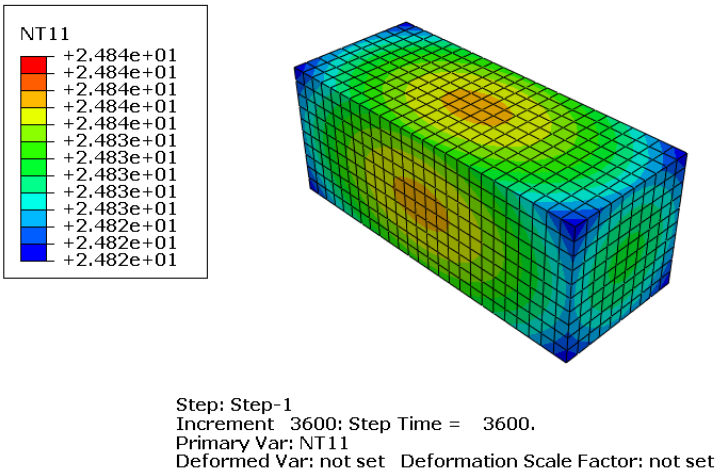

Figure 4-3: Simulated temperature for the second single block benchmark

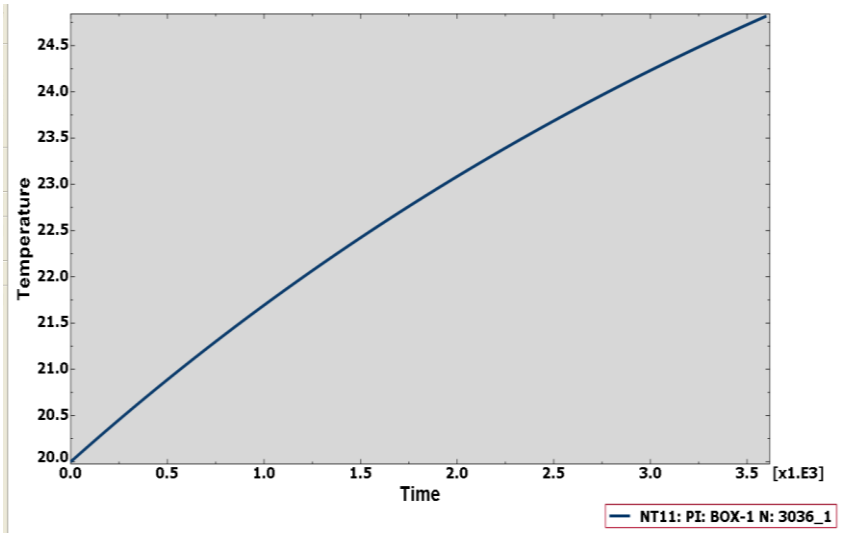

Figure 4-4: Nodal temperature showing temperature increase from 20°C to 24.84°C with an exponential decay trend

4.1.1.3 **Benchmark (Assembly)**

This benchmark is aimed for two objectives,

1) Confirming the reliability of the mathematical relationship used to calculate BHF values for predicting temperature flow in an assembly and to simulate heat distribution originating from those complex or rotating structures where thermal sensors are difficult to install. For example, spindle bearing temperature cannot easily be measured directly therefore the data has to be obtained from the external surface of the spindle carrier/housing.

2) To observe the behaviour of the TCC on the heat flow across the joint.

The assembly benchmark simulation was carried out using the steel blocks, as shown in Figure 4-5. The middle block had the dimensions of 40mm x 40mm x 40mm. Both attached blocks had dimensions of 40mm x 40mm x 20mm.

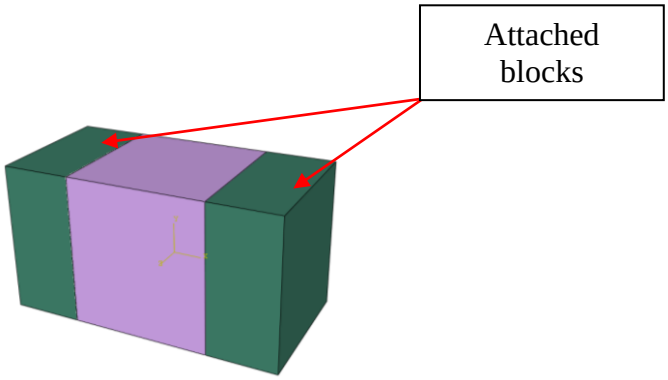

Figure 4-5: Created assembly in Abaqus

New body heat flux values were calculated for the middle block which is considered as a heat source and is expected to raise the temperature of the attached blocks by at least 5°C. Similar procedure was used to calculate the BHF as used for the single block i.e. the boundary conditions (convection coefficient of 6W/m^2/°C and ambient temperature of 20°C for all blocks) followed by the use of equation 3.6. Since similar conditions are used as used for the second single block benchmark, the BHF value is expected to raise the temperature of side blocks with the target magnitude of 24.84°C.

4.1.1.3.1 Body Heat Flux (BHF) calculations (Assembly)

The energy required to raise the temperature of side blocks was calculated using the full volume i.e. all three blocks. To obtain the BHF, the volume of the heat source which in this case was the middle block was used to divide the obtained energy *(Q')* to represent the BHF generated by the middle block. The calculation data and calculations for the first iteration are shown below.

Mass of blocks	= 0.000999 tonnes
Temperature difference (T_2-T_1)	= 5°C (00139°C for the first iteration)
Total time	= 3600s (for the first iteration, the time is 1s)
Convection coefficient (h)	= 0.006 mW/mm^2/°C

Exposed area of the middle block = 6400 mm^2

Ambient air temperature = 20°C

Exposed area of side blocks = 4800 x 2 = 9600 mm^2

Total area of blocks = 16000 mm^2

By applying these values in equation 3.6, the value for the *Q'* is

Q' = 656.3804 mW

To obtain the BHF value, the value of *Q'* is required to be divided by the volume of the heat source (middle block).

$\acute{q}$ = 656.3804 mW / 64000 mm^3 which gives a body heat flux value of

$$\acute{q} = 0.010256 \text{ mW/mm}^3$$

Using the similar approach as used in single block benchmark, an averaged BHF value was obtained.

$$\boldsymbol{Q' = 0.014 \text{ mW/mm}^3}$$

For this benchmark a very large TCC value was assumed and applied across the joint surfaces (1.e^8 W.m^2.°C) in order to achieve negligible resistance to the heat flowing through the assembly joints to observe if the calculated heat load can generate the targeted temperature of 24.84°C.

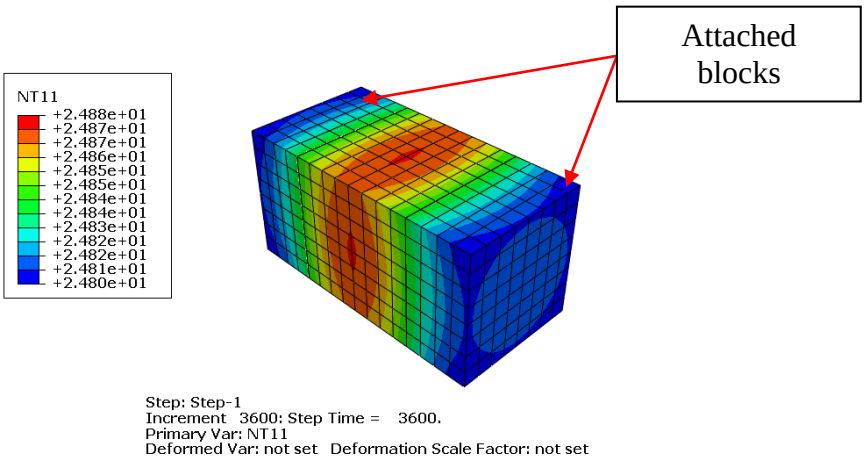

Figure 4-6: Simulated temperatures in assembly with very large TCC (1.e^8 W/m^2/°C)

The result (Figure 4-6) confirmed the application of the simulation technique to thermal assemblies giving a good correlation within 0.04°C. This relates to a thermal expansion error of just 0.4µm/m which is negligible for this application.

4.1.1.3.2 Effect of thermal contact conductance

The initial assembly benchmark had a large TCC value therefore additional benchmarks were conducted to observe the behaviour of the assembly with the lowest measured contact conductance value (1300W.m^2.°C - Chapter 3) and a higher assumed value (10000W.m^2.°C) applied to the joints. These benchmarks were specifically targeted towards those machine joints where the contact conductance value is not known with a high level of certainty. The simulated temperature drop due to both contact conductance values at the joint were observed to ensure the level of achievable accuracy prediction based on the calculated body heat flux value. The results are shown in Figure 4-7 and Figure 4-8. Same constant BHF value was used in this benchmark as used previously for the assembly benchmark. Selected node locations are visible in Figure 4-7. Table 4-1 shows the temperatures at selected middle and corner nodes obtained at different values of TCC. The predicted surface temperature on the attached blocks was found to be within 0.1°C of the expected 24.84°C. This is also shown graphically in Figure 4-9. Although a slightly larger error, the effect on distortion is still negligible being just 1µm/m.

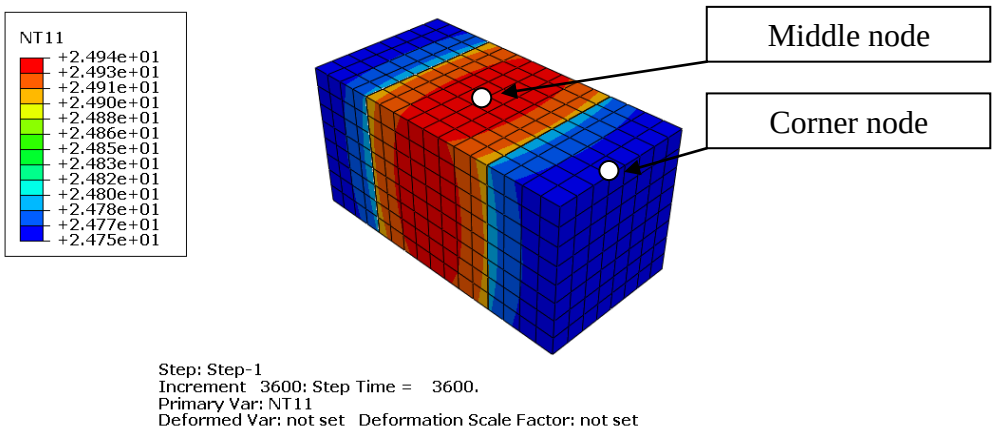

Figure 4-7: Simulated temperatures in assembly with lowest contact conductance (1300W/m^2/°C)

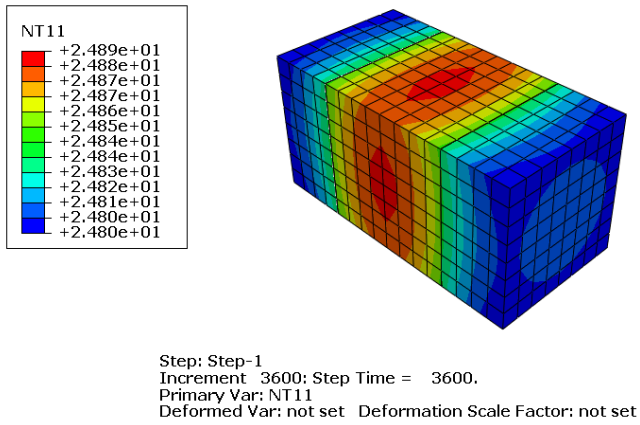

Figure 4-8: Simulated temperatures in assembly with an assumed higher contact conductance (10000W/m^2/°C)

Thermal contact conductance (W/m^2/°C)	**Middle node temperature (°C)**	**Side node temperature (°C)**
1300	24.94	24.75
10000	24.89	24.80
1.e^8	24.88	24.80

Table 4-1: Temperature at selected nodes of the model simulated with different values of thermal contact conductance

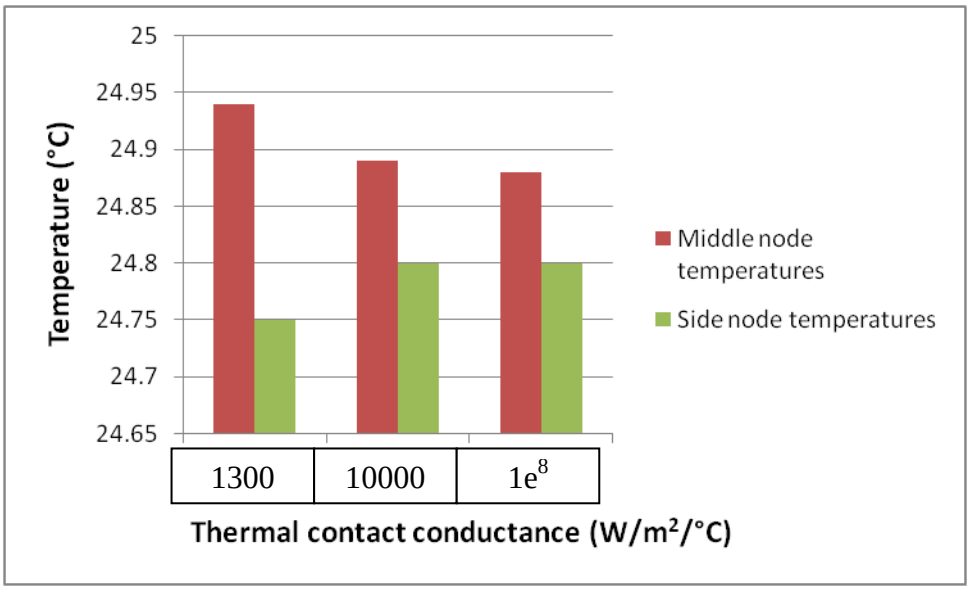

Figure 4-9: Temperature trend comparison between the middle and side nodes at different TCC values

This section detailed heat transfer benchmarks where the method of calculating body heat flux value is confirmed. Assembly benchmarks confirmed the compromise on the

accuracy of thermal contact conductance value will still result in more than 90% temperature correlations.

4.1.2 Abaqus mesh benchmark testing

This benchmark aims to compare the results of two type of meshing which Abaqus normally uses to discretize a structure in order to have confidence in the accuracy of the predicted results based on the fact that hexahedron (linear brick) elements are well known to reveal better FEA accuracy. A linear brick hexahedron element has all surfaces at 90° angles (right angles) and this cause them to be evenly distributed within structure compared to other element types which may have surfaces at angles other than 90° and may have a risk of element surfaces being skewed. It is anticipated that both meshing techniques will give similar results, however due to the above explained reasons, the prediction accuracy may differ and therefore this benchmark must compare them. A negligible difference will justify that it may not be required to simplify complex geometry by re-sectioning in order for it to be able to mesh using hexahedron elements as this is a time consuming procedure and can be difficult to apply on imported models from CAD packages. This research aims to maintain simplicity in the method for thermal error prediction.

Two popular meshing techniques, 8-node linear brick (hexahedron) and a 4-node linear tetrahedron were compared in this benchmark. Hexahedron meshing is a default selection in Abaqus CAE and is mainly applied to mesh simple models, however the tetrahedron meshing technique is used for structures with complex geometries where hexahedron meshing is not applicable or often fails. By default the software selects the meshing method for a model; therefore both meshing techniques can be used to mesh the machine models where applicable. A simple block was used to perform benchmark tests to compare the performance of both meshing techniques to predict the thermal error and review the error difference.

4.1.2.1 **Hexahedron meshing**

The same steel block model with dimensions of 100mm x 40mm x 40mm was simulated after discretizing using the hexahedron meshing technique. Approximate element size was chosen to be 4mm (seeding) that discretized the structure into 2500

linear hexahedral elements. The block was allowed to displace in only one axial direction therefore all other axial movements and rotational movements were constrained. The same thermal data was used in this benchmark as previously used i.e. thermal displacements of the block were monitored when subjected to a 5°C change over an hour. Thermal expansion of 5.85µm is expected for this block which is calculated using the equation 3.4. Figure 4-10 shows the thermal deformation of the block when subjected to 5°C temperature change. A corner node was selected to measure the overall displacement of the block and was observed to be 6.073µm revealing a difference of 0.223µm from the expected which is considered negligible for this research. This value will be compared with the displacements shown by the tetrahedron meshing method.

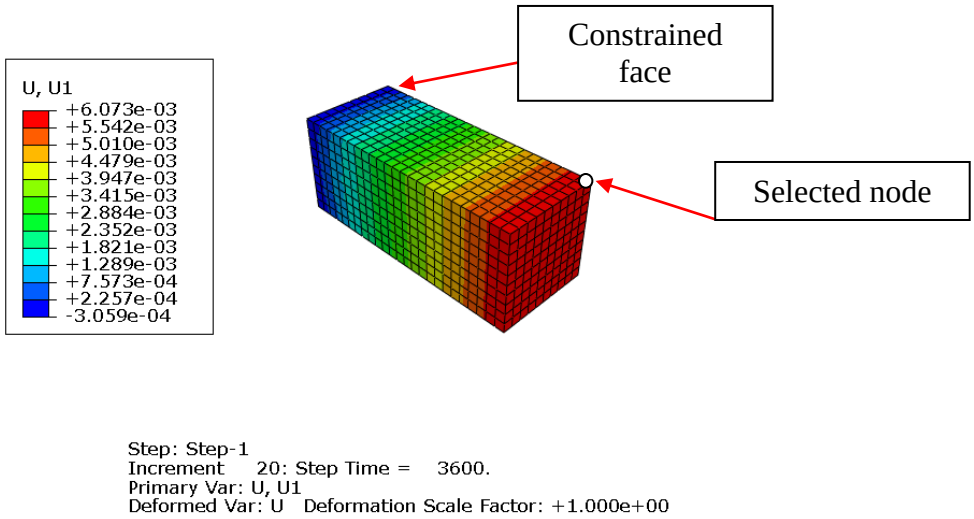

Figure 4-10: Thermal deformation of the block (Hex meshing)

4.1.2.2 **Tetrahedron meshing**

Using the similar method, the block was simulated with the tetrahedron meshing technique. The approximate element size was also chosen to be 4mm (seeding) in this benchmark that discretized the structure into 17814 linear tetrahedral elements. Figure 4-11 shows the thermal deformation of the block when subjected to 5°C change. The overall displacement at the corner node was measured to be 6.113µm revealing a negligible difference of 0.263µm compared from the expected.

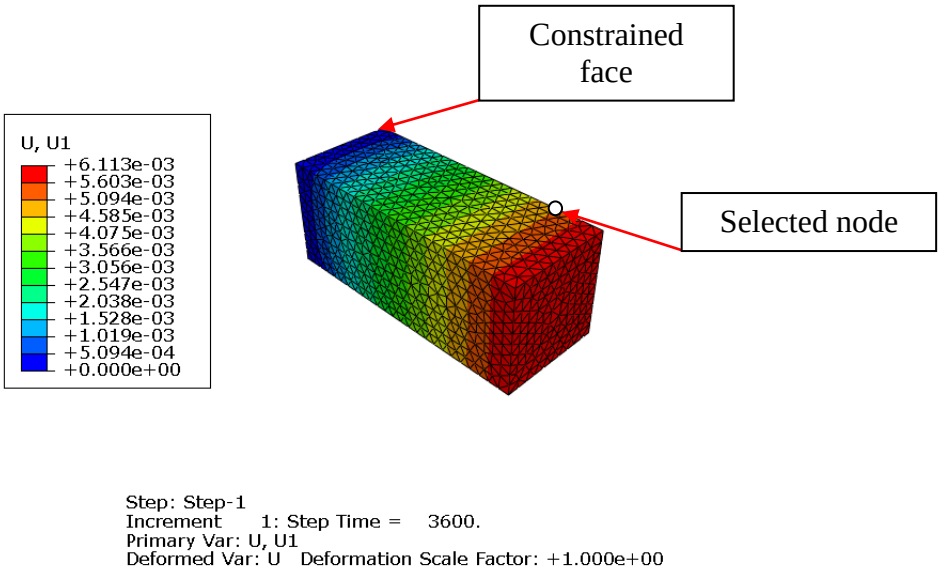

Figure 4-11: Thermal deformation of the block (Tetrahedral meshing)

The displacements shown by both hexahedron (6.073µm) and tetrahedron (6.113µm) methods were then compared with each other and found to be very close in prediction with a negligible difference of just 0.04µm which justifies the confidence to use both the default meshing techniques in Abaqus and can avoid time consuming structural simplifications to achieve hexahedron meshing.

In this section the heat transfer benchmarks confirmed the applicability and accuracy of the approach to individual models and assemblies resulting in temperatures within the accepted correlation ranges. The following sections detail the experimental testing and FEA simulations.

4.2 Machine CAD modelling

Computer resource usage, modelling time and the time required for the analyses (simulation time) were given a high priority when creating models. Complex geometry details of machine structural elements such as chamfers, fillets, bolt holes etc, which do not contribute significantly to the overall thermal behaviour were either simplified or removed where necessary. Contrary to modifying existing 3D models, in this case where 2D drawings were being interpreted to generate the 3D models, this can reduce modelling effort. These simplifications help reduce computer analysis time.

4.2.1 Symmetry

The machine structure was found to be symmetrical in the X axis direction, further inspection revealed that the internal heat sources such as bearings, motors and belt drives were also symmetrical. This allowed the creation of a halved CAD model assembly as the temperature gradients have the tendency to evenly disseminate into the structure in this direction.

The assembly of the machine is shown in Figure 4-12 and Figure 4-13. Structural parts are annotated where easily visible. Symmetry can be easily identified. The created individual CAD models are presented in Appendix B.

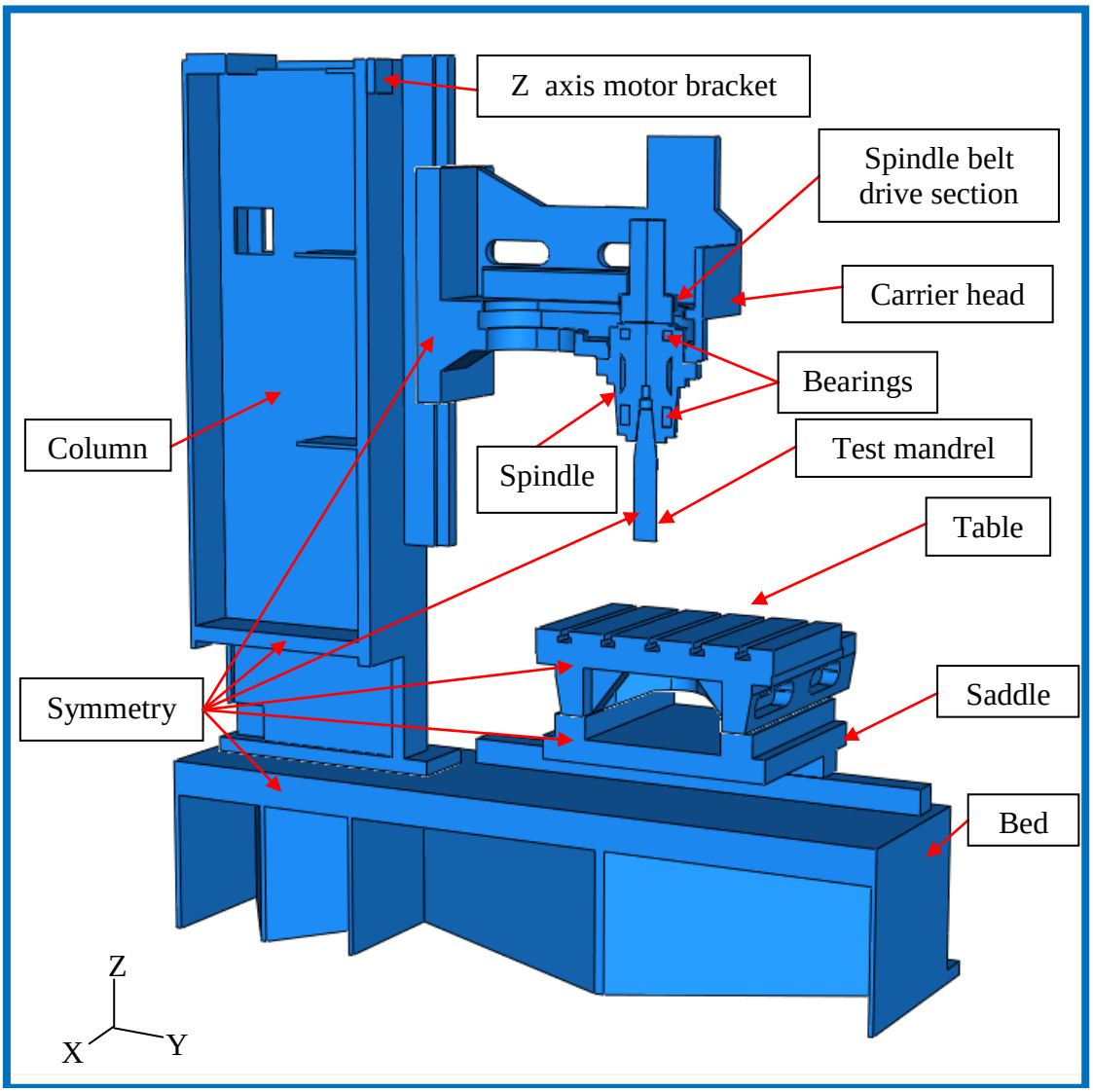

Figure 4-12: Assembly of the machine (view 1)

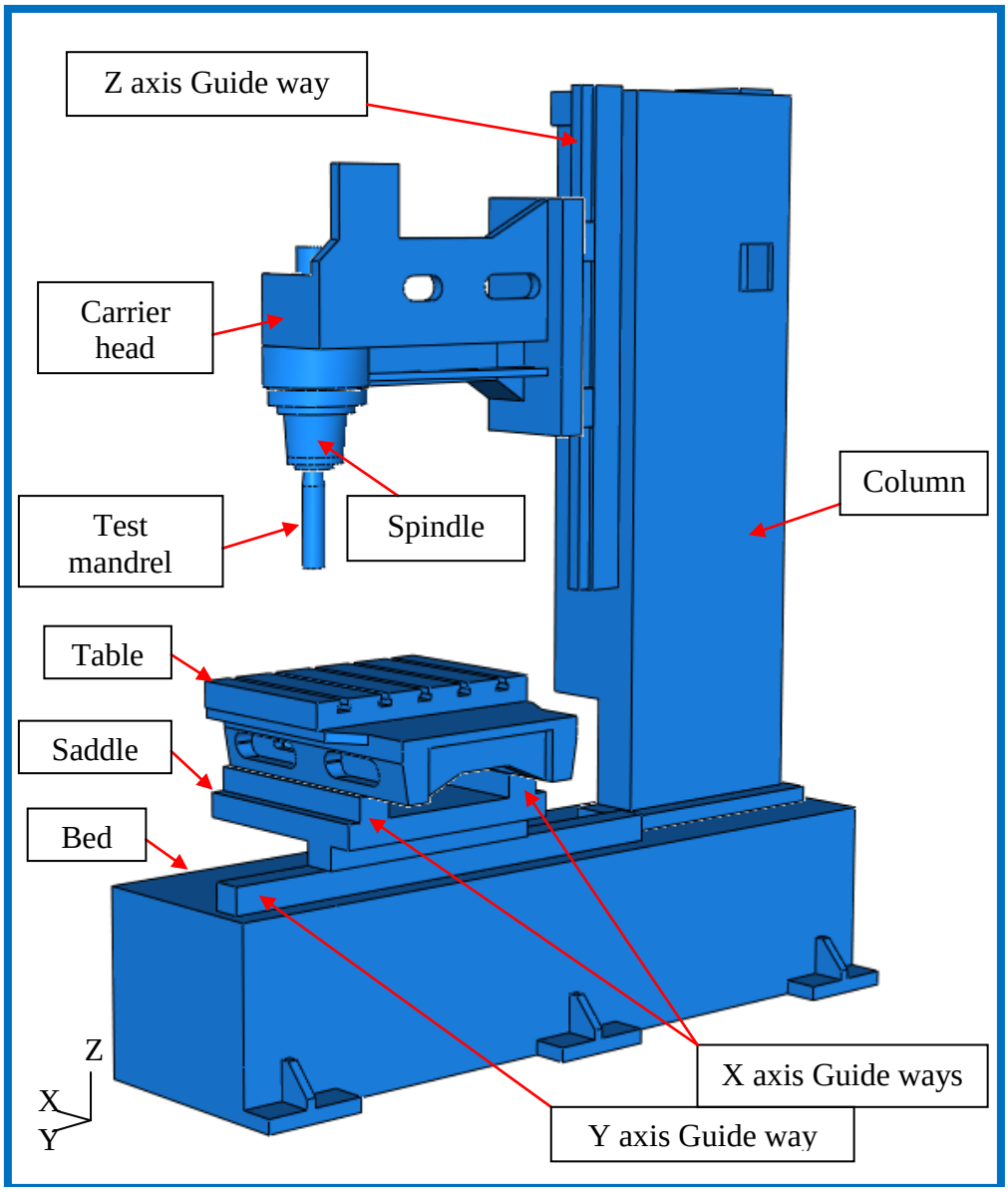

Figure 4-13: Assembly of the machine (view 2)

4.2.2 Machine FEA modelling setup

4.2.2.1 Meshing and applied constraints

The model was meshed using tetrahedral, hexahedron and hexahedron dominated (hexahedron/wedge) elements where applicable. A higher density mesh was chosen for the spindle and carrier compared to the rest of structure to ensure sufficient nodes for data extractions and comparisons which is discussed in chapter 7.

The machine model was applied with the symmetry constraint at surfaces from where the machine was halved. The base was fixed from the bottom of the supports using

displacement constraint. Boundary conditions were applied with measured initial and ambient (sink) temperatures explained in later sections. Figure 40 shows the meshed assembly of the machine. The meshing information is given in Table 4-2. Figure 4-15 and Figure 4-16 shows the information about the applied symmetry and displacement constraints position respectively.

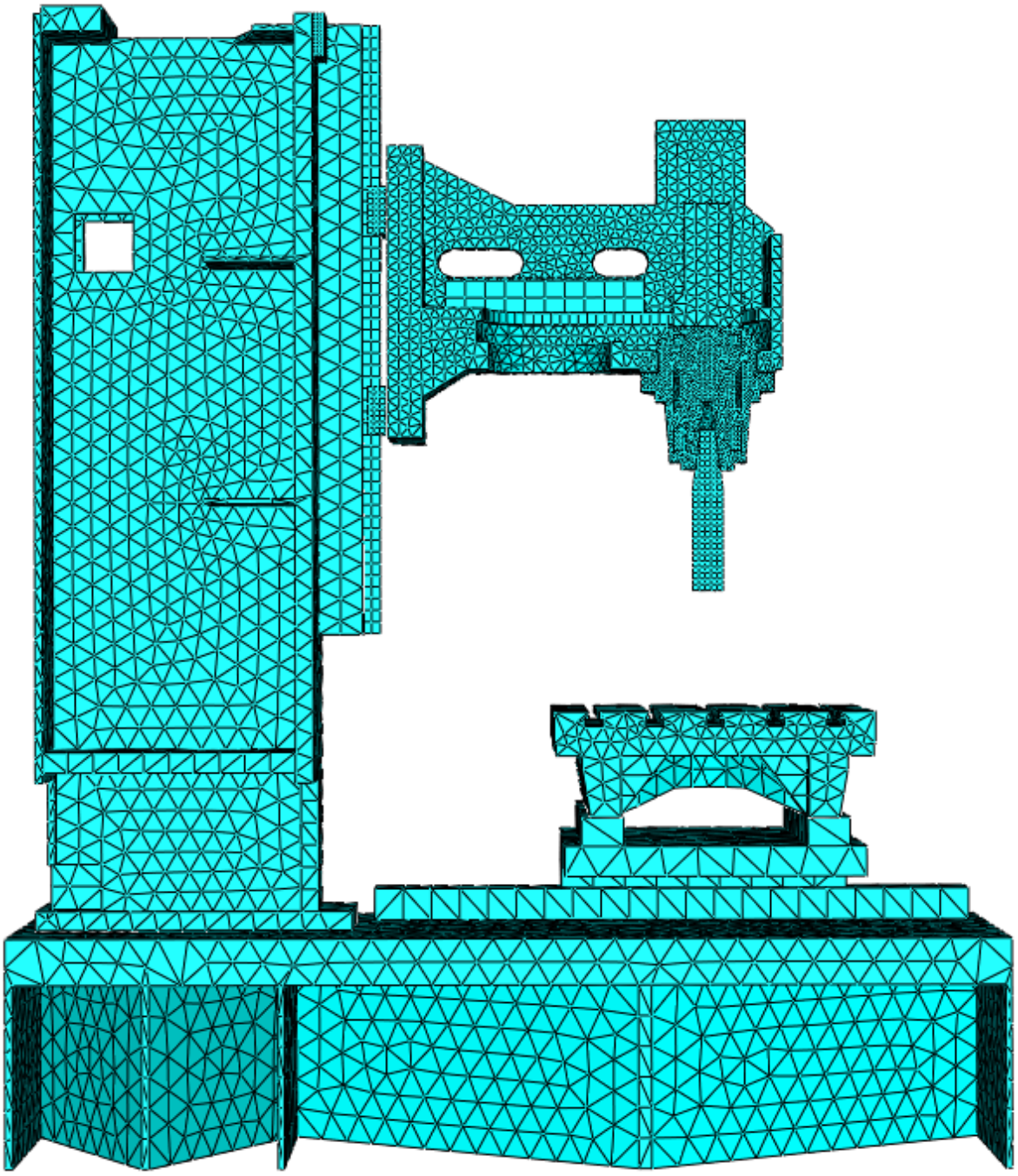

Figure 4-14: Meshed model of the machine

Structural part	Elements	Nodes	Meshing type
Column	11110	3496	Tetrahedron
Carrier	16040	4113	Tetrahedron
Spindle	16488	3772	Tetrahedron
Base	10238	3155	Tetrahedron
Bearings	432	760	Hexahedron
Table	6186	1735	Tetrahedron
Saddle	774	267	Tetrahedron
Test mandrel	351	560	Hexahedron
Belt drive section	622	195	Tetrahedron
Carrier belt drive	66	208	Hexahedron
Spindle belt drive	222	532	Hexahedron
Guideway	208	477	Hexahedron
Motor support	20	66	Hexahedron
Carriages	352	648	Hexahedron
Motor heat plate	40	126	Hexahedron
Total	**49919**	**20418**	

Table 4-2: Machine FE model meshing information

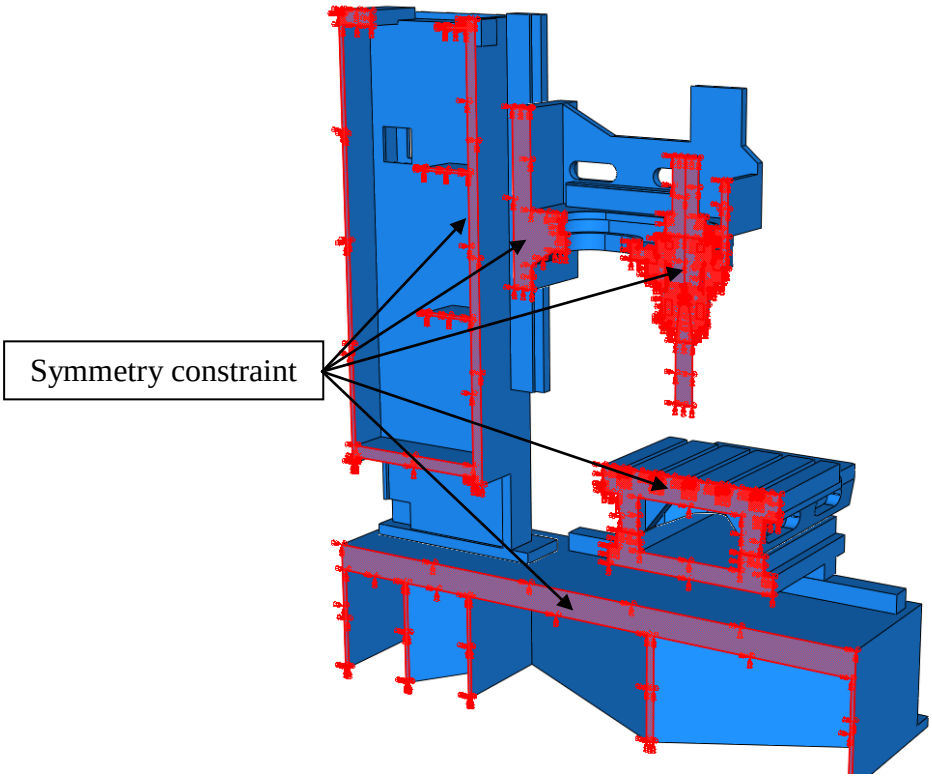

Figure 4-15: Location of the applied symmetry constraint

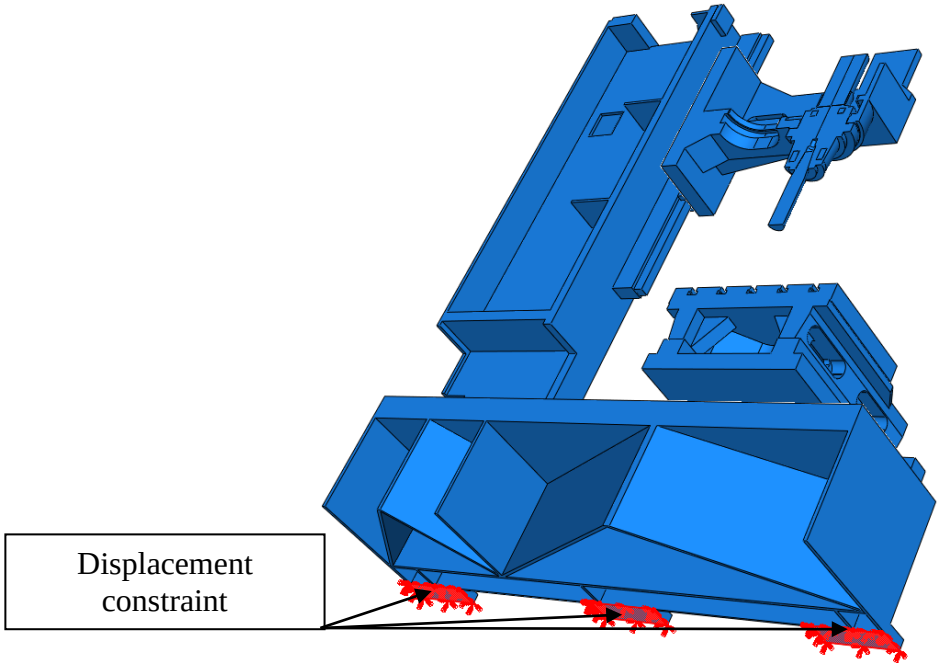

Figure 4-16: Location of the applied displacement constraint

4.2.2.2 **Location of modelled heat sources in the FE model**

Figure 4-17 shows main regions of the FE model considered as heat sources for applying body heat fluxes defined in later sections.

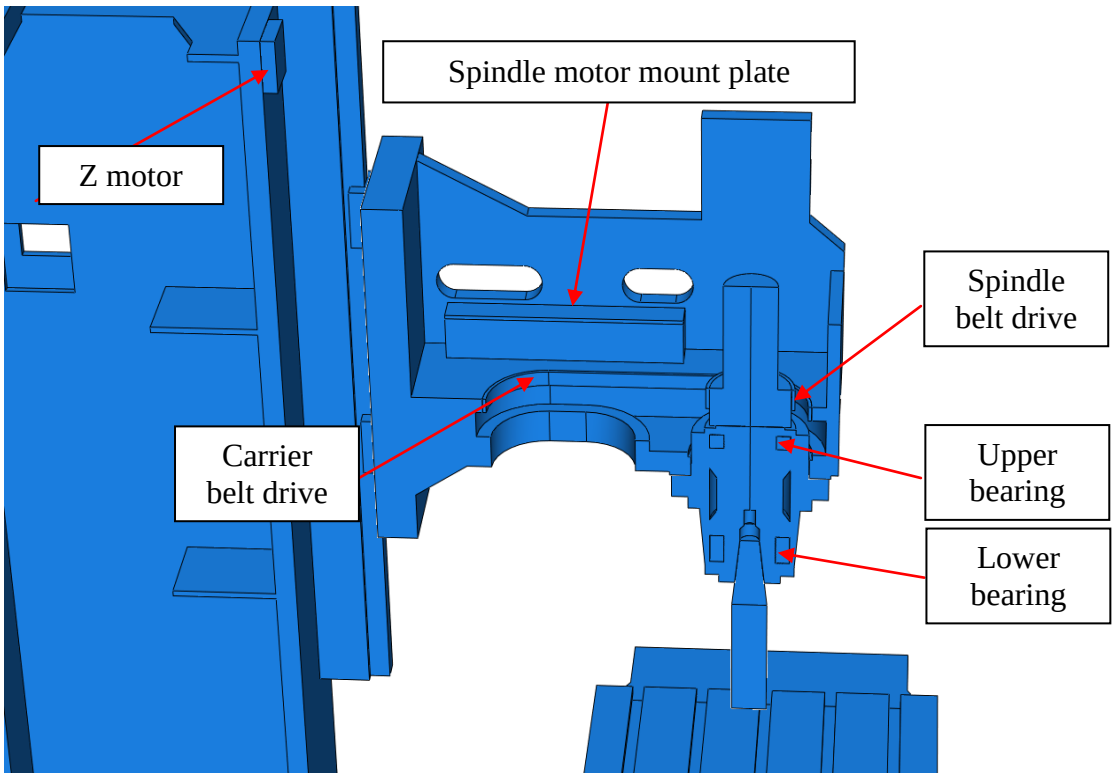

Figure 4-17: location of modelled heat sources in the FE model

4.2.2.3 **Computer specifications**

All simulations are performed as transient thermal simulations. The computer used to perform them had main specifications as follows

Processor = AMD Phenom 9950 Quadcore 2.60 GHz

RAM = 4.00GB

Graphics = NVIDIA GeForce 9400 GT

Operating system = Windows XP 32bit

4.3 Thermal study of the machine

The study commenced by monitoring thermal behaviour of the machine by rotating the spindle at its maximum speed of 8000rpm for a pre-determined time period. The maximum speed was selected to exhibit the machine's maximum thermal behaviour. The data was recorded using the metrology equipment as follows:

- Dallas DS18S20 temperature sensors

Unlike thermocouples, these temperature sensors have an advantage of communicating serially on a 1-wire bus system which significantly reduces the cabling and interface effort. These sensors can be applied individually but in this work also on a unique flexible circuit board, shown in Figure 4-18, enabling a convenient application of many sensors at a minimum spatial resolution of 15mm while handling surface irregularities with bend radii as little as 1mm. The sensors have a measuring range from -55°C to +125°C, an accuracy of ±0.5°C from -10°C to 85°C and resolution of 0.063°C. [3, 114].

Figure 4-18: Temperature sensors with flexible circuit board

- Flir ThermaCAM S65 Thermal Imaging Camera

Thermal imaging is a non-contact measuring technique effectively used for measuring temperatures of rotating parts and coverage of large surface areas as well as providing much greater detail of thermal gradients. The camera used in this research has a thermal sensitivity of 0.08°C and a quoted accuracy of ±2°C however, much higher accuracy approaching ±0.2°C can be achieved with careful set-up [114]. Figure 4-19 shows the thermal imaging camera.

Figure 4-19: ThermaCAM S65 thermal imaging camera

- Non Contact Displacement Transducers (NCDTs)

These sensors works on the eddy current principal which enables non-contact and therefore vibration and wear free measurement of rotating objects that can be either ferromagnetic or non-ferromagnetic. This sensor is ideal for harsh industrial environmental due its immunity to dirt, oil, dust, moisture, interference fields etc. The sensor has the measurement range of 0-1mm and resolution of 0.1µm.

4.3.1 Machine testing

The machine was tested for a one hour heating and one hour cooling cycle. This was chosen to allow thermal error to occur but short enough to represent an efficient test for the project. This test is referred to as Basic Machine Operation in this thesis.

4.3.2 Basic machine operation at 8000rpm

The machine was tested for three hours incorporating one hour stabilization, followed by one hour heating cycle and one hour cooling cycle. The stabilization period was performed in order to achieve stabilized initial thermal state before the actual testing to reduce thermal error uncertainties. Stabilization was achieved by de-activating the E-Stop, this causes axis motors and drives which are used to hold structural parts in position to activate, for example for the machine under research, the Z axis motor serves to hold the vertical Z axis in position causing the Z axis motor to heat up and heat to flow into the column resulting in column bending.

Thermal data was recorded using 65 temperature sensors located in strips at the surface of the carrier and spindle boss considered as thermal key points explained by White [3]. An additional surface sensor was placed attached on the upper surface of the spindle carrier adjacent to the upper spindle bearing, 7 surface sensors positioned to measure the column temperature and one surface sensor was placed inside the base to measure the base temperature shown in Figure 4-61. Discussion about the placements of ambient temperature sensors is presented in section 4.3.6

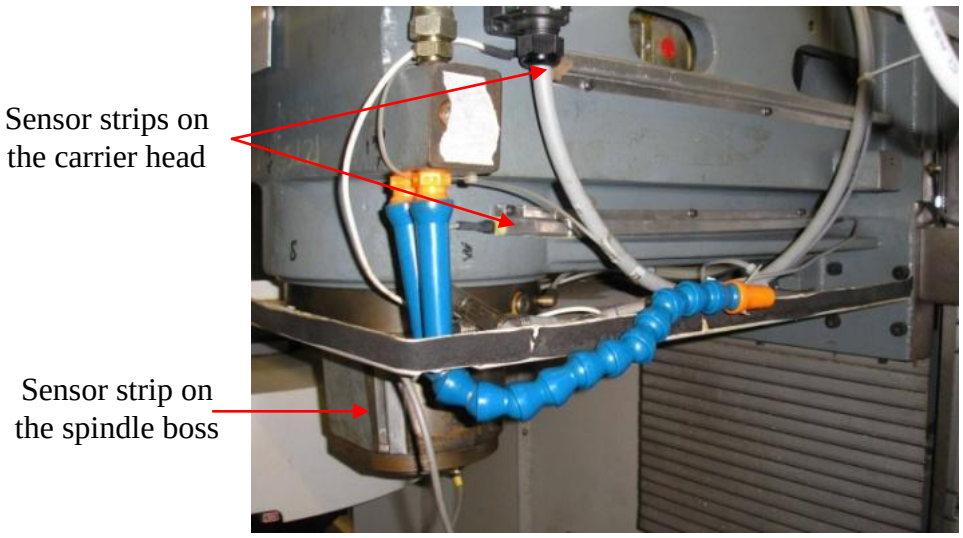

Figure 4-20: Thermal sensors location on the machine

Thermal imaging was also used to observe the spatial temperature distribution within the structure and to locate the heat sources. Figure 4-21 is a thermal image showing the thermal distribution and thermal gradients in the spindle/carrier structures. Figure 4-22 shows the top view of the carrier head where rotating heat sources are visible. The

spindle belt drive is at a higher temperature due to the heat generated by friction, the heat disseminates into the carrier as well as the spindle structure over which the belt rotates and is a significant additional heat source to the lower and upper spindle bearings.

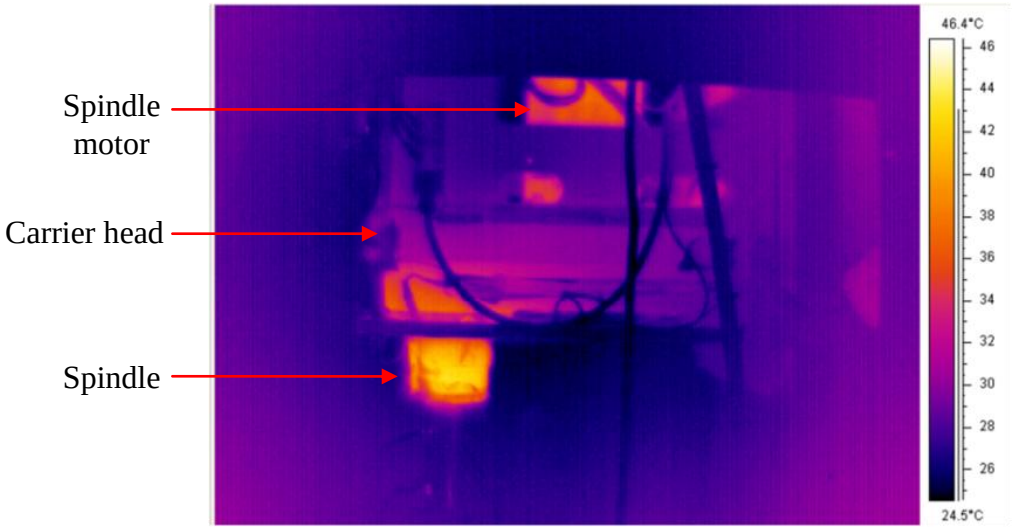

Figure 4-21: Thermal image of machine head after one hour heating (8000rpm)

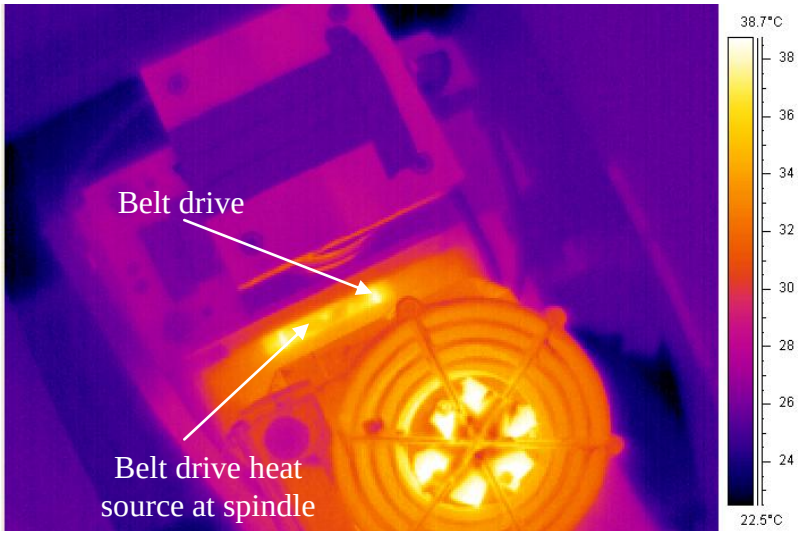

Figure 4-22: Top view thermal image of the machine (8000rpm)

4.3.2.1 **Displacement monitoring**

A nest of six NCDTs were placed around the test mandrel (Figure 4-23) to monitor the displacement of the tool in X, Y and Z and tilt about X and Y due to the thermal effects produced during the one hour spindle heating and cooling test. Figure 4-24 shows the placement and arrangement of NCDTs nest on the machine table. The lower spindle bearings are fixed axially as well as radially so the thermal datum is near to the cutting tool. The movement of the tool should in theory be synchronised with the movement of

the structure, however the complexities associated with the spindle mechanism, such as bearing preloads, tool taper movement and tension of the belt driving the spindle, often result in spindle movement unsynchronised with the tool movement. To check this the Z axis was measured at the test mandrel as well as at the spindle boss (lower spindle bearing housing). When correlating measured and simulated results, the displacements obtained from the bottom NCDTs are used. The NCDTs placed at the top are for monitoring the tilt of the test mandrel which is further discussed in chapter 8.

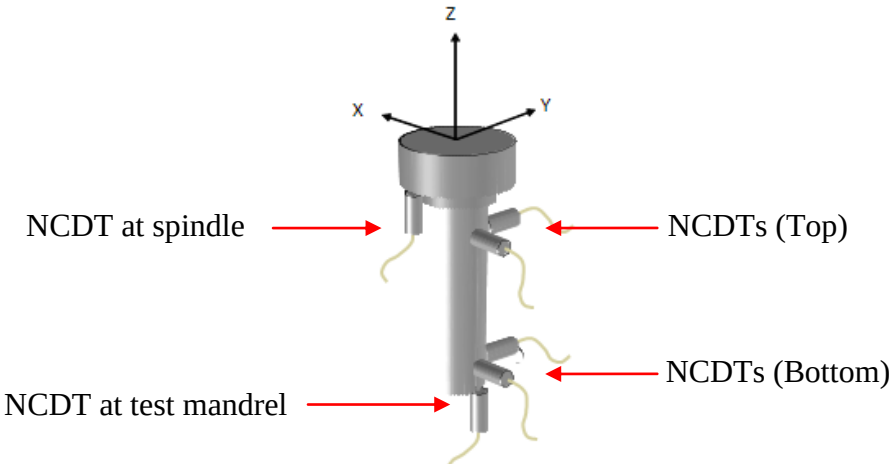

Figure 4-23: NCDTs located around the test mandrel

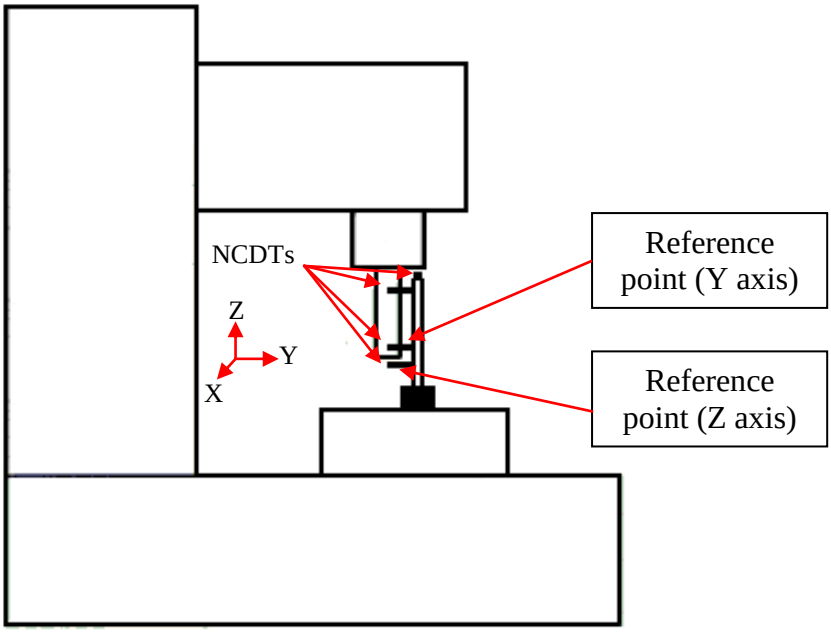

Figure 4-24: Position of the NCDT nest located on the table

During the initial stabilization period an error range of approximately 1.3 µm in Y and 3 µm in Z were measured and suspected to be caused by column bending. Figure 4-25

and Figure 4-26 shows the displacement profiles in Y and Z axes respectively, and Figure 4-27 shows the pictorial representation of the machine behaviour.

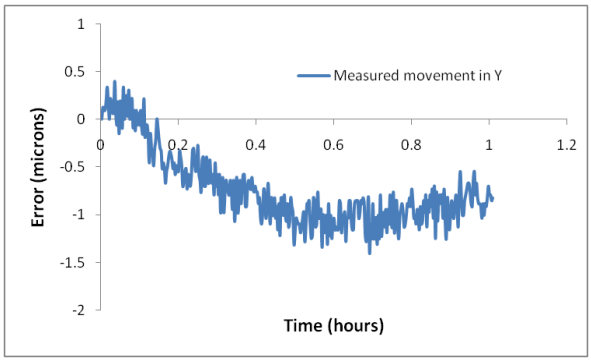

Figure 4-25: Movement of the machine in Y direction during one hour stabilisation period

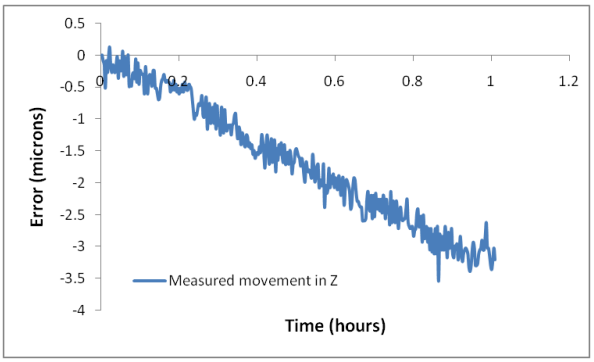

Figure 4-26: Movement of the machine in Z direction during one hour stabilisation period

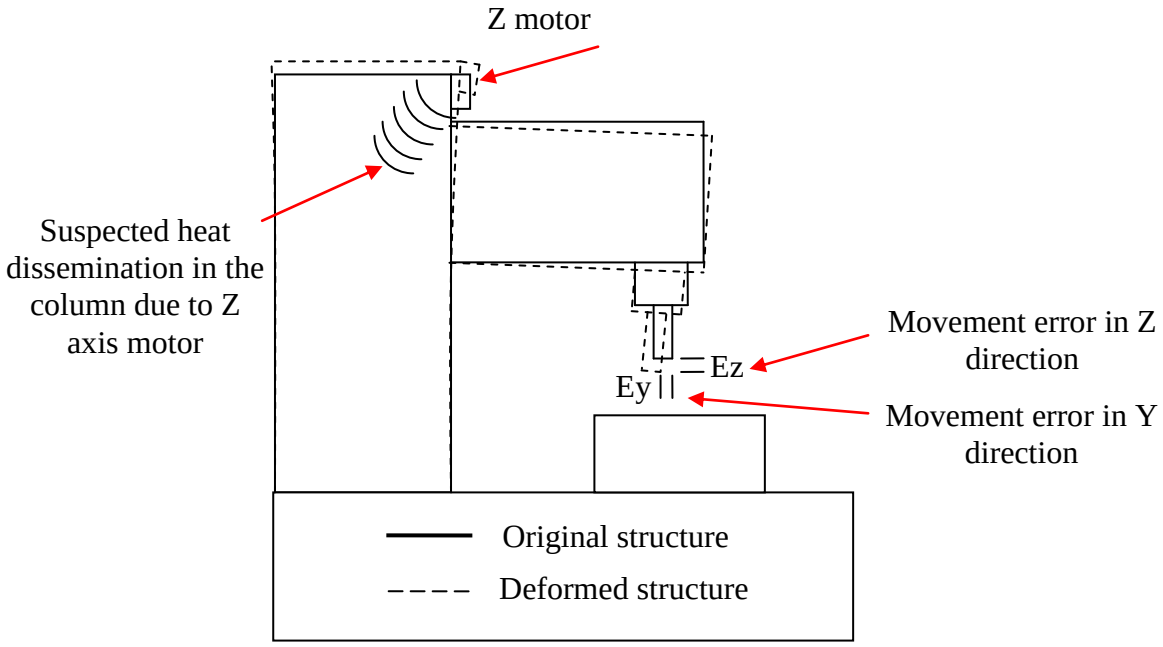

Figure 4-27: Machine behaviour during one hour stabilisation test

During the one hour heating and cooling test, the machine was observed to exhibit a displacement error of 70µm in Y, 23µm in Z (test mandrel) and negligible error of 2µm in X. The graph in Figure 4-28 shows the measured temperature near the lower spindle bearings and Figure 4-29 and Figure 4-30 shows the level of displacement error. The stabilization period was omitted however its effect i.e. the error was not subtracted. Higher errors in Y and Z axes caused them to be given high priority to correlate with

offline simulations whereas X axis was considered negligible due to the small error magnitude.

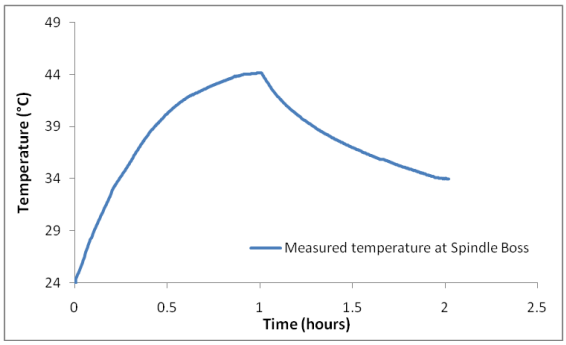

Figure 4-28: Measured temperature at Spindle Boss (Basic machine operation)

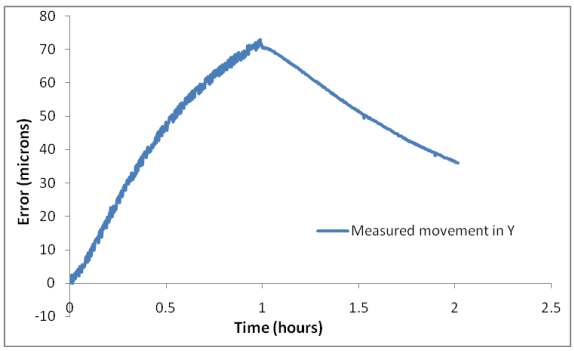

Figure 4-29: Y axis error (approx. 70µm)

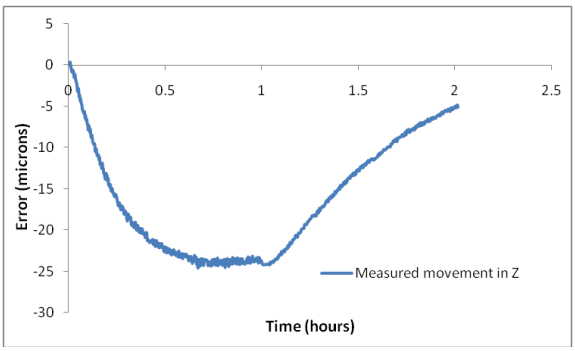

Figure 4-30: Z axis error (approx. 23µm)

The displacement monitored at the spindle boss and the test mandrel is plotted in Figure 4-31. The profiles confirm unsynchronized movement with an error difference of approximately 6µm. As explained earlier, the error difference may be due to the complexities involved with spindle pre-load which are not modelled in this research. However, the difference is not a significant parameter for this machine compared to the main structural errors. The priority was given to the Z axis movements obtained from the test mandrel to compare the simulated results for all testing regimes because the test mandrel (tool) is a critical component for machining operations and fits with the ISO standard test.

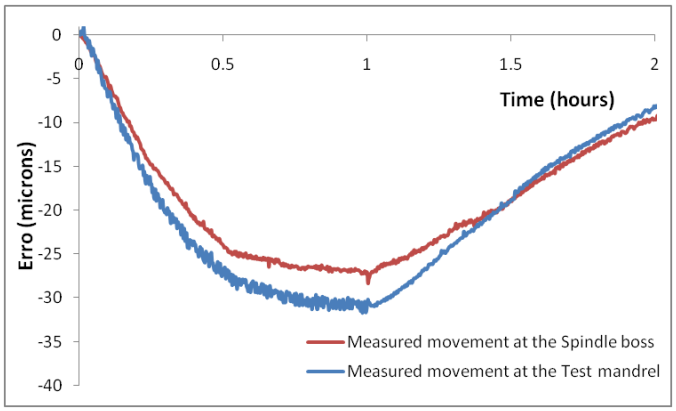

Figure 4-31: Measured Z displacements at the Spindle boss and the test mandrel

4.3.3 FEA modelling and transient simulations

A method was needed to reduce the uncertainties associated with simulating heat sources. Using the spatially detailed temperature information in thermal imaging small structures around the heat sources can be selected and considered separately and by using equation (3.6 - chapter 3) the energy output or BHF can be estimated by balancing the energy loss. These uncertainties are generally smaller because of the mechanical information known and the other parameters such as convection and thermal contact conductance obtained experimentally.

Thermal data obtained from the basic operation test was analyzed and applied to the FEA simulation model for offline transient thermal behaviour assessment. The temperature data obtained from the machine surface sensors were converted into thermal loads i.e. body heat flux values for the heat sources. An average of the spindle boss sensors was used to calculate the BHF for the lower bearing. The two carrier head strips have 62 temperature sensors. The sensors closest to the relevant heat source were selected for calculating the BHF. Selection of structural volumes to obtain body heat fluxes are discussed in the following section.

4.3.3.1 Volume selections to obtain BHF values

The thermal image data revealed the interaction of the heat sources within the carrier head assembly (Figure 4-20, Figure 4-21 and Figure 4-22). Based on the methodology stated previously, the BHFs were calculated by discretizing the machine structure into specific volumes representative of temperature rise by the induced heat from sources housed inside or near to them. Only heating cycle data was considered for calculating

BHF values. Figure 4-32 and Figure 4-33 shows the positions of the surface sensors and heat sources on the carrier head and spindle assembly respectively. Their positions are utilised to select the structure volumes as shown in Figure 4-34 for calculating BHFs generated from the heat sources.

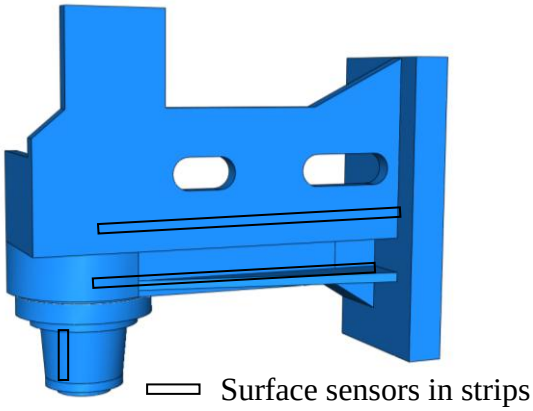

Figure 4-32: Carrier head model surface sensor strips

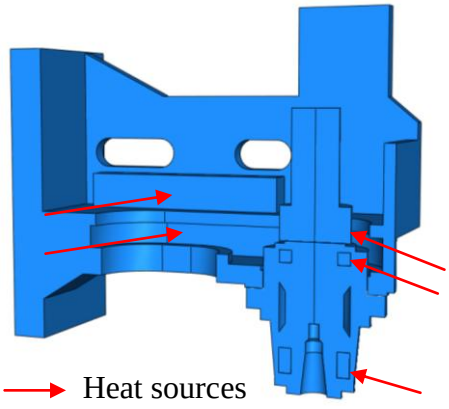

Figure 4-33: Carrier head model showing location of possible heat sources

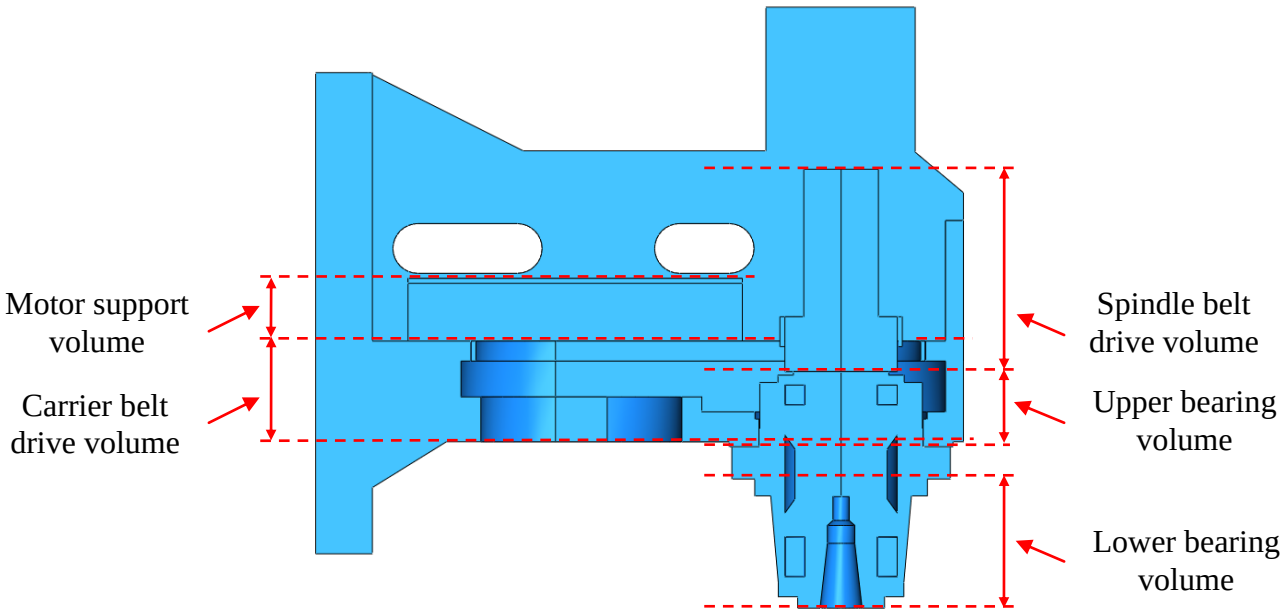

Figure 4-34: Overview of structure volume selection procedure for calculating BHFs

The machine under research has three major materials i.e. steel, cast iron and an invar test mandrel therefore the selected volumes for BHF calculations used their respective material properties. The material properties of cast iron and invar are presented in Appendix A. These material properties were also used in the FEA simulations to represent the structural models i.e. cast iron was applied to the Carrier head; steel was

applied to the Spindle, bearings, column, guide ways, carriages, base, saddle and table and invar applied to the test mandrel.

4.3.3.1.1 Spindle (bearings and spindle belt drive heat sources)

The spindle structure was divided into three sections, the top section is the volume representing the structure affected by the heat generated by the belt drive, the middle section is the volume affected by the heat generated by the upper bearing and the lower section is the volume affected by the heat generated by the lower bearings set as shown in Figure 4-35, Figure 4-36, Figure 4-37 and Figure 4-38. The remaining volume was excluded as being a central part of spindle where heat flow vectors are expected to be in a state of equilibrium. This approach may be of critical importance in spindles where heat flow is not stable. (Further discussion is in chapter 8). Separate BHF calculations were performed for each selected volume of the spindle. Heat sources were treated as integral parts to the structure therefore BHF values also included heat source volumes. BHF calculations for the lower bearing is shown in section 4.3.3.2.1 where as BHF calculations for other heat sources are presented in Appendix C.

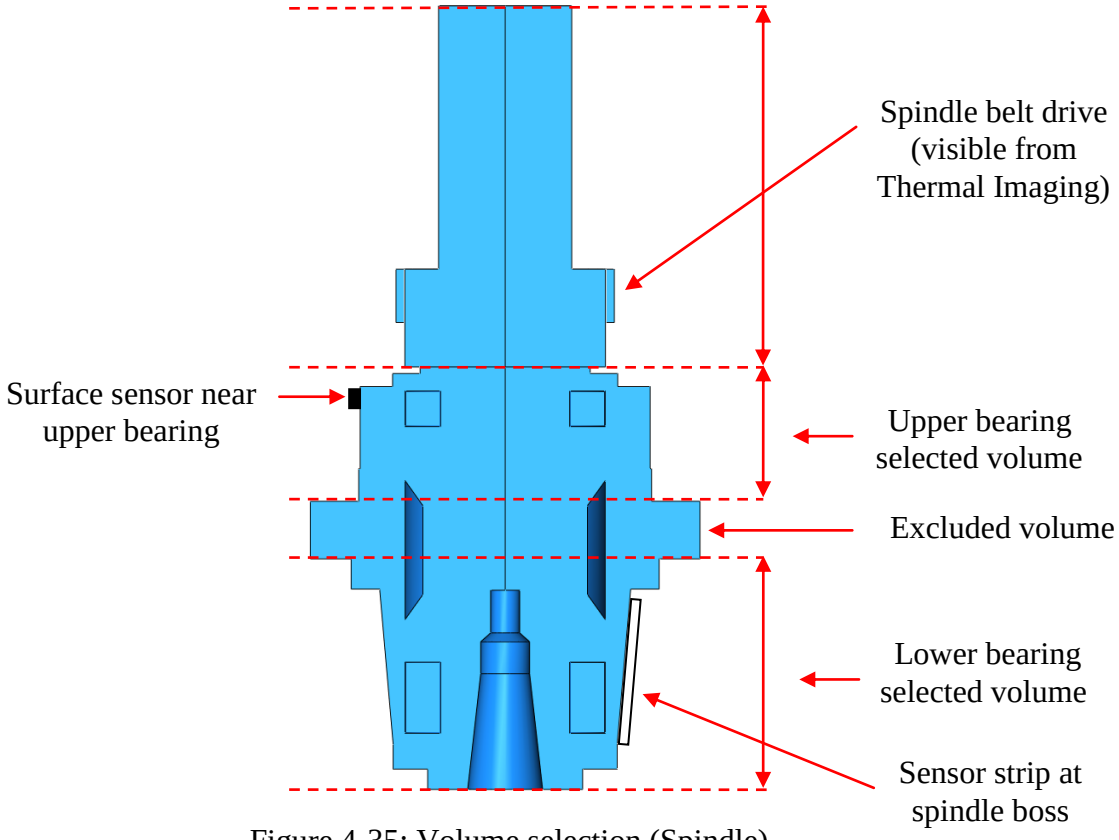

Figure 4-35: Volume selection (Spindle)

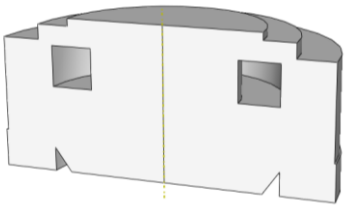

Figure 4-36: Selected volume for the upper bearing

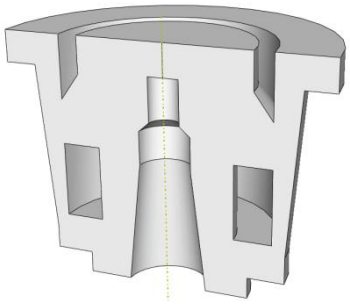

Figure 4-37: Selected volume for lower bearings set

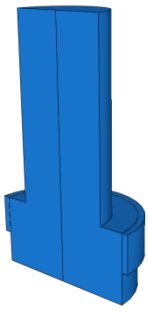

Figure 4-38: Selected volume for the spindle belt drive heat source

4.3.3.1.2 Carrier head (belt drive and spindle motor mount plate heat sources)

The extracted temperature data and careful observations of thermal images revealed possible heat sources in the carrier head. The belt drive is another significant heat source which resides inside the carrier head structure (see Figure 4-22). The final main heat source is the main spindle motor which is clamped on a steel plate through which heat disseminates into the carrier head structure. Calculations are shown in Appendix C. Figure 4-43 shows the obtained temperature data from the carrier head sensors.

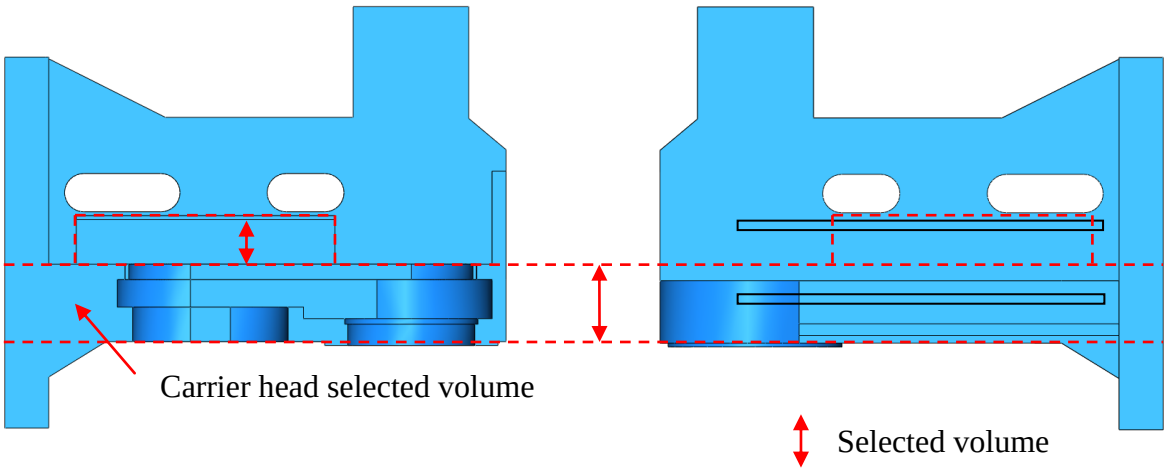

Figure 4-39: Volume selection (Carrier)

Figure 4-40: Temperature sensor strip location

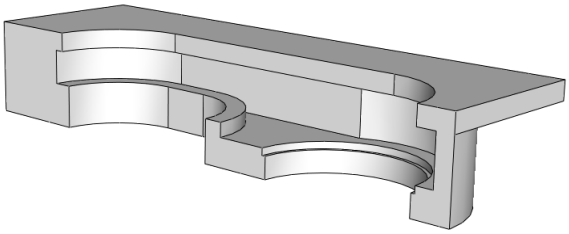

Figure 4-41: Selected volume for the belt drive heat source

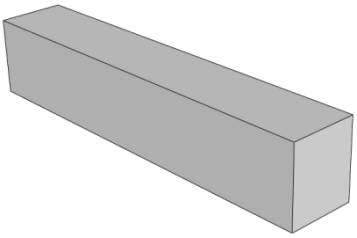

Figure 4-42: Selected volume for the spindle motor mount plate heat source

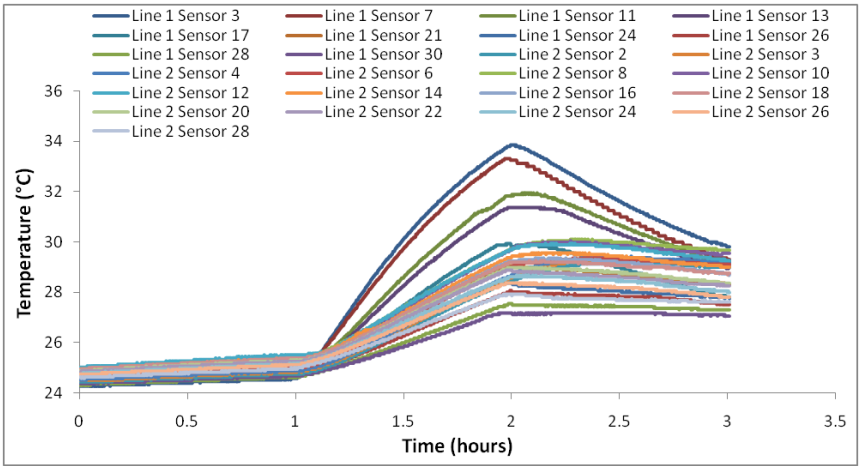

Figure 4-43: The temperature data was selected from this set for BHF calculations

4.3.3.1.3 Z axis motor bracket

As discussed earlier in section 4.3.2, the Z axis motor heats up after de-activating the E-Stop, this heat flows into the column which results in producing temperature gradients. Thermal imaging was used to monitor the temperature from the Z axis motor. Temperatures were obtained from two points on the thermal image shown in Figure 4-45. In Figure 4-46 a temperature rise of approximately 1.7°C was observed in both profiles within 25 minutes which followed a stabilized trend in the end. Therefore both temperature change magnitudes were taken from that period of 25 minutes and averaged to 1.6°C for BHF calculations. The area up to the two points was used to calculate the BHF value from the Z motor bracket over a 1500 seconds (25 minutes) period. Calculations are shown in Appendix C.

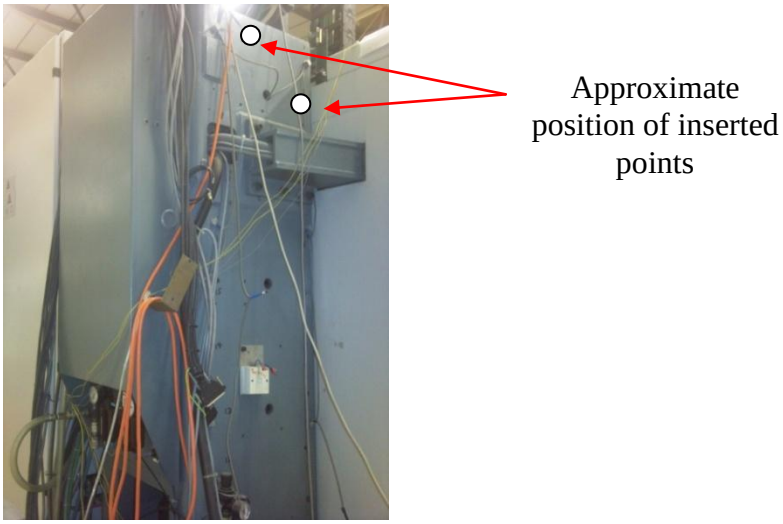

Figure 4-44: Machine column (back side)

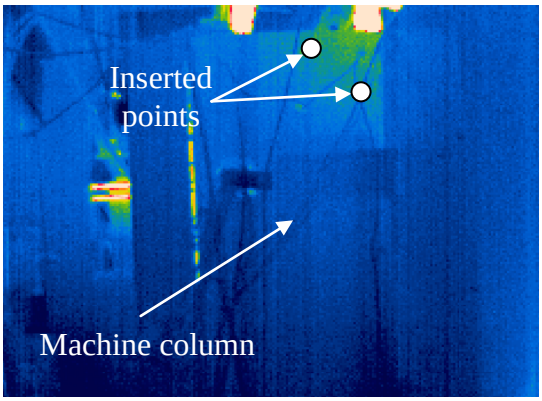

Figure 4-45: Thermal image of machine column (back side)

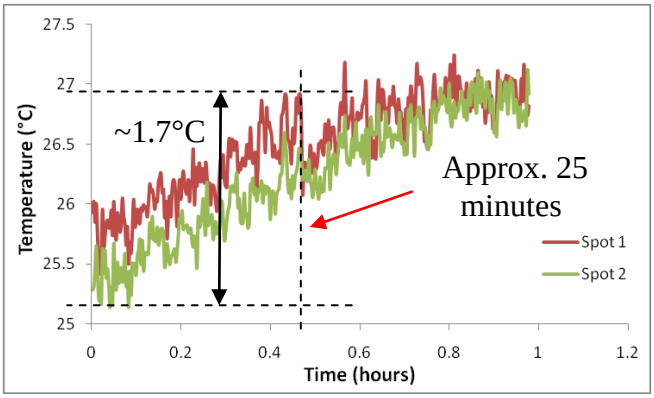

Figure 4-46: Temperature data obtained from inserted points

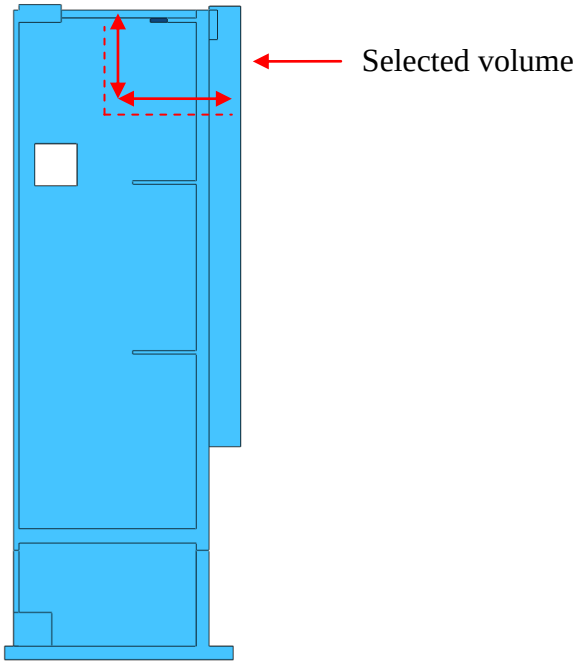

Figure 4-47: Volume selection (Column)

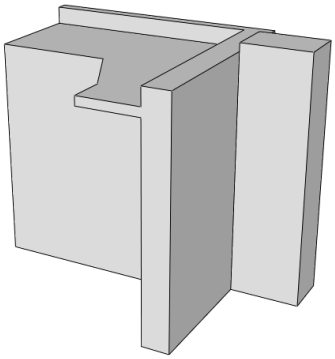

Figure 4-48: Selected volume for the Z axis motor heat source

4.3.3.1.3.1 Conduction across guideways

The heat flows across guideways through carriages. On this machine rolling element guideways are used which has relatively small contacting areas; it was assumed that the conduction will occur at a lower rate. It was not within the scope of this research to model the thermal behaviour across guideways in detail therefore an averaged value of the thermal conductance of approximately 2000 $W/m^2/°C$ (Chapter 3 - Table 3-3) was applied to the interfacing surfaces of guideways for FEA. Further detail can be found in chapter 8.

4.3.3.2 **BHF results**

The following shows a brief overview of the procedure used to calculate BHF values. The calculations involved obtaining the energy required for a temperature change using the specific heat capacity of the associated material in each volume.

4.3.3.2.1 BHF calculations for the lower bearing

For the lower bearing BHF, the lower selected volume (Figure 4-32) of the spindle was taken. Using the similar approach for the assembly benchmark, the volume of the heat source which in this case is the lower bearing, was used to divide the total energy *Q'* obtained to obtain the BHF value for the lower bearing.

The heating data from the spindle boss sensor was used. Figure 4-49 is a trend line that was plotted to refine the sensor data. Table 4-3 shows the data of the lower bearing used to calculate the BHF value.

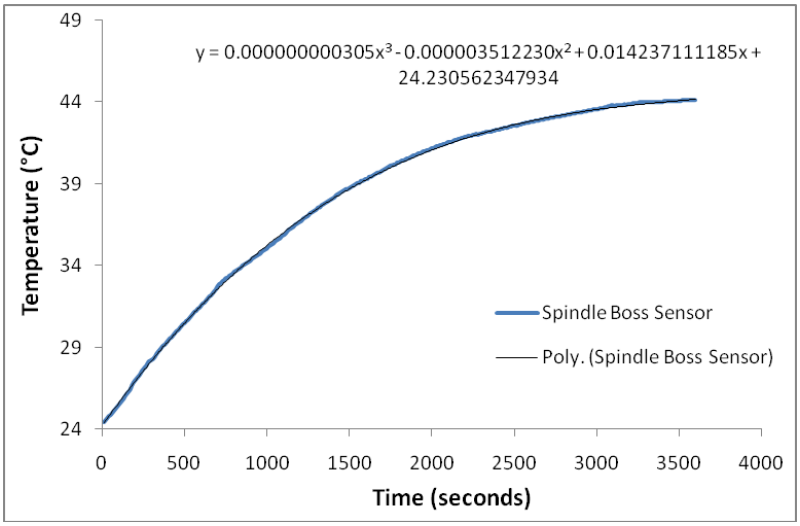

Figure 4-49: Trend line plotted on the spindle boss sensor data

Lower bearing	Value	Units
Volume of the lower spindle housing	7.35E+05	mm^3
Volume of the lower bearing	116490	mm^3
Total volume	8.51E+05	mm^3
Area of the lower spindle bearing	3.69E+04	mm^2
Total mass	6.65E-03	tonnes
Density of Steel	7.81E-09	$tonne/mm^3$
Cp of Steel	4.73E+08	mJ/tonnes/°C

Time	10	s
h	0.006	mW/mm^2/°C
Initial ambient temperature	24.438	°C

Table 4-3: Lower bearing data used for BHF calculations

Calculations for the energy *(Q')* were performed transiently. The main iteration that obtained the BHF for the lower bearing is presented.

Total volume = 8.51E+05 mm^3

Total mass = 6.65E-03 tonnes

Temperature difference (ΔT) = 0.12°C (first 10 seconds – see page 111 for explanation)

Total time = 3600s (10s is used for calculations)

Convection coefficient (h) = 0.006 mW/mm^2/°C

Exposed area = 3.69E+04 mm^2 (see Figure 4-50)

Ambient temperature change = Varied from 24.438°C to 25.563°C during the heating cycle – Used transiently during calculations

By applying these values in equation 3.6, the value for the *Q'* is

Q' = 37320.06 mW

The value of *Q'* is required to be divided by the volume of the heat source which in this case is the volume of the lower bearing.

q' = 44438.3 mW / 116490 mm^3 which gives the BHF value as

q' = 0.38 mW/mm^3

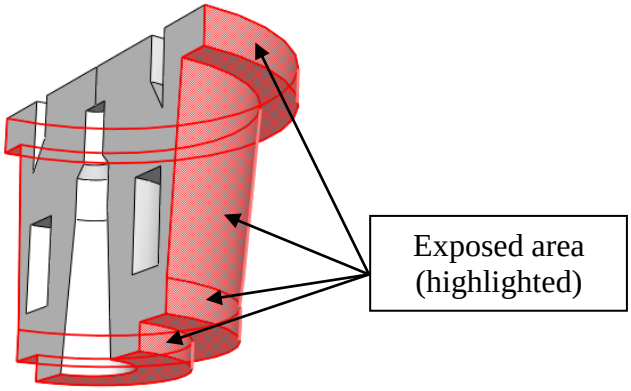

Figure 4-50: Exposed area of the lower spindle housing

To calculate the total BHF value generated by the lower bearing, the thermal image (Figure 3-19) and the plot in Figure 3-20 were carefully observed which shows the temperature rise at the upper area of the test mandrel. This temperature rise is due to the heat flow into the test mandrel during the heating cycle from the spindle and is considered in the energy loss from the spindle for calculating BHF value and added to the calculated lower bearing BHF.

This BHF for the test mandrel was obtained by extracting temperature data from the thermal imaging (Figure 3.18- Chapter 3) and applying to the upper and lower halves of the test mandrel (Figure 4-51). Each half was treated as a separate heat source that can increase its own volume temperature (though the heat was coming from the spindle) i.e. similar to the single block benchmark where the full volume was considered as the heat source itself. The test mandrel data is given in Table 4-4.

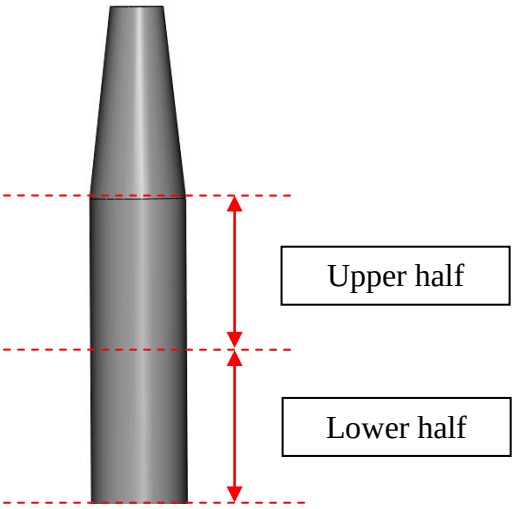

Figure 4-51: Test mandrel selected areas

Test mandrel (Upper and lower half)	Value	Units
Volume of the test mandrel (upper half)	81284	mm^3
Total volume	81284	mm^3
Area of the test mandrel (upper half)	6502	mm^2
Total mass	6.67E-04	tonnes
Density of Invar	8.20E-09	$tonne/mm^3$
Cp of Invar	525000000	mJ/tonnes/°C
Time	3600	s
H	0.092	$mW/mm^2/°C$
Ambient temperature	24.438	°C

Table 4-4: Test mandrel data used for BHF calculations

The test mandrel is considered as a neighbouring heat source that contributes a relatively small amount towards the total thermal deformation of the machine compared to the main heat sources. Therefore for simplification, a non-transient calculation was performed using the full analysis time.

Total volume = 81284 mm^3

Total mass = 6.67E-04 tonnes

Temperature difference (T_2-T_1) = 3.7 °C

Total time = 3600s

Convection coefficient (h) = 0.092 $mW/mm^2/°C$ (during rotation)

Ambient temperature change = 1.125°C (during the heating cycle)

Exposed area = 6502 mm^2

By applying these values in equation 3.6, the value for the *Q'* is

Q' = 2.57E+03 mW

The value of *Q'* is divided by the volume of the heat source which in this case is the test mandrel upper half itself.

$\dot{q}$ = 1.03E+03 mW / 81284 mm^3 which gives the BHF value as

$$\dot{q} = 0.013 \text{ mW/mm}^3$$

In the case of test mandrel lower half, the temperature difference was 1°C which revealed the BHF values as

$$q' = 0.009 \text{ mW/mm}^3$$

After adding all obtained BHF values, the total BHF value for the lower bearing was obtained as

$$\mathbf{q' = 0.40 \text{ mW/mm}^3}$$

Unlike the benchmarks where an averaged BHF value was applied to generate the required temperature increase, the BHF obtained from the initial data of the heating cycle (first 10s data) was considered for the simulations. This initial period the temperature difference, and therefore heat transfer, is at its greatest and gives a good BHF value. This was done to account for the complexities in machine tools bearings such as variation in pre-load, viscosity of lubrication etc which varies the BHF over time. Figure 4-52 confirms graphically that the temperature difference at very initial stage of 0 to 10s is higher than the temperature difference between 2000s and 2010s

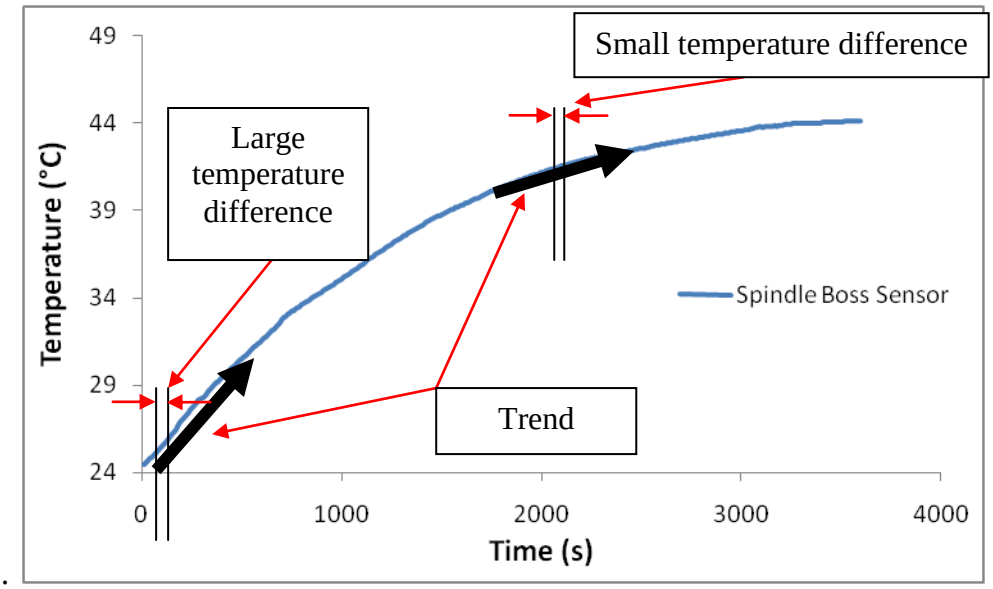

Figure 4-52: Measured spindle boss temperature at 8000rpm

Similar approach is used for the other heat sources using the measured temperature data and selected volumes. Calculations for the other heat sources are shown in Appendix C. The calculated BHF values for 8000 rpm spindle speed are shown in Table 4-5.

	Body heat flux (mW/mm^3)
Lower bearings	0.40
Upper bearing	0.49
Carrier belt drive	1
Spindle belt	0.56
Z axis motor bracket	0.23
Spindle motor mount plate	0.14

Table 4-5: Calculated body heat flux values at 8000rpm spindle speed

It should be noted that the use of a single BHF value for heat sources was desirable for long term simulations where the actual temperature data will not be readily available to predefine BHF values for generating required temperature profiles. Single BHF values for each heat source based on a short term test should ideally be able to predict temperatures for long term real world testing regimes.

To validate the use of single BHF value, a separate test was conducted where the machine spindle was operated at 4000rpm for one hour. Using the similar approach explained above, the BHF value for the lower bearing was calculated as $0.06mW/mm^3$. Figure 4-53 shows the comparison between the measured and simulated profiles where both profiles matched to reveal 83% correlation and validates the use of a single BHF value.

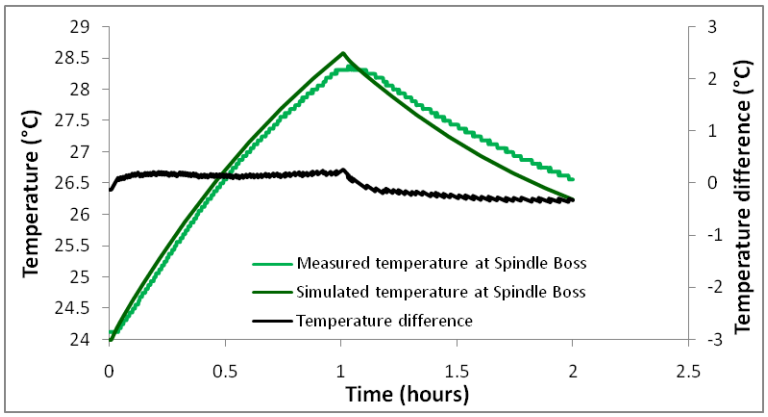

Figure 4-53: Initial test at 4000rpm to validate the use of a single BHF value

As a secondary validation was completed using the single BHF value obtained for 8000rpm to simulate and compare the machine behaviour. Figure 4-54 shows the correlation plot of simulated and measured temperature at the spindle boss which revealed a shorter exponential time constant in the experimental data.

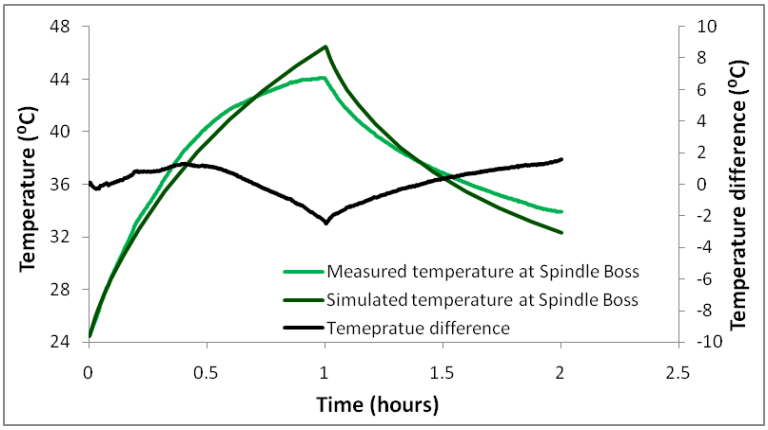

Figure 4-54: Initial stage temperature profiles correlation (8000rpm)

It has been discussed earlier that the spindle bearings are suspected to exhibit a complex thermal behaviour. This may be the cause of one or the combination of several factors such as the change of bearing preload over time and the behaviour of the friction in the bearings due to lubrication viscosity change. The BHF plot (Figure 4-55) showed variation with an exponential relationship with time which is evidence that the heat generated in the bearing is not constant.

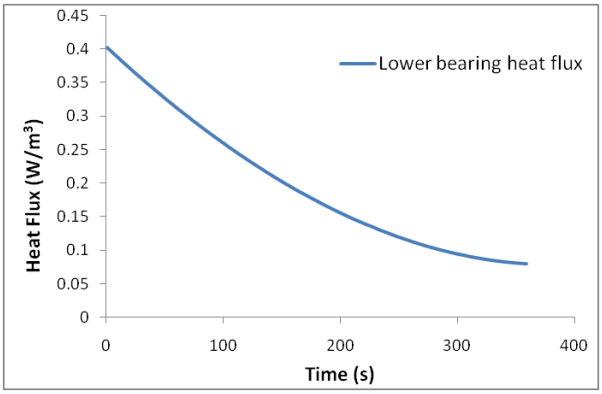

Figure 4-55: Heat flux obtained for the lower bearing at 8000rpm

Since the complexities of the individual components such as rolling element bearings or the spindle behaviour are not modelled in this research, and that it was intended to use single BHF values for simulations, a method had to be found to effectively change the heat flux in the model as an alternate, for which, temperature based specific heat capacity

(Cp) values (Figure 4-56) were obtained and applying them to the bearings to simulate the physical effects occurring in the real spindle. A method was then investigated in the Abaqus simulation software to generate exponential temperature behaviour in the spindle bearings.

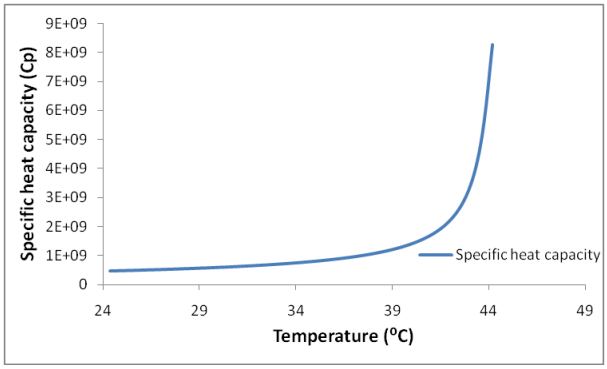

Figure 4-56: Cp based on the temperatures at 8000rpm

Abaqus provides the feature for manual programming. This was considered as a simple method to modify the specific heat capacity (Cp) of the spindle bearing. A high value of Cp relates to an increased temperature input for a degree change. Using this approach, Cp values were calculated iteratively as function of temperature from the spindle temperature data. A dummy material named 'Artificial' was created where the calculated Cp values were defined. New Cp values were applied to the bearings and programmed to be active only during the heating cycle to achieve the exponential heat input. The calculations and Cp values are shown in Appendix C.

4.3.3.2.2 Abaqus Keywords Editor programming

This Abaqus Keyword Editor programming aims to use new Cp values during the heating cycle to achieve a shorter exponential time constant for the simulated spindle boss temperature. Once this is done, the standard Cp property is called during the cooling cycle using the Editor.

The procedure is shown in Appendix C. Two separate bearing sets were created in Abaqus, the first bearing set was created with new Cp values defined in the Field '1' and the second bearing set was created with the Cp value defined in the Field '2'. Using the Abaqus Keywords Editor 'SetSteel 1.0' (bearing set with the Field '1' Cp values) is called using the 'Predefined Fields' for using it during the heating cycle simulation.

The model was simulated again with the newly defined 'Artificial' material. The correlation results are shown in Figure 4-57, it can be observed that the simulated temperature profile shows an exponential form with improved correlation (**81%)** with the measured temperature. The temperature difference of 2°C was considered low and progressive in nature. The approach of using Cps was then followed during all simulations conducted at 4000rpm and 8000rpm.

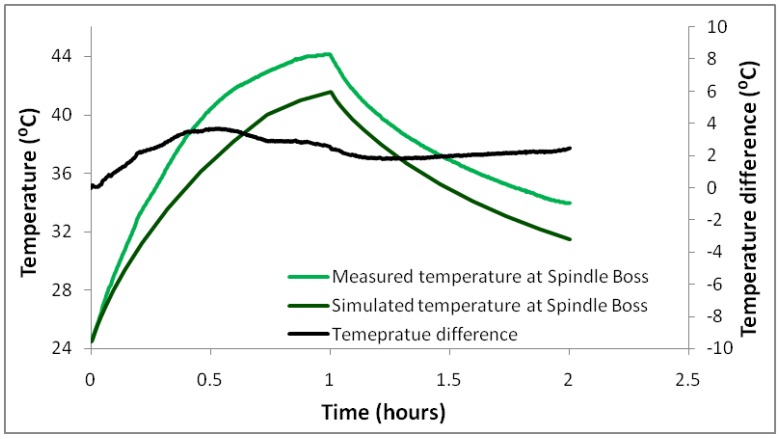

Figure 4-57: Correlations for temperature profiles (8000rpm/programmed)

4.3.3.3 **Application of TCC values to the structural joints**

The previously obtained thermal contact conductance values (chapter 3) were applied at the model joint surfaces. The applied torque values to the fastening bolts were identified from OEM engineering drawings. In case of a torque value not in range, the thermal contact conductance value was extrapolated, for example, from machine manufacturer data the spindle is clamped to the carrier using 6 bolts tightened to 70Nm in dry conditions. Contact conductance value of 2520 $W/m^2/°C$ was extrapolated using exponential curve fitting technique and used at the carrier/spindle interface.

4.3.3.4 **Application of ambient temperatures to the FEA model**

Figure 4-58, Figure 4-59 and Figure 4-60 show highlighted structures where convection and sink temperatures are applied. The test mandrel (Figure 4-61) was kept separate for applying convection due to variable convection coefficient, however the sink temperature obtained from the inside air sensor was applied.

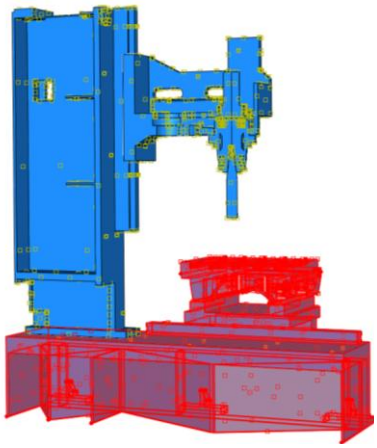

Figure 4-58: Convection applied to the base and table

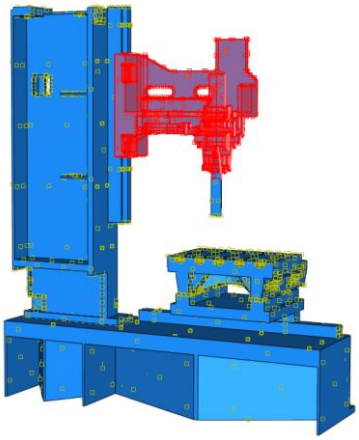

Figure 4-59: Convection applied to the spindle and carrier

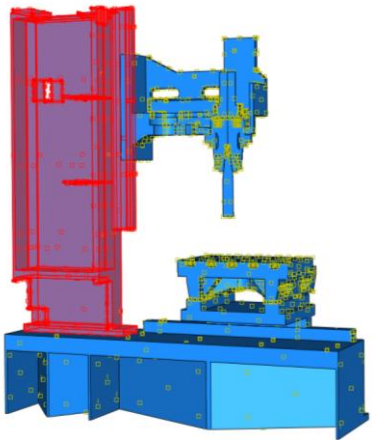

Figure 4-60: Convection applied to the column

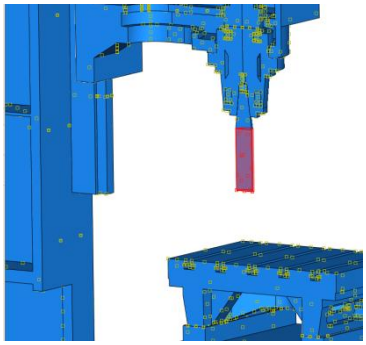

Figure 4-61: Convection applied to the test mandrel

The obtained convection value of 6W/m^2/°C was applied to the full machine structure during simulations apart from the test mandrel which was applied with 92W/m^2/°C during the 8000rpm heating cycle as explained in chapter 3 section 3.6.1 The sink temperatures (Abaqus ambient film conditions) represent the ambient temperature to which structural surfaces are exposed. The values applied to these exposed surfaces in the software were selected from the experimentally measured ambient temperatures. Figure 4-62, Figure 4-63 and Figure 4-64 show the temperature measured by the inside ambient sensor, column ambient sensor and base ambient sensor respectively. It should be noted that since this research aims to provide a simple and easy method for thermal behaviour predictions, the constant convection value of 6W/m^2/°C was applied to the full structure, however it is possible to apply different heat transfer coefficient values to the surfaces by selecting them individually in the software using the similar method shown above which may be difficult and complex in terms of selecting a specified area where partitioning may be required. On this machine the test mandrel is the area where

convection coefficient can significantly change and this is experimentally proved in section 3.6 – Chapter 3.

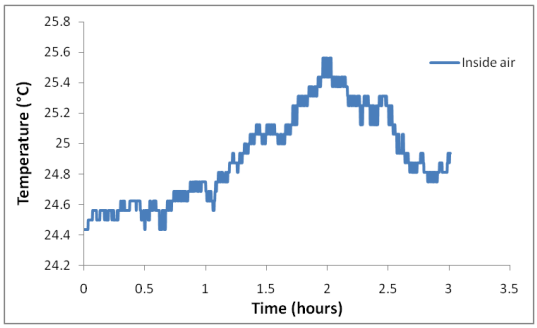

Figure 4-62: Ambient temperature measured inside the machine (8000rpm)

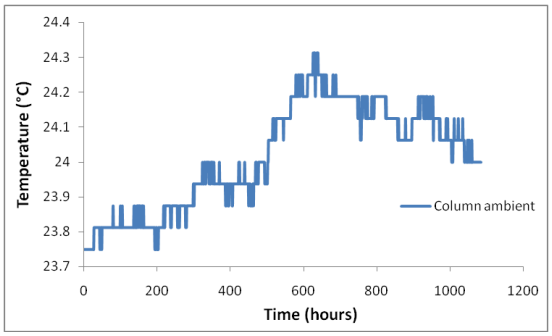

Figure 4-63: Ambient temperature measured at machine column (8000rpm)

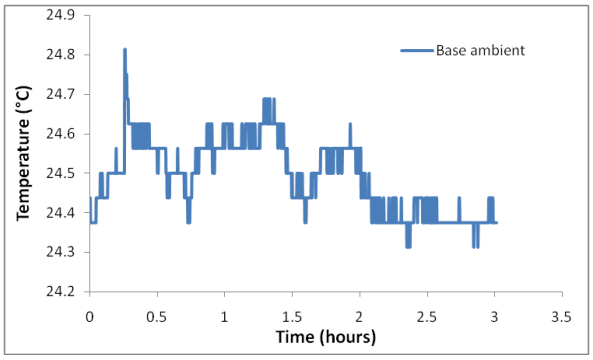

Figure 4-64: Ambient temperature measured at table and base structures (8000rpm)

The values of the ambient temperatures can be applied as a transient function in the software using tabular amplitude technique (as it is used in chapter 6 for long term environmental simulations). Since the variations in the temperatures during this short term test were not significant, it was decided to use single averaged values to define sink temperatures in the software. This simplifies simulation setup and helps reduce simulation times. The temperature data from the inside ambient sensor was applied to the column/carrier face with 25°C. The temperature data from the column ambient sensor was applied to the column with 24°C. The temperature data from the base ambient sensor (Figure 3-22 – chapter 3) was considered applied to the base/table face with 24.5°C.

4.3.4 Correlations (Stabilization period)

The first step was to correlate the simulated stabilization period result with the experimental stabilization period result. The simulated data was extracted from the nodes

located at the actual displacement sensor locations used to monitor Y and Z axes as shown in Figure 4-65.

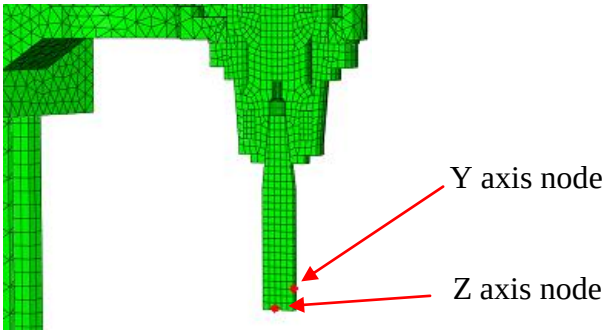

Figure 4-65: Nodes used to extract displacement data for both axes

The error difference range in Figure 4-66 and Figure 4-67 was observed to be less than a micron and therefore considered negligible. The axis scale was increased to observe the profile shape. Figure 4-68 shows the simulated temperature gradients and thermal bending caused by the Z axis motor heating. NT11 refers to nodal temperatures.

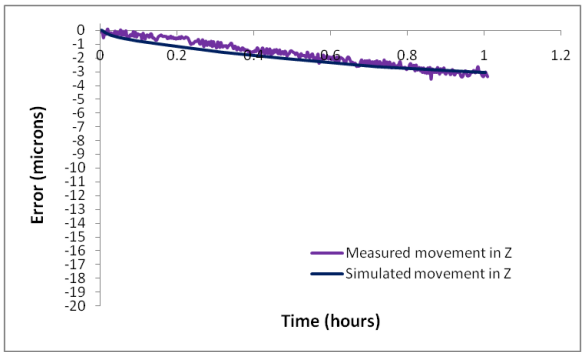

Figure 4-66: Z-axis movement during the stabilization period

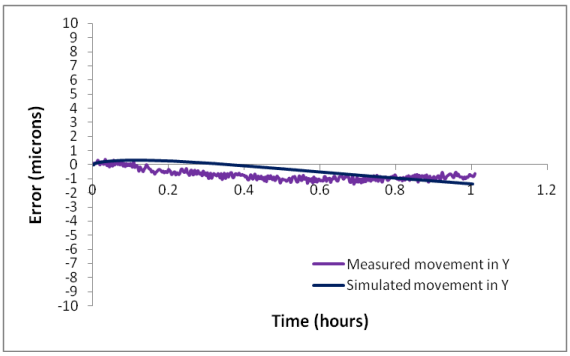

Figure 4-67: Y-axis movement during the stabilization period

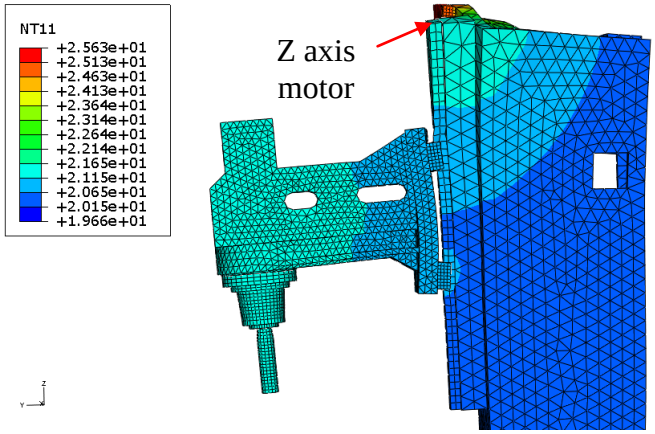

Figure 4-68: Column bending resulted in machine deformations in Y and Z axes

4.3.5 Correlations (Machine thermal behaviour)

The calculated heat fluxes were fed into the FEA model for a simulation period of three hours. The simulation for temperature and displacement analyses took approximately 18 and 12 minutes respectively (total 30 minutes). It was important to obtain an acceptable match between the experimental and simulated temperature gradients across the structure, in this case the carrier head. Figure 4-69 and Figure 4-70 show the experimental and simulated temperature gradients at one instance in time. The change in the temperature gradients, showing the heat flow, were considered similar for the duration of the test which confirmed the location and magnitude of the artificial heat sources responding to the calculated BHF values.

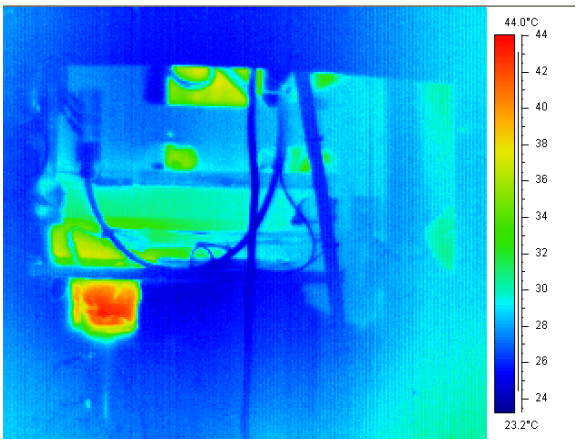

Figure 4-69: Thermal image showing temperature gradients across the carrier head

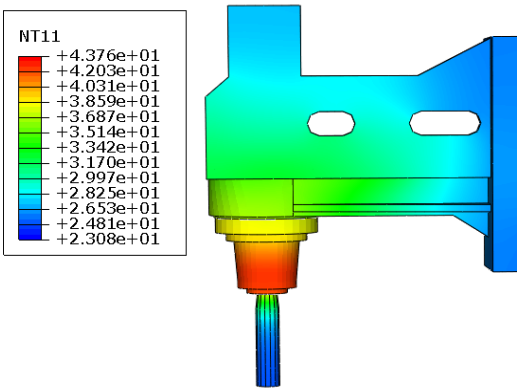

Figure 4-70: Simulated temperature gradients across the carrier head

4.3.5.1.1 Calculating correlations

Correlations were obtained using the measured, simulated and the error difference data. The error difference data is first obtained by subtracting the transient simulated data from the transient measured data. Then the overall magnitude range of the measured data and the error difference data is obtained. This overall error difference magnitude range is then divided by the overall magnitude range of the measured data to obtain a number which is subtracted from 1 to finally obtain the correlation value and shows the percentage of the simulated profile matching with the measured data profile. The correlation value is then multiplied by 100 to obtain the percentage correlation. For example the displacement correlations of **88%** was obtained for the Y axis which was calculated as follows

Maximum range of the measured data = 72.9µm

Maximum range of the error difference data = 8.67µm

Dividing reveals (8.67µm/72.9µm = 0.118)

Percent Correlation = 1- 0.118 reveals 0.88 which is multiplied by 100 to finally obtain 88%.

Using the same method, the correlation for the Z axis was obtained as 50%. The graphs are shown in Figure 4-79 and Figure 4-80 (section 4.3.6) for direct comparison with other results. The low correlation and lack of profile convergence in the Z axis direction was investigated. A brief discussion was outlined earlier about the presence of air pockets that reduce the cooling rate on the surrounding surfaces. The experimental results show a faster Z axis stabilisation which could be a result of additional carrier and column bending caused by unstable ambient temperatures due to the aforementioned air pockets. Similarly the drift in the simulated Y axis and consequential error progression from the measured error is also suspected to be due to the slow rate of change of structural ambient temperature due to air pockets within the carrier head. For simplicity in this initial simulation, the measured ambient temperatures were applied as a single value to each structure and the values kept constant during both heating and cooling cycle simulations. This potentially underestimates the slow rate of change of the actual ambient

temperature around local structure air pockets and resulted in a higher simulated cooling rate compared with online measurements.

4.3.6 Re-testing the machine

The number of ambient temperature sensors was increased and placed in proximity to the main identified air pockets. Figure 4-71 shows the location of the new sensors. The front of the column is close to the carrier head and the gap between the column and the carrier head serves to be a potential air pocket. The column itself is a hollow structure used to route machine cables which also generate a localised heat source. Figure 4-72, Figure 4-73, Figure 4-74 show the local ambient changes detected by these new temperature sensors. The original measured column ambient temperature is also plotted in each to observe the differences between ambient temperatures.

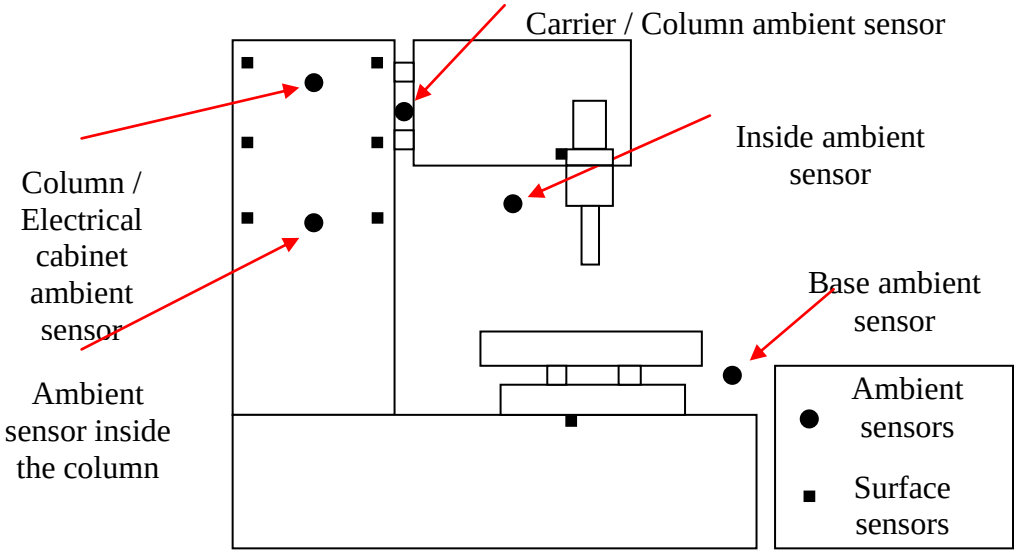

Figure 4-71: Position of the ambient sensors around the machine

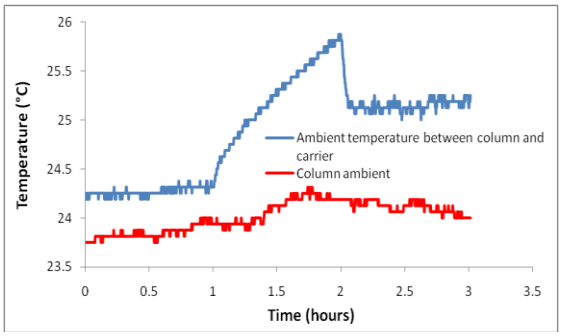

Figure 4-72: Measured ambient temperature between column and carrier (8000rpm)

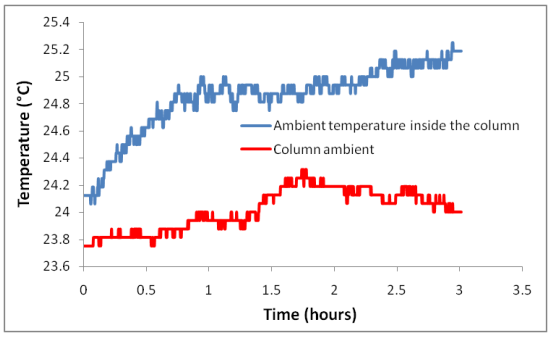

Figure 4-73: Measured ambient inside the column (8000rpm)

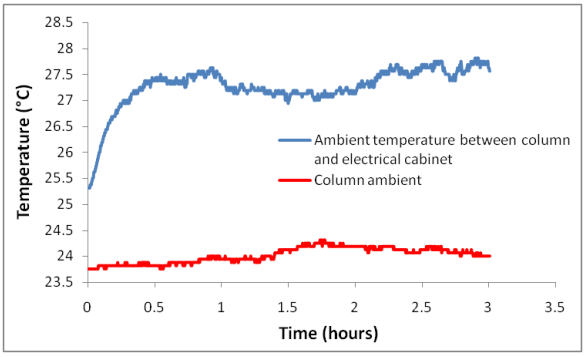

Figure 4-74: Measured ambient temperature between column and electrical cabinet (8000rpm)

Previously the whole column was applied a constant ambient (sink) temperature, however the above plots confirm that ambient temperature around the column is not constant. The local temperature change was selected from each plot and applied to the respective column sides as sink temperature. The column/carrier face was applied a temperature of 25.538°C considering approximately 1.6°C temperature change occurred at that face from the start of the test (23.938°C surface temperature measured at the column). Similarly the inside face of the column was applied 25.438°C considering approximately 1.5°C temperature change and the column/Electrical cabinet face was applied with 27.438°C considering approximately 3.5°C temperature change from the initial column temperature of 23.938°C. Figure 4-75, Figure 4-76, Figure 4-77 and Figure 4-78 show the column faces where ambient magnitudes obtained from the new test were applied.

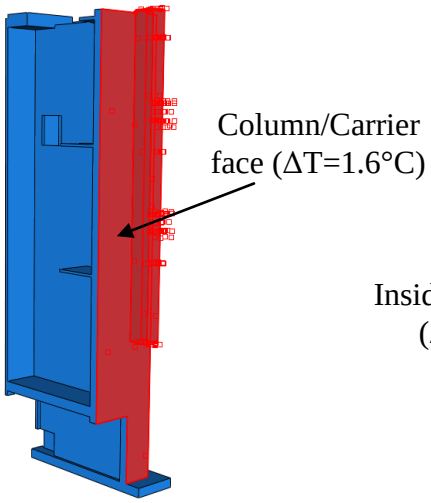

Figure 4-75: Column sink temperature (1)

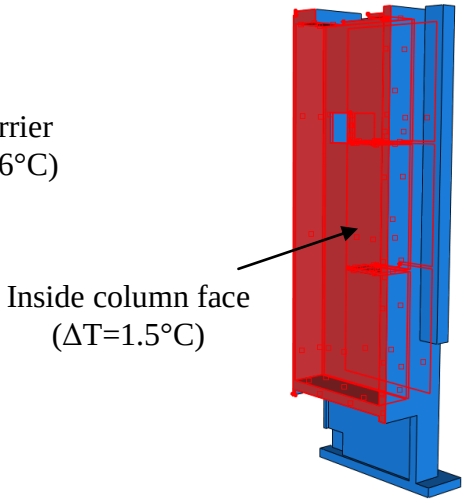

Figure 4-76: Column sink temperature (2)

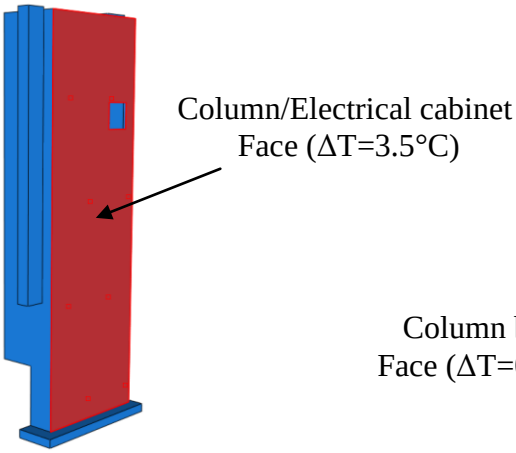

Figure 4-77: Column sink temperature (3)

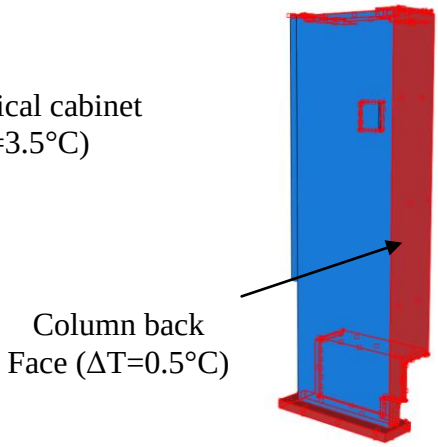

Figure 4-78: Column sink temperature (4)

The simulation was repeated and Figure 4-79 and Figure 4-80 show the correlation results for Y and Z axes respectively where a comparison can be made between the profiles with and without considerations to airpockets.

Importantly, the correlation in the Z axis revealed an improved correlation of 62% from the original 50%. The Y axis remained the same. The residual errors for both axes were less than 10µm which represents the total range of the error difference data or the range of the data left unpredicted.

These correlation improvements and profile convergences are significant for a machine with high error ranges specifically during the heating cycle which occurs during the cutting process which is a crucial phase. Hence this test revealed the significance of

considering air pockets where confined ambient temperatures are critical towards the overall thermal behaviour of the machine.

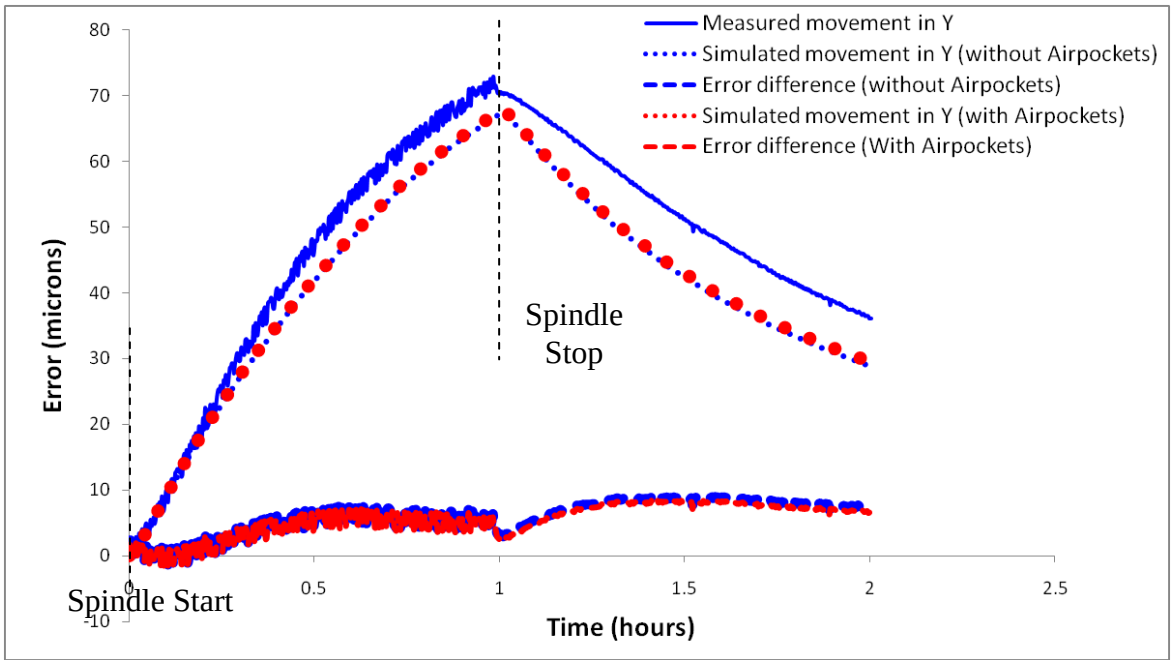

Figure 4-79: Y-Displacement profiles correlation (8000rpm)

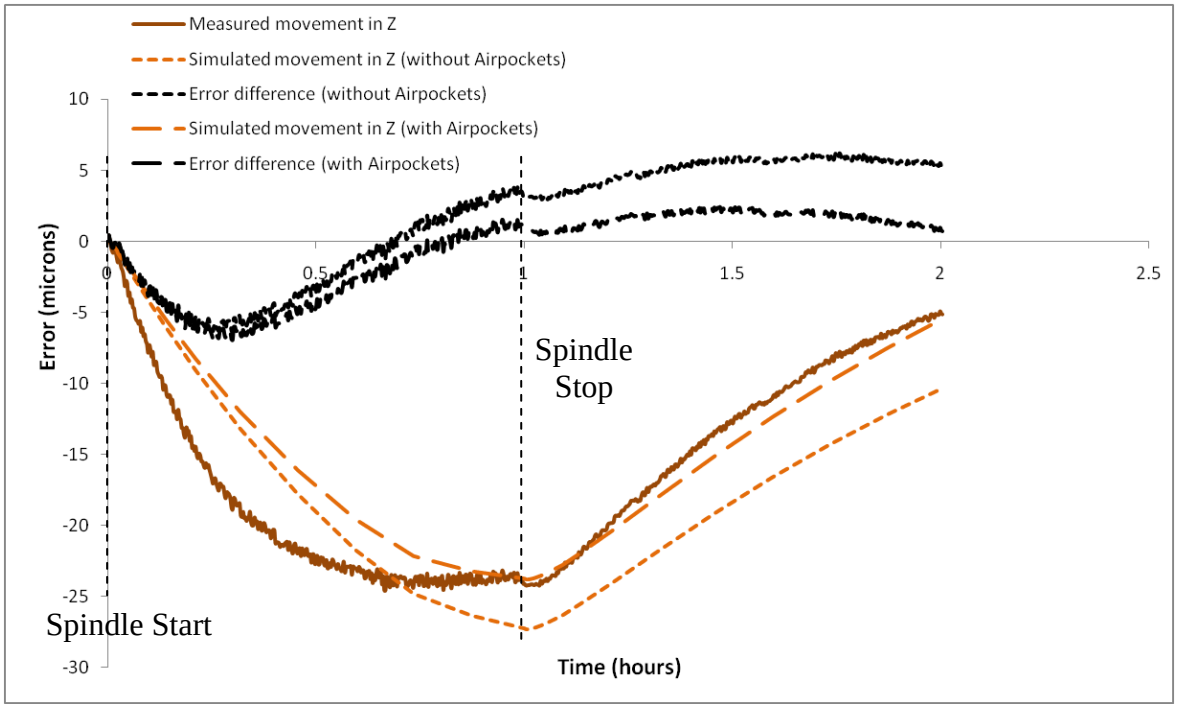

Figure 4-80: Z-Displacement profiles correlation (8000rpm)

For a short term test, the behaviour of the machine is subjected to various ambiguities such as an immediate structure response to quickly changing local temperature gradients

and concentrations which start to build up instantly after excitations of the heat sources. Structural constituents start to respond according to those gradients until a state of thermal equilibrium is achieved. Similar behaviour can be observed in Figure 4-80 where the Z axis behaviour shows a lack of convergence during the very initial phase of the heating cycle and starts to converge later. It is suspected that these ambiguities may also be the cause of a lower predicted magnitude of the temperature (approximately 2°C) at the spindle boss. The movement at the spindle boss was also plotted against the simulated, the results also revealed very good correlation of 76% with the maximum residual error of 6.8µm. shown in Figure 4-81. Figure 4-82 shows the visual representation of the simulated deformation of the machine.

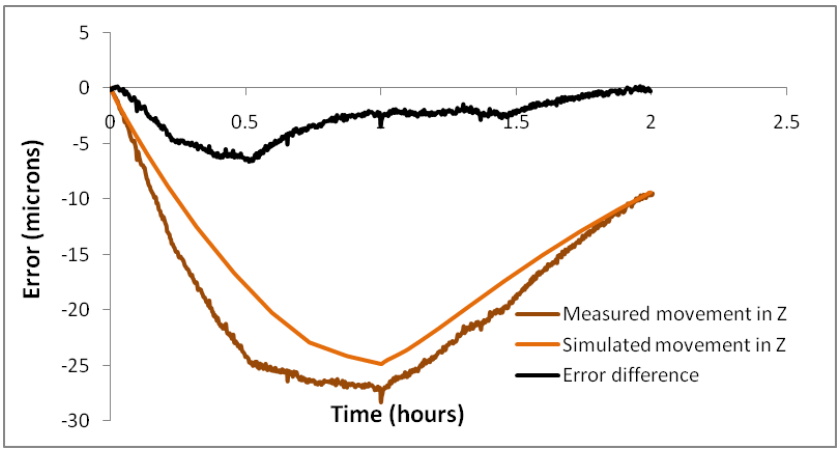

Figure 4-81: Spindle boss Z-Displacement profiles correlation (8000rpm)

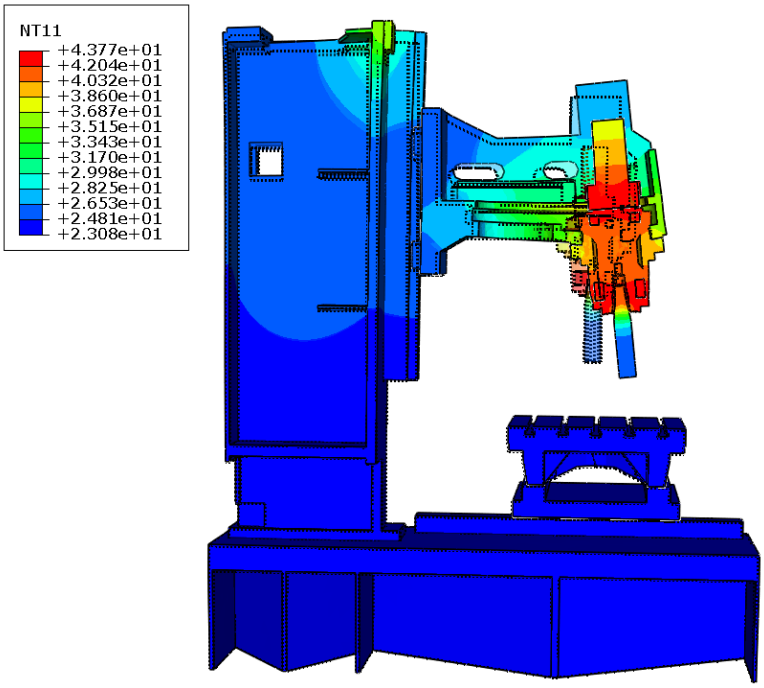

Figure 4-82: Simulated visual representation of deformation of the machine due to internal heating

4.3.7 Basic machine operation at 4000rpm

A new test was conducted where the machine was operated for an identical duty cycle i.e. basic machine operation at 4000rpm spindle speed. The same procedure was followed for calculating new BHF values for 4000rpm using the information obtained from the surface sensors. Calculations are presented in Appendix C, the calculated BHF values for 4000rpm spindle speed rpm are shown in Table 4-6. Similarly using similar procedure (section 3.6.1 - Chapter 3) new averaged convection coefficient *'h'* of 58W/m^2/C was obtained for the rotating test mandrel during the heating cycle at 4000rpm and applied to the test mandrel during the heating cycle simulations conducted.

	Body heat flux (mW/mm^3)
Lower bearings	0.06
Upper bearing	0.11
Carrier belt drive	0.37
Spindle belt	0.33
Z axis motor bracket	0.23
Spindle motor mount plate	0.08

Table 4-6: Calculated body heat flux values for 4000rpm spindle speed

It should be noted that BHFs calculated for 4000rpm have shown to have a non-linear reduction in magnitude as the spindle speed was halved from 8000rpm for example with lower bearings. The value for the lower bearing at 8000rpm and 4000rpm were obtained to be 0.42mW/mm^3 and 0.06W/mm^3 respectively. Since the BHFs were obtained using the temperature information which can be viewed in Figure 4-83 (both temperatures profiles were intentionally caused to start from the same point), this shows a non-linear relationship of temperature increase between both speeds. This explains the non-linearity of bearing behaviour at both speeds and is suspected to be due to the reasons explained earlier i.e. bearing preload, friction levels etc. Similar case can be observed with other heat sources BHF values.

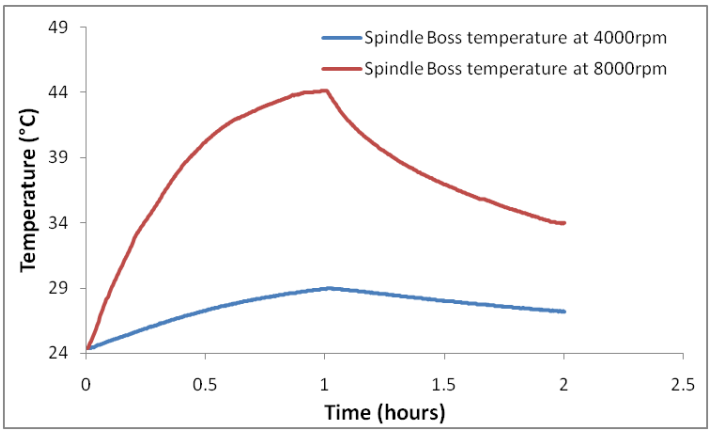

Figure 4-83: Comparison of the spindle temperature at 4000rpm and 8000rpm speeds

Figure 4-84 and Figure 4-85 shows the temperature measured by the inside ambient sensor and the column ambient temperature sensor respectively.

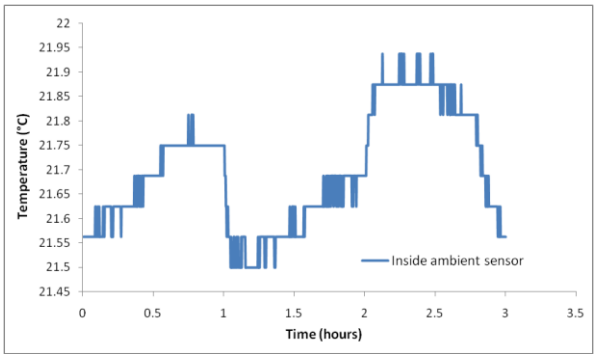

Figure 4-84: Ambient temperature measured inside the machine

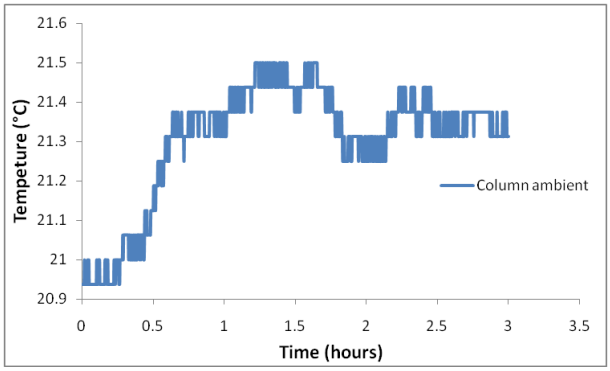

Figure 4-85: Ambient temperature measured at the column

The base and table ambient temperatures were expected to be stable even for longer test periods (Chapter 5) because these structures are far from the heat sources i.e. the spindle and the carrier. Figure 4-87 shows the obtained ambient temperature measured for a long term testing regime. The plot shows a stable ambient during the heating cycle

with a negligible change of approximately 0.2°C. Since the ambient temperature has not changed significantly during the heating cycle, the overall change of approximately 0.5°C was applied in the simulations for all testing regimes conducted at 4000rpm.

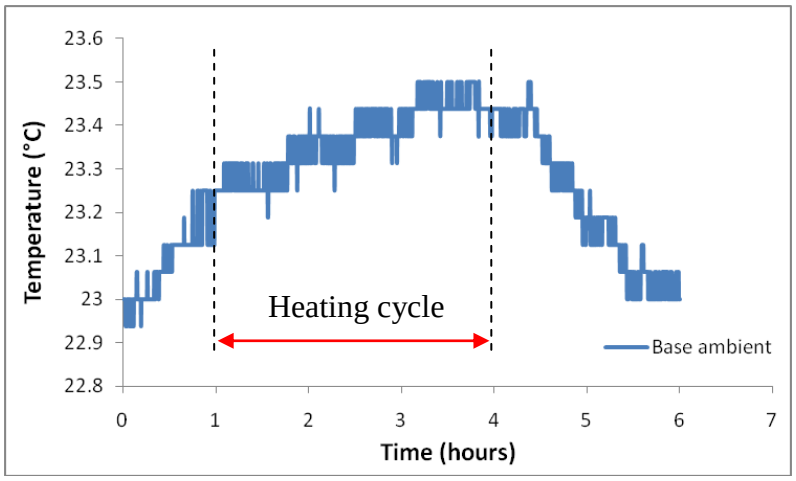

Figure 4-86: Ambient temperature measured at table and base structures

The information of ambient temperatures and BHF values were applied to the FEA model as shown previously in section 4.3.3.4. The transient simulation for temperature and displacement analyses took approximately 8 and 11 minutes respectively (total 19 minutes). The results revealed good correlations of 85% for the full temperature profile, 75% for the Y axis and 73% for the Z axis profiles with non-significant convergence lacks. The results are presented later for direct comparison with the second set of results from the simulation using the new arrangement of ambient temperature sensors. Figure 4-87, Figure 4-88 and

Figure 4-89 shows the ambient information obtained at suspected air pockets from the basic machine operation. The original measured column ambient temperature is also plotted in each to observe the differences between ambient temperatures. The plots clearly show that ambient conditions around the column also differ at lower speeds. These ambient temperatures were applied to the column faces as they were applied for the 8000rpm repeated test in section 4.3.7.

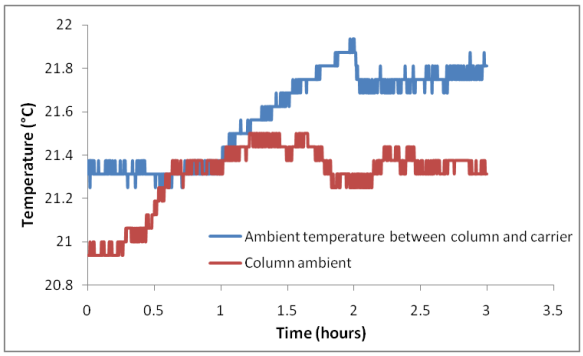

Figure 4-87: Measured ambient temperature between column and carrier (4000rpm)

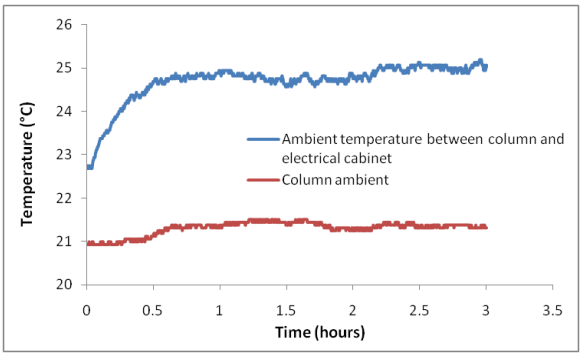

Figure 4-88: Measured ambient inside the column (4000rpm)

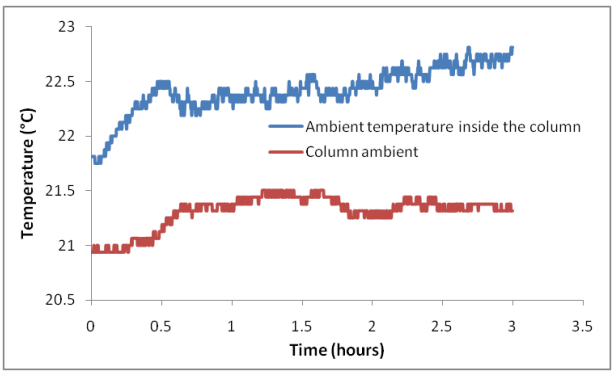

Figure 4-89: Measured ambient temperature between column and electrical cabinet (4000rpm)

The displacement correlations are 71% and 77% for the Y and Z axes respectively and 83% for the spindle boss temperature. Importantly the residual errors are just 6µm for the Y axis and less than 2µm for the Z axis. Figure 4-90, Figure 4-91 and Figure 4-92 show the comparison of correlations obtained for Temperature, Y axis and Z axis respectively.

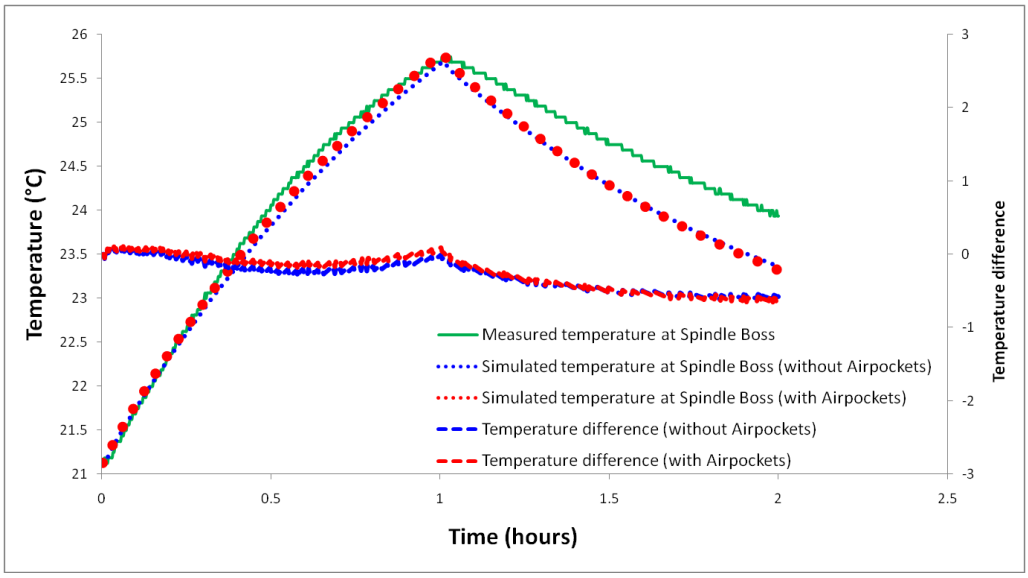

Figure 4-90: Temperature profiles correlation (4000rpm)

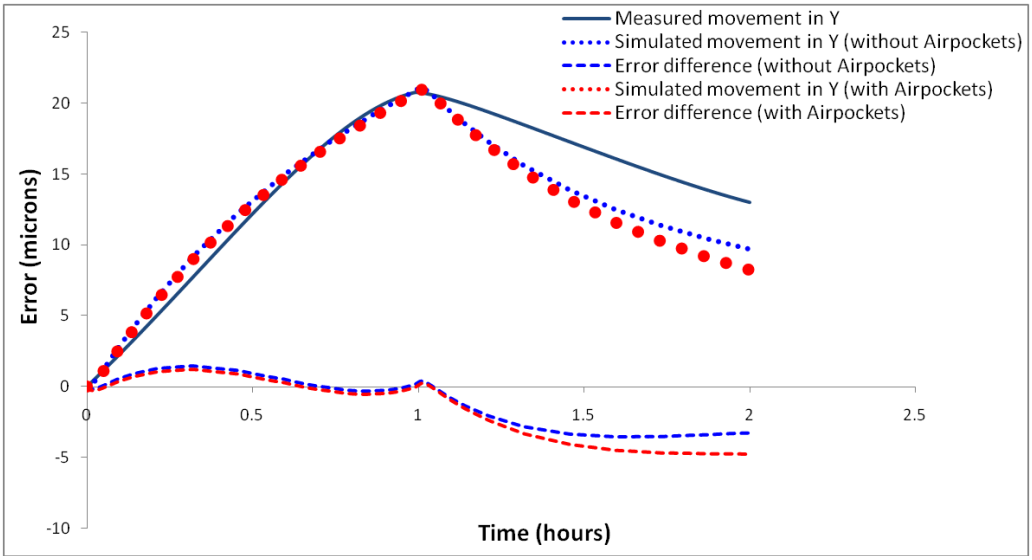

Figure 4-91: Y-Displacement profiles correlation (4000rpm)

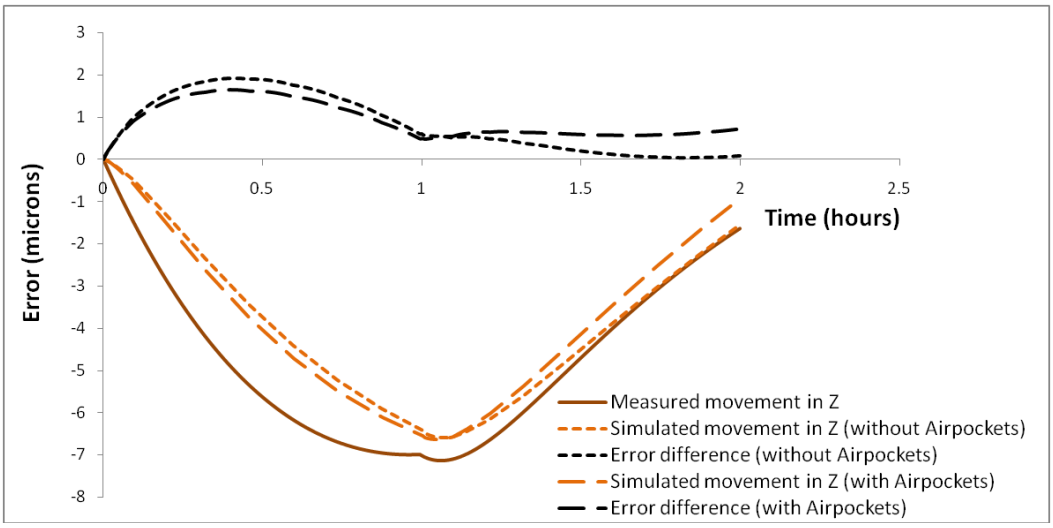

Figure 4-92: Z-Displacement profiles correlation (4000rpm)

It can be elaborated that unlike high spindle speed test where the consideration of air pockets significantly improved the results, air pockets do not have a major affect on the correlations and error residuals during a short term slower spindle speed operation. Nevertheless the significance of air pockets is expected to be higher for long term machining operations at a low spindle speed.

It should be noted that simulation times for both basic machine operations (8000rpm and 4000rpm) differs. 8000rpm simulation took a longer time due to the use of variable Cp values which caused Abaqus to take a relatively longer time to carry out numerical calculations.

4.4 Summary of the chapter

This chapter has presented an approach to conduct quick and efficient parameter identification exercise and FEA to analyse the thermal behaviour of a 3 axis VMC when running the main spindle. To validate the potential approach, benchmarks were conducted which not only confirmed the approach but also confirmed that the obtained accuracy was within the required range. The new approach is to calculate Body Heat Flux (BHF) values for the potential heat sources using descretization of the surrounding structure and spatially detailed surface temperature measurement.

Initially the machine spindle was rotated at its highest speed of 8000rpm for obtaining its maximum thermal behaviour. The temperature information was used to calculate BHF values for the heat sources which were applied in the FEA software. Simulations were

then conducted to obtain the thermal behaviour offline. Initially the temperature profile at the spindle boss was correlated but revealed a lack of convergence. This problem was solved after using a software programming feature to include non stable energy output from the spindle bearings. The results then revealed very good correlations for temperature and Y axis movement profiles, however Z axis results did not correlate as well. This led to the consideration of suspected air pockets around the carrier and column. A further test revealed that the ambient temperature varies around the column. The data obtained from air pockets were applied in the simulation which revealed improved correlation in Z movement confirming the significance of air pockets.

The approach of calculating BHF values and the findings of 8000rpm test were validated by operating the machine at 4000rpm. Excellent correlations of over 70% were obtained. It was found that for a short term lower speed test, the thermal air pockets did not have such a significant effect; however it is suspected that air pockets will have a contribution at lower spindle speed if the machine is operated for long term.

It should be noted that the most significant benefits from this project are from long and very long term simulations that are impractical or unfeasible to complete experimentally. The effort applied to concentrate on maximising the short term correlation in the Z axis was not a priority once the target correlation of 60% was achieved.

CHAPTER - 5

5 VALIDATION OF THE APPROACH WITH LONG TERM TESTING

The previous chapter presented an approach to conduct quick and efficient thermal parameter identification and FEA for analyzing the thermal behaviour of a 3 axis VMC. Two short term tests were conducted at different spindle speeds and simulated. The correlation results revealed the applicability of calculated BHF values and also highlighted the significance of the air pockets for accurate simulations.

This chapter will focus on maximising the reduction of the machine downtime associated with the long term machine testing. This will be achieved by simulating the machine for long term tests and obtaining a correlated thermal behaviour while validating the BHF calculation approach and confirming modelling priorities such as air pockets that affect the overall thermal behaviour of the machine over long durations.

5.1 Long term operation

Extended thermal trials on production machine tools necessitates expensive or impractical machine down time, therefore, one of the greatest advantages of improving offline simulation capability is to enable characterization of the machine to an acceptable accuracy over such medium and long term periods. The anticipation was to use the same BHF values listed in (Table 4-6 - Chapter 4) for extended long term simulations and to correlate them with experimental results.

It was shown in the previous chapter that for a basic machine operation test, the behaviour of air pockets was significant at high spindle speeds and less critical at lower spindle speeds. Therefore a long term operation was carried out to first validate the BHF values calculated using the basic machine operation test. The validation will confirm the ability to dramatically reduce machine testing and therefore downtime. Secondly the tests will confirm the significance of modelling the air pockets during the longer tests. The same procedure was followed with the simulation conducted in two phases, the first simulation included the ambient temperature information obtained from only three

sensors (Figure 3-22– Chapter 3) and the second simulation added the ambient information obtained from the new sensor arrangement (Figure 4-71– Chapter 4).

The machine was tested over a period of 6 hours involving 1 hour stabilization, 3 hours heating and 2 hours cooling. The spindle was rotated at 4000rpm and the data was recorded using the same sensor arrangement as used in the basic machine testing. The BHF values listed in (Table 4-6 - Chapter 4) were used in the simulation along with the same method and same convection parameters such as 58W/m^2/°C for the rotating test mandrel during the heating cycle and 6W/m^2/°C during the cooling cycle. Figure 5-1 and Figure 5-2 show the ambient temperatures monitored inside the machine and at the column respectively. The ambient temperature obtained from the bed sensor is shown in section 4.3.7 of chapter 4. This temperature information was applied to the FEA model as shown previously in section 4.3.3.4 of chapter 4. The transient simulation for temperature and displacement analyses took approximately 12 and 15 minutes respectively (total 27 minutes).

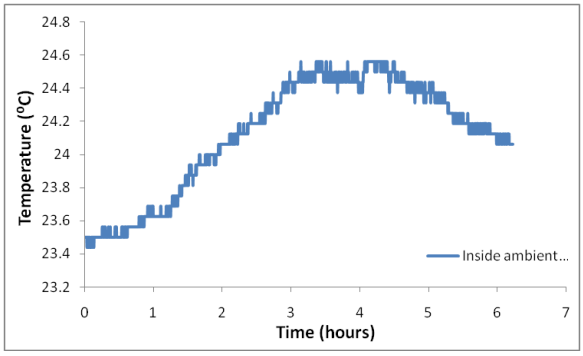

Figure 5-1: Measured ambient temperature inside the machine (long-term 4000rpm)

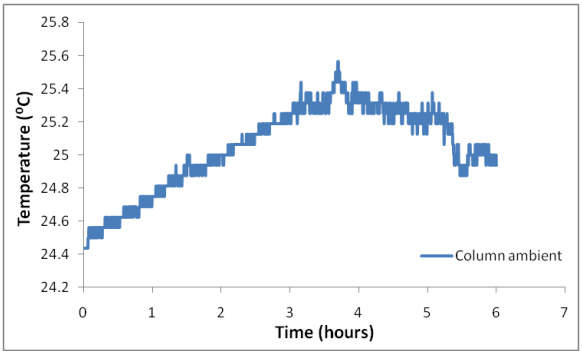

Figure 5-2: Measured ambient temperature at the column (long-term 4000rpm)

The predicted spindle boss temperature was slightly higher (1.5°C) as well as the predicted Y axis displacement (approximately 4µm) during the heating cycle, nevertheless 66% correlations were achieved for the full temperature profile, 81% for the displacement profile in the Y axis direction and 74% correlation for the Z axis direction. The residuals error was approximately 6µm for the Y axis and 3µm for the Z axis. The results are presented later in this section (Figure 5-7 and Figure 5-8) for direct comparison with other obtained results. The excellent correlations clearly show the compatibility of the calculated BHFs with extended thermal testing and simulations. This is an achievement towards reducing machine downtime where the machine behaviour can

be predicted by using only the data obtained from a basic and short term machine operation test.

A good correlation percentage may not sometimes represent a good profile match i.e. the Z axis response lacked convergence during the heating cycle even with a good correlation percentage. Therefore additional simulations were undertaken after including the ambient data obtained from the air pockets. The data was applied to the column surfaces as previously explained in section 4.3.6 of chapter 4. Figure 5-3, Figure 5-4 and Figure 5-5 shows the obtained ambient temperatures from the air pockets. The original measured column ambient temperature is also plotted in each to observe the differences between ambient temperatures.

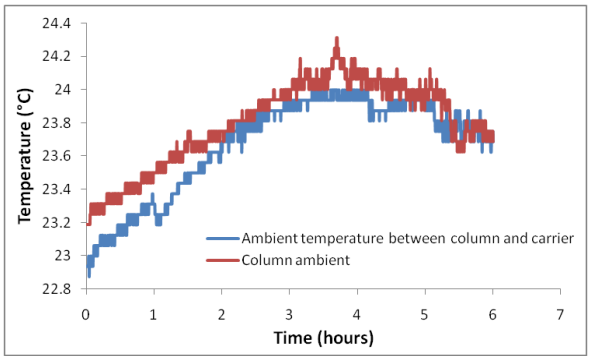

Figure 5-3: Measured ambient temperature between column and carrier (4000rpm)

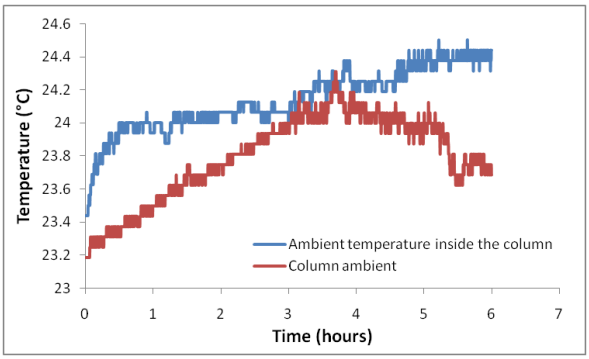

Figure 5-4: Measured ambient inside the column (4000rpm)

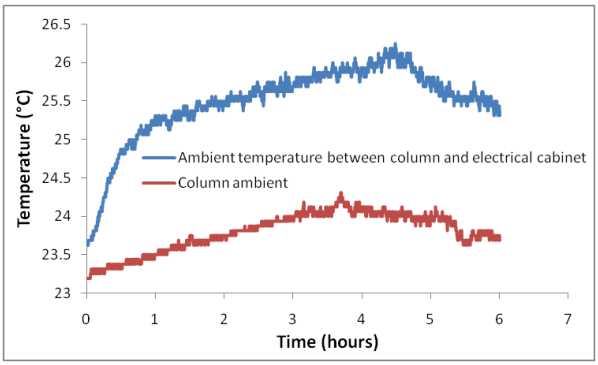

Figure 5-5: Measured ambient temperature between column and electrical cabinet (4000rpm)

The effect of the model changes was mostly negligible for this test and the residual errors remain at a very low 6µm for the Y axis and less than 4µm for the Z axis. Figure 5-6, Figure 5-7 and Figure 5-8 shows the comparisons of correlations obtained for Temperature, Y axis and Z axis respectively. As previously explained (section 4.3.5.1.1 – chapter 4), the drift in the simulated Y and Z axis profiles from the measured error is

suspected to be due to the slow rate of change of structural ambient temperature due to air pockets which may have reduced the natural convection within the carrier head as the measured ambient temperatures and the convection coefficient of 6W/m^2/°C were applied as single values to each structure and the values kept constant during both heating and cooling cycle simulations.

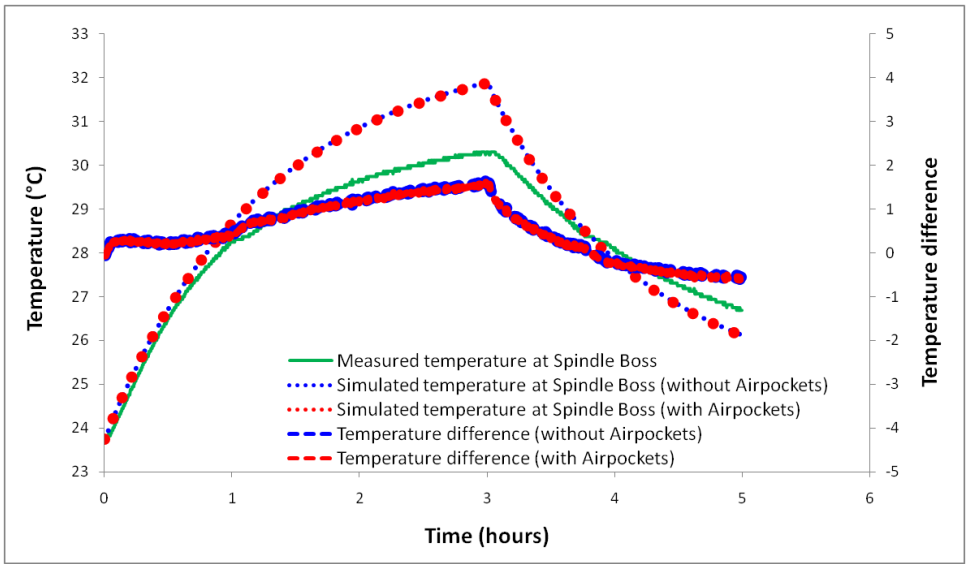

Figure 5-6: Temperature profiles correlation (4000rpm)

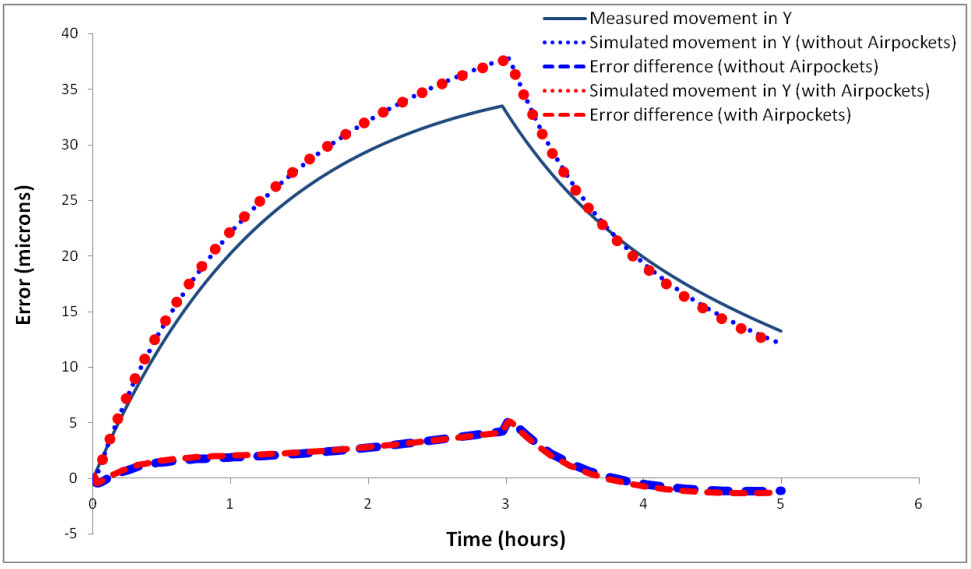

Figure 5-7: Y-Displacement profiles correlation (4000rpm)

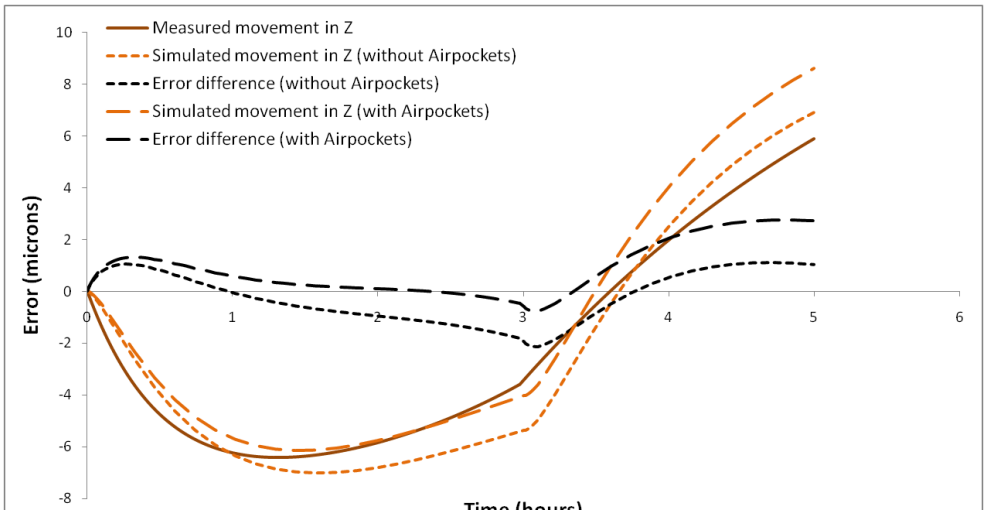

Figure 5-8: Z-Displacement profiles correlation (4000rpm)

5.1.1 Complex duty cycle operation

This section validates the methodology against a long term complex duty cycle using the already established coefficients.. The duty cycle was 9 hours and composed of 1 hour stabilization, two 2 separate 1 hour heating cycles with 1 hour cooling gap and 3 hours cooling at the end. As usual, the transient simulation was conducted twice; first with the ambient temperature information obtained from only three sensors (Figure 3-22 – Chapter 3) whereas the second simulation added the ambient information obtained from the new arrangement of ambient sensors (Figure 4-71– Chapter 4). The simulation used the same parameters from the 4000rpm BHF values, convection values and the ambient information obtained from the long term ambient testing. After simulations, the machine was then tested for the same duty cycle at the spindle speed of 4000rpm.

The initial simulation results revealed very good correlations of 66% for the full temperature profile, 81% for the displacement profile in the Y axis direction and 66% correlation for the Z axis direction. The simulation for temperature and displacement analyses took approximately 16 and 17 minutes respectively (total 33 minutes). The quality of the correlations have again confirmed the compatibility of BHF values obtained for the 4000rpm and in addition confirmed the applicability for reducing machine testing. The model was re-simulated with the new ambient temperature sensors arrangement. A better convergence of profiles was observed with improved correlations of 82% for the Y axis and 70% for the Z axis, the residual errors were less than 7µm for both axes. The correlations are presented in Figure 5-9, Figure 5-10 and Figure 5-11.

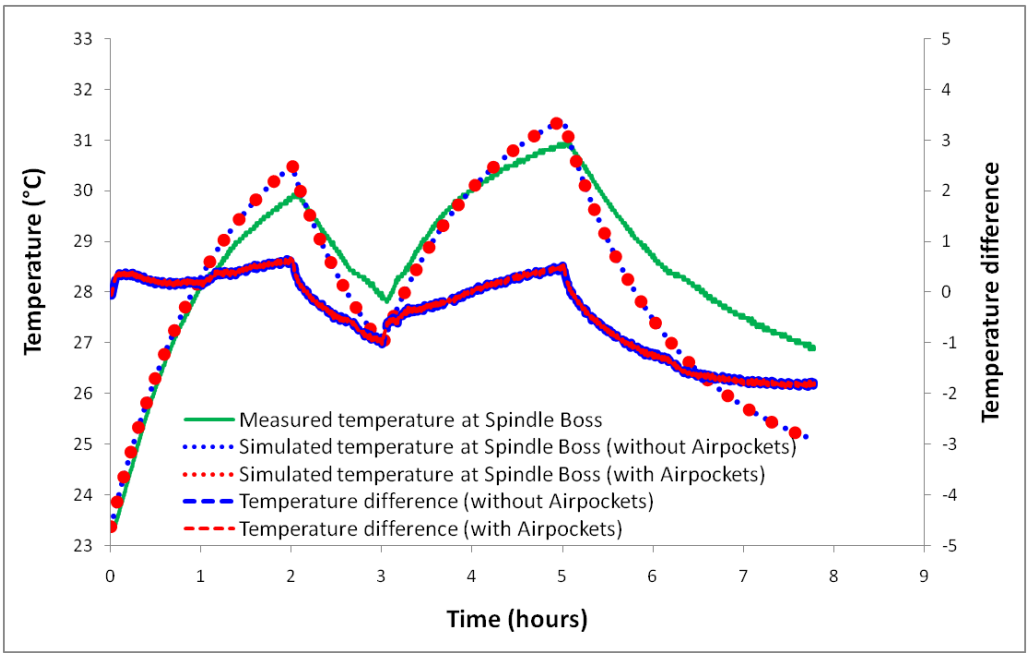

Figure 5-9: Correlations for temperature profiles (complex duty cycle)

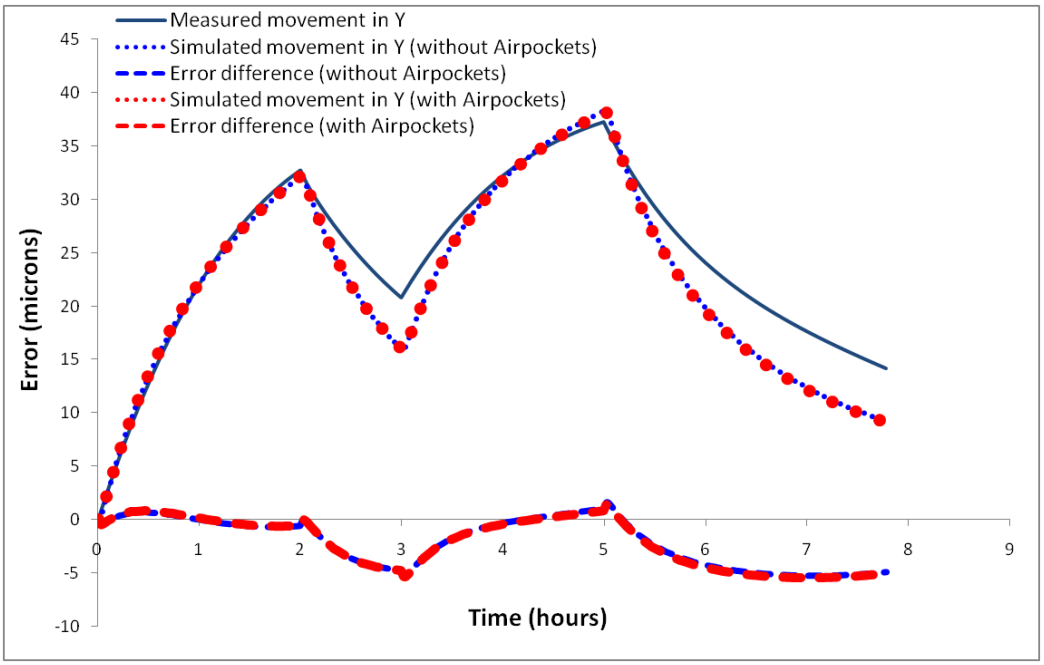

Figure 5-10: Correlations for Y axis displacement profiles (complex duty cycle)

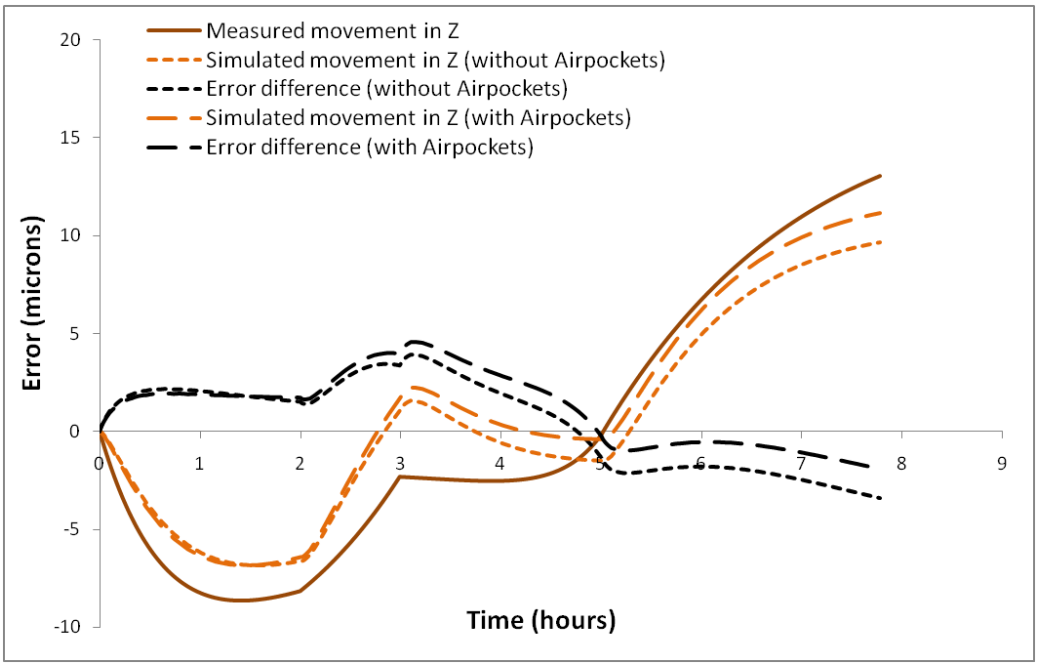

Figure 5-11: Correlations for Z axis displacement profiles (complex duty cycle)

The results obtained from all testing regimes were shown to have a well matched profile with overall correlations well above the desired 60%. Therefore it can be concluded that the technique of obtaining BHF values from a short term test can predict thermal behaviour of a machine when operated for a long term. Long term use can either be a simple heat and cool operation or a complex duty cycle. Thermal error predictions using Abaqus FEA technique were quick to run. The maximum time taken by any simulation did not exceed 33 minutes and can therefore be used to run various operating scenarios to maximise the return on the initial investment made to create the models and obtain the parameters from the short term tests. The offline thermal behaviour assessments will benefit industries where machine availability is not compromised over extended thermal trials.

5.2 Assumptions made for calculations and internal heating simulations

Sections and Topics	Assumptions made	Explanation
Thermal Contact Conductance (TCC) - Section 3.5.1.1 Calculations for using equation 3.6 $Q' = mCp(T_2 - T_1)/t + hA(T_{surf} - T_{air})$	Convection coefficient h=6 W/m^2/°C	-This value was experimentally obtained. -Secondary validations were also conducted for that value -Used as a constant value during calculations.
Clamping force - Section 3.5.1.1 $Pi = T / KD$	-Thread coefficient of friction (μt) 0.14 for dry conditions 0.12 for oiled conditions -Collar coefficient of friction (μc) 0.20 for dry conditions 0.14for oiled conditions	- For calculating K, collar and thread coefficients were used as averaged.
TCC - Section 3.7 and Section 4.3.3.1.3 Sliding surfaces / guideways	TCC=2000 W/m^2/°C	The machine dynamics was not considered in this research therefore an averaged value of the experimentally obtained TCC was used in FEA simulations.
Benchmarks - Section 4.1 Equation 3.6 $Q' = mCp(T_2 - T_1)/t + hA(T_{surf} - T_{air})$	-Energy balance -Constant ambient temperature T_{air} = 20°C - Convection coefficient h=6 W/m^2/°C -TCC values 1300 W/m^2/°C 10000 W/m^2/°C 1.e^8 W/m^2/°C	-Energy balance equation therefore conduction was not considered -In benchmark calculations, the ambient temperature was kept constant at 20°C. -Value of h was used as a constant value for calculating BHFs in benchmarks and all other calculations using equation 3.6. -TCC values were used in benchmarks for testing the effect of them on the temperature values.

FEA simulations (Abaqus) Section 4.3.3.4	-Sink temperatures Spindle/Carrier = 25°C Column = 24°C Base = 24.5°C	Ambient temperature change was not significant therefore averaged values were considered from the ambient temperature profiles for using them as sink temperatures during simulations.

5.3 Summary of the chapter

This chapter presented the validation of the BHF values that were calculated from a short term basic operation test, by application on long term machine thermal trials thus extending the potential for educing machine downtime. The chapter also focussed on the significance of air pockets around the machine structure and the behaviour of machine during long term operations at low spindle speeds.

The spindle was operated at 4000rpm for long term using two types of duty cycles; the first represented a simple but long heat and cool operation and the second used multiple cycles over an even longer period.

Very good correlations were achieved between the simulated and measured results for both tests which confirmed that the BHF values can be used for long term tests. Considerations of air pockets improved convergences of the profiles, specifically for the Z axis movement.

It can be concluded that a short term basic machine operation test should be enough to obtain the required parameters for an FEA simulation to be able to predict long term thermal behaviour of a machine tool thereby avoiding potentially significant machine downtime while increasing the potential for exploring varying operation scenarios.

The short run time should not preclude running multiple simulations with the axes re-positioned to pick up position dependent thermal errors, for example, the effect of column bending.

CHAPTER - 6

6 MACHINE TOOL ENVIRONMENTAL TEMPERATURE TESTING AND OFFLINE MODELING

Previous chapters detailed the effects of internal heating of a machine tool structure which was analysed and predicted using FEA simulations. This chapter discusses the importance of considering environmental temperature fluctuations that produce thermal errors in machine tools. A number of external sources have already been discussed that cause temperature changes around the vicinity of machine.

Machine tools are susceptible to environmental temperature changes the most significant and common of which is usually the day and night transitions. The temperature swings generate thermal gradients and result in structural deformation whether the machine is in operation or not. These environmental effects add to the thermal errors caused by internal heating often resulting in a higher magnitude of total error during extensive long term machining regimes.

This chapter looks into two online testing regimes conducted on the VMC to monitor the thermal error produced by long term environmental temperature variations. The first test was conducted in summer and the second in winter to observe seasonal effects on the machine behaviour. The experiments were followed by FEA simulations for prediction of the thermal error.

6.1 Long term environmental testing (summer)

In order to avoid axis movements caused by detected drifts in the linear scale feedback devices, the machine was set on emergency stop prior to the test to measure only the structural drifts caused by the environmental temperature changes. The machine was tested in summer for three days with temperature data recorded using three ambient sensors placed at the column, base and inside the machine (Chapter 3). The displacements between tool and workpiece were recorded using the NCDT nest as explained in chapter 4. This time the machine carrier head was moved up in the Z direction to give a change in the machine position used previously for internal testing.

This was done to have conditions with different machine orientation. A longer sensor post was needed therefore it was made of invar which is a steel alloy with a very low thermal expansion coefficient (Appendix A) to avoid the uncertainties involved with the post being affected by the changing environment. Figure 6-1 shows the model of the machine with carrier head in its raised position.

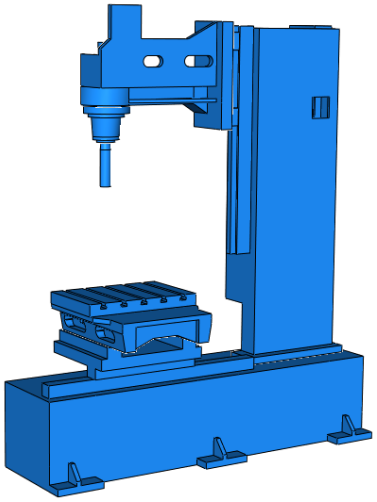

Figure 6-1: Model of the machine with carrier head moved upward

Figure 6-2 shows the measured ambient temperatures around the machine over the three day period. Figure 6-3 and Figure 6-4 shows the machine movement in Y and Z direction plotted against the temperature measured by the inside ambient sensor. The overall temperatures varied by 4˚C inside the machine and approximately 2˚C at the base during the 3 day period. A vertical temperature gradient averaging about 1°C can be observed between the base ambient sensor and the column ambient sensor. The overall movement varied by 12µm in the Y axis direction and 28µm in the Z axis direction. The variations are relatively small, primarily because the machine is small yet the results give a clear picture of machine sensitivity to environmental variations. Both axis movements followed the profile of the temperature variation however the Z axis displacement lags behind. This lag is due to the low response time of the structural components affecting this direction. The results confirm that the environmental temperature variations exist and play an important role in producing thermal drifts over longer production periods.

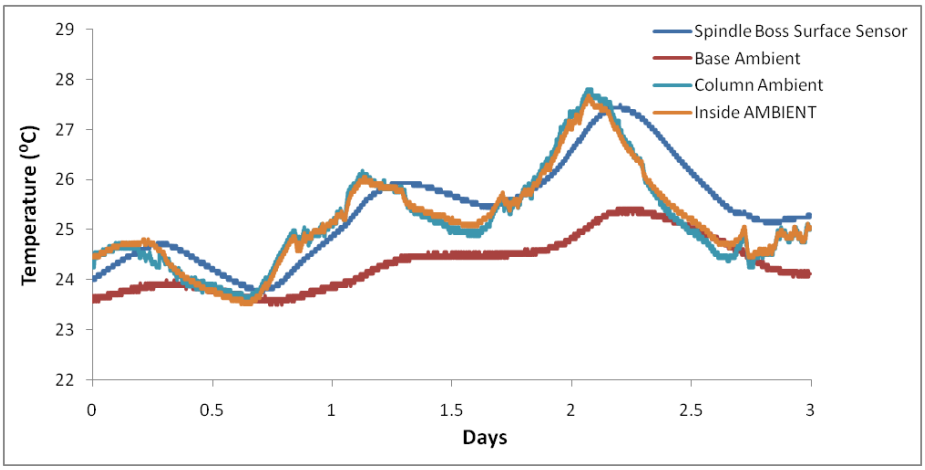

Figure 6-2: Temperature profiles obtained over 3 days period

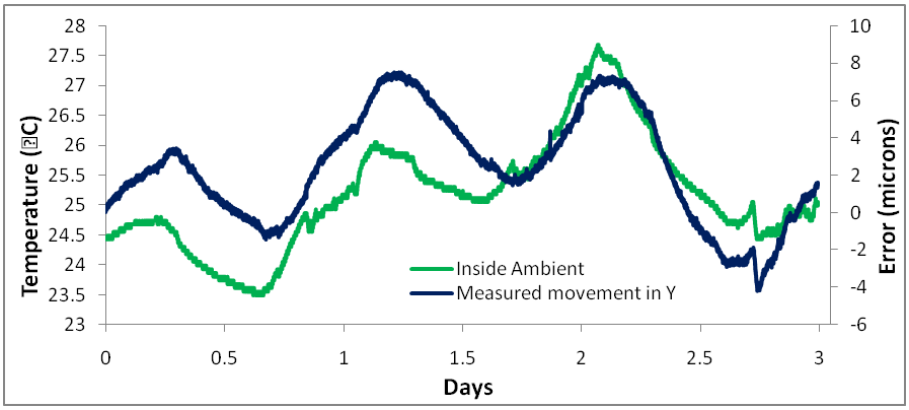

Figure 6-3: Measured movement in Y

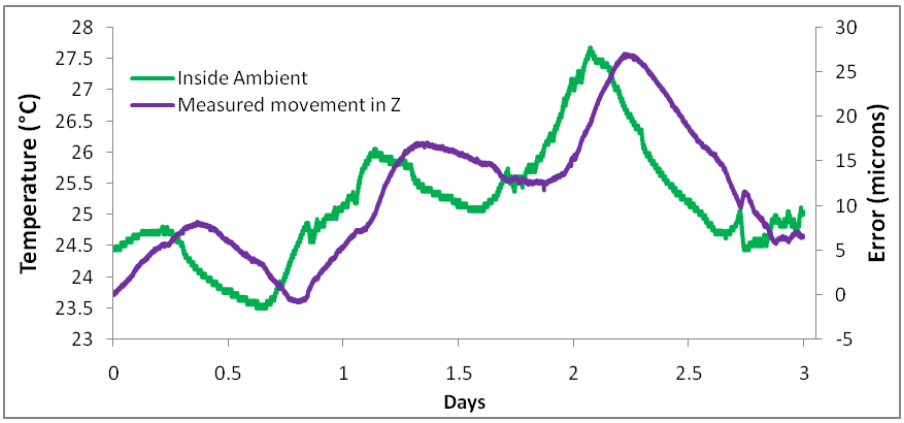

Figure 6-4: Measured movement in Z

6.2 FEA simulations (summer test)

Temperature information obtained during the environmental test was extracted and applied into the FEA simulation. Intuitively the data from the base temperature sensor was applied to the base of the FEA model, the column sensor to the column and inside sensor data applied to the carrier/spindle/tool and the table. The model surfaces were

applied with the 6W/m^2/°C convective heat transfer coefficient previously measured in chapter 3.

6.2.1 Setup of FEA initial conditions

Prior to the start of experimental tests, the machine elements exhibit variations in temperature due to the existence of vertical temperature gradients and memory from previous conditions. It was not possible to accurately set initial temperatures of the components in the Abaqus software using 'Predefined Fields' to match this condition, therefore the average of the initial measured temperature magnitudes of 24°C was selected and applied as a uniform parameter to the full model of the machine as a 'Predefined Field'. The effect of this is to cause an error in the simulation where the model absorbs the ambient temperature to settle down or synchronize with the applied sink temperatures. The settling down time is termed as the settling zone. After this settling, the error in the FEA model diminishes enabling it to be used to simulate the machine behaviour. Figure 6-5 shows the plot of Y axis movement where both profiles were found similar but offset from each other.

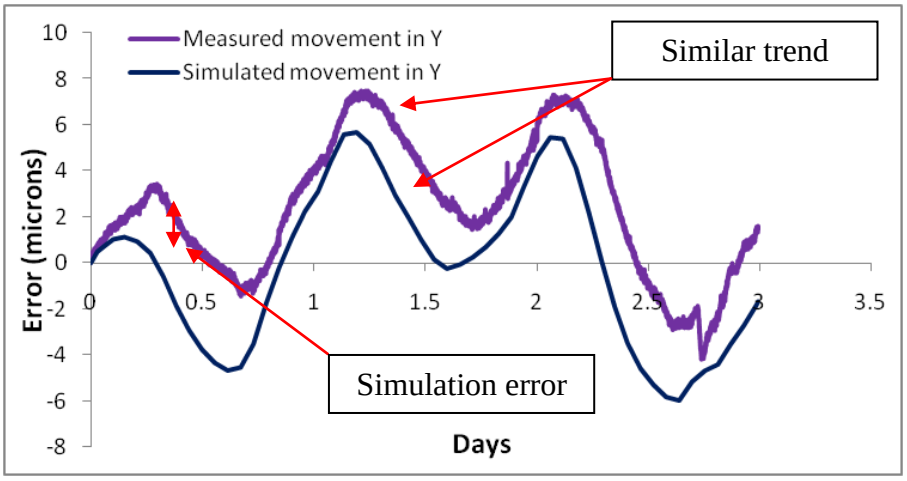

Figure 6-5: Axis offset is caused by the use of constant temperature values

6.2.2 Determination of the settling zone

To account for the problem of setting initial conditions in the simulation, a new technique of a two-step simulation was applied. The first step determines the time span to achieve a required thermal state of the machine model. This will enable the selection of the measured initial temperature data for the first step and to approximately replicate the model's thermal state with the measured thermal state after the end of the first step

simulation. This time span will represent the settling zone of the machine model. This is followed by the second step of normal environmental simulation with the remaining data i.e. excluding the relatively small data set used for the settling zone.

6.2.2.1 **Application of the technique**

The simulation was set up with an applied initial temperature of 24°C (Predefined Field). To estimate the time, the model was simulated for it to achieve a temperature change indicative of the variation between the global assumed 24°C and measured temperatures of the main structural components previously mentioned. A change of 1°C was selected and for which the simulation revealed the time span requirement of approximately twelve and half hours to achieve 25°C. This suggests that because the machine initial thermal state was unknown at the start of the simulation, the machine model requires twelve and half hours to absorb the applied sink temperatures to represent a realistic thermal state. Therefore this scientific estimation has enabled the selection of the settling zone of twelve and half hours for this machine model. It is anticipated that this approach will estimate the surface temperatures within an accepted ±0.2°C range.

This approach may not only achieve the initial thermal state of the machine but may also generate more realistic temperature gradients in all structures, therefore may be a convenient way of achieving an initial thermal state of the machine.

6.2.3 Use of real sink temperatures for the first step

The first step must provide not only the correct temperature profile but also the correct thermal memory to match the starting condition of the real machine, therefore measured data for the identified time period of twelve and half hours must be used. Data from the column ambient sensor, inside ambient sensor and the base ambient sensor was applied to the respective structures as transient sink temperatures in the first step. This was followed by the creation of the second step with the remaining measured environmental data i.e. excluding the first twelve and half hours of data, using the output from the first step as the initial conditions. Figure 6-6 shows the temperature gradients and profiles using the new method.

Initial surface temperature magnitudes were compared with the measured data and shown in Table 6-1 and revealed to be within ±0.2 °C range which confirms it to be a

reliable approach towards eliminating the ambiguity one might have with the uncertainty of setting up initial temperatures for simulations. The simulation for temperature and displacement analyses took approximately 30 and 40 minutes respectively (total 1 hour 10 minutes).

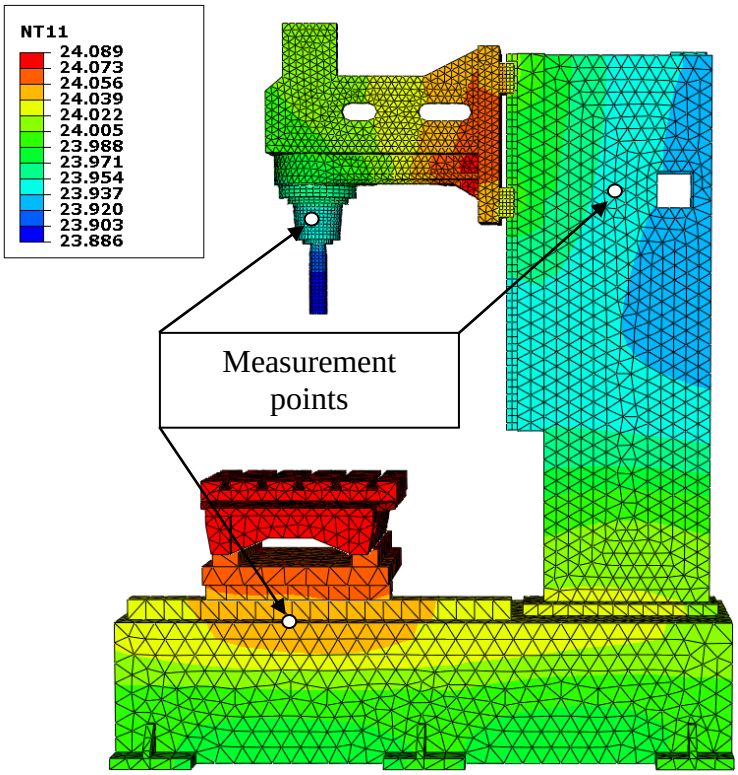

Figure 6-6: Thermal state of the machine after first step (summer test)

Structure	Measured temperature (°C)	Simulated temperature (°C)
Spindle Boss surface	24.125	23.96
Column surface	24.063	23.94
Base surface	23.938	24.03

Table 6-1: Comparison of measured and simulated surface temperatures after twelve hours (summer test)

6.2.4 Summer test correlations

The measured and simulated profile results were plotted for the main second step simulation. Compared to the measured results, the correlations were 60% for the Y movement profiles (Figure 6-7) and 63% for the Z movement profiles (Figure 6-8). The residual errors were less than 5µm for the Y axis and less than 11µm for the Z axis.

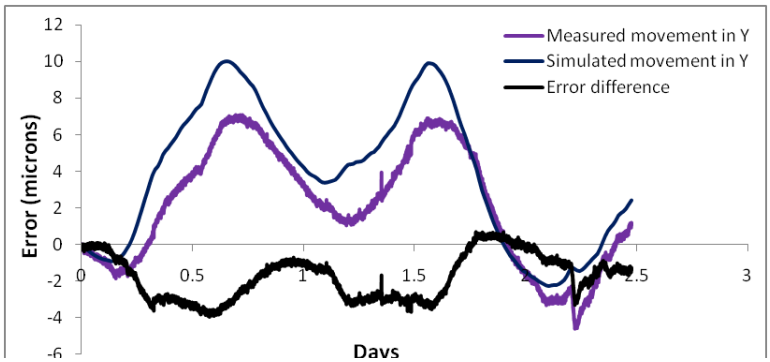

Figure 6-7: Correlation between the measured and simulated Y axis movement with settling zone removed

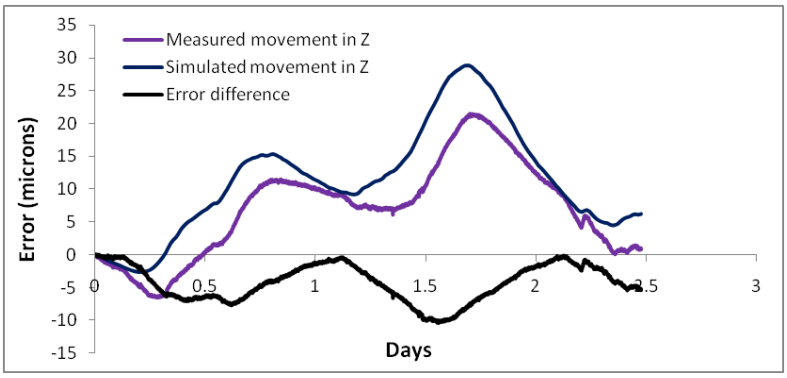

Figure 6-8: Correlation between the measured and simulated Z axis movement with settling zone removed

6.3 Long term environmental testing (winter)

This test was carried out to observe the machine behaviour in a winter season. The machine was monitored for 3 continuous days to highlight thermal behaviour during normal 24 hour periods experiencing single shift workshop heating patterns often encountered to maintain environmental temperature for the machine operators. The machine under test had winter environment control using heaters in the day time while turned off during the night. The machine orientation and setup was used in this test as used during the summer environment test.

The temperature information obtained from the ambient sensors and the spindle boss surface sensors are shown in Figure 6-9. An average vertical temperature gradient of 1°C can be observed between the base sensor and the column sensor. The spikes are suspected to be from the short periods for opening of workshop doors for deliveries which caused the shop floor environmental temperature to decrease.

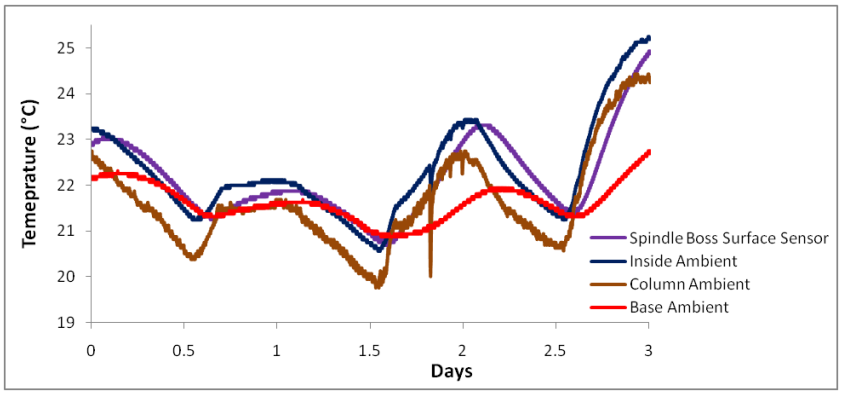

Figure 6-9: Temperature data obtained over 3 days period

Figure 6-10 and Figure 6-11 show the measured inside air temperature and deformation of the machine in Y axis and Z axis respectively. The movement of both axes followed the temperature variation while the Z axis displacement followed with a lag similar to the summer test. The overall movement is 18 µm in the Y axis and 35 µm in the Z axis for an overall temperature swing of approximately 5°C over the 3 days.

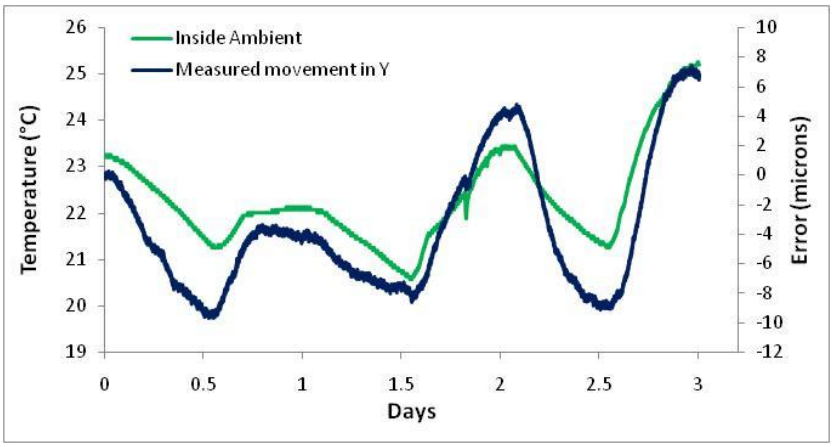

Figure 6-10: Measured movement in Y

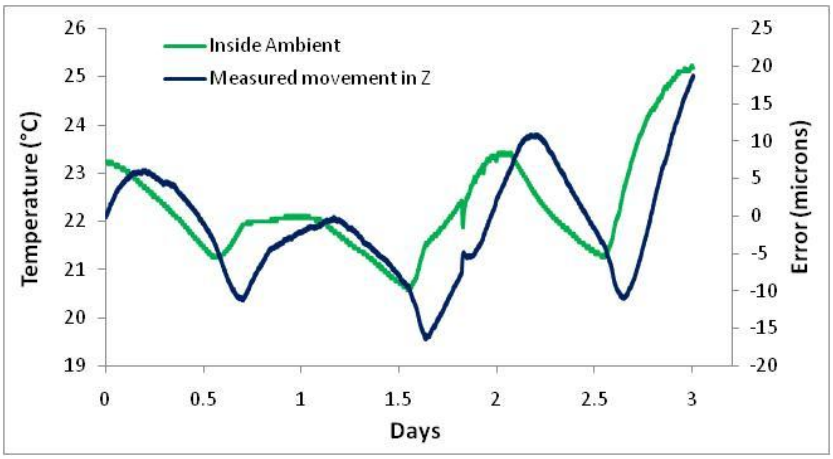

Figure 6-11: Measured movement in Z

As expected, the overall machine movement and temperature swing were higher than measured in summer due to the workshop heating in the day time and cold nights..

6.4 FEA simulations (winter test)

A similar procedure was followed for simulating the model using the average initial temperature for the entire model as predefined field and consideration of the settling zone.

6.4.1 Setup of initial conditions and time span selection

The average of the initial temperature magnitudes (22.5°C) was applied as a 'Predefined Field' prior to the creation of the two separate steps. For the first step, twelve and half hours of the measured data was used for the settling zone as before followed by the creation of the second step. Figure 6-12 shows the thermal state of the machine after the first step. Initial surface temperature magnitudes were compared and shown in Table 6-2 which again revealed to be within ±0.2°C range.

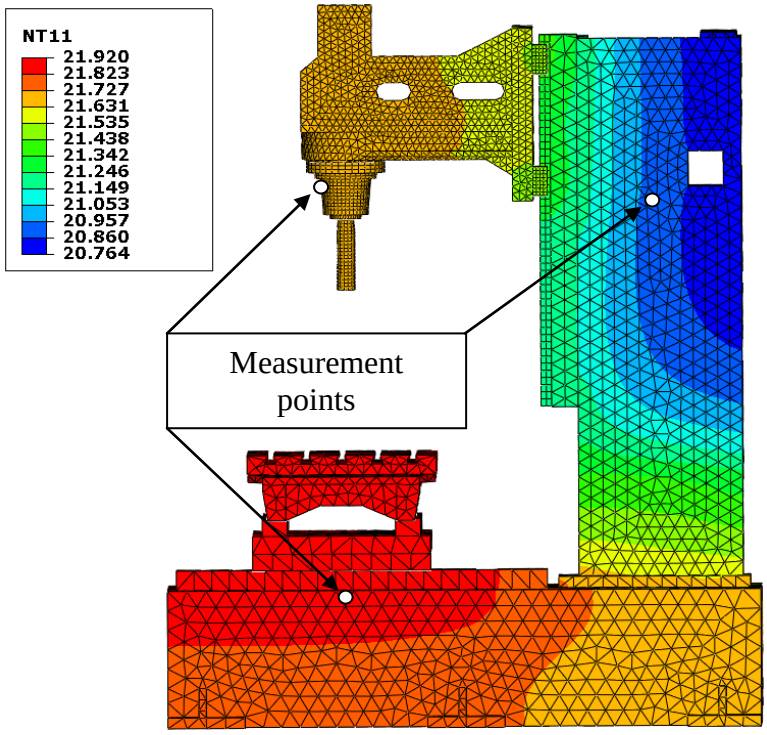

Figure 6-12: Thermal state of the machine after first step (winter test)

Structure	Measured temperature (°C)	Simulated temperature (°C)
Spindle Boss surface	21.688	21.65
Column surface	21	20.90
Base surface	21.938	21.90

Table 6-2: Comparison of measured and simulated initial surface temperatures (winter test)

6.4.2 Winter test correlations

The simulated results showed similar profile behaviour of the machine compared with the measured profile.. The results revealed very good correlations of 63% for the Y movement profiles (Figure 6-13) and 67% for the Z movement profiles (Figure 6-14). The residual errors were less than 7µm in Y and less than 12µm in Z.

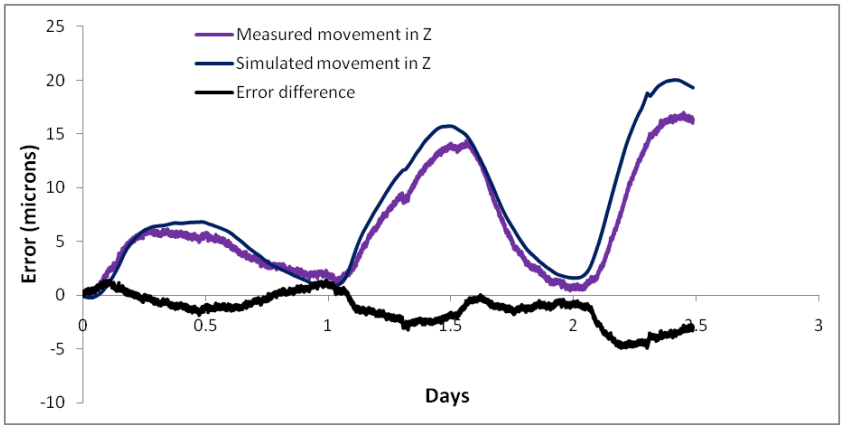

Figure 6-13: Correlation between the measured and simulated Y axis movement with settling zone removed

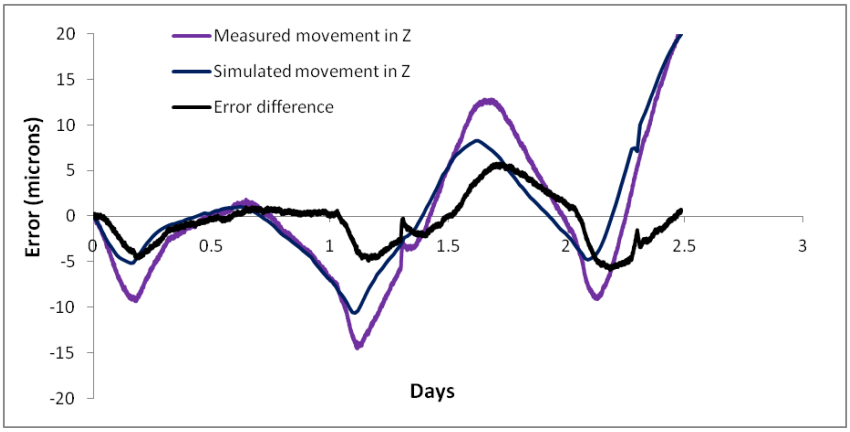

Figure 6-14: Correlation between the measured and simulated Z axis movement with settling zone removed

Both environmental experiments were found well correlated with the simulated FEA results which have validated the fact that environmental fluctuation causes thermal

distortions in machine structure which deteriorates the overall thermal accuracy of machine tools throughout the year. It was identified that vertical temperature gradients in a shop floor vary with height which can be critical to large or tall machines. A procedure is suggested to track vertical temperature gradients by measuring ambient temperatures at a vertical distance of at least 500mm apart so that detailed sink temperatures can be obtained and applied to individual components of the machine for an increased FEA modelling accuracy. Similarly due to vertical temperature gradients it was impossible to accurately apply initial temperatures to individual structural elements of the machine for FEA. To solve this problem, a new method of two-step simulation was developed in this chapter where the first step considers the settling zone for the machine model allowing it to achieve a thermal state and thermal memory. This is followed by the creation of second step to simulate the machine for the environmental behaviour potentially over long periods of time with a high degree of accuracy. This method has eliminated the ambiguity of applying initial temperatures to the individual machine structure for modelling.

6.5 Summary of the chapter

It has been observed that the accuracy of a machine tool can be adversely affected by environmental temperature variations. Experimental and simulated movements between the tool and workpiece during summer and winter environmental tests, each lasting 3 days, have correlated well.

Temperature data obtained from the ambient temperature sensors was applied to the FEA simulations as time variable sink temperatures. Initial temperatures of the machine structure in the simulation do not match the initial conditions of the actual machine due to vertical temperature gradients and long term thermal memory. This creates an error in the simulation that can be removed by creating an initial simulation step that allows the determination of settling zone for the machine model.

In this research the machine was tested while static in order to get displacement data for validation, however temperature measurement can be implemented easily on a production machine tool by placing additional ambient temperature sensors to record during machining operations; which means no machine downtime is required during the measurements, and the data obtained from the machine vicinity and that particular shop

floor could be added to thermal compensation models. This will increase the accuracy of the machine tool by eliminating the deformation uncertainty that varying environments impose on the machine structure during long term machining operations.

CHAPTER - 7

7 FEA NODAL MANIPULATIONS

Previous chapters have presented simulated machine tool behaviour, when subjected to internal and environmental heat sources that correlate well with experimental results. This method therefore provides a platform to use FEA modelling as an offline tool to determine not only machine behaviour, but also help with the development of compensation models. In this chapter it is used for determining the location of nodes whose displacements are sensitive to a temperature change. This is the most common form of modelling method available in modern controllers. Typically they are limited to spindle growth compensation using a linear relationship between a motor or bearing sensor and expansion. Other modelling methods are discussed in Chapter 2.

This chapter details a method and software for the offline assessment of the FEA data and help determine the temperature-displacement sensitive nodes based on search parameters and their physical locations within the FEA model. These will contribute for the development and enhancement of new and existing thermal error compensation methods respectively by updating them with the location information. The information can be used to retrofit sensors for compensation; however there can be practical limitations to their attachment. It will also help at the machine design and build stages by advising where to install temperature sensors within the machine structure.

7.1 Nodal data extraction

The Abaqus simulation software provides the facility to extract surface and sub-surface nodal data within the FEA model. The extracted nodal data can then be used to find nodes of interest. In this case the dependant parameters are slope and hysteresis.

The slope is simply the magnitude of displacement for any given change in temperature (°C/µm). Hysteresis is caused by the time lag involved with typical surface temperature measurement which is proportional to the distance between the temperature sensor and the true effective temperature which is causing the distortion. A node location with high slope sensitivity and with the lowest hysteresis will represent that area that

relates well to thermal displacement but also responds quickly whether the machine is being heated or cooled.

Nodal data is extracted in two phases, first the temperature is extracted for all nodes and secondly the displacement data from the test mandrel nodes. Abaqus saves nodal information as a report file with file extension of '.rpt'. These files are converted and imported into Matlab software. Matlab functions were written to calculate the slope and hysteresis for each node and feed back the good ones with respect to an axis.

7.2 Internal heating test - Carrier sensitivity against the Y axis displacement

Nodal data extraction was applied to the simulation of spindle carrier to locate nodes that are sensitive to Y axis movement during internal heating. Temperature data for all the spindle carrier nodes were used from the 8000rpm simulation as shown in Figure 7-1. This shows the spindle carrier with all nodes selected and the Abaqus dialog box indicating the nodes selected.

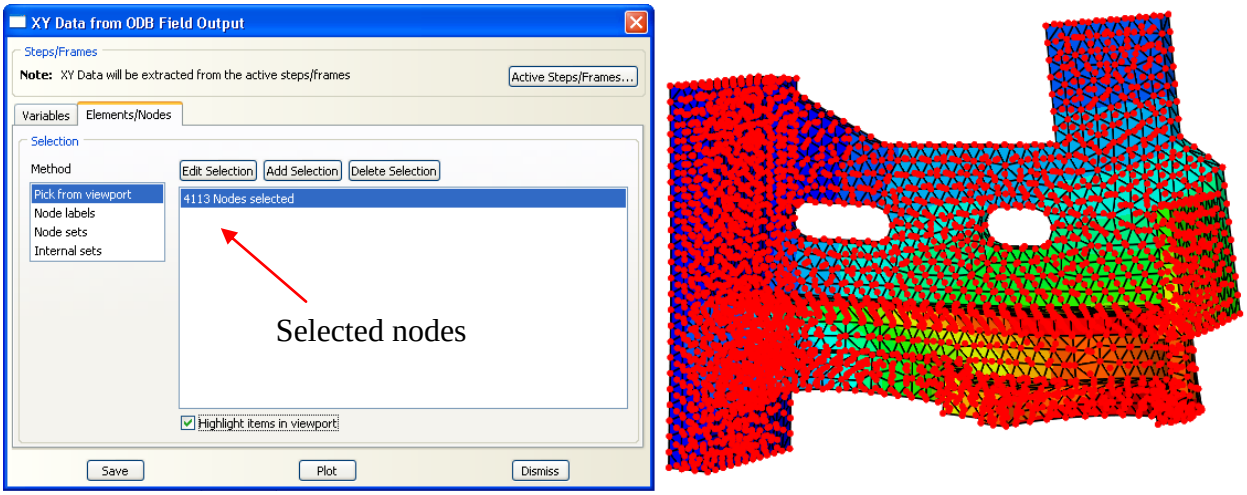

Figure 7-1: Temperature data extraction for spindle carrier

7.2.1 Matlab program routines

Two Matlab functions were written (Appendix D) to manipulate the nodal data for the sensitivity analyses. The first imports the nodal data and calculates the slope and hysteresis for the selected nodes. Figure 7-3 shows an example of the plot of slope and hysteresis for two randomly selected nodes (1499 and 2508) shown in Figure 7-2.

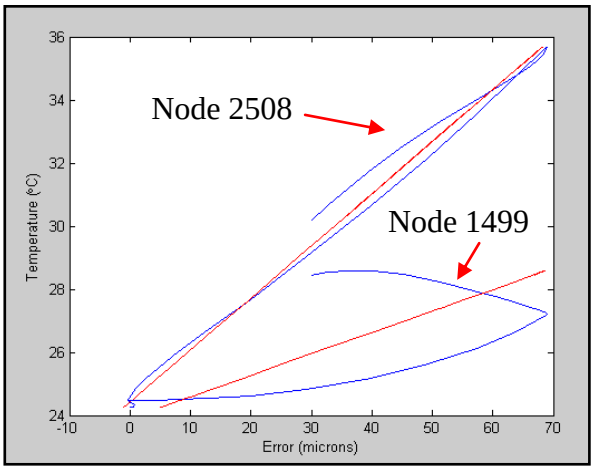

Figure 7-2: Slope and hysteresis plot for two random nodes

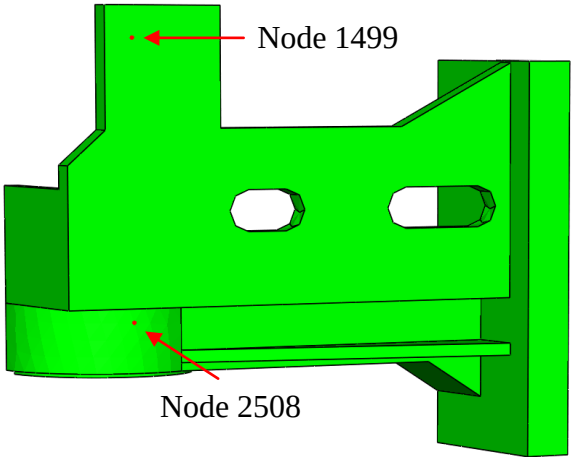

Figure 7-3: Node locations on the carrier

A linear hysteresis curve corresponds to a sensitive response of the structure to a temperature change and the variation in relationship between heating and cooling conditions. The above figures show the time taken by each structural node in response to temperature change. Node 2508 shows a linear hysteresis indicating a high sensitivity to a temperature change however node 1499 has a response lag which results in a non-linear curve which demonstrates that the structure where that node is located possesses high thermal memory characteristics and therefore the displacement response is slower to a temperature change compared with the node 2508. This explains that a node location with a faster thermal response will have a quicker impact on the workpiece error than a node with a slower response. Therefore nodes with faster response are targeted for the development of simple linear compensation models to compensate for the error arising from that area with an approach of, the better the node the better will be the compensation. This Matlab program therefore enables an understanding of the thermal behaviour of individual nodes.

The second Matlab function imports the nodal data and calculates the slope (°C/µm) using a least square fit and hysteresis (µm), using deviation from the straight line, for all nodes. These are compared against a predefined set of ranges to filter out acceptable structural nodes. The range may be set based on the resolution of the temperature sensors and required accuracy for compensation. If no nodes are found then the range must be widened. For example, the program first searches the node with the highest slope sensitivity within the slope sensitivity array and similarly searches for the node with the

minimum hysteresis value within the hysteresis sensitivity array. These values are used to set the maximum limit for the slope range and minimum limit for the hysteresis range and then each parameter range is widen to filters out sensitive node numbers. The code then compares both filtered node number arrays to further match nodes numbers to finally obtain node numbers that are within the given ranges of the slope sensitivity and hysteresis. This two stage method was used to maintain flexibility so that different nodes can be used for different jobs, not always both. The final filtered node numbers are then used to locate their positions in the FEA simulation of the carrier. Figure 7-4 shows the function calls where comparison takes place using a specified range, in this case the range for the slope sensitivity is from 0.17 to 0.2046 (max) and 5.446 (min) to 8 for the hysteresis. The first and second lines filter out node numbers for the slope sensitivity and hysteresis respectively using the range. The third line is then used to match node numbers in both arrays (chkSlope and chkHyst) and obtain the matched nodes numbers. Figure 7-5 shows the Matlab array editor displaying 8 nodes filtered out from the total of 4113. The first column shows node number, the second column shows slope sensitivities and the third column shows the hysteresis values. These 8 nodes have shown to have the highest slope sensitivities (Figure 7-6) and the lowest hysteresis values and will effectively be used to place permanent temperature sensors for use in the error compensation system. It can also be observed that nodes 738 and 739 posses the highest slope sensitivity among the other filtered nodes and a slightly high hysteresis values relative to other filtered nodes, however an agreement was obtained to prioritize the selection of nodes that were located at the surface for practical installation of temperature sensors. This priority may not be the case if slope sensitivities and hysteresis values are significant at node positions inside the structure.

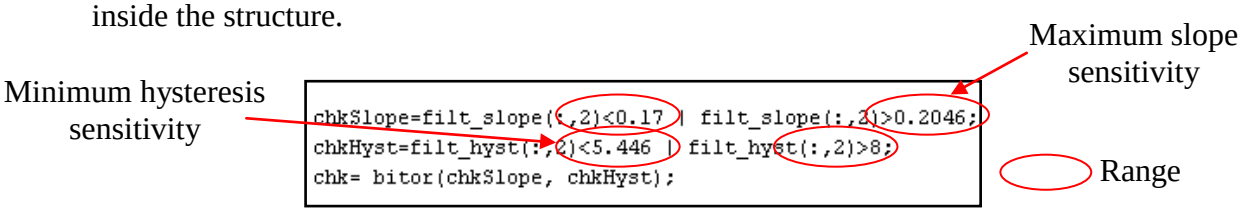

Figure 7-4: Part of Matlab program code for assigning range (8000rpm-Y axis)

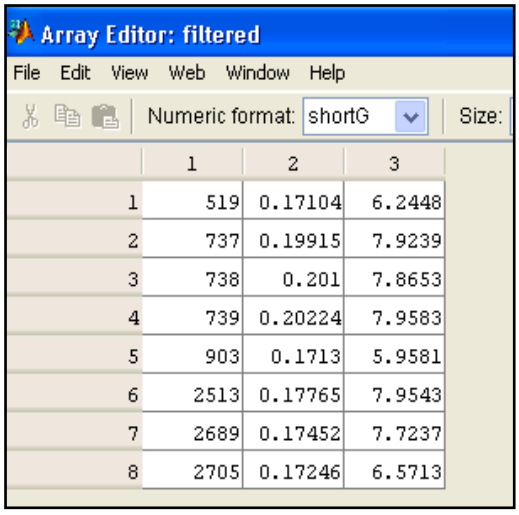

	1	2	3
1	519	0.17104	6.2448
2	737	0.19915	7.9239
3	738	0.201	7.8653
4	739	0.20224	7.9583
5	903	0.1713	5.9581
6	2513	0.17765	7.9543
7	2689	0.17452	7.7237
8	2705	0.17246	6.5713

Figure 7-5: Filtered nodes (8000rpm-Y axis)

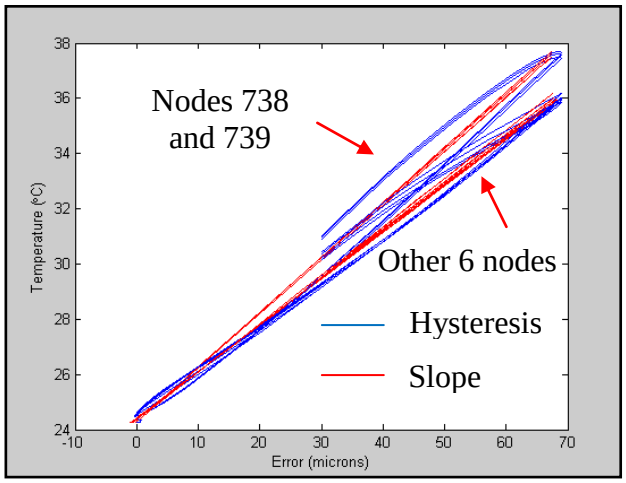

Figure 7-6: Slope and hysteresis plot (8000rpm-Y axis)

Figure 7-7 shows the location of the eight filtered nodes on the carrier model. It can be observed that out of eight nodes, two were found on the outer surface of the carrier, three were located within the solid structure and the other three located at the spindle carrier interface, therefore the outer surface nodes would be the most convenient to use. Using the Abaqus GUI, the outer surface node numbers were found to be 519 and 2513. The nodes 737, 738 and 739 were found at the carrier/spindle interface and the others were found inside the structure. An alternative selection criterion is simply to provide the 'n' best.

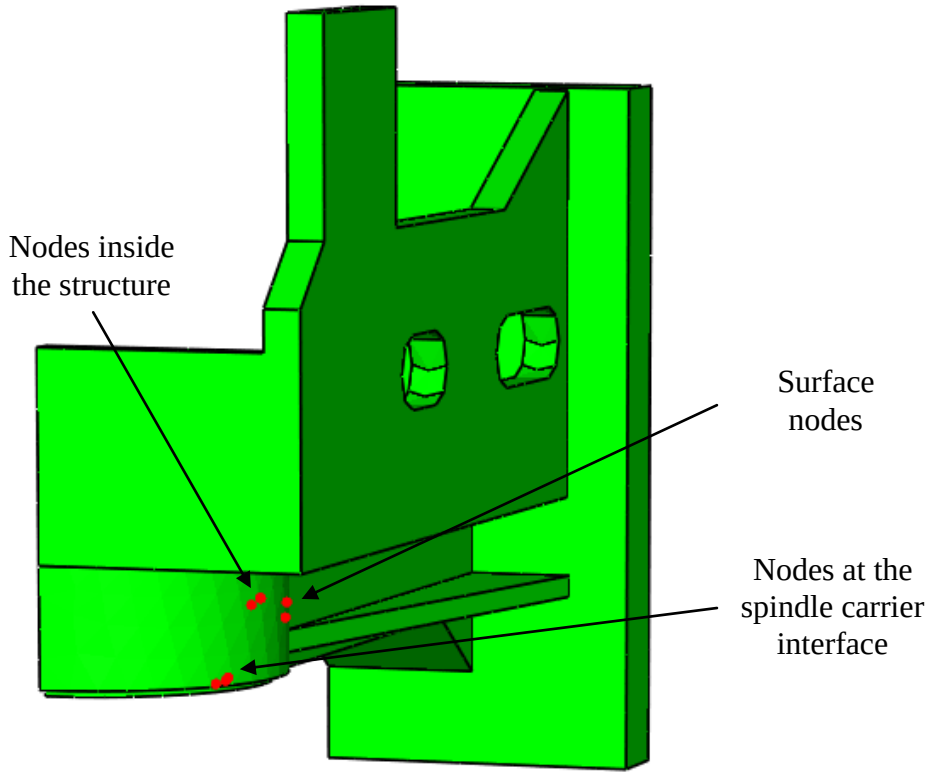

Figure 7-7: Y axis carrier node location - 8000rpm

7.3 Internal heating test- Carrier sensitivity against the Z axis displacement

A similar procedure was used to locate nodes sensitive to the Z movement. Both Matlab program routines were used to observe the behaviour of nodes and determine nodal slopes and hysteresis. Using the given range (Figure 7-8), the second Matlab program filtered 7 nodes sensitive to the Z movement of the machine and are shown in Figure 7-9 with slope and hysteresis curves (Figure 7-10), again the priority was given to locate the surface nodes.

```
chkSlope=filt_slope(:,2)<-0.5116 | filt_slope(:,2)>-0.493;
chkHyst=filt_hyst(:,2)<7.0573 | filt_hyst(:,2)>9.9;
chk= bitor(chkSlope, chkHyst);
```

Range

Figure 7-8: Part of Matlab program code for assigning range (8000rpm-Z axis)

Array Editor: filtered

File Edit View Web Window Help

Numeric format: shortG Size: 7

	1	2	3
1	736	-0.49305	9.8342
2	737	-0.49773	9.7452
3	738	-0.50236	9.7305
4	739	-0.50548	9.7678
5	740	-0.50716	9.8479
6	741	-0.51007	9.8552
7	2535	-0.49349	9.8836

Figure 7-9: Filtered nodes (8000rpm-Z axis)

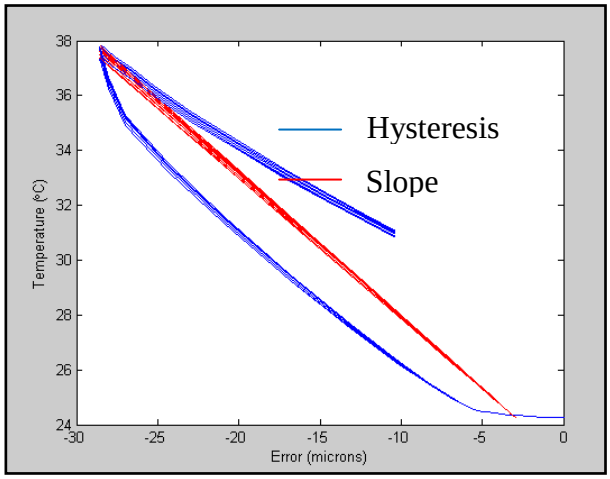

Figure 7-10: Slope and hysteresis plot (8000rpm-Z axis)

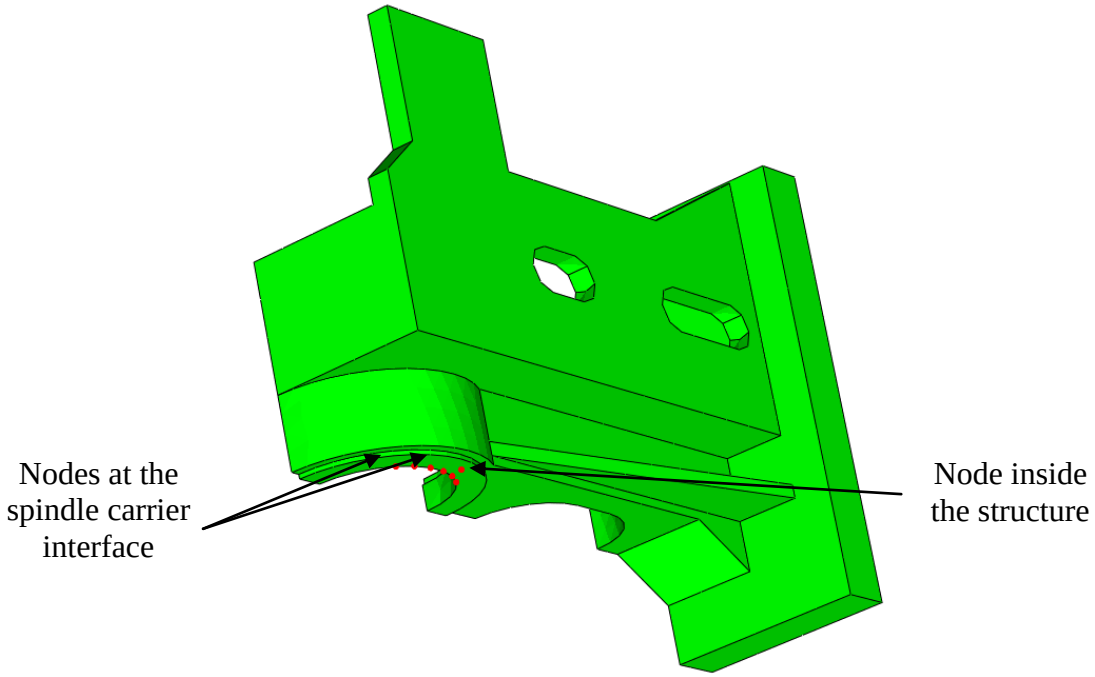

Figure 7-11: Z axis carrier node location - 8000rpm

Figure 7-11 shows the location of the 8 filtered nodes on the carrier. Within the given range, no surface node were obtained, however it can be noticed that nodes 737, 738 and 739 were found common for both Y and Z axes. These nodes may therefore be given higher priority for sensor installation because one temperature sensor can be used for compensation of both Y axis and Z axis errors. If considered at the design and build stage, this would be practical, otherwise a compromise may be needed for retrofit onto an existing spindle.

7.4 Environmental test –Sensitivity against the Y axis displacement

In this case, the simulated environmental data was used to locate sensitive node positions. Main structural elements of the machine i.e. carrier head, column, base and table were analysed for their temperature sensitivity against Y axis movement of the test mandrel. Similar procedure was followed to extract temperature information from structures and displacement data from the test mandrel.

7.4.1 Carrier head

The carrier head nodes were analysed for their temperature sensitivity against Y axis movement of the test mandrel. Figure 7-12 shows the specified range to filter nodes sensitive to the Y movement of the machine due to environmental temperature fluctuations. Figure 7-13 shows the six filtered nodes and Figure 7-14 shows the plot of the slopes and hysteresis obtained from them.

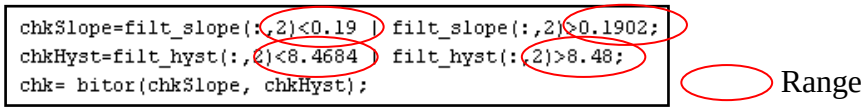

Figure 7-12: Matlab function calls for assigning filter range (Env-Y axis carrier head)

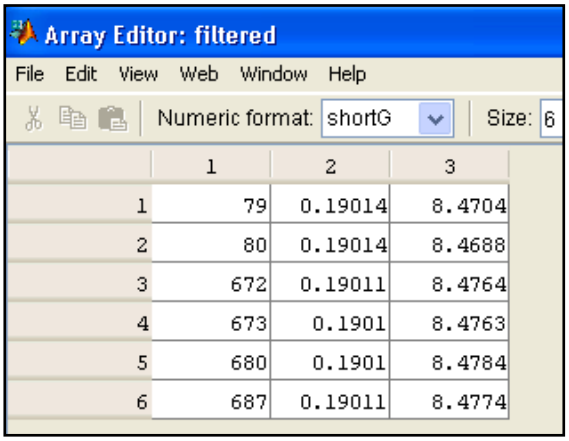

	1	2	3
1	79	0.19014	8.4704
2	80	0.19014	8.4688
3	672	0.19011	8.4764
4	673	0.1901	8.4763
5	680	0.1901	8.4784
6	687	0.19011	8.4774

Figure 7-13: Filtered nodes (Env-Y axis carrier head)

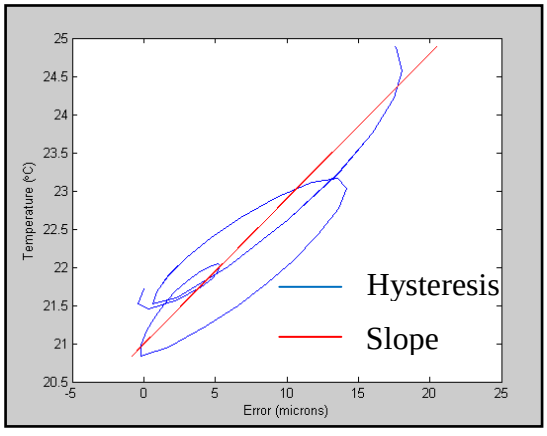

Figure 7-14: Slope and hysteresis plot (Env-Y axis carrier head)

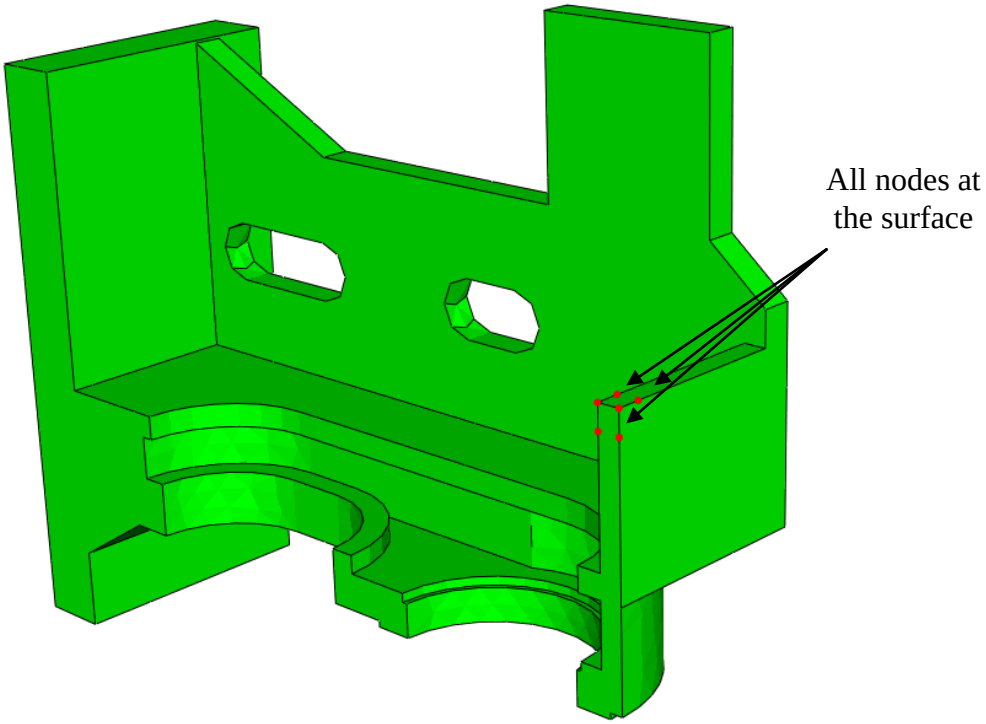

Figure 7-15: Y axis carrier node location - Environment

Figure 7-15 shows the location of the six filtered nodes on the carrier; all sensitive nodes were found on the surface of the carrier elaborating the most affected sensitive structural area within the carrier.

7.4.2 Column

The column nodes were analysed for their temperature sensitivity against Y axis movement of the test mandrel. Figure 7-16 shows the specified range to filter nodes sensitive to the Y movement of the machine due to environmental temperature fluctuations. Figure 7-17 shows the seven filtered nodes and Figure 7-18 shows the plot of the slopes and hysteresis obtained from them. Figure 7-19 shows the location of the seven filtered nodes on the column.

```
chkSlope=filt_slope(:,2)<0.1915 | filt_slope(:,2)>0.19228;
chkHyst=filt_hyst(:,2)<6.2405 | filt_hyst(:,2)>6.25;
chk= bitor(chkSlope, chkHyst);
```

Range

Figure 7-16: Matlab function calls for assigning filter range (Env-Y axis column)

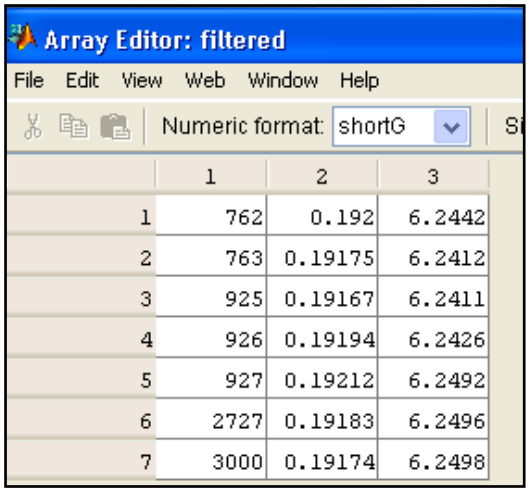

	1	2	3
1	762	0.192	6.2442
2	763	0.19175	6.2412
3	925	0.19167	6.2411
4	926	0.19194	6.2426
5	927	0.19212	6.2492
6	2727	0.19183	6.2496
7	3000	0.19174	6.2498

Figure 7-17: Filtered nodes (Env-Y axis column)

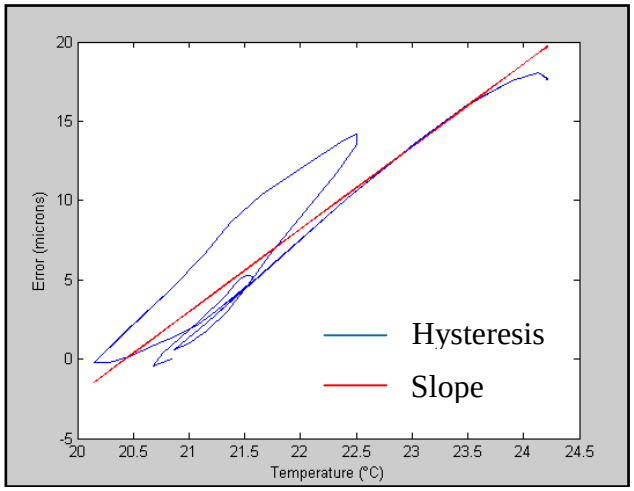

Figure 7-18: Slope and hysteresis plot (Env-Y axis column)

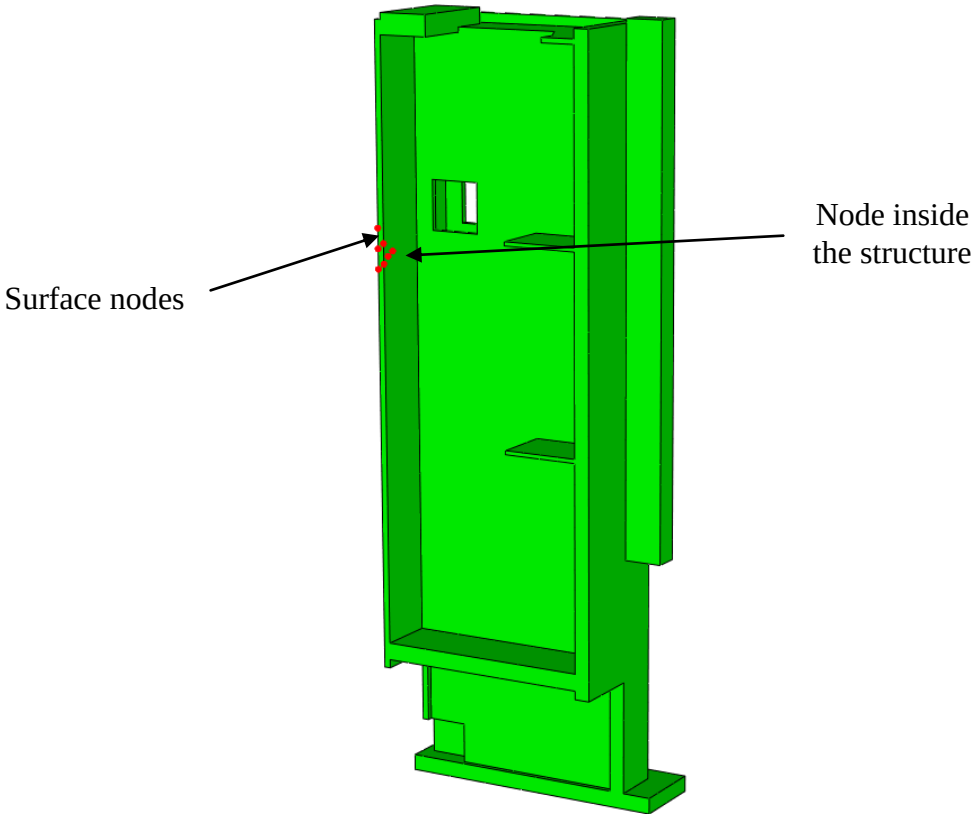

Figure 7-19: Y axis column node location - Environment

7.4.3 Base

The base nodes were analysed for their temperature sensitivity against Y axis movement of the test mandrel. Figure 7-16 shows the specified range to filter nodes sensitive to the Y movement of the machine due to environmental temperature fluctuations. Figure 7-21 shows the nine filtered nodes and Figure 7-22 shows the plot of

the slopes and hysteresis obtained from them. Although the nodes were found with the minimum hysteresis however the plot showed that the hysteresis was still large and have shown a non-linear relationship with the temperature change. Therefore these nodes may not be considered for temperature sensors however the software (Abaqus) has given the possibility to obtain the knowledge of the location of these nodes. Figure 7-23 shows the location of the nine filtered nodes on the base.

```
chkSlope=filt_slope(:,2)<0.1542 | filt_slope(:,2)>0.1546;
chkHyst=filt_hyst(:,2)<14.644 | filt_hyst(:,2)>17.2;
chk= bitor(chkSlope, chkHyst);
```

Range

Figure 7-20: Matlab function calls for assigning filter range (Env-Y axis base)

Array Editor: filtered

File Edit View Web Window Help

Numeric format: shortG

	1	2	3
1	440	0.15429	17.152
2	441	0.15428	17.152
3	485	0.15428	17.153
4	486	0.15424	17.151
5	1171	0.15447	17.151
6	1286	0.15444	17.151
7	2705	0.15439	17.152
8	2707	0.15429	17.151
9	2929	0.15435	17.152

Figure 7-21: Filtered nodes (Env-Y axis base)

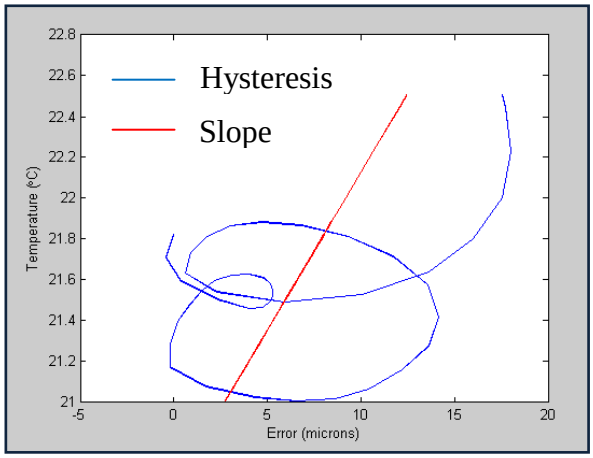

Figure 7-22: Slope and hysteresis plot (Env-Y axis base)

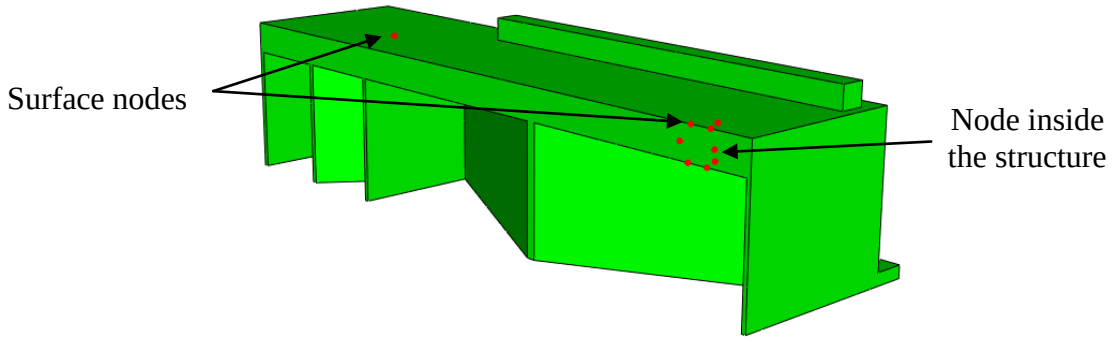

Figure 7-23: Y axis base node location - Environment

7.4.4 Table

The table nodes were analysed for their temperature sensitivity against Y axis movement of the test mandrel. Figure 7-16 shows the specified range to filter nodes sensitive to the Y movement of the machine due to environmental temperature fluctuations. Figure 7-25 shows the five filtered nodes and Figure 7-26 shows the plot of the slopes and hysteresis obtained from them. Figure 7-27 shows the location of the five filtered nodes on the table.

```
chkSlope=filt_slope(:,2)<0.1288 | filt_slope(:,2)>0.12899;
chkHyst=filt_hyst(:,2)<11.795 | filt_hyst(:,2)>12;
chk= bitor(chkSlope, chkHyst);
```

Range

Figure 7-7-24: Matlab function calls for assigning filter range (Env-Y axis table)

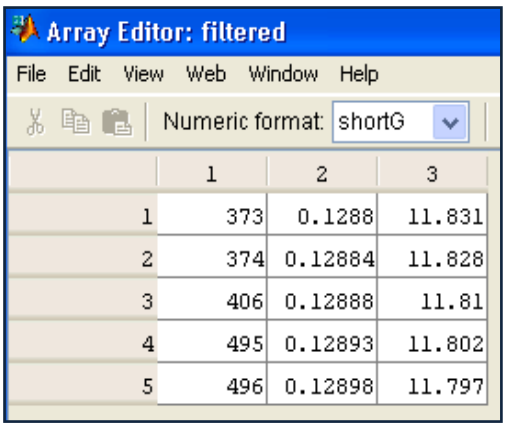

	1	2	3
1	373	0.1288	11.831
2	374	0.12884	11.828
3	406	0.12888	11.81
4	495	0.12893	11.802
5	496	0.12898	11.797

Figure 7-25: Filtered nodes (Env-Y axis table)

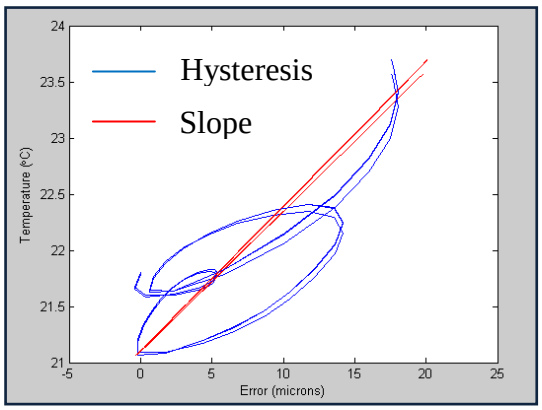

Figure 7-26: Slope and hysteresis plot (Env-Y axis table)

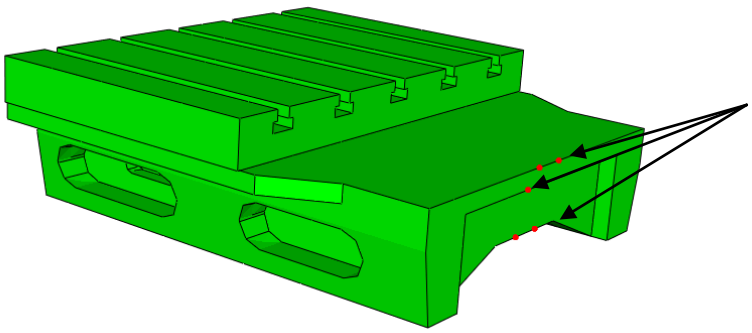

All surface nodes

Figure 7-27: Y axis table node location - Environment

7.5 Environmental test –Sensitivity against the Z axis displacement

The main structural elements of the machine were also analysed for their temperature sensitivity against Z axis movement of the test mandrel.

7.5.1 Carrier head

A similar procedure was followed to locate nodes on the carrier head sensitive to the Z movement due to environmental fluctuations. Eight nodes sensitive to the Z movement of the machine were filtered using the given range shown in Figure 7-28 and are shown in Figure 7-29 with slope and hysteresis plots (Figure 7-30).

```
chkSlope=filt_slope(:,2)<0.1481 | filt_slope(:,2)>0.16066;
chkHyst=filt_hyst(:,2)<3.917 | filt_hyst(:,2)>3.98;
chk= bitor(chkSlope, chkHyst);
```

Range

Figure 7-28: Part of Matlab program code for assigning range (Env-Z axis carrier head)

Array Editor: filtered

File Edit View Web Window Help

Numeric format: shortG Size: 8

	1	2	3
1	2381	0.14811	3.9774
2	2607	0.14814	3.9793
3	2925	0.14814	3.9792
4	2926	0.14811	3.9765
5	2927	0.14815	3.9784
6	2975	0.14811	3.9754
7	3394	0.14812	3.9778
8	3395	0.14815	3.9797

Figure 7-29: Filtered nodes (Env-Z axis carrier head)

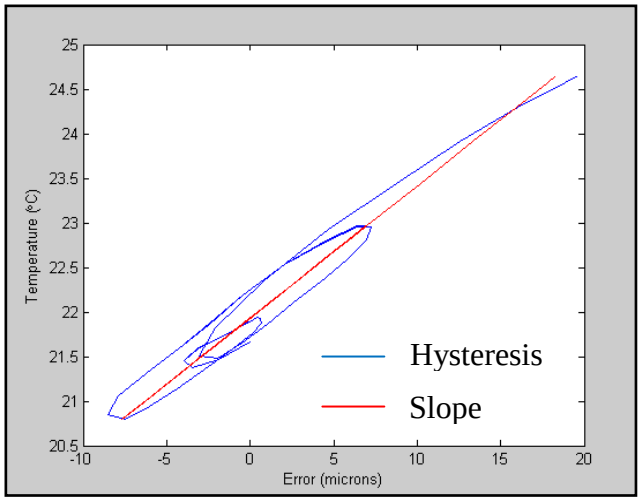

Figure 7-30: Slope and hysteresis plot (Env-Z axis carrier head)

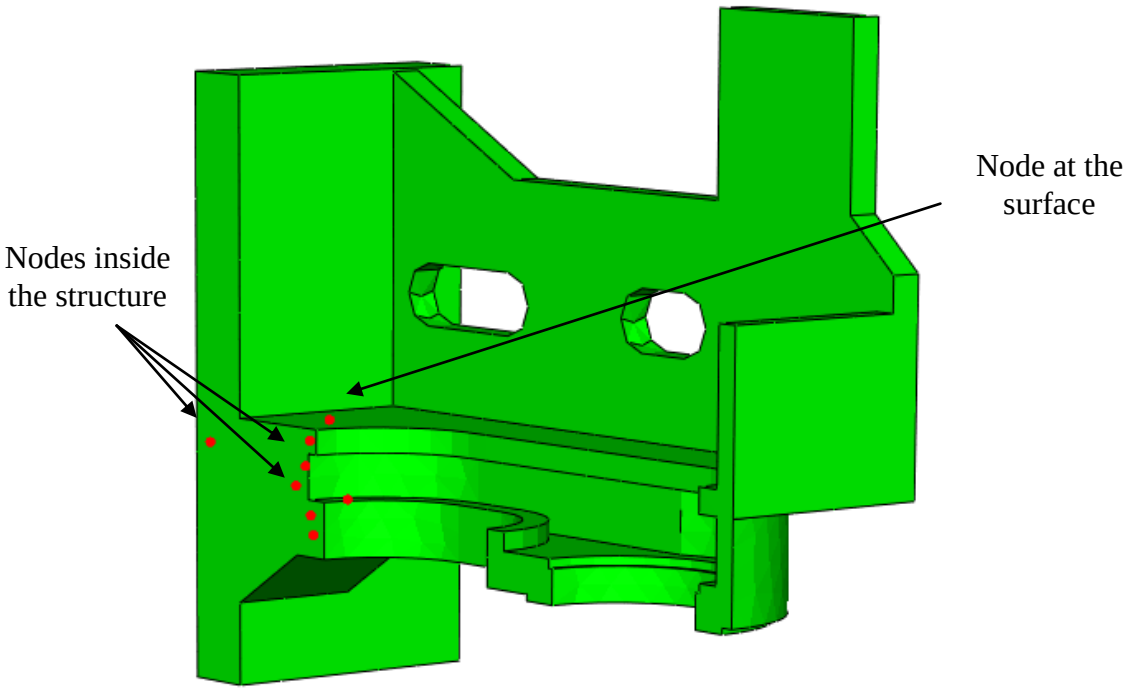

Figure 7-31: Z axis carrier head node location - Environment

Figure 7-31 shows the location of the eight filtered nodes on the carrier. Only one node (2381) was found on the surface of the carrier and its location may be used for temperature sensor installation.

7.5.2 Column

The column nodes were analysed for their temperature sensitivity against Z axis movement of the test mandrel. Figure 7-32 shows the specified range to filter nodes sensitive to the Z movement of the machine due to environmental temperature fluctuations. Figure 7-33 shows the six filtered nodes and Figure 7-34 shows the plot of the slopes and hysteresis obtained from them. Figure 7-35 shows the location of the six filtered nodes on the column.

```
chkSlope=filt_slope(:,2)<0.163 | filt_slope(:,2)>0.17747;
chkHyst=filt_hyst(:,2)<4.2642 | filt_hyst(:,2)>6.97;
chk= bitor(chkSlope, chkHyst);
```

Range

Figure 7-32: Part of Matlab program code for assigning range (Env-Z axis column)

Array Editor: filtered

File Edit View Web Window Help

Numeric format: shortG

	1	2	3
1	450	0.16354	6.963
2	451	0.16357	6.9681
3	1019	0.16316	6.8866
4	1884	0.16345	6.9323
5	2096	0.16363	6.968
6	2857	0.16368	6.9699

Figure 7-33: Filtered nodes (Env-Z axis column)

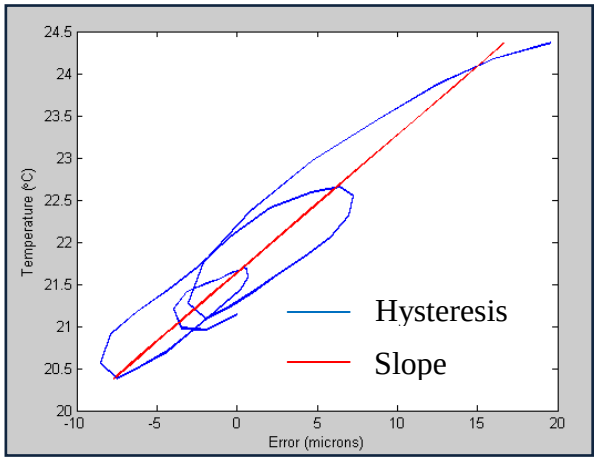

Figure 7-34: Slope and hysteresis plot (Env-Z axis column)

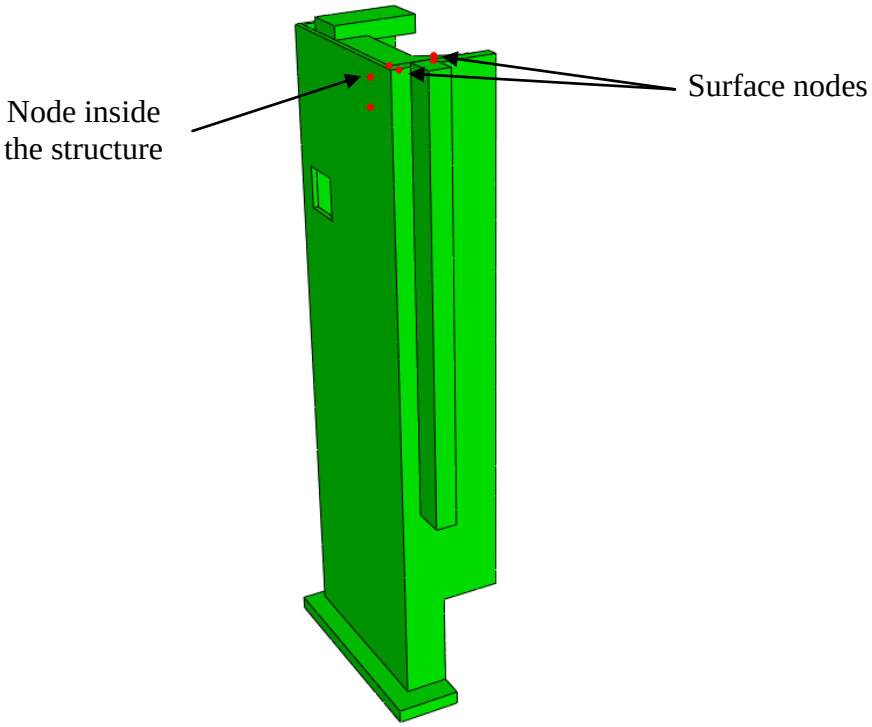

Figure 7-35: Z axis column node location - Environment

7.5.3 Base

The base nodes were analysed for their temperature sensitivity against Z axis movement of the test mandrel. Figure 7-7-36 shows the specified range to filter nodes sensitive to the Z movement of the machine due to environmental temperature fluctuations. Figure 7-37 shows the six filtered nodes and Figure 7-38 shows the plot of the slopes and hysteresis obtained from them. Figure 7-39 shows the location of the six filtered nodes on the base.

```
chkSlope=filt_slope(:,2)<0.0715 | filt_slope(:,2)>0.07228;
chkHyst=filt_hyst(:,2)<4.5046 | filt_hyst(:,2)>4.6;
chk= bitor(chkSlope, chkHyst);
```

Range

Figure 7-7-36: Part of Matlab program code for assigning range (Env-Z axis base)

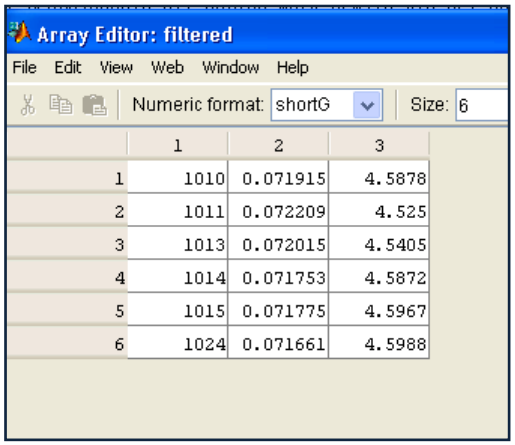

	1	2	3
1	1010	0.071915	4.5878
2	1011	0.072209	4.525
3	1013	0.072015	4.5405
4	1014	0.071753	4.5872
5	1015	0.071775	4.5967
6	1024	0.071661	4.5988

Figure 7-37: Filtered nodes (Env-Z axis base)

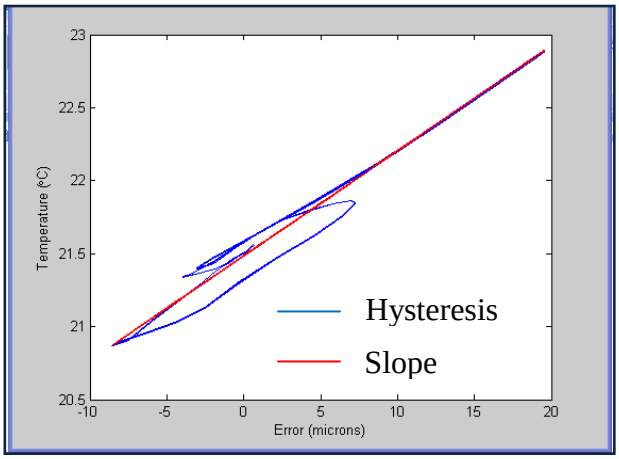

Figure 7-38: Slope and hysteresis plot (Env-Z axis base)

All nodes at the surface

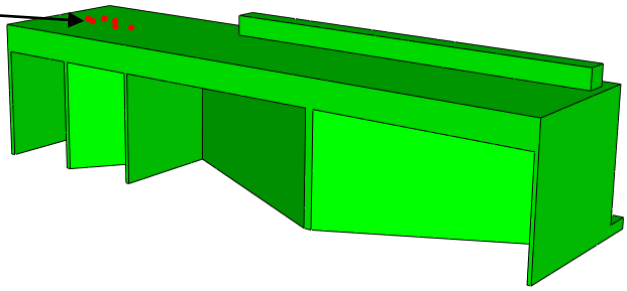

Figure 7-39: Z axis base node location - Environment

7.5.4 Table

The table nodes were analysed for their temperature sensitivity against Z axis movement of the test mandrel. Figure 7-40 shows the specified range to filter nodes sensitive to the Z movement of the machine due to environmental temperature fluctuations. Figure 7-41 shows the six filtered nodes and Figure 7-42 shows the plot of the slopes and hysteresis obtained from them. Figure 7-43 shows the location of the six filtered nodes on the table.

```
chkSlope=filt_slope(:,2)<0.091 | filt_slope(:,2)>0.096713;
chkHyst=filt_hyst(:,2)<3.0871 | filt_hyst(:,2)>3.47;
chk= bitor(chkSlope, chkHyst);
```

Range

Figure 7-40: Part of Matlab program code for assigning range (Env-Z axis table

Array Editor: filtered

File Edit View Web Window Help

Numeric format: shortG Size

	1	2	3
1	159	0.091223	3.4695
2	160	0.091077	3.4476
3	250	0.091222	3.452
4	252	0.09131	3.4656
5	959	0.091026	3.4241
6	967	0.09109	3.4359

)

Figure 7-41: Filtered nodes (Env-Z axis table)

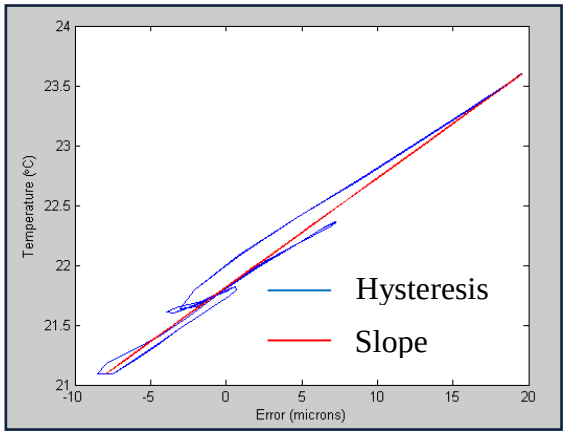

Figure 7-42: Slope and hysteresis plot (Env-Z axis table)

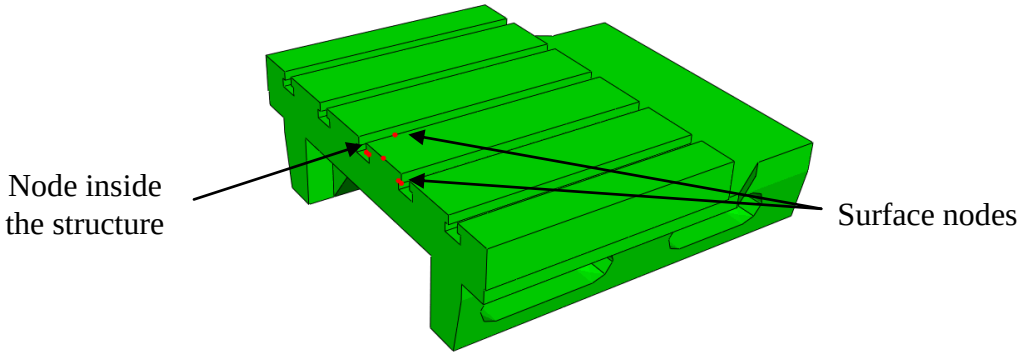

Figure 7-43: Z axis table node location - Environment

7.6 Summary of the chapter

It has been observed that the FEA simulation builds up a solid platform for offline assessment of the machine behaviour. The correlations of the simulated results with the online measurements (both internal heating and environmental temperature fluctuations) are greater than 60%, and in most cases greater than 70%.

This chapter has looked into exploiting the detailed data obtainable from the FEA simulation by locating nodes whose change in temperature relates to the error at the tool. The nodes are obtained using the criteria of lowest hysteresis value i.e. linear with the same profile whether heating or cooling with the lowest thermal memory and with the highest slope i.e. temperature change to error (°C/µm).

FEA results from both internal heating and environmental temperature fluctuation simulations were used to locate nodes in the carrier head and in main structural elements respectively that were sensitive to the movement of machine structure in Y and Z axes. The simulation temperature data from all nodes and displacement data for both Y and Z axes from the test mandrel were extracted. Two Matlab functions were written to manipulate the data; the first function plots the hysteresis and slope for any given node and the second node filters out sensitive node locations by using a range of highest slope sensitivity and lowest hysteresis value. The location of the filtered nodes were analysed using the Abaqus GUI. The priority is given to surface nodes rather than the internal nodes for the real practicality of temperature sensor installation on the machine. By determining the best linear relationships, simple models are available and compatible with the common thermal compensation methods available in most modern NC controllers.

CHAPTER - 8

8 Conclusions and suggestions for future work

This research into FE based simulation of thermal errors on CNC machine tools has provided a novel and efficient strategy for practical implementation and comprehensive validation. This contributes signifcantly towards assuring the future of efficient thermal model development to facilitate widespread industrial application of thermal compensation.

Industry strives to produce high volumes of components with high precision and CNC machine tools are most commonly chosen due to their ability to automate production with reliability, stability and repeatability. The volumetric accuracy of these machines depends primarily on the magnitude of the geometric, non-rigid and thermal errors. Machine thermal instability is dependent on a variety of internal and external heat sources and their overall affect results in machine structural deformation that often occurs in a complex manner due to the non-linear behaviour and interaction of the machine structural elements.

Pre-calibrated compensation has gained popularity among machine tool builders and users as a cost effective method for reducing the affect of geometric errors and modern NC systems have this facility as standard. The existing thermal compensation is usually limited to simple linear relationships to compensate, for example, spindle growth based on a motor or bearing sensor. Both of these standard compensation methods, despite their established nature are rarely fully utilised because of the effort or inconvenience, particularly machine down time, required to obtain the pre-calibrated data. The cost of reducing thermal errors or their effect by design can escalate significantly with increasing accuracy requirement, particularly environmental temperature control and therefore significant research has been done over the last few decades into more advanced compensation methodologies. This research reviewed a number of sophisticated techniques for modelling, estimation and compensation of thermal errors such as neural networks and regression techniques. The review revealed that these methods can be complicated and often required a significant amount of training time to

calibrate and can be sensitive to changes in the way the machine is used and to the location and performance of temperature sensors. These issues have a considerable contribution towards machine downtime therefore cost which, combined with the inherent complexity of some of the methods, has meant that comprehensive thermal compensation is mostly absent within manufacturing industry. The majority of the reviewed work has also been concentrated on solving internally generated heat related problems therefore costly temperature controlled environments are often still as the only solution to counter the adverse effects of environmental temperature fluctuations.

To overcome downtime issues, Finite Element Analysis (FEA) has been applied, primarily within research, due to proven capabilities for offline prediction of thermal errors. The published literature revealed a number of successful applications of FEA but in most cases it has been used as part of the research as a validation tool on discrete structural elements of the machine.

In this research FEA is used to simulate the thermal behaviour of the entire structure of a small milling machine using Abaqus/CAE Standard FEA software. The model of the machine assembly was generated using the CAD facility in the software. A study was conducted to understand the heat flow mechanism across structural joints requiring Thermal Contact Conductance (TCC) values. This research contributes experimentally obtained, and therefore accurate, TCC values for structural interface conditions compatible with CNC machine tool joints not previously available. These ensure a realistic thermal behaviour across assembly joints. This was followed by the investigation of the thermal behaviour of the machine due to both internal heat and external environmental fluctuations.

The research first investigated the thermal behaviour of the machine due to internal heating at two spindle speeds of 8000rpm and 4000rpm. In accordance with the aim of the research, only a short term test for a selected spindle speed was sufficient to obtain the required parameters for the FEA software to simulate and predict the thermal behaviour of the machine for short and, critically, even for long term tests and therefore provides a validated method where offline simulations can replace long term machine thermal trials that will reduce significant amount of machine downtime while enhancing the available data.

Key to this accuracy and efficiency is the novel method of calculating the body heat flux (BHF) values using carefully sectioned structural volumes surrounding the heat source and balancing the energy equation. This method can be further enhanced, in terms of accuracy; in the future using an identified technique involving contour matching described in the future work section.

The BHF calculation method also identified a variable and non-linear heat output from the bearings. A solution was found using the programming capabilities of the Abaqus FEA software to simulate the effect of changing the body heat flux value in the simulation by changing the Cp based on the temperature.

The work has provided an efficient method to calculate the convective heat transfer coefficient (h) due to airflow across test mandrels or generic tooling during spindle rotation. The method uses thermal imaging and a temperature sensor to obtain required paramters for calculations of *'h'*, and apply to the rotating tools in the software to accurately simulate thermal behaviour across rotating parts.

This research has validated the importance of identifying and including air pockets in the simulation. Air pockets were found to be local areas within the structure where normal convective flow is restricted and which reduce the cooling rate of the affected machine surfaces. The air temperature within those localized areas remains relatively high compared with the bulk ambient which effectively causes the associated structures to respond differently. It was also found that the effect of air pockets grows in significance with heat input i.e. higher spindle speeds in this case, and length of test.

The information obtained from internal heating tests was used for FEA thermal simulations. All required parameters i.e. body heat fluxes, convection coefficients and sink (ambient) temperatures were fed into the FEA software. The simulations results were found to be well correlated with the experimental results obtained from all internal heating trials, with an average residual error of less than 7µm.

The most significant cost benefits from this project may result from the long and very long term simulations that are impractical or unfeasible to complete experimentally. The effort applied to concentrate on maximising the short term correlation in the Z axis was

not a priority once the target correlation of 60% was achieved. In fact, in most cases the simulated movement matched the experimental by more than 70%.

This work has validated the FEA modelling strategy for simulating the thermal behaviour of the machine during environmental temperature fluctuations. The machine was tested in two seasons i.e. summer and winter, both tests were conducted for three continuous days. It was found that the overall temperature fluctuation was approximately 4°C in summer and approximately 5°C in winter and caused significant thermal deformations in the machine. This is often much higher and depends on the building susceptibility and climate A vertical temperature gradient was found to be approximately 1°C/m which causes each structural element to have a different initial temperature.

The complexity for defining initial temperatures to individual structural elements in the software was solved in this research by using a constant temperature for the full machine model followed by utilizing a new method of two-step simulation. In this method, the first step is used to determine the settling zone for the machine model to represent initial thermal state. This is followed by the second step of normal environmental simulation. The results of the environmental FEA simulations were also well correlated with the experimental results and revealed an average residual error of less than 8µm.

Well achieved correlations provided an offline platform to further assess FEA models and results. The assessments were carried out on the spindle carrier for internal heating simulations and on the main machine structural elements for environmental simulations to locate nodes and their positions whose displacements were sensitive to temperature change to effectively install temperature sensors permanently at those positions for simple linearly correlated thermal error compensation for compatibility with the existing capability within modern NC system but enhance the scope of the error being compensated. Two Matlab programs were written with an approach to find nodes with the highest slope sensitivity and with lowest hysteresis. The programs successfully found the nodes; and the Abaqus GUI was used to determine their position in the FEA model, effectively showing the importance of the software to visualize the location of the nodes.

This work targeted Abaqus as a standard commercially available FEA package to ensure the overall methodology was practical and available. The maximum time taken by any individual FEA simulation (internal and environmental) did not exceed more than 60 minutes. This enables multiple simulations to be completed for a variety of conditions.

To further conclude, machine downtime is a dominant issue within manufacturing industries that prevents testing and implementation for compensation. This research provides a method where the machine downtime can be reduced using offline simulation techniques for extended and complex real world machine operations. Rapid CAD model development; testing of the machine for a small period and the use of the calculated parameters at a selected spindle speed are efficient and all that is required to then run extended simulations without further testing on the machine. From such detailed data, new models can be created and tested offline. In this work, the linear compensation capabilities of existing NC system have been targeted by finding the best nodes that indicate where to physically place temperature sensors and their model coefficients.

8.1 Suggestions for future work

8.1.1 Contour plotting

Preliminary work has been completed to analyse thermal images using a Matlab program written to plot contours on identified isotherms calculated from thermal images to observe the dissemination of the heat flow. This provides an additional facility to locate heat sources in machines tools by analysing heat concentrations, temperature gradients and flow direction. The future application is to use the directional flow of the isotherms to further optimize the body heat flux values calculated for the heat sources. An example is determining the structural areas where contours are in a state of equilibrium indicating negligible conduction. Figure 8-1 shows the thermal image of the spindle and carrier head. Figure 8-2 shows the plotted contours on isotherms showing heat concentrations.

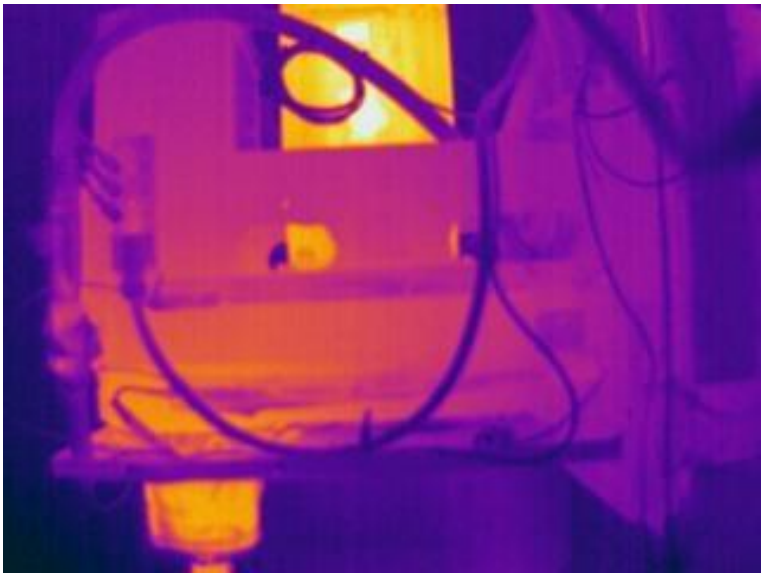

Figure 8-1: Thermal image

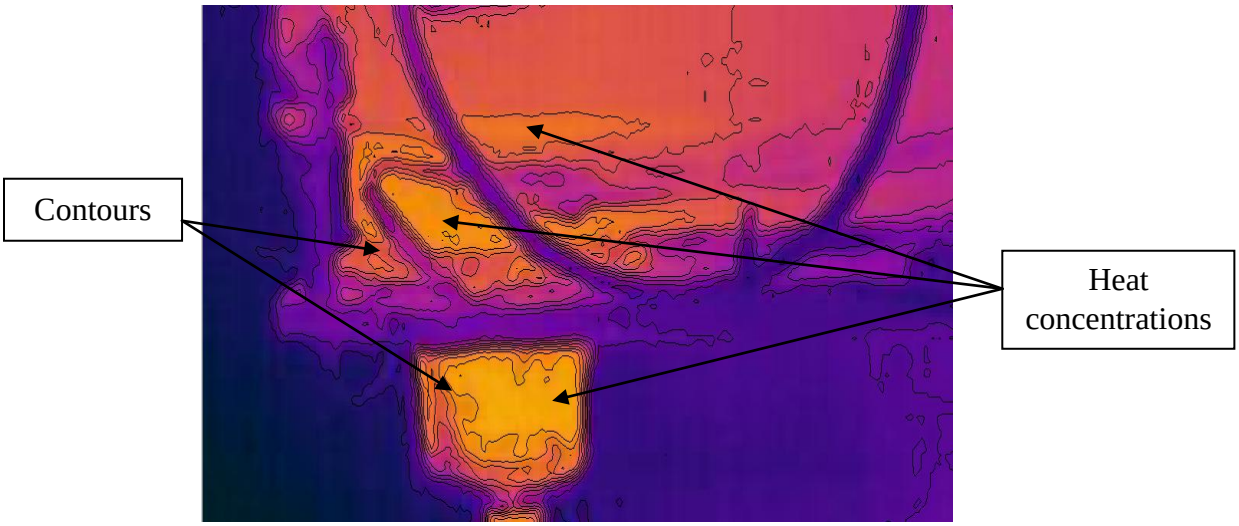

Figure 8-2: Contours plotted

A further important advancement will be the calculation of similar contours from the surface nodes of the FEA model to enable a contour matching algorithm to optimise the heat flux and FE model to optimise the accuracy of modelling complex distortions in highly complex areas such as the carrier of this machine. This will improve the shape/tilt accuracy as discussed in the following section.

8.1.2 Y axis tilt

Although the bottom part of the tool (test mandrel) is the most crucial area responsible for cutting, complex spindle thermal behaviour often produces a tilt in cutting tools which is of prime importance especially with cutting tools varying in length significantly

or large diameter tools. Figure 8-3 shows an illustration of a tilt in the tool caused by the thermal distortions.

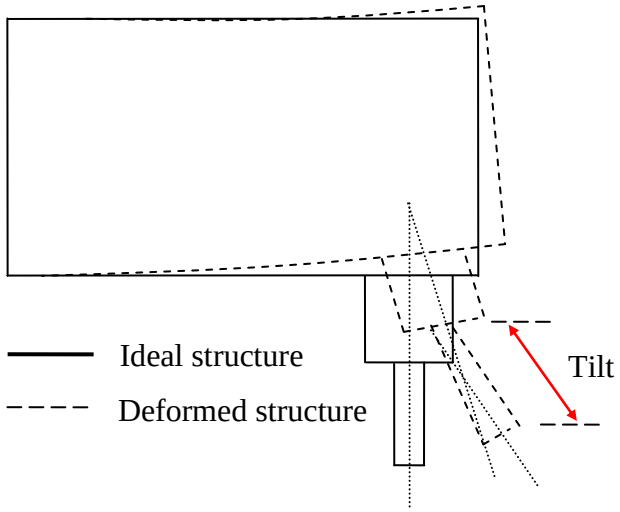

Figure 8-3: Cutting tool tilt

8.2 Workpiece modelling

Workpiece accuracy is further hindered by the increase in machining of thermally sensitive materials such as aluminium which can produce significant differential expansion between the machine and workpiece as well as non-uniform distortion within the workpiece itself. Detailed CAD models of the workpiece are becoming increasingly applied within Computer Aided Manufacturing (CAM) systems and these can be added into the simulation to enhance the accuracy simulating the real tool to workpiece interface in a relatively simple way.

LIST OF REFERENCES

1. Joe Jablonowski, N.E.-M., *The 2009 world machine-tool output*, in *The Free Library*. 2009, Metalworking Insiders' Report, Gardner Publications, Inc.
2. Postlethwaite, S.R., *Electronic based accuracy enhancement of CNC machine tools*, in *School of Computing and Engineering*. 1992, Huddersfield Polytechnic. p. 199.
3. White , A., *Experimental thermal error analysis and correction applied to CNC machine tools*, in *Thesis*. 2000, University of Huddersfield: Huddersfield.
4. Longstaff, A.P., S. Fletcher, A. Myers, *Volumetric compensation for precision manufacture through a standard CNC controller.* 20th Annual Meeting of the American Society for Precision Engineering, Norfolk, VA., 2005.
5. Mou (University of Illinois), J., Liu, C.R.(Purdue University, Indiana), *A robust error correction method for multi-axis machines.* Dynamic Systems and Control, 1994. **2**: p. 1011-1018.
6. Ferreira (University of Illinois), P.M., Liu, C.R. (Perdue University, W.Lafayette), *A method for estimating and compensating quasistatic errors of machine tools.* Journal of Engineering for Industry, 1993. **115**: p. 149-159.
7. Kiridena, V.S., Ferreira, P.M. (University of Illinois, Urbana), , *Parameter estimation and model verification of first order quasistatic error model for three axis machining centres.* International Journal of Machine Tools & Manufacturing, 1994. **34**: p. 101-125.
8. Kiridena, V.S., Ferreira, P.M. (University of Illinois, Urbana), *Kinematic modelling of quasistatic errors of three axis machining centres.* International Journal of Machine Tools & Manufacturing, 1994. **34**: p. 85-100.
9. Fletcher, S., *Computer Aided System for Intelligent Implementation of Machine Tool Error Reduction Methodologies*, in *School of Computing and Engineering*. 2001, University of Huddersfield: Huddersfield.
10. Bryan, J., *International Status of Thermal Error Research (1990).* CIRP Annals - Manufacturing Technology, 1990. **39**(2): p. 645-656.
11. Allen, J.P., et al., *Practical Thermal Error Correction for CNC Machine Tools.* 1996.
12. Longstaff, A.P., S. Fletcher, and D.G. Ford, *Practical experience of thermal testing with reference to ISO 230 Part 3*, in *Laser Metrology and Machine Performance VI*, D.G. Ford, Editor. 2003, WIT Press: Southampton. p. 473-483.
13. Postlethwaite, S.R., J.P. Allen, and D.G. Ford, *Machine tool thermal error reduction - An appraisal.* Proceedings of the Institution of Mechanical Engineers, Part B: Journal of Engineering Manufacture, 1999. **213**(1): p. 1-9.
14. Ramesh, R., M.A. Mannan, and A.N. Poo, *Error compensation in machine tools -- a review: Part II: thermal errors.* International Journal of Machine Tools and Manufacture, 2000. **40**(9): p. 1257-1284.
15. Li, J., et al., *Thermal-error modeling for complex physical systems: the-state-of-arts review.* The International Journal of Advanced Manufacturing Technology, 2009. **42**(1): p. 168-179.
16. Kaminski, J. and B. Alvelid, *Temperature reduction in the cutting zone in water-jet assisted turning.* Journal of Materials Processing Technology, 2000. **106**(1-3): p. 68-73.
17. Moise Cummings, M.M., *Addressing Machine Tool Errors* Manufacturing Engineering, 2009. **142**: p. 101-111.

18. Pascual, R., V. Meruane, and P.A. Rey, *On the effect of downtime costs and budget constraint on preventive and replacement policies.* Reliability Engineering & System Safety, 2008. **93**(1): p. 144-151.
19. Dorf, R.C. and A. Kusiak, *Handbook of design, manufacturing, and automation*. 1994, New York: Wiley.
20. Wang, C., *Quality 101 - Calibration of Machine Tools: Why, What and How*, in *Quality*. 2008, Hitchcock Pub. Co.]: Wheaton, Ill. p. 18.
21. *ISO 230-3:2007 Test code for machine tools -- Part 3: Determination of thermal effects*. 2007: International Organization for Standardization.
22. *Energy-efficient machine tool technologies*, in *Engineer Live*. 2009.
23. Jiang, S. and H. Mao, *Investigation of variable optimum preload for a machine tool spindle.* International Journal of Machine Tools and Manufacture, 2010. **50**(1): p. 19-28.
24. Corning, D., *Discovering the Secrets of Proper Bearing Lubrication* Machinery Lubrication, 2007.
25. Kushnir, E.F., M.R. Patel, and T.M. Sheehan, *Material Considerations in Optimization of Machine Tool Structure.* American Society of Mechanical Engineers, Pressure Vessels and Piping Division (Publication) PVP, 2000. **432**: p. 133-137.
26. Abele, E., Y. Altintas, and C. Brecher, *Machine tool spindle units.* CIRP Annals - Manufacturing Technology, 2010. **59**(2).
27. Chang, C.F., et al., *A Theory of Ball-screw Thermal Compensation.* 2009.
28. Sagar, P., *Temperature variations can crush accuracy.* Manufacturing Engineering, 2001. **126**(3): p. 80-82+84+86.
29. Weck, M., et al., *Reduction and Compensation of Thermal Errors in Machine Tools.* CIRP Annals - Manufacturing Technology, 1995. **44**(2): p. 589-598.
30. Hoff, M., *Critical coolant questions.* Manufacturing Engineering, 2000. **124**(5).
31. Boelkins, C., *MQL: lean and green.* Cutting Tool Engineering, 2009. **61**(3): p. 71-75.
32. Sreejith, P.S. and B.K.A. Ngoi, *Dry machining: Machining of the future.* Journal of Materials Processing Technology, 2000. **101**(1-3): p. 287-291.
33. Sharma, V.S., M. Dogra, and N.M. Suri, *Cooling techniques for improved productivity in turning.* International Journal of Machine Tools and Manufacture, 2009. **49**(6): p. 435-453.
34. Donmez, M.A., M.H. Hahn, and J.A. Soons, *A Novel Cooling System to Reduce Thermally-Induced Errors of Machine Tools.* CIRP Annals - Manufacturing Technology, 2007. **56**(1): p. 521-524.
35. Allen, J., *A general approach to CNC machine tool thermal error reduction*. 1997.
36. Jedrzejewski, J. and W. Kwasny, *Modelling of angular contact ball bearings and axial displacements for high-speed spindles.* CIRP Annals - Manufacturing Technology, 2010. **59**(1): p. 377-382.
37. Suh, J.D. and D.G. Lee, *Thermal characteristics of composite sandwich structures for machine tool moving body applications.* Composite Structures, 2004. **66**(1-4): p. 429-438.
38. *Linear Scales Improve Lathe Accuracy*, in *Modern Machine Shop*. 2009, Gardner Publications: Cincinnati, OH 45244-3029.
39. Fletcher, S., *A Case Study Conducted On a large Twin Spindle Gantry Machine For Airbus*. 2003, Internal Report: Centre for Precision Technologies, University of Huddersfield.

40. Chen, J.S., *Fast calibration and modeling of thermally-induced machine tool errors in real machining.* International Journal of Machine Tools and Manufacture, 1997. **37**(2): p. 159-169.
41. Yang, M. and J. Lee, *Measurement and prediction of thermal errors of a CNC machining center using two spherical balls.* Journal of Materials Processing Technology, 1998. **75**(1-3): p. 180-189.
42. Kim, K.D. and S.C. Chung, *On-machine inspection system: Accuracy improvement using an artifact.* Journal of Manufacturing Systems, 2003. **22**(4): p. 299-308.
43. Allen, J.P., S.R. Postlethwaite, D.G. Ford, *Practical application of thermal error correction - 4 case studies.* Proc. 3rd Int. Conf. on Laser Metrology and Machine Performance — LAMDAMAP, 1997: p. 359-369.
44. Chen, J.S. and G. Chiou, *Quick testing and modeling of thermally-induced errors of CNC machine tools.* International Journal of Machine Tools and Manufacture, 1995. **35**(7): p. 1063-1074.
45. Chen, J.S., *A study of thermally induced machine tool errors in real cutting conditions.* International Journal of Machine Tools and Manufacture, 1996. **36**(12): p. 1401-1411.
46. Ahn, K.G. and D.W. Cho, *In-process modelling and estimation of thermally induced errors of a machine tool during cutting.* International Journal of Advanced Manufacturing Technology, 1999. **15**(4): p. 299-304.
47. Kang, Y., et al., *Modification of a neural network utilizing hybrid filters for the compensation of thermal deformation in machine tools.* International Journal of Machine Tools and Manufacture, 2007. **47**(2): p. 376-387.
48. Kang, Y., et al., *Estimation of thermal deformation in machine tools using the hybrid autoregressive moving-average - Neural network model.* Proceedings of the Institution of Mechanical Engineers, Part B: Journal of Engineering Manufacture, 2006. **220**(8): p. 1317-1323.
49. Yang, H. and J. Ni, *Dynamic neural network modeling for nonlinear, nonstationary machine tool thermally induced error.* International Journal of Machine Tools and Manufacture, 2005. **45**(4-5): p. 455-465.
50. Ramesh, R., et al., *Thermal error measurement and modelling in machine tools. Part II. Hybrid Bayesian Network--support vector machine model.* International Journal of Machine Tools and Manufacture, 2003. **43**(4): p. 405-419.
51. Horvath, G. and T. Szabo, *CMAC Neural Network with Improved Generalization Property for System Modelling.* 2002.
52. Yang, S., J. Yuan, and J. Ni, *The improvement of thermal error modeling and compensation on machine tools by CMAC neural network.* International Journal of Machine Tools and Manufacture, 1996. **36**(4): p. 527-537.
53. Hwang, R.M. and K.C. Cha, *Construction of a prediction model for the structural stability of a surface grinder using backpropagation neural network.* International Journal of Advanced Manufacturing Technology, 2008. **37**(11-12): p. 1093-1104.
54. Vanherck, P., J. Dehaes, M. Nuttin, *Compensation of thermal deformations in machine tools with neural nets.* 1997.
55. Guo, Q., J. Yang, and H. Wu, *Application of ACO-BPN to thermal error modeling of NC machine tool.* International Journal of Advanced Manufacturing Technology, 2010: p. 1-9.

56. Hao, W., Z. Hongtao, G. Qianjian, W. Xiushan, Y. Jianguo, *Thermal error optimization modeling and real-time compensation on a CNC turning center.* Journal of Materials Processing Technology, 2008. **207**(1-3): p. 172-179.
57. Wang, X., Y. Li, Y. Yu,, *Thermal error robust modeling and real time compensation based on the GA-BPN theory on a vertical machine centre.* Adv. Mater. Res. Advanced Materials Research, 2010. **97-101**: p. 3211-3214.
58. Yang, J.G., Y.Q. Ren, and Z.C. Du, *An application of real-time error compensation on an NC twin-spindle lathe.* Journal of Materials Processing Technology, 2002. **129**(1-3): p. 474-479.
59. Yang, J.G., et al., *Testing, variable selecting and modeling of thermal errors on an INDEX-G200 turning center.* International Journal of Advanced Manufacturing Technology, 2005. **26**(7-8): p. 814-818.
60. Tseng, P.C., *A real-time thermal inaccuracy compensation method on a machining centre.* International Journal of Advanced Manufacturing Technology, 1997. **13**(3): p. 182-190.
61. Tseng, P.C. and J.L. Ho, *A Study of High-Precision CNC Lathe Thermal Errors and Compensation.* The International Journal of Advanced Manufacturing Technology, 2002. **19**(11): p. 850-858.
62. Chen, J.S., J. Yuan, J. Ni, *Thermal error modelling for real-time error compensation.* International Journal of Advanced Manufacturing Technology, 1996. **12**(4): p. 266-275.
63. Pahk, H. and S.W. Lee, *Thermal Error Measurement and Real Time Compensation System for the CNC Machine Tools Incorporating the Spindle Thermal Error and the Feed Axis Thermal Error.* The International Journal of Advanced Manufacturing Technology, 2002. **20**(7): p. 487-494.
64. Pahk, H.J., S.W. Lee, and H.D. Kwon, *Thermal error measurement and modelling techniques for the five-degree-of-freedom spindle drifts in computer numerically controlled machine tools.* Proceedings of the Institution of Mechanical Engineers, Part C: Journal of Mechanical Engineering Science, 2001. **215**(4): p. 469-485.
65. Du, Z.C., et al., *Modeling approach of regression orthogonal experiment design for the thermal error compensation of a CNC turning center.* Journal of Materials Processing Technology, 2002. **129**(1-3): p. 619-623.
66. Liu, G.L., et al., *Real-time error compensation technique and its application on NC machine tools*. 2004. p. 587-591.
67. Lin, Z.C. and J.S. Chang, *The building of spindle thermal displacement model of high speed machine center.* International Journal of Advanced Manufacturing Technology, 2007. **34**(5-6): p. 556-566.
68. Tachiya, H., et al., *Approximation of Thermal Deformation Behaviour of a Machine Tool to Improve its Process Precision.* KEY ENGINEERING MATERIALS, 2007. **345/346**: p. 181-184.
69. Mukherjee, I. and P.K. Ray, *A review of optimization techniques in metal cutting processes.* Computers & Industrial Engineering, 2006. **50**(1-2): p. 15-34.
70. Yang, H. and J. Ni, *Adaptive model estimation of machine-tool thermal errors based on recursive dynamic modeling strategy.* International Journal of Machine Tools and Manufacture, 2005. **45**(1): p. 1-11.
71. Lee, D.S., J.Y. Choi, and D.H. Choi, *ICA based thermal source extraction and thermal distortion compensation method for a machine tool.* International Journal of Machine Tools and Manufacture, 2003. **43**(6): p. 589-597.

72. Zhu, J., J. Ni, and A.J. Shih, *Robust machine tool thermal error modeling through thermal mode concept.* J Manuf Sci Eng Trans ASME Journal of Manufacturing Science and Engineering, Transactions of the ASME, 2008. **130**(6): p. 0610061-0610069.
73. Delbressine, F.L.M., et al., *Modelling thermomechanical behaviour of multi-axis machine tools.* Precision Engineering, 2006. **30**(1): p. 47-53.
74. Yun, W.S., S.K. Kim, and D.W. Cho, *Thermal error analysis for a CNC lathe feed drive system.* International Journal of Machine Tools and Manufacture, 1999. **39**(7): p. 1087-1101.
75. Attia, M.H. and S. Fraser, *A generalized modelling methodology for optimized real-time compensation of thermal deformation of machine tools and CMM structures.* International Journal of Machine Tools and Manufacture, 1999. **39**(6): p. 1001-1016.
76. Attia, M.H., S. Fraser, and M.O.M. Osman, *On-line estimation of time-variant thermal load applied to machine tool structures using a s-domain inverse solution.* International Journal of Machine Tools and Manufacture, 1999. **39**(6): p. 985-1000.
77. Fraser, S., M.H. Attia, and M.O.M. Osman, *Modelling, identification and control of thermal deformation of machine tool structures, Part 1: Concept of generalized modelling.* Journal of Manufacturing Science and Engineering, Transactions of the ASME, 1998. **120**(3): p. 623-631.
78. Fraser, S., M.H. Attia, and M.O.M. Osman, *Modelling, Identification and Control of Thermal Deformation of Machine Tool Structures, Part 2: Generalized Transfer Functions.* TRANSACTIONS- AMERICAN SOCIETY OF MECHANICAL ENGINEERS JOURNAL OF MANUFACTURING SCIENCE AND ENGINEERING, 1998. **120**(3): p. 632-639.
79. Tseng, P.-C. and S.-L. Chen, *The Neural-fuzzy Thermal Error Compensation Controller on CNC Machining Center*. JSME International Journal Series C Mechanical Systems, Machine Elements and Manufacturing, 2002. **45**(2): p. 470-478.
80. Zhou, E.P. and D.K. Harrison, *Improving error compensation via a fuzzy-neural hybrid model.* Journal of Manufacturing Systems, 1999. **18**(5): p. 335-344.
81. Lee, J.-H., J.-H. Lee, and S.-H. Yang, *Thermal Error Modeling of a Horizontal Machining Center Using Fuzzy Logic Strategy.* Journal of Manufacturing Processes, 2001. **3**(2): p. 120-127.
82. White, A.J., S. R. Postlethwaite, D. G. Ford, *An identification and study of mechanisms causing thermal errors in CNC machine tools.* International, conference th,, 1999.
83. White, A.J., S. R. Postlethwaite, D. G. Ford, *A general purpose thermal error compensation system for CNC machine tools.* Laser Metrology and Machine Performance V, 2001: p. 3-13.
84. White, A.J., S. R. Postlethwaite, D. G. Ford, *Measuring and modelling thermal distortion on CNC machine tools.* Laser Metrology and Machine Performance V, 2001: p. 69-79.
85. Allen, J.P., S.R. Postlethwaite, D.G. Ford, *A Novel Approach to Thermal Error Reduction on CNC Machine Tools.* Proceedings of the Second International Conference on Laser Metrology and Machine Performance - LAMDAMAP '95, Southampton Institute, 1995: p. 297-308.
86. Allen, J.P., S.R. Postlethwaite, D.G. Ford, *Practical Thermal Error Correction for CNC Machine Tools.* Proceedings of the 11th Annual Meeting for the American

Society of Precision Engineering, ASPE, held at Monterey, California, 1996: p. 648-653.
87. Widiyarto, M.H.N. and H. University of, *Modelling and passive correction investigation of vibration induced machining errors on CNC machine tools*. 2006, Huddersfield: University of Huddersfield.
88. Min, X., J. Shuyun, and C. Ying, *An improved thermal model for machine tool bearings.* International Journal of Machine Tools and Manufacture, 2007. **47**(1): p. 53-62.
89. Haitao, Z., Y. Jianguo, and S. Jinhua, *Simulation of thermal behavior of a CNC machine tool spindle.* International Journal of Machine Tools and Manufacture, 2007. **47**(6): p. 1003-1010.
90. Jedrzejewski, J., et al., *High-speed precise machine tools spindle units improving.* Journal of Materials Processing Technology, 2005. **162-163**(SPEC. ISS.): p. 615-621.
91. Creighton, E., et al., *Analysis of thermal errors in a high-speed micro-milling spindle.* International Journal of Machine Tools and Manufacture, 2010. **50**(4): p. 386-393.
92. Wu, C.H. and Y.T. Kung, *Thermal analysis for the feed drive system of a CNC machine center.* International Journal of Machine Tools and Manufacture, 2003. **43**(15): p. 1521-1528.
93. Kim, S.K. and D.W. Cho, *Real-time estimation of temperature distribution in a ball-screw system.* International Journal of Machine Tools and Manufacture, 1997. **37**(4): p. 451-464.
94. Denkena, B.S., C. Krüger, M., *Experimental investigation and modeling of thermal and mechanical influences on shape deviations in machining structural parts.* International Journal of Machine Tools and Manufacture, 2010. **50**(11): p. 1015-1021.
95. Rai, J.K. and P. Xirouchakis, *FEM-based prediction of workpiece transient temperature distribution and deformations during milling.* International Journal of Advanced Manufacturing Technology, 2009. **42**(5-6): p. 429-449.
96. Ratchev, S., et al., *An advanced FEA based force induced error compensation strategy in milling.* International Journal of Machine Tools and Manufacture, 2006. **46**(5): p. 542-551.
97. Zhou, J.M., M. Andersson, and J.E. Ståhl, *Identification of cutting errors in precision hard turning process.* Journal of Materials Processing Technology, 2004. **153-154**(1-3): p. 746-750.
98. Kim, J.J., Y.H. Jeong, and D.W. Cho, *Thermal behavior of a machine tool equipped with linear motors.* International Journal of Machine Tools and Manufacture, 2004. **44**(7-8): p. 749-758.
99. Denkena, B., K.-H. Scharschmidt, *Thermal Compensation Method for Machine Tools.* Proceedings of the Topical Meeting: Thermal Effects in Orecision Systems - Maastricht, 2007: p. 19-21.
100. Jedrzejewski, J., W. Modrzycki, Z. Kowal, W. Kwaśny, Z. Winiarski, *Precise modelling of HSC machine tool thermal behaviour.* Journal of Achievements in Materials and Manufacturing Engineering, 2007. **24**(1): p. 245-252.
101. Huo, D., et al., *A Novel FEA Model for the Integral Analysis of a Machine Tool and Machining Processes.* 2004. p. 45-50.
102. Mayr, J., S. Weikert, K.Wegener, *Comparing the thermo- mechanical behaviour of machine tool frame designs using a FDM - FEM simulation approach.* Proc. form ASPE Annual Meeting, 2007: p. 17-20.

103. Mayr, J., Markus Ess, Sascha Weikert, Konrad Wegener, *Compensation of Thermal Effects on Machine Tools using a FDEM Simulation Approach.* Laser Metrology and Performance IX, 2009: p. 38-47.
104. Attia, M.H., L. Kops, *Importance of contact pressure distribution on heat transfer in structural joints of machine tools.* Transactions of the ASME, Journal of engineering for industry, 1980. **102**: p. 159-167.
105. Incropera, F.P. and D.P. DeWitt, *Introduction to heat transfer*. 2002, New York, NY [u.a.]: Wiley.
106. Hagen, K.D., *Heat transfer with applications*. 1999, Upper Saddle River, N.J.: Prentice Hall.
107. Özisik, M.N., *Heat transfer : a basic approach*. 1985, New York: McGraw-Hill.
108. Tirovic, M. and G.P. Voller, *Interface Pressure Distributions and Thermal Contact Resistance of a Bolted Joint.* Proceedings: Mathematics, Physical and Engineering, 2005. **461**(2060): p. 2339-2354.
109. Euler, G.D. (2002) *Bolt Preload Calculation*.
110. Euler, G.D. (2002) *Standard Metric Bolt Shank Dimensions*.
111. Shigley, J.E., C.R. Mischke, and R.G. Budynas, *Shigley's mechanical engineering design*. 2006, New York; London: McGraw-Hill Higher Education ; McGraw-Hill [distributor].
112. *ABAQUS/CAE User's Manual 6.1*. 2000: Hibbitt, Karlsson and Sorensen, Inc., Pawtucket, RI 02860-4847, USA.
113. Zhang, B., D.M. Maijer, and S.L. Cockcroft, *Development of a 3-D thermal model of the low-pressure die-cast (LPDC) process of A356 aluminum alloy wheels.* Materials Science and Engineering: A, 2007. **464**(1-2): p. 295-305.
114. Fletcher, S., A.P. Longstaff, A. Myers, *Measurement methods for efficient thermal assessment and error-compensation.* Proceedings of the Topical Meeting: Thermal Effects in Orecision Systems - Maastricht, 2007.

APPENDIX A - MATERIAL PROPERTIES AND BENCHMARK CALCULATIONS

Properties of materials

Material	Thermal Conductivity (W/m/°C).
Air	0.024
Cast iron	52.329
Machine lubricating oil	0.15
Steel	51.9
Water as coolant	0.58

Table A-1: Thermal conductivity values for common machine tool associated materials

Material	Coefficient of thermal expansion (α) in μm/m°C
Aluminium	22
Cast Iron	9
Invar	1.2
Steel	11.7

Table A-2: List of thermal expansion coefficients for common metals

	Steel	Cast iron	Invar	Units (mm)
Conductivity (k)	51.9	52.329	15	mJ/mm°C
Density	7.805×10^{-9}	7.2×10^{-9}	8.20×10^{-9}	tonne/mm^3
Specific heat capacity (Cp)	$473 \times 10^{+6}$	$506 \times 10^{+6}$	$525 \times 10^{+6}$	mJ/tonne/°C
Modulus of elasticity	205000	124000	145000	N/mm^2
Coefficient of linear expansion	11.7×10^{-6}	9×10^{-6}	1.2×10^{-6}	m/m°C
Poisson's ratio	0.3	0.24	0.3	

Table A-3: Properties of steel, cast iron and invar used in Abaqus

APPENDIX B - CAD MODELLING OF MACHINE STRUCTURAL PARTS

Machine drawings in 2D format were provided by the machine tool manufacturer for construction of the structural parts. The models were created separately before the assembly took place. The parts are as follows:

Carrier head	Test mandrel
Column	Guide ways
Table	Carriages
Base	Motor support
Saddle	Motor heat structure
Spindle	Two Belt drive structures
Bearings	Z axis motor

Carrier head

The carrier head was simplified by removing unnecessary details such as fillets, chamfers etc. The vents were considered to have a significant effect on thermal cooling and therefore included. Figure B-1 and Figure B-2 show the two views of the created model of the carrier. The model indicates the areas where symmetry constraints were applied. The model was halved due to symmetrical nature in X axis.

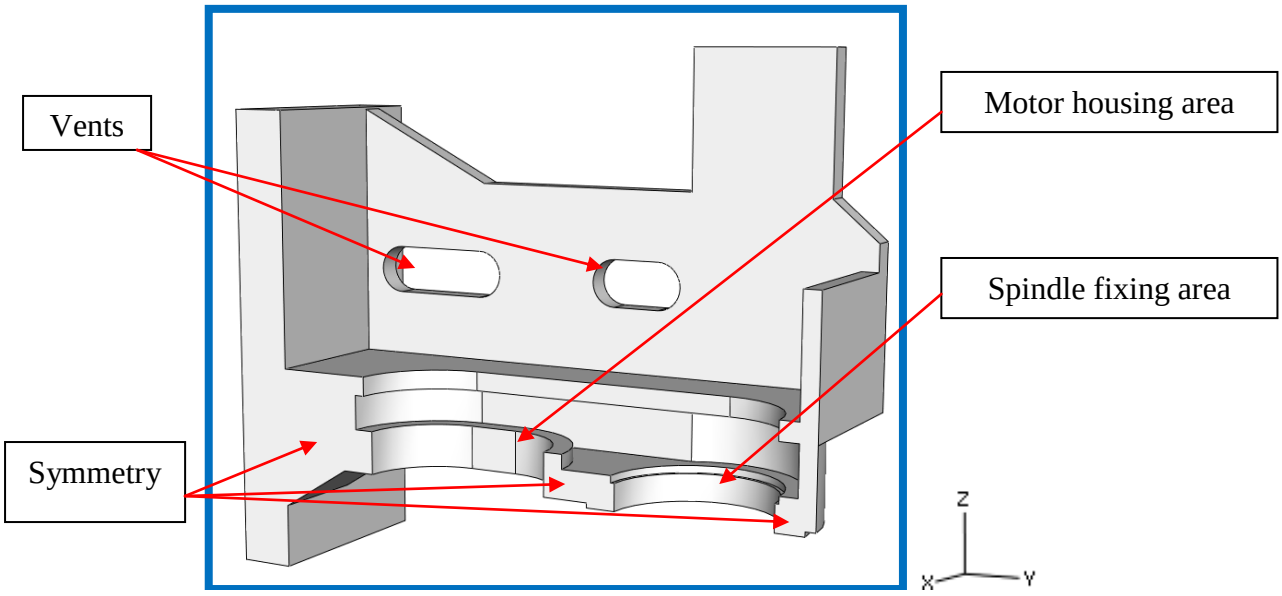

Figure B-1: Machine Carrier head (view1)

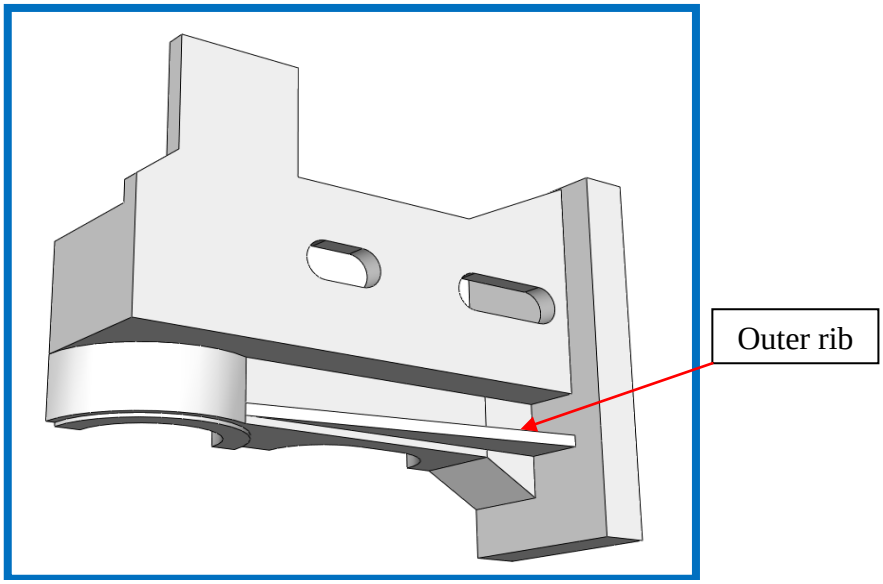

Figure B-2: Machine Carrier head (view 2)

Column

Column was created after simplifications. Geometrical details for example filleted curves on the guide ways were simplified and represented as rectangular blocks. Internal ribs were created since these add stiffness to the tall structure. Guide ways were represented as rectangular blocks. Figure B-3 and Figure B-4 shows the two views of the created model of the column.

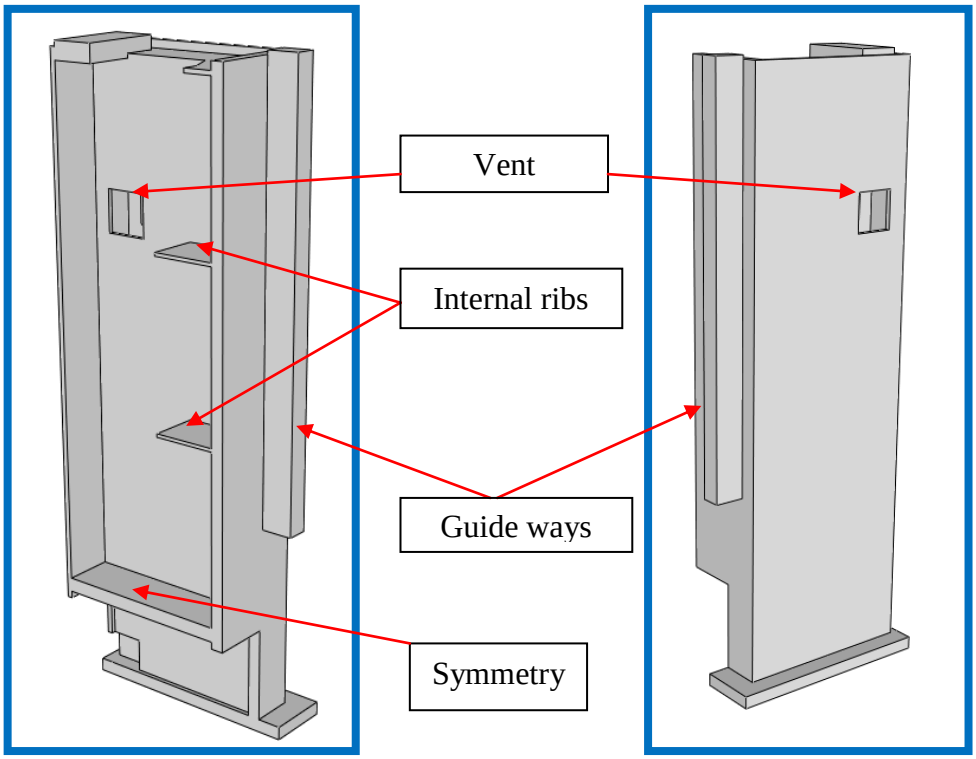

Figure B-3: Machine Column (view1)

Figure B-4: Machine Column (view2)

Table

Simplified CAD model of the Table was created that also includes the ribs and vents. The model was halved and the symmetry was applied in the software. Figure B-5 and Figure B-6 shows two views of the created CAD model of machine table. Internal ribs and symmetry are shown.

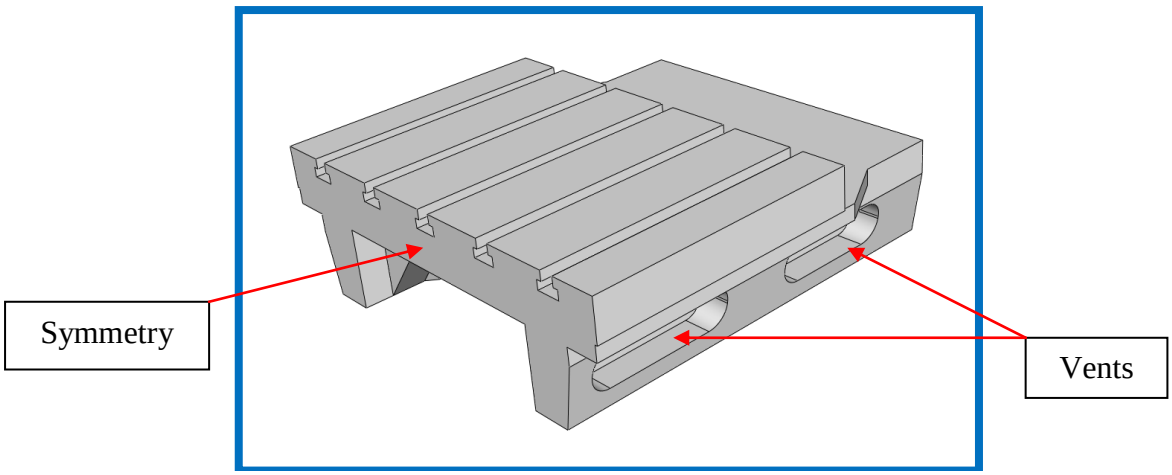

Figure B-5: Machine Table (view1)

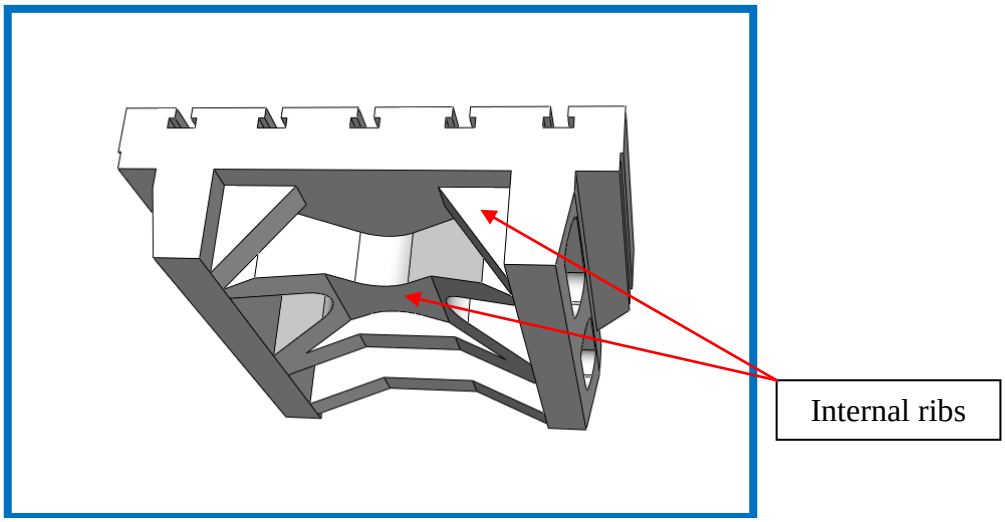

Figure B-6: Machine Table (view2)

Base

The base was created after simplifying guide ways. Guide ways were represented as rectangular blocks as shown in Figure B-7. Figure B-8 shows internal ribs and the symmetry applied.

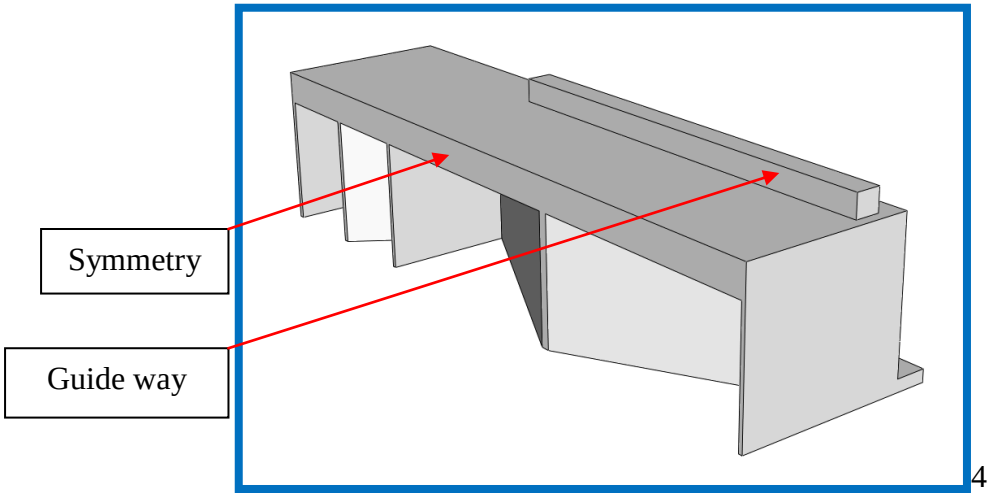

4

Figure B-7: Machine Base (view1)

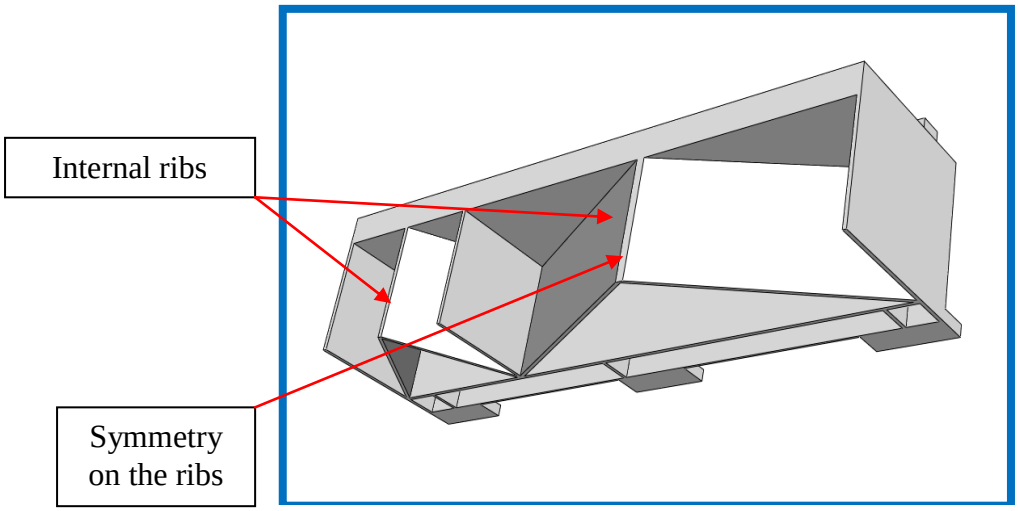

Figure B-8: Machine Base (view2)

Saddle

The saddle was created after simplifying, again the guide ways were represented as rectangular blocks. Figure B-9 and Figure B-10 shows two views of the created CAD model of the table.

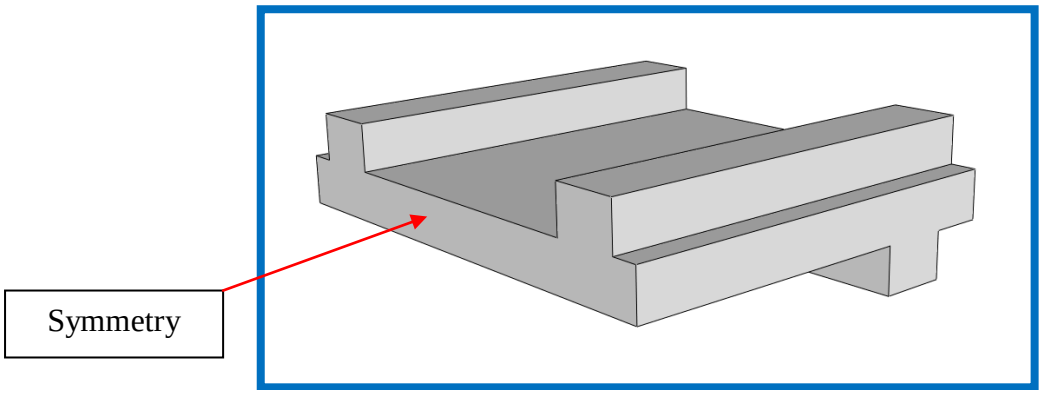

Figure B-9: Machine Saddle (view1)

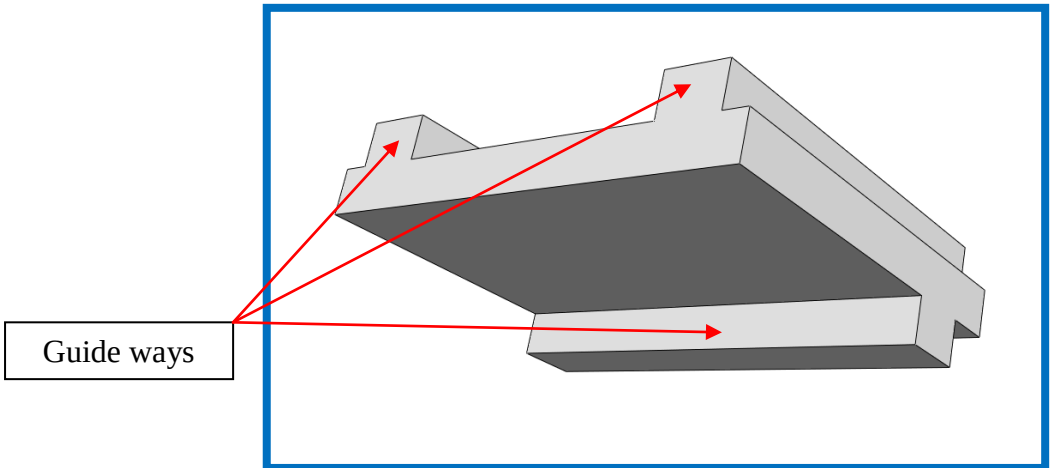

Figure B-10: Machine Saddle (view2)

Spindle

Spindle was created in two stages. The top part shown in Figure B-11 was created separately to specifically represent location for the belt drive. The spindle is rotated using the belt drive which acts as a heat source by which the heat flows into the spindle through the contacting areas. The belt drive section was modelled and simplified and the gear teeth were removed.

The lower part shown in Figure B-12 was created separately and assembled, slots were created to position the bearings. Voids were created as per manufacturing diagram.

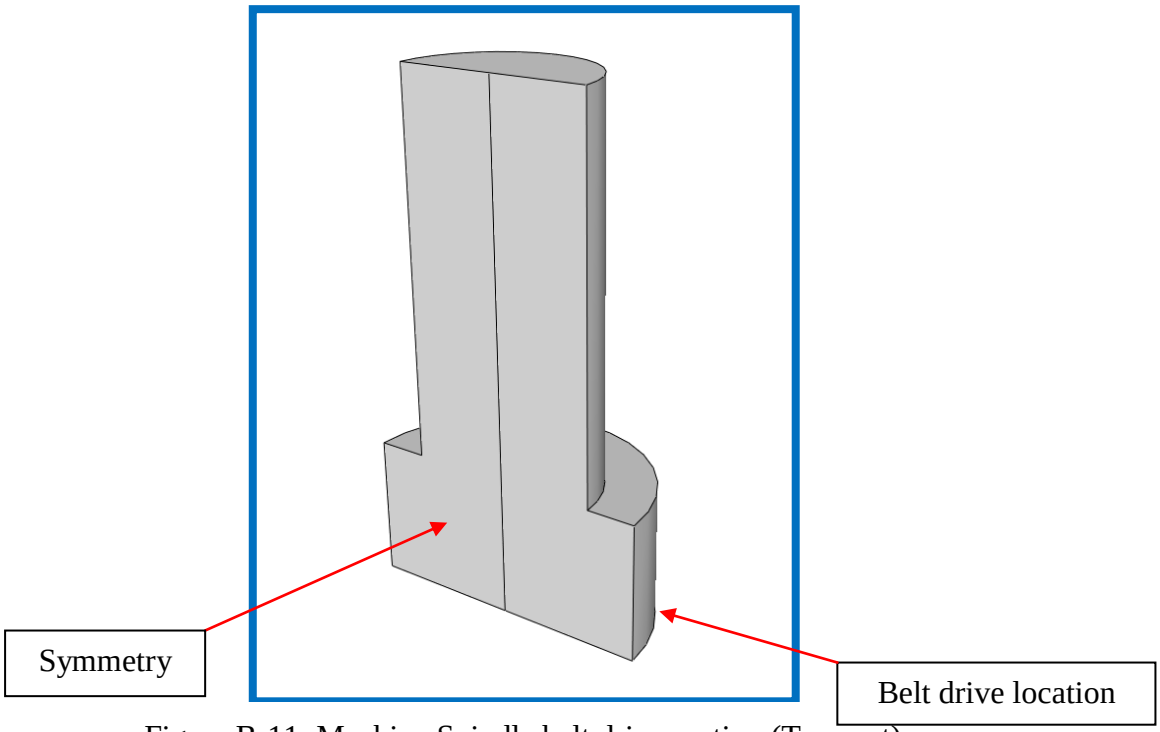

Figure B-11: Machine Spindle belt drive section (Top part)

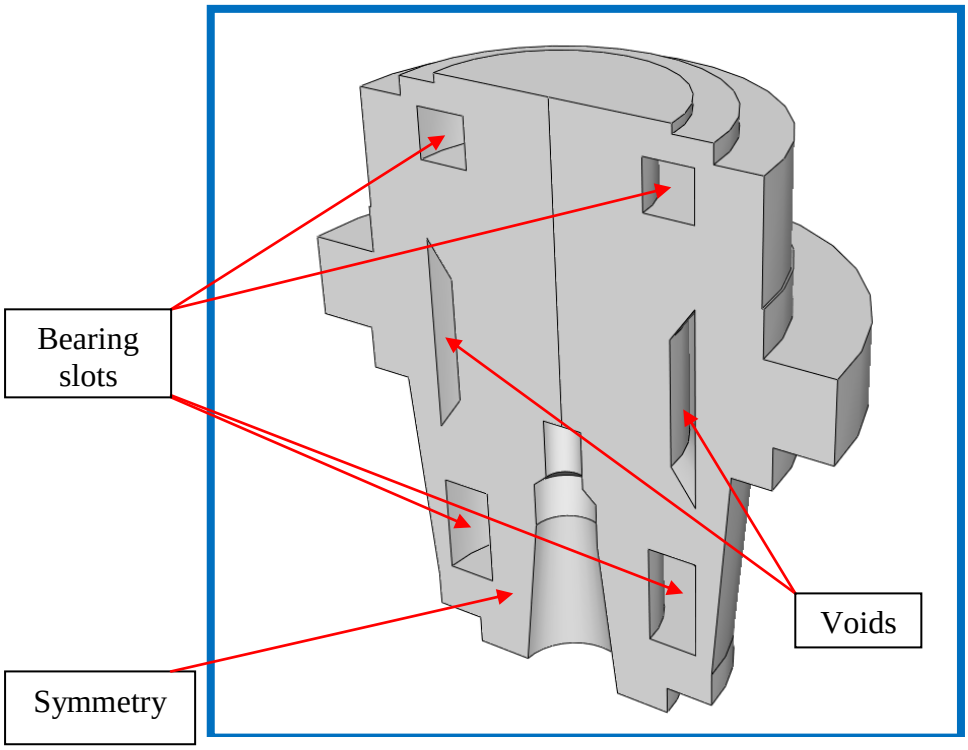

Figure B-12: Machine Spindle (Bottom part)

Spindle bearings

Spindle bearings (main heat sources) were created and represented as annular blocks after simplifications as shown in Figure B-13.

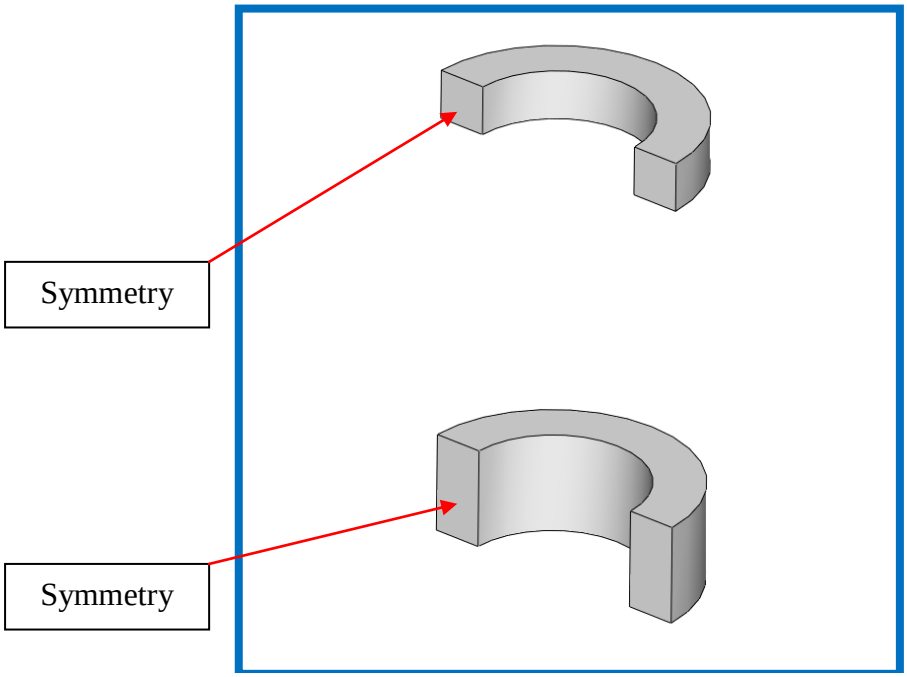

Figure B-13: Upper and lower Bearings

Test mandrel

Test mandrel was created after simplification. Symmetry was applied as shown in Figure B-14.

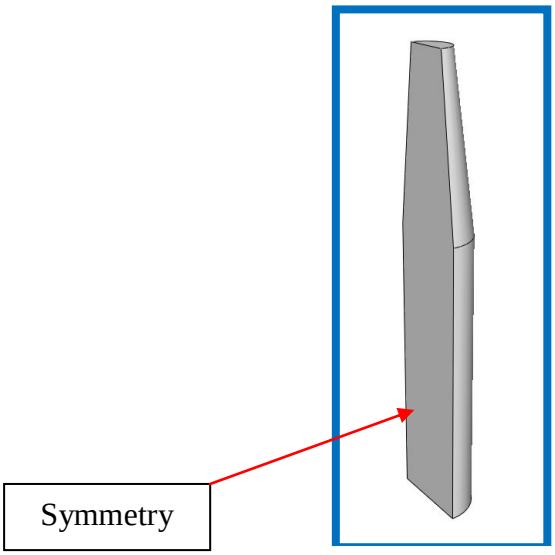

Figure B-14: Test mandrel

Guide ways

Guide ways were created and represented as extruded rectangular blocks after simplification as shown in Figure B-15. There is no symmetry associated to this structure.

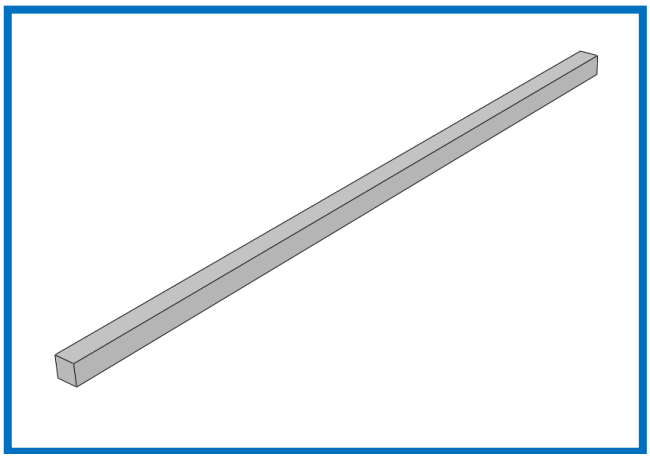

Figure B-15: Guide ways for Column

Carriages

Carriages were created and represented as simplified blocks as shown in Figure B-16. There is no symmetry associated to this structure.

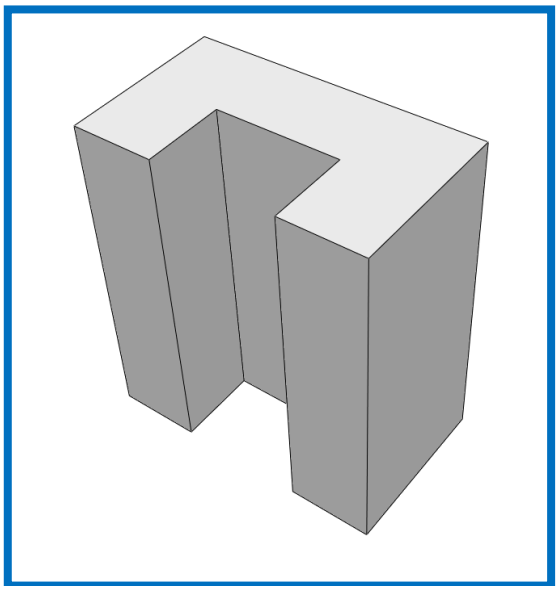

Figure B-16: Carriage

Motor Support

This is an integral part of the carrier head over which the spindle motor housing is fixed. It was created as a rectangular block as shown in Figure B-17. There is no symmetry associated to this structure.

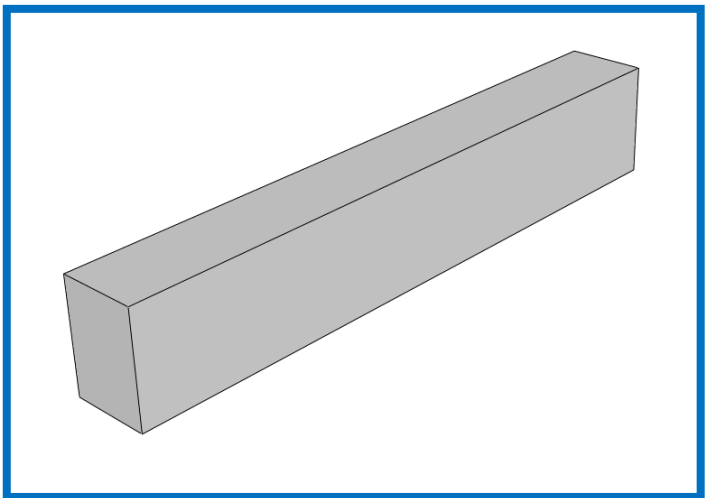

Figure B-17: Motor support structure

Spindle motor mount plate

The heat generated by the spindle motor travels through the mounting plate and disseminates into the structure through the motor support structure. This plate was modelled and represented as a simplified rectangular structure as shown in Figure B-18. There is no symmetry associated to this structure.

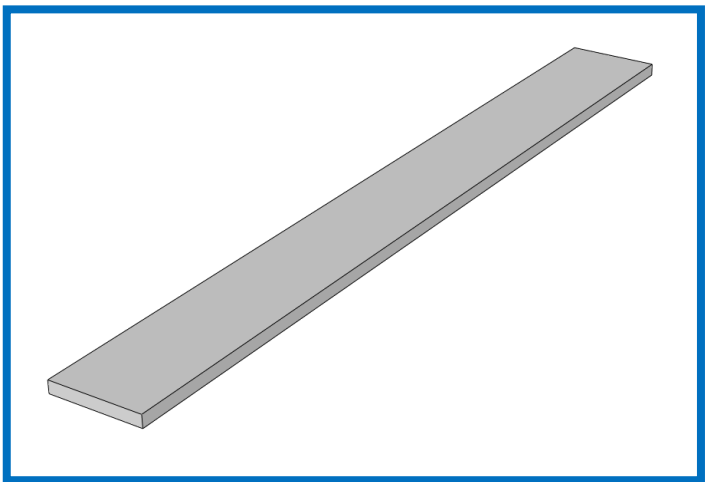

Figure B-18: Structure representing spindle motor housing mount plate

Belt drive structures

Two separate structures were created to represent the spindle belt drive which drives the spindle through the spindle motor. The belt drive acts as a heat source due to the friction with associated gear teeth. Figure B-19 shows the first structure of the belt drive and Figure B-20 shows the second structure of the belt drive. Symmetry was applied and shown.

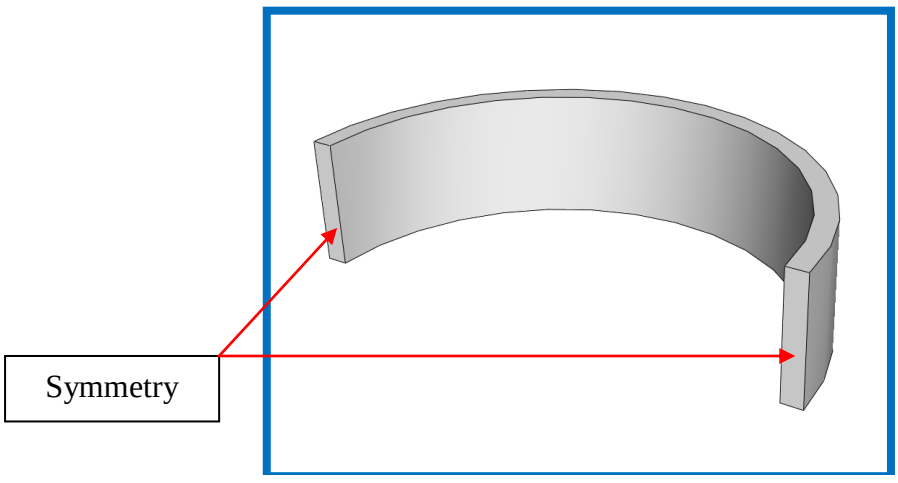

Figure B-19: Structure representing the belt drive heat source at Spindle

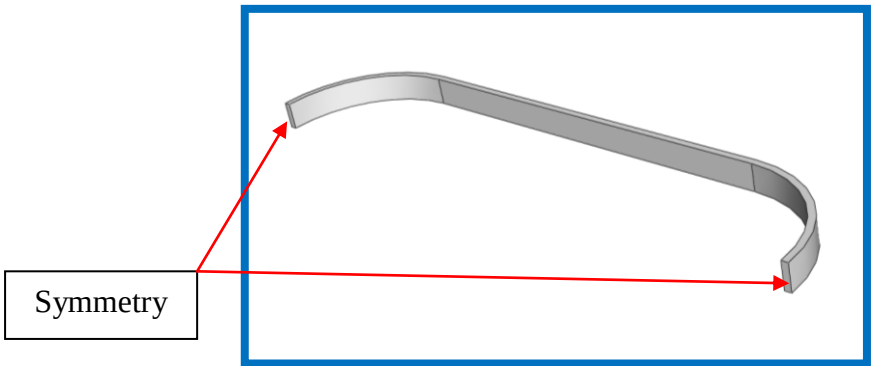

Figure B-20: Structure representing the belt drive heat source inside Carrier head

Z axis drive motor support bracket

The Z axis drive motor support bracket provides means of supporting the Z axis drive motor which serves to translate and hold the axis in position. Figure B-21 shows the simplified CAD model representing the Z axis drive motor support bracket. There is no symmetry associated to this structure.

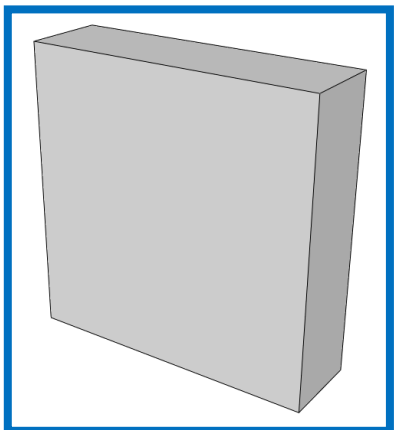

Figure B-21: Structure representing Z axis drive motor support bracket

APPENDIX C - BHF CALCULATIONS FOR HEAT SOURCES

The procedure used to obtain BHF values using equation 3.6 for benchmarks (chapter 4) is followed to obtain the BHF values for the heat sources present in the machine.

$$Q' = mCp(T_1 - T_2)/t + hA(T_{surf} - T_{air}) \ldots\ldots\ (3.6)$$

Upper bearing (8000rpm)

For the upper bearing BHF, the upper selected volume (Figure 4-33 – chapter 4) of the spindle was taken. The volume of the upper bearing was used to divide the total energy *Q'* obtained to obtain the BHF value for the lower bearing.

The heating data from the upper bearing sensor was used. Similar to lower bearing, a trend line was plotted on the upper bearing data to refine it. Figure C-1 shows the trend line plotted on the upper bearing sensor data. Table C-1 shows the data of the lower bearing used to calculate the BHF value.

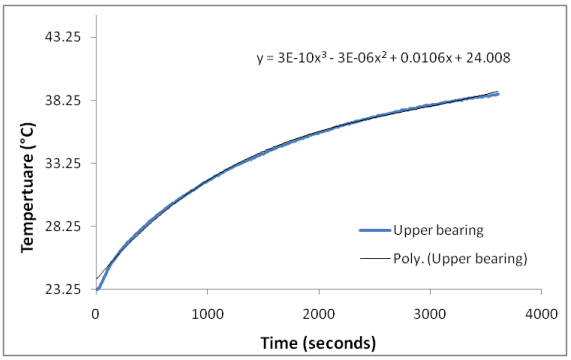

Figure C-1: Trend line plotted on the upper bearing sensor data

Upper bearing	Value	Units
Volume of the upper spindle housing	6.73E+05	mm^3
Volume of the upper bearing	58240	mm^3
Total volume	7.31E+05	mm^3
Area of the upper spindle bearing	2.10E+04	mm^2
Total mass	5.71E-03	tonnes
Density of Steel	7.81E-09	$tonne/mm^3$
Cp of Steel	4.73E+08	mJ/tonnes/°C
Time	10	s
h	0.006	$mW/mm^2/°C$
Initial ambient temperature	24.438	°C

Table C-1: Upper bearing data used for BHF calculations

The main iteration that obtained the transient BHF for the upper bearing is presented.

Total volume = 6.73E+05 mm^3

Total mass = 5.71E-03 tonnes

Temperature difference (T_2-T_1) = 0.1051021°C (between two logs)

Total time = 10s (logging time interval)

Convection coefficient (h) = 0.006 $mW/mm^2/°C$

Ambient temperature change = Varied from 24.438°C to 25.563°C during the heating cycle – Used transiently during calculations

Exposed area = 2.10E+04mm^2

By applying these values in equation 3.6, the value for the Q' is

Q' = 28421.49399 mW

The value of Q' is required to be divided by the volume of the heat source which in this case is the volume of the upper bearing.

q' = 28421.49399 mW / 58240 mm^3 which gives the BHF value as

q' = 0.49 mW/mm^3

Carrier belt drive and spindle motor mount plate (8000rpm)

BHF values were calculated for the two heat sources present in the carrier head, carrier belt drive (Figure 4-41– chapter 4) was considered as main heat source and spindle motor mount plate (Figure 4-42– chapter 4) was considered as a neighbouring heat source. Following the similar procedure, the volume of each heat source was used to divide the total energy Q' obtained to obtain the BHF values.

The heating data for the carrier belt drive was obtained from the sensor closest to the heat source (highest temperature magnitude) and was found to be the sensor number 3 in the sensor strip 1. Similarly sensor number 10 was found with the highest temperature

magnitude as being closest to the heat source in the sensor strip 2 for the spindle motor mount plate.

For the carrier belt drive BHF, a trend line was plotted on the Line 1 sensor 3 data to refine it. Figure C-2 shows the trend line plotted on the upper bearing sensor data. Table C-2 shows the data of the carrier belt drive used to calculate the BHF value.

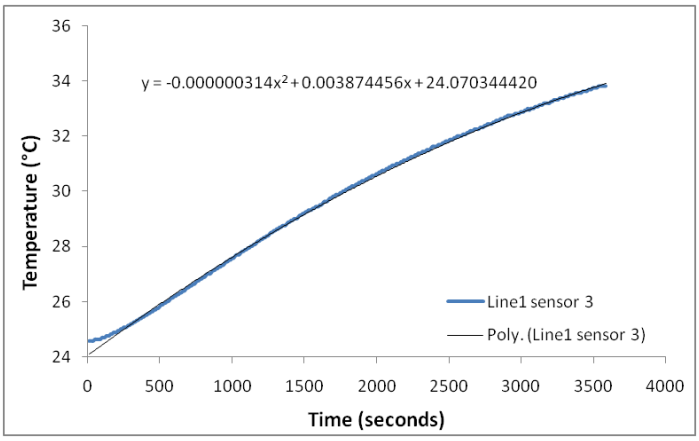

Figure C-2: Trend line plotted on the Line 1 sensor 3sensor data

Carrier belt drive	**Value**	**Units**
Volume of the selected carrier structure	3.76E+06	mm^3
Volume of the belt drive	54606	mm^3
Total volume (selected carrier structure and belt drive)	3.82E+06	mm^3
Total area (selected carrier structure and belt drive)	3.30E+05	mm^2
Total mass	2.75E-02	tonnes
Density of Cast Iron	7.20E-09	$tonne/mm^3$
Cp of Cast Iron	506000000	mJ/tonnes/°C
Time	10	s
h	0.006	$mW/mm^2/°C$
Initial ambient temperature	24.438	°C

Table C-2: Carrier belt drive data used for BHF calculations

The main iteration that obtained the transient BHF for the carrier belt drive is shown below.

Total volume = 6.73E+05 mm^3

Total mass = 5.71E-03 tonnes

Temperature difference (T_2-T_1) = 0.03865036°C (between two logs)

Total time = 10s (logging time interval)

Convection coefficient (h) = 0.006 mW/mm^2/°C

Ambient temperature change = Varied from 24.438°C to 25.563°C during the heating cycle – Used transiently during calculations

Total exposed area = 3.30E+05 mm^2

By applying these values in equation 3.6, the value for the Q' is

Q' = 54422.21475 mW

The value of Q' is required to be divided by the volume of the heat source which in this case is the volume of the carrier belt drive.

$\dot{q}$ = 54422.21475 mW / 54606 mm^3 which gives the BHF value as

$\dot{q}$ = 1 mW/mm^3

Spindle motor mount plate	**Value**	**Units**
Volume of the motor support and carrier side	1.29E+06	mm^3
Volume of the mount plate	63840	mm^3
Total volume (motor support and carrier side and the mount plate)	1.36E+06	mm^3
Total area (motor support and carrier side and the mount plate)	6.32E+04	mm^2
Total mass	9.78E-03	tonnes
Density of Cast Iron	7.20E-09	tonne/mm^3
Cp of Cast Iron	506000000	mJ/tonnes/°C
Time	10	s
h	0.006	mW/mm^2/°C
Initial ambient temperature	24.438	°C

Table C-3: Spindle motor mount plate data used for BHF calculations

The spindle motor mount plate is considered as a neighbouring heat source therefore to simplify, these calculations were performed using the full analysis time.

Total volume = 1.36E+06 mm^3

Total mass	= 9.78E-03 tonnes
Temperature difference (T_2-T_1)	= 5.25°C
Total time	= 3600s
Convection coefficient (h)	= 0.006 mW/mm^2/°C
Ambient temperature change	= Varied from 24.438°C to 25.563°C during the heating cycle – Used transiently during calculations
Total exposed area	= 6.32E+04 mm^2

By applying these values in equation 3.6, the value for the *Q'* is

Q' = 9.20E+03 mW

The value of *Q'* is required to be divided by the volume of the heat source which in this case is the volume of the mount plate.

q' = 9.20E+03 mW / 63840 mm^3 which gives the BHF value as

q' = 0.14 mW/mm^3

Spindle belt (8000rpm)

For the spindle belt BHF, the selected volume (Figure 4-35 – chapter 4) for the spindle belt was taken. Using the similar approach, the volume of the spindle belt was used to divide the total energy *Q'* obtained to obtain the BHF value.

Thermal imaging (Figure 4-20 – chapter 4) was used to extract temperature data for the spindle belt. Figure C-3 shows the trend line plotted on the temperature data from thermal imaging to refine it. Table C-4 shows the data of the spindle belt used to calculate the BHF value.

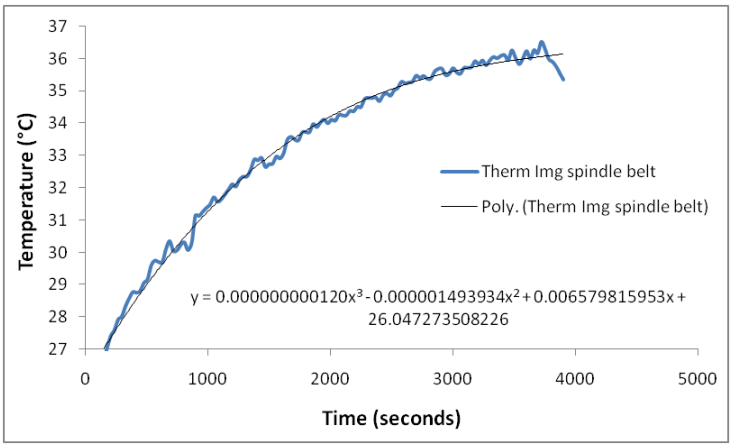

Figure C-3: Trend line plotted on the temperature data from thermal imaging

Spindle belt	Value	Units
Volume of the upper belt drive structure	602712	mm^3
Volume of the small belt drive	27803	mm^3
Total volume (upper belt drive structure and small belt drive)	630515	mm^3
Total area (upper belt drive and lower belt drive)	3.99E+04	mm^2
Total mass	4.92E-03	tonnes
Density of Steel	7.81E-09	$tonne/mm^3$
Cp of Steel	473000000	mJ/tonnes/°C
Time	30	s
h	0.006	$mW/mm^2/°C$
Initial ambient temperature	24.438	°C

Table C-4: Spindle belt data used for BHF calculations

The main iteration that obtained the transient BHF for the spindle belt is shown below.

Total volume = 630515 mm^3

Total mass = 4.92E-03 tonnes

Temperature difference (T_2-T_1) = 0.196053178 °C (between two logs)

Total time = 30s (logging time interval)

Convection coefficient (h) = 0.006 $mW/mm^2/°C$

Ambient temperature change = Varied from 24.438°C to 25.563°C during the heating cycle – Used transiently during calculations

Total exposed area = 3.99E+04 mm^2

By applying these values in equation 3.6, the value for the Q' is

Q' = 15596.73591 mW

The value of Q' is required to be divided by the volume of the heat source which in this case is the volume of the small belt drive.

$\acute{q}$ = 15596.73591 mW / 27803 mm^3 which gives the BHF value as

$\acute{q}$ = 0.56 mW/mm^3

Z-axis motor bracket (4000 and 8000rpm)

Similar to the test mandrel and spindle mount plate, the Z motor is also considered as a neighbouring heat source that contributes relatively lesser towards total thermal deformation of the machine compared to the main heat sources. Since Z-axis motor holds the axis in position, the energising rate is independent of spindle speeds, therefore the calculated BHF was used for both tests (4000 and 8000rpm).

For the Z-axis BHF, the selected volume (Figure 4-39 – chapter 4) from the column was taken and the volume of the Z-axis motor was used to divide the total energy Q' obtained to obtain the BHF value. Thermal imaging (Figure 4-36 – chapter 4) was used to extract temperature data from the inserted points using the thermal imaging software. Table C-5 shows the data of the Z-axis motor used to calculate the BHF value.

Z-axis motor bracket	Value	Units
Volume of the selected column area	4.53E+06	mm^3
Volume of the Z-axis motor bracket	9.80E+04	mm^3
Total volume (selected column area and the Z-axis motor bracket)	4.63E+06	mm^3
Total area (selected column area and the Z-axis motor bracket)	4.82E+05	mm^2
Total mass	0.03612154	tonnes
Density of Steel	7.81E-09	tonne/mm^3

Cp of Steel	473000000	mJ/tonnes/°C
Time	1500	s
h	0.006	mW/mm^2/°C
Initial ambient temperature	24.438	°C

Table C-5: Z-axis motor mount plate data used for BHF calculations

The main iteration that obtained the transient BHF for the Z axis motor bracket is shown below.

Total volume = 4.63E+06 mm^3

Total mass = 0.03612154 tonnes

Temperature difference (T_2-T_1) = 1.7°C

Total time = 1500s

Convection coefficient (h) = 0.006 mW/mm^2/°C

Ambient temperature change = 1°C (during the stabilization cycle)

Total exposed area = 4.82E+05mm^2

By applying these values in equation 3.6, the value for the *Q'* is

Q' = 22853.81 mW

The value of *Q'* is required to be divided by the volume of the heat source which in this case is the volume of the Z axis motor bracket.

$\acute{q}$ = 22853.81 mW / 9.80E+04 mm^3 which gives the BHF value as

$\acute{q}$ = 0.23 mW/mm^3

Same procedure was followed to obtain BHF values for the 4000rpm speed. Trend lines were plotted on the data obtained from the sensors to refine them.

Lower bearing (4000rpm)

Figure C-4 shows the trend line plotted on the temperature data obtained from the lower bearing at 4000rpm. The dimensional data for the lower bearing (chapter 4) was

used and same calculation procedure was followed to calculate the BHF value for the lower bearing at 4000rpm as used for the 8000rpm BHF calculations.

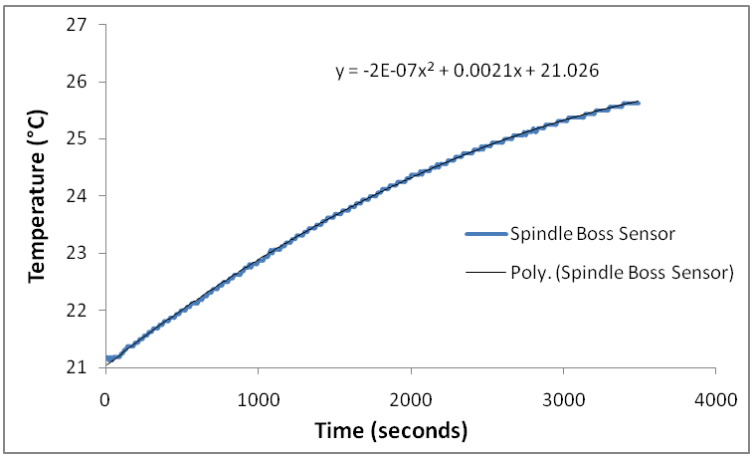

Figure C-4: Trend line plotted on the temperature data from lower bearing

Temperature difference (T_2-T_1) = 0.02094°C (between two logs)

Ambient temperature change = 0.25°C (during the heating cycle)

The BHF obtained for the lower bearing is

$$q' = 0.057518097 \text{ mW/mm}^3$$

The energy loss was calculated using the test mandrel dimensional data (chapter 4). The lower half of the test mandrel was neglected because of negligible temperature magnitude.

Temperature difference (T_2-T_1) = 0.25°C

The BHF obtained for the test mandrel upper half is

$$q' = 0.001757788 \text{ mW/mm}^3$$

The total BHF obtained after adding both BHFs

$$\mathbf{q' = 0.06 \text{ mW/mm}^3}$$

Upper bearing (4000rpm)

Figure C-5 shows the trend line plotted on the temperature data obtained from the upper bearing at 4000rpm. The dimensional data for the lower bearing (Table C-1) was used to calculate the BHF value for the upper bearing at 4000rpm.

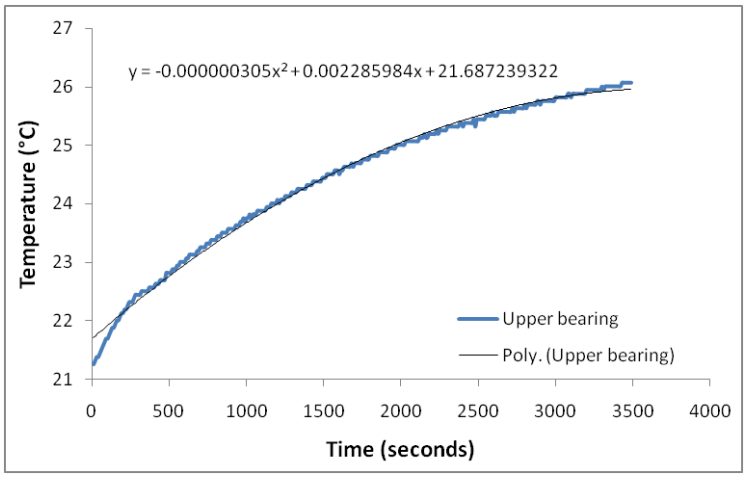

Figure C-5: Trend line plotted on the temperature data from upper bearing

Temperature difference (T_2-T_1) = 0.063°C (between two logs)

Ambient temperature change = 0.25°C (during the heating cycle)

The BHF obtained for the upper bearing is

$$q' = 0.11 mW/mm^3$$

Carrier belt drive and spindle motor mount plate (4000rpm)

Figure C-6 shows the obtained temperature data from the carrier head sensors. Figure C-7 shows the trend line plotted on the temperature data obtained from the sensor number 4 in strip 1 (closest to the heat source with highest temperature magnitude) at 4000rpm. The dimensional data for the carrier belt drive (Table C-2) was used to calculate the BHF value for the carrier belt drive at 4000rpm.

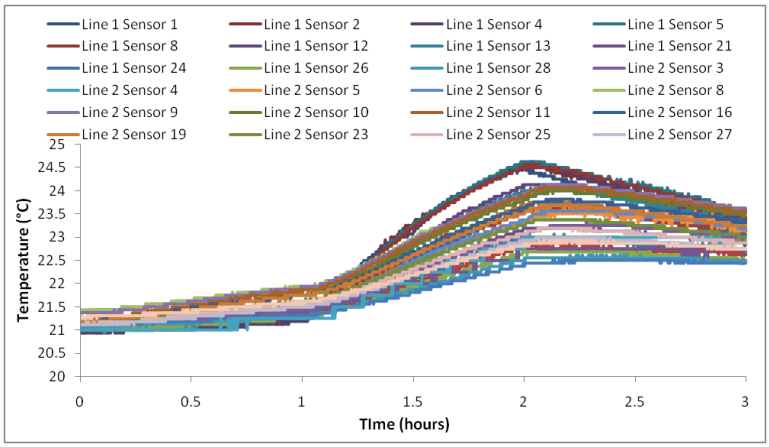

Figure C-6: The temperature data was selected from this set for BHF calculations (4000rpm)

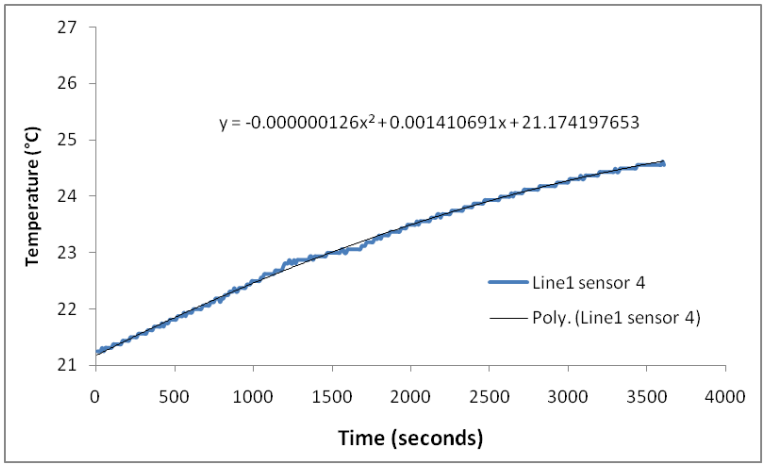

Figure C-7: Trend line plotted on the temperature data from carrier belt drive

Temperature difference (T_2-T_1) = 0.02094°C (between two logs)

Ambient temperature change = 0.25°C (during the heating cycle)

$$\boldsymbol{q' = 0.37\ mW/mm^3}$$

The BHF for the spindle motor mount plate was calculated using the spindle motor mount plate dimensional data (Table C-3). The sensor closest to the heat source with highest temperature magnitude was sensor number 11 in strip 2.

Temperature difference (T_2-T_1) = 2.813°C (between two logs)

The BHF obtained for the spindle motor mount plate is

$$\boldsymbol{q' = 0.08\ mW/mm3}$$

Spindle belt (4000rpm)

Figure C-8 shows the trend line plotted on the temperature data obtained from the spindle belt at 4000rpm using thermal imaging. The dimensional data for the spindle belt (Table C-4) was used to calculate the BHF value for the spindle belt at 4000rpm. Logging time interval of 10s was used.

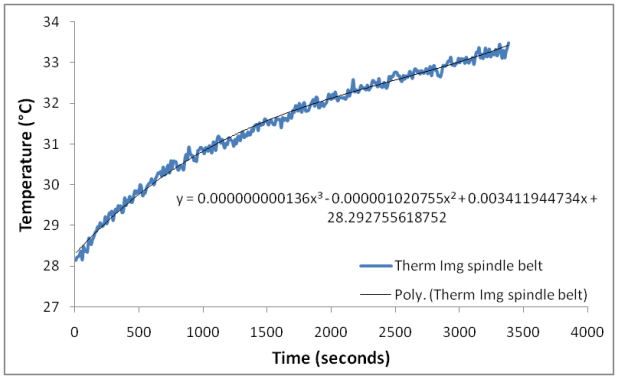

Figure C-8: Trend line plotted on the temperature data from thermal imaging

Temperature difference (T_2-T_1) = 0.033814173°C (between two logs)

Ambient temperature change = 0.25°C (during the heating cycle)

$\dot{q}$ = 0.33 mW/mm3

Specific heat capacity (8000rpm)

For calculations of specific heat capacity (Cp) mentioned in section 4.3.5 of chapter 4, temperature data from the spindle boss sensor was used. An 'Artificial' material was defined with the defined Cp values and was applied to both upper and lower spindle bearings.

The calculations were performed on the data obtained from the spindle boss sensor as this is the place where the temperature was measured. Using the trend lined data (Chapter 4), Cps were calculated iteratively as a function of temperature. The values of Cps have shown an increasing trend which explains the stabilization of the temperature at the spindle boss during the test length. The values of Cp and the respective temperature data were averaged. The averaging was kept up to 90 points i.e. four Cp values were obtained to define an increasing trend. Equation 3.5 was transformed for the specific heat capacity as shown in equation C-1.

$$Cp = Q / m(T_2 - T_1)$$ .....(C-1)

Table C-6 shows the obtained Cp values corresponding to the spindle boss temperature magnitudes.

Trend lined spindle boss temperature (°C)	**Cp**
25.07234784	473000000
25.19027694	474497186
25.30783393	476003879
25.42501882	477520172
25.54183161	479046156
25.65827229	480581924
25.77434087	482127570
25.89003735	483683191
26.00536172	485248884
26.120314	486824745
26.23489416	488410875
26.34910223	490007375
26.4629382	491614345
26.57640206	493231891
26.68949381	494860116
26.80221347	496499127
26.91456102	498149030
27.02653647	499809936
27.13813982	501481955
27.24937106	503165197
27.36023021	504859778
27.47071724	506565811
27.58083218	508283413
27.69057501	510012703
27.79994574	511753800
27.90894437	513506825
28.01757089	515271901
28.12582532	517049154
28.23370764	518838709
28.34121785	520640694
28.44835597	522455241
28.55512198	524282479
28.66151588	526122544
28.76753769	527975570
28.87318739	529841695
28.97846499	531721059
29.08337049	533613802
29.18790388	535520069
29.29206517	537440004
29.39585436	539373756
29.49927145	541321473
29.60231643	543283308
29.70498931	545259414
29.80729008	547249949
29.90921876	549255070
30.01077533	551274939
30.1119598	553309719
30.21277216	555359575
30.31321243	557424676
30.41328059	559505192
30.51297665	561601297
30.6123006	563713167
30.71125245	565840980
30.8098322	567984917
30.90803985	570145162
31.00587539	572321902
31.10333883	574515328
31.20043017	576725630
31.2971494	578953005
31.39349654	581197652
31.48947157	583459772
31.58507449	585739570
31.68030532	588037253
31.77516404	590353034
31.86965066	592687127
31.96376517	595039750
32.05750758	597411124
32.15087789	599801475
32.2438761	602211031
32.3365022	604640025
32.42875621	607088693
32.5206381	609557275
32.6121479	612046014
32.70328559	614555159
32.79405118	617084962
32.88444467	619635679
32.97446606	622207570
33.06411534	624800900
33.15339252	627415938
33.24229759	630052958
33.33083057	632712238
33.41899144	635394062
33.5067802	638098717
33.59419687	640826495
33.68124143	643577696
33.76791389	646352622
33.85421425	649151580
33.9401425	651974885
34.02569865	654822856
34.1108827	657695817
34.19569465	660594099
34.28013449	663518038
34.36420223	666467975
34.44789787	669444261
34.5312214	672447248
34.61417283	675477298
34.69675216	678534778
34.77895939	681620064
34.86079451	684733534
34.94225753	687875579
35.02334845	691046592
35.10406726	694246977
35.18441397	697477142
35.26438858	700737507
35.34399109	704028496
35.42322149	707350543
35.50207979	710704089
35.58056599	714089586
35.65868008	717507491
35.73642208	720958272
35.81379197	724442406
35.89078975	727960378
35.96741544	731512685
36.04366902	735099830
36.1195505	738722330
36.19505987	742380710
36.27019714	746075504
36.34496231	749807260
36.41935538	753576535
36.49337634	757383898
36.56702521	761229929
36.64030196	765115220
36.71320662	769040375
36.78573917	773006011
36.85789962	777012757
36.92968797	781061257
37.00110422	785152165
37.07214836	789286152
37.1428204	793463903
37.21312033	797686115
37.28304817	801953502
37.3526039	806266793
37.42178752	810626734
37.49059905	815034083
37.55903847	819489620
37.62710579	823994139
37.69480101	828548452
37.76212412	833153389
37.82907513	837809800
37.89565404	842518551
37.96186085	847280530
38.02769555	852096646
38.09315815	856967827
38.15824865	861895021
38.22296704	866879202
38.28731333	871921363
38.35128752	877022523
38.41488961	882183722
38.47811959	887406027
38.54097747	892690530
38.60346325	898038348
38.66557692	903450627
38.72731849	908928538
38.78868796	914473283
38.84968533	920086093
38.91031059	925768228
38.97056375	931520982
39.03044481	937345677
39.08995376	943243674
39.14909062	949216364
39.20785537	955265174
39.26624801	961391571
39.32426856	967597055
39.381917	973883169
39.43919334	980251494

39.49609757	986703653
39.5526297	993241313
39.60878973	999866185
39.66457766	1.007E+09
39.71999349	1.013E+09
39.77503721	1.02E+09
39.82970883	1.027E+09
39.88400834	1.034E+09
39.93793575	1.042E+09
39.99149106	1.049E+09
40.04467427	1.056E+09
40.09748538	1.064E+09
40.14992438	1.071E+09
40.20199128	1.079E+09
40.25368607	1.087E+09
40.30500877	1.095E+09
40.35595936	1.103E+09
40.40653785	1.111E+09
40.45674423	1.119E+09
40.50657851	1.128E+09
40.55604069	1.136E+09
40.60513077	1.145E+09
40.65384874	1.154E+09
40.70219461	1.163E+09
40.75016838	1.172E+09
40.79777005	1.181E+09
40.84499961	1.19E+09
40.89185707	1.2E+09
40.93834243	1.21E+09
40.98445568	1.219E+09
41.03019683	1.229E+09
41.07556588	1.24E+09
41.12056283	1.25E+09
41.16518767	1.26E+09
41.20944041	1.271E+09
41.25332105	1.282E+09
41.29682958	1.293E+09
41.33996601	1.304E+09
41.38273034	1.316E+09
41.42512257	1.327E+09
41.46714269	1.339E+09
41.50879071	1.351E+09
41.55006663	1.364E+09
41.59097045	1.376E+09
41.63150216	1.389E+09
41.67166177	1.402E+09
41.71144927	1.415E+09
41.75086468	1.429E+09

41.78990798	1.442E+09
41.82857918	1.456E+09
41.86687827	1.471E+09
41.90480526	1.485E+09
41.94236015	1.5E+09
41.97954294	1.515E+09
42.01635363	1.531E+09
42.05279221	1.547E+09
42.08885869	1.563E+09
42.12455306	1.579E+09
42.15987533	1.596E+09
42.1948255	1.613E+09
42.22940357	1.631E+09
42.26360954	1.649E+09
42.2974434	1.667E+09
42.33090516	1.686E+09
42.36399481	1.705E+09
42.39671237	1.725E+09
42.42905782	1.745E+09
42.46103117	1.765E+09
42.49263241	1.786E+09
42.52386155	1.808E+09
42.55471859	1.83E+09
42.58520353	1.852E+09
42.61531636	1.876E+09
42.64505709	1.899E+09
42.67442572	1.924E+09
42.70342225	1.949E+09
42.73204667	1.974E+09
42.76029899	2.001E+09
42.78817921	2.028E+09
42.81568732	2.056E+09
42.84282333	2.084E+09
42.86958724	2.114E+09
42.89597905	2.144E+09
42.92199875	2.175E+09
42.94764635	2.207E+09
42.97292185	2.24E+09
42.99782524	2.274E+09
43.02235653	2.309E+09
43.04651572	2.345E+09
43.07030281	2.382E+09
43.09371779	2.421E+09
43.11676067	2.46E+09
43.13943145	2.502E+09
43.16173013	2.544E+09
43.1836567	2.588E+09
43.20521117	2.633E+09

43.22639353	2.68E+09
43.2472038	2.729E+09
43.26764196	2.78E+09
43.28770802	2.832E+09
43.30740197	2.887E+09
43.32672383	2.944E+09
43.34567357	3.003E+09
43.36425122	3.064E+09
43.38245677	3.128E+09
43.40029021	3.195E+09
43.41775155	3.264E+09
43.43484078	3.337E+09
43.45155791	3.413E+09
43.46790295	3.492E+09
43.48387587	3.575E+09
43.4994767	3.663E+09
43.51470542	3.755E+09
43.52956204	3.851E+09
43.54404655	3.953E+09
43.55815897	4.06E+09
43.57189928	4.173E+09
43.58526749	4.292E+09
43.59826359	4.419E+09
43.61088759	4.553E+09
43.62313949	4.695E+09
43.63501929	4.847E+09
43.64652698	5.009E+09
43.65766257	5.182E+09
43.66842606	5.368E+09
43.67881745	5.567E+09
43.68883673	5.782E+09
43.69848391	6.014E+09
43.70775899	6.265E+09
43.71666196	6.539E+09
43.72519283	6.837E+09
43.7333516	7.164E+09
43.74113827	7.523E+09
43.74855283	7.921E+09
43.75559529	8.362E+09
43.76226565	8.856E+09
43.7685639	9.413E+09
43.77449005	1.004E+10
43.7800441	1.076E+10
43.78522605	1.16E+10
43.79003589	1.257E+10
43.79447363	1.372E+10
43.79853927	1.51E+10
43.80223281	1.679E+10

43.80555424	1.891E+10
43.80850357	2.164E+10
43.81108079	2.53E+10
43.81328592	3.043E+10
43.81511894	3.818E+10
43.81657986	5.123E+10
43.81766867	7.783E+10
43.81838539	1.619E+11
43.81873	2.029E+12
43.8187025	1.396E+11
43.81830291	7.228E+10
43.81753121	4.877E+10
43.81638741	3.68E+10
43.8148715	2.954E+10
43.8129835	2.468E+10
43.81072339	2.119E+10
43.80809117	1.857E+10
43.80508686	1.652E+10
43.80171044	1.488E+10
43.79796192	1.354E+10
43.79384129	1.242E+10
43.78934857	1.147E+10
43.78448374	1.065E+10
43.77924681	9.945E+09
43.77363777	9.326E+09
43.76765663	8.78E+09
43.76130339	8.294E+09
43.75457805	7.859E+09
43.7474806	7.468E+09
43.74001105	7.113E+09
43.7321694	6.791E+09
43.72395565	6.497E+09
43.71536979	6.227E+09
43.70641183	5.979E+09
43.69708177	5.749E+09
43.6873796	5.537E+09
43.67730533	5.34E+09
43.66685896	5.156E+09
43.65604049	4.985E+09
43.64484991	4.824E+09
43.63328723	4.674E+09
43.62135245	4.532E+09
43.60904556	4.399E+09
43.59636657	4.274E+09
43.58331548	4.156E+09
43.56989229	4.043E+09
43.55609699	3.937E+09
43.54192959	3.836E+09

43.52739009	3.741E+09
43.51247849	3.65E+09

Table C-6: Obtained Cp values with spindle boss temperature

The averaged Cp values used to define the ‘Artificial’ material are shown in Table C-7.

Temperature (°C)	**Cp**
29.77482022	554200801.9
37.58293333	834268351.2
41.84681111	1749373477
43.7162	37159431678

Table C-7: Cp values and the corresponding temperature values (averaged to 90 points)

Creating and defining ‘Artificial’ material in Abaqus

Figure C-9 and Figure C-10 shows creation of the ‘Artificial’ material where Cp values were defined as temperature dependent property in two separate ‘Fields’. The Field ‘1’ is defined for the heating cycle and Field ‘2’ was defined for the cooling cycle. Abaqus Keyword Editor was then used to call each Field during the simulation. Figure C-11. Figure C-12 shows the call of ‘SetSteel 2.0’ (bearing set with Field ‘2’ Cp value) during the cooling cycle.

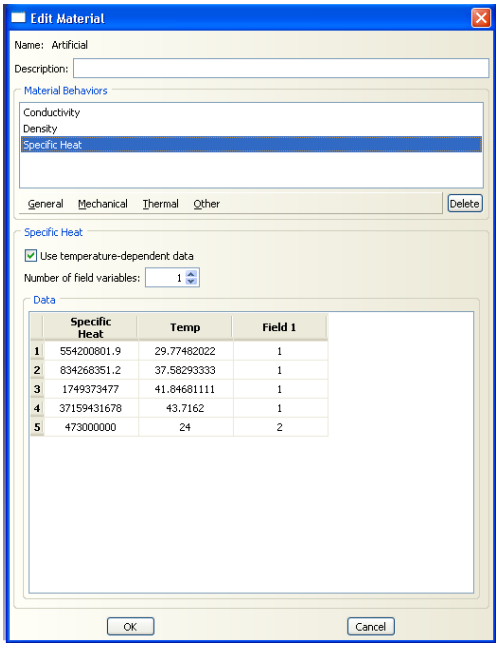

Figure C-9: Calculated Cp values applied within 'Artificial' material

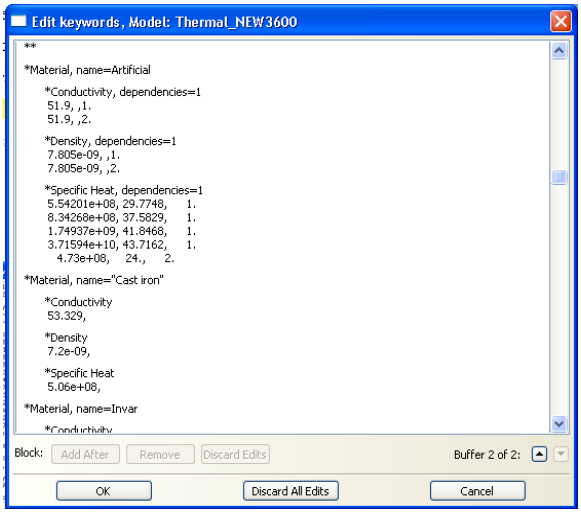

Figure C-10: Method of defining material within Abaqus Keywords editor

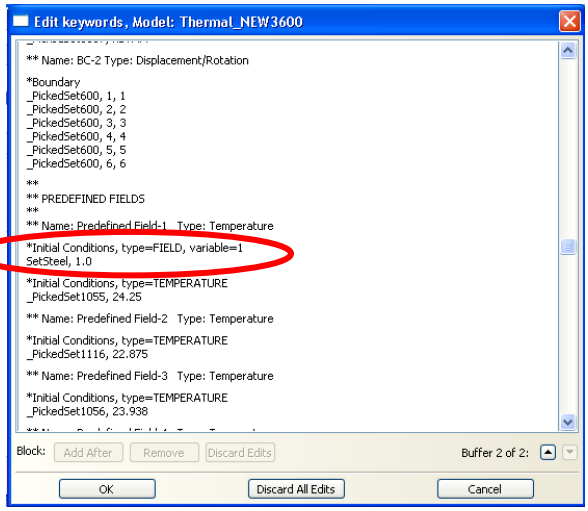

Figure C-11: Defining material for the heating cycle

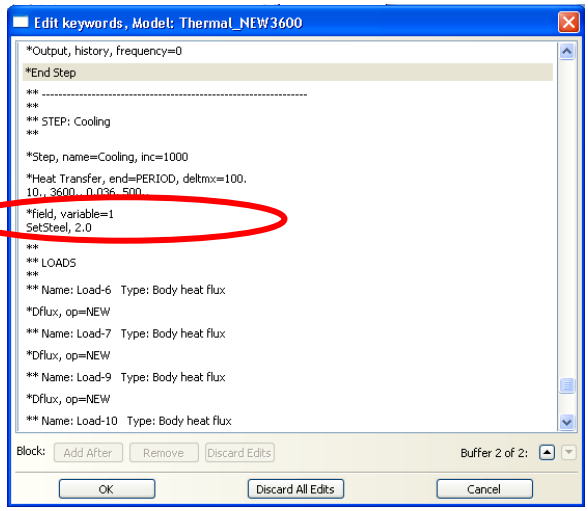

Figure C-12: Defining material for the cooling cycle

APPENDIX D – MATLAB FUNCTIONS

PROGRAM 1

This program imports the nodal temperature data obtained from the Abaqus output file. The program plots the slope and the hysteresis for a user defined node number.

```
global c d
ad=uiimport;
% import Thermal data

if isfield(ad,'datastruct')
%read the data from structures

   data1=ad.datastruct;
% Save into data1

end

if ~isempty(data1)
%check if data1 is not empty

   fieldname=fieldnames(data1);
% extract fieldnames

   Th=getfield(data1,fieldname{1});
%get the field and save into Th

else
   disp('No thermal data loaded!');
%else show no data loaded

End

Th(:,1) = [];
% remove the first (time) column

ad=uiimport;
%import Displacement data

if isfield(ad,'datastruct')
   data2=ad.datastruct;
end

if ~isempty(data2)
   fieldname=fieldnames(data2);
   dsp=getfield(data2,fieldname{1});
   dsp=dsp*1000;
% change into microns

else
   disp('No displacement data loaded!');
end
dsp(:,1) = [];
%remove the first (time) column

while (1);
Nth = input('Enter Node Number (Thermal): ');
% Thermal node number for data plot

while (Nth<1 | Nth>size(Th([],:)))
%Node number has to be within the size of the columns

disp(['Please enter node numbers between ', int2str(size(Th([],:)))])
   Nth = input('Enter Node Number (Thermal): ');
   end

plot(Th(:,Nth),dsp(:,1))
%plot given thermal node against displacment node (484 from FEA)
```

```
   xlabel('Temperature (\circC)') %axis labels
   ylabel('Error (microns)')

   hold on
   input('Press Enter for the slope: '); %Slope plot
[m,c,r,v]=linearls([Th(:,Nth) dsp(:,1)],1);
%linearls function for slope plot

   m
%show slope value

   hold on;
end
```

PROGRAM 2

This program imports the nodal temperature data obtained from the Abaqus output file. The code filters nodes with the highest slope and lowest hysteresis using a range given (%range).

```
clear all
global c d

ad=uiimport;
if isfield(ad,'datastruct')
   data1=ad.datastruct;
end

if ~isempty(data1)
   fieldname=fieldnames(data1);
   Th=getfield(data1,fieldname{1});
else
   disp('No thermal data loaded!');
end

Th=ref_cols(Th);
Th(:,1) = [];

ad=uiimport;
if isfield(ad,'datastruct')
   data2=ad.datastruct;
end

if ~isempty(data2)
   fieldname=fieldnames(data2);
   dsp=getfield(data2,fieldname{1});
   dsp=dsp*1000;
else
   disp('No displacement data loaded!');
end
dsp(:,1) = [];

%%%%%%% FOR SLOPE %%%%%%%
for i=1:size(Th,2) % (size(Th,2)..size of Th and take second number, 0 4099)check the size of Th and range it to highest (0 4099)

   [m,c,r,v]=linearls([Th(:,i) dsp(:,1)],0);
   Slope_Sens(i,1)=i;                    % first row first column put i
   Slope_Sens(i,2)=1/m;                  % Second row second column put 1/m for getting C/microns sensitivity
   max_slope=max(Slope_Sens(:,2));
   min_slope=min(Slope_Sens(:,2));
   filt_slope=Slope_Sens;

%     hold on;
end
% figure, stem(Slope_Sens(:,1),Slope_Sens(:,2)) %stem plot of m

%%%%% FOR HYSTERESIS %%%%%%%
for i=1:size(Th,2)
% (size(Th,2)..size of Th and take second number, 0 4099)check the
```

```
size of Th and range it to highest (0 4099)

[m,c,r,v]=linearls([Th(:,i) dsp(:,1)],0);
% All thermal data but only one displacement data

Hyst_slope=v-v;
Hyst_curve=dsp(:,1)-v;
%same column for displacement data

rge=abs(max(Hyst_curve))+abs(min(Hyst_curve));
Hyst_range(i,1)=i;
   % first row first column put i

Hyst_range(i,2)=rge;
% Second row second column put range (rge)
min_Hyst=min(Hyst_range(:,2));
filt_hyst=Hyst_range;
end

chkSlope=filt_slope(:,2)< %range | filt_slope(:,2)> %range;
%criteria for removing from Slope array (1's will be removed) only middle range is filtered

chkHyst=filt_hyst(:,2)<5.446 | filt_hyst(:,2)>8;
%criteria for removing from Sens array (1's will be removed)

chk=bitor(chkSlope, chkHyst);
%combine the criteria

rem=filt_slope(chk);

%grab all the column numbers to be removed using above
criteria..%any one could be used either filt_hyst or filt_slope...it
is multiplying and filtering out those nodes that multiplies with 0.
i.e. rem will end up in those nodes that are not required or have
values beyond the defined criteria.

filt_slope(rem,:)= [];

%remove these columns from Slope array...i.e. all columns from
filt_slope will be deleted that are in rem leaving only those which
meets the criteria

filt_hyst(rem,:)= [];
 %remove these columns from Sens array ...same as above

filtered=filt_slope;
filtered(:,3)=filt_hyst(:,2);
```